UNIVERSIDAD COMPLUTENSE DE MADRID
FACULTAD DE CIENCIAS FÍSICAS

TESIS DOCTORAL

Nano-estructuras tridimensionales funcionales (alúmina 3D y redes de nanohilos interconectados en las 3 direcciones del espacio)

Functional 3D Nanostructures (3D alumina membranes and 3D nanowire-networks)

MEMORIA PARA OPTAR AL GRADO DE DOCTOR

PRESENTADA POR

Alejandra Ruiz de Clavijo García-Serrano

Directoras

Marisol Martín González
Olga Caballero Calero

Madrid

UNIVERSIDAD COMPLUTENSE DE MADRID

FACULTAD DE CIENCIAS FÍSICAS

TESIS DOCTORAL

Nano-estructuras tridimensionales funcionales
(alúmina 3D y redes de nanohilos interconectados
en las 3 direcciones del espacio)

Functional 3D Nanostructures
(3D alumina membranes and 3D nanowire-networks)

MEMORIA PARA OPTAR AL GRADO DE DOCTORA

PRESENTADA POR

Alejandra Ruiz de Clavijo García-Serrano

DIRECTORAS

Prof. Marisol Martín González y Dra. Olga Caballero Calero

Agradecimientos

A lo largo de estos años de trabajo he contado con el apoyo y ayuda de diversas personas, a las cuales en estas pocas líneas me gustaría agradecerles hoy su contribución al desarrollo de esta Tesis. Mención especial merecen mis directoras, la Prof. Marisol Martín González y la Dra. Olga Caballero Calero, quienes me han guiado a lo largo de este trabajo, tanto con conocimientos científicos como con su apoyo. De ellas he recibido una experiencia enriquecedora en lo profesional y lo personal, y les agradezco especialmente la oportunidad que me han dado y confianza depositada en mí. Ambas son mujeres con gran pasión por la ciencia que contagian su dedicación y entusiasmo.

A mi tutor, el Dr. Lucás Peréz, por la ayuda prestada y su colaboración en esta tesis, con quien siempre he podido contar para tratar tanto temas académicos como burocráticos.

Gracias a mis compañeros y miembros de grupo: Begoña, Marta, Jaime, Liliana, Pedro, Rut, Rafa, Cristina, Alba y Pablo, con los que tantos momentos buenos he compartido fuera y dentro del laboratorio. En particular, quería mencionar especialmente a Liliana, ya que haber vivido esta experiencia con ella ha sido una suerte, y me siento privilegiada por ello. También agradecer el tiempo compartido con las incorporaciones tardías al 105, Mica y Dani.

Gracias a todos los magníficos investigadores con los que he tenido la tremenda suerte de colaborar, sus conocimientos en otras áreas y campos científicos me han enriquecido a mí y a este trabajo. Dr. Ruy Sanz y Dr. David Navas unos cracks del magnetismo y magníficas personas. Gracias también al Dr. Lucas Pérez (otra vez) y a la Dra. Sandra Ruiz Gómez, quienes fueron imprescindibles para comenzar mi andadura en el ámbito del magnetismo. A los doctores Xavier Álvarez y Alberto Beardo, grandísimos científicos teóricos con unas mentes brillantes, muy didácticos y con mucha paciencia, a lo que unen una enorme calidad humana. También quería agradecerles al Dr. Eric Garcia Hemme y al Dr. David Pastor su ayuda en este trabajo, enseñándome y permitiéndome realizar medidas en su sistema Hall.

On the other hand, I would like to thank the people involved in my scientific stays. I am very grateful to Prof. Kornelius Nielsch, who received me at the Leibniz Institute for solid state and materials research (IFW) in Dresden (Germany). During this time, I could access their facilities and they taught me to work with new systems and techniques. In particular, I would like to thank Dr. Nicolas Pérez for all his time, with whom I worked and learned there the most.

Also, during a brief stay at Jean Lamour institute, located in Mezt (France) I had the pleasure to meet and work with Dr. Nicolas Stein, to whom I am grateful to let me use all their measurement systems, for sharing with me his expertise and being such a nice and good person. And Melanie with her patience during my stay there, thank you to show me around.

Por último, me gustaría también agradecer a mi familia, a toda ella, aunque a veces seamos muchos y un poco pesados, simplemente por estar siempre ahí.

Table of contents

List of Figures

List of tables

Resumen

Este trabajo de tesis se centra en el desarrollo de nanoestructuras funcionales interconectadas para diversas aplicaciones, desde la obtención de color estructural a la fabricación de metamateriales magnéticos con propiedades modificadas, así como metamateriales termoeléctricos de alta eficiencia. En todos estos casos, la fabricación de estas nanoestructuras se ha basado en dos procesos: anodización de aluminio y crecimiento electroquímico. Ambos son procesos químicos que no requieren de vacío y que son muy conocidos a nivel industrial. Los resultados que se presentan en este manuscrito muestran el estado del arte en ambas técnicas, lo que queda patente por las publicaciones científicas a las que este trabajo ha dado lugar.

Brevemente, el objetivo principal de esta Tesis ha sido probar la versatilidad de un tipo de membranas de alúmina desarrolladas recientemente para el desarrollo de futuras aplicaciones nanotecnológicas. Estas membranas consisten en poros longitudinales que están unidos por poros transversales más pequeños que forman canales que los conectan. Estas membranas de alúmina tridimensionales (3D-AAO, del inglés 3D Anodic Aluminum Oxide) se han estudiado, por un lado, como plataformas para la generación de dispositivos en sí mismas, y, por otro lado, como plantillas para crecer en su estructura porosa distintos materiales y nanoestructurarlos, modificando de este modo sus propiedades. Los distintos temas tratados en este trabajo son los siguientes:

(1) Crecimiento de las muestras 3DAAO por anodización pulsada.

(2) Caracterización de las propiedades ópticas de las membranas 3DAAO: formación de color estructural e ingeniería de la modificación del bandgap fotónico de acuerdo con las propiedades estructurales. Aplicaciones como sensores colorimétricos.

(3) Nanoestructuración de Ni, Co, aleaciones de Ni- Co y Bi_2Te_3, formando redes interconectadas de nanohilos tridimensionales mediante el depósito electroquímico de estos materiales en la estructura porosa de las alúminas 3D. Esto requiere encontrar las

condiciones de depósito óptimos para el Ni y el Co, así como para la co-deposición de las aleaciones y el teluro de bismuto, lo que implica el depósito simultáneo de ambos elementos, Ni y Co en un caso, y Bi y Te en el otro.

(4) Análisis exhaustivo de la correlación entre las propiedades magnéticas de las nano-redes 3D y los parámetros estructurales, tales como el diámetro de los nanohilos, y prestando especial atención a la influencia de la presencia de las conexiones transversales (TCs, del inglés, Transverse Connections) a lo largo de los nanohilos (por ejemplo, modificando la distancia de estas conexiones transversales).

(5) Evaluación de las propiedades de transporte del Bi_2Te_3, material termoeléctrico ampliamente conocido, cuando se nanoestructura formando una nanored tridimensional, para buscar aumentar su eficiencia termoeléctrica. La adición de conexiones transversales a lo largo de los nanohilos produce cambios en sus propiedades de transporte eléctrico y térmico cuando se compara con arreglos de nanohilos convencionales (no interconectados).

Los resultados de estas nanoestructuras funcionales han podido estudiarse gracias al desarrollo y control preciso de los procesos de crecimiento, así como a la caracterización exhaustiva de sus propiedades, que ha permitido entender y modificar estas propiedades. Por ello, para dar cabida a todos estos resultados, el manuscrito está dividido en seis capítulos, comenzando por una introducción a las nanoestructuras desarrolladas, el conjunto de técnicas de fabricación y caracterización utilizadas y, finalmente, tres capítulos dedicados a las nanoestructuras y sus propiedades en el campo de la óptica, magnetismo y termoelectricidad, respectivamente. En detalle, la distribución del manuscrito es la siguiente:

El Capítulo 1 proporciona una visión general sobre las nanoestructuras más relevantes y prometedoras desarrolladas recientemente y que pueden resultar en soluciones novedosas a diversos problemas tecnológicos. De entre estas nanoestructuras, nos centraremos en la técnica económica y fácilmente escalable a la industria de la fabricación de membranas porosas de óxido de aluminio (AAO). En este capítulo se introduce también el concepto de la dimensionalidad de las nanoestructuras, típicamente divididas en 2-D (en el caso de láminas), 1-D (nanohilos) y 0-D (puntos cuánticos), añadiendo la

categoría 3-D como las nanoarquitecturas fabricadas en este trabajo (en contraposición a la consideración de 3D como volumen).

En el Capítulo 2 se resumen las técnicas experimentales utilizadas en este trabajo de tesis, desde las empleadas en el crecimiento de la alúmina 3D y las redes 3D de nanohilos interconectados a las técnicas de caracterización estructurales, ópticas, magnéticas y de transporte utilizadas con las distintos materiales nanoestructurados estudiados (óxido de aluminio, níquel, cobalto y telururo de bismuto).

El Capítulo 3 presenta los resultados experimentales obtenidos en cuanto al estudio de las propiedades ópticas de las estructuras de alúmina 3D (3DAAOs) fabricadas con distintas distancias de separación entre los canales transversales para producir determinadas respuestas fotónicas que pueden asociarse a distintos colores estructurales. Las medidas experimentales están soportadas por simulaciones teóricas para predecir la formación de color estructural en este tipo de 3DAAOs para diseñar sensores colorimétricos (variando la distancia de los canales porosos transversales).

El Capítulo 4 está dedicado al estudio de las propiedades magnéticas de nanoestructuras 3D interconectadas de Ni, Co, y aleaciones de Ni-Co, donde la presencia de las conexiones transversales entre los nanohilos se asocia a sitios de fijado de paredes de dominio magnético. La influencia de la energía magnetocristalina en las propiedades magnéticas de estas nanoestructuras 3D también se muestra, siendo investigada a través de aleaciones de Ni-Co en distintas proporciones. Así mismo, se realizaron simulaciones micromagnéticas para ayudar a interpretar el comportamiento magnético de las nanoestructuras 3D.

El Capítulo 5 discute el efecto de la morfología característica de estas estructuras 3D interconectadas en las propiedades del teluro de bismuto, que es un material termoeléctrico ampliamente conocido y utilizado para aplicaciones alrededor de temperatura ambiente. La completa caracterización de estas nanoestructuras 3D incluye la medida de su coeficiente Seebeck, conductividad eléctrica y conductividad térmica, medidas en distintas configuraciones y en distintas orientaciones, siempre que fuera posible. El modo en que esta nanoestructuración modifica las propiedades y cómo este entendimiento ha dado lugar a un metamaterial termoeléctrico de alta eficiencia también es tratado en este capítulo.

El Capítulo 6 presenta un resumen de las conclusiones más relevantes de los resultados de este trabajo de tesis, presentando también las direcciones de investigación futuras que complementarían este trabajo.

Finalmente, el manuscrito concluye con la lista de publicaciones, contribuciones a conferencias y premios relacionados con este trabajo de tesis, así como una sección de bibliografía. Adicionalmente, se han incluido tres apéndices (A, B y C) como extensión de la información dada en los Capítulos 3, 4 y 5, respectivamente.

Abstract

This Thesis has been focused on the development of functional nanostructures for a variety of applications, from structural coloring to magnetic nanostructures with tailored properties and highly efficient thermoelectric metamaterials. In all cases, the fabrication of such nanostructures has been based on two processes: aluminum anodization and electrochemical growth. Both are chemical processes, which need no vacuum and that are well known at the industrial level. The results that are presented in this manuscript represent the state of the art of both techniques, which is well endorsed by the publications that have resulted from it.

In brief, the main objective pursued in this Ph.D. Thesis has been to prove the versatility of a recent kind of alumina membranes, consisting of longitudinal pores that are transversely perforated by smaller pore channels, in the development of future nanotechnology applications. These 3D-Anodic alumina templates (3D AAO) have been studied by themselves, but also used as templates to grow different materials and tune their properties. The different topics covered in this work can be listed as follows:

(1) Growth by MA/HA pulsed anodization technique of the 3D AAO templates.

(2) Characterization of the optical properties of 3D AAO membranes: structural color formation and photonic band gap engineering according to the structural properties of the 3D porous structure. Finding applications for the development of colorimetric sensors.

(3) Nanostructuring of Ni, Co, Ni-Co alloys, and Bi_2Te_3 in the form of interconnected 3D nanowire networks, by filling the porous structure of such 3D alumina membranes through chemical electrodeposition. This requires finding the optimized deposition conditions for Ni and Co single elements as well as for the co-deposition of the alloys, Ni-Co and Bi_2Te_3, which entails simultaneous deposition of both elements, Ni and Co, and Bi and Te species, respectively.

(4) Extensive analysis of the correlation between the magnetic properties of the magnetic 3D nano-networks and the structural parameters of the networks, regarding the diameter of the nanowires, and paying special attention to the influence of the presence of transverse connection (TCs) along the wires (i.e. varying the distance between transverse connections).

(5) Evaluation of the transport properties of well-known thermoelectric material, such as Bi_2Te_3, when nanostructured forming a 3D network, looking to enhance its thermoelectric performance. The addition of transverse connections along the length of the wires will bring changes in the electrical and thermal transport compared to more conventional non-interconnected nanowires.

The outcomes of these functional nanostructures have been not only possible thanks to the development and precise control of the fabrication processes, but also through their thorough characterization which has allowed us to understand and modify their properties. Therefore, to cope with all these results, this Thesis is divided into six different chapters, which will present an introduction to the nanostructures developed, the different fabrication and characterization techniques used, and finally, three chapters devoted to the optical, magnetic, and thermoelectric nanostructures and their properties. In detail, the distribution of the manuscript is as follows.

Chapter 1 provides a background view of some of the most relevant and promising nanostructures that have been recently developed and that can bring novel solutions to the problems encountered in the present technology. But, bringing the focus towards a non-expensive, and easily scalable technology that employs anodic aluminium oxide (AAO) membranes. This Chapter introduces also a new concept regarding the dimensionality of the nanostructures, typically labeled as bulk, 2-D (for films), 1-D (for nanowires), and 0-D (quantum dots), in which we must include a new category 3D nanoarchitectures when 3D materials were often considered as bulk.

Chapter 2 summarizes the experimental techniques employed in this Thesis work, covering all steps from the growth of the 3D alumina and 3D nanowire networks to the characterization of the structural, optical, magnetic, and transport properties of the different nanostructured materials (aluminium oxide, nickel, cobalt, and bismuth telluride).

Chapter 3 presents experimental results concerning the optical properties of 3D AAO membranes fabricated with different separation distances between transversal pore channels, in order to produce specific photonic responses that can be associated with different structural coloring. The experimental measurements are supported by theoretical simulations on the prediction of structural color formation on this type of 3D AAOs (with the distance between transverse pore channels) for the design of colorimetric sensors.

Chapter 4 is devoted to the study of the magnetic properties of Ni, Co, and Ni-Co alloys synthesized in the form of 3D nanowire networks, where the presence of transverse connections along the nanowires is envisioned to act as pinning sites of domain wall motion. The influence of the magnetocrystalline energy over the magnetic properties of the 3D nano-networks was also investigated through alloying of Ni and Co in different proportions. Micromagnetic simulations were performed to help interpret the magnetic behaviour of the 3D networks.

Chapter 5 discusses the effect of the characteristic morphology of the 3D networks on the transport properties of a well-known thermoelectric material bismuth telluride. Complete characterization of the transport properties of the 3D nanostructures include the determination of the Seebeck coefficient, electrical conductivity, and thermal conductivity measured in different configurations, in-plane and out-of-plane, when possible. How the nanostructuration modifies the thermoelectric performance of this material is also presented in this chapter, giving rise to an enhanced thermoelectric metamaterial.

Chapter 6 summarizes the most relevant conclusions concerning the results in the Thesis work and gives several different future research directions which would complement the Thesis work.

Finally, the Thesis concludes with the list of publications, contributions to conferences, and awards related to this Thesis work, and a Bibliography Section. Additionally, three appendixes, A to C, were added with supporting information as an extension of Chapters 3, 4 and 5, respectively.

1. Chapter 1: Introduction

In this Thesis, novel functional nanostructures have been fabricated, characterized, and optimized. The main interest in the manipulation of materials at the nano-scale is to have access to properties and characteristics that are not available when dealing with bulk materials. Recent technological advances for the fabrication and characterization of controlled structures at this scale have triggered most of the latest technological advances of our society, which are based on nanotechnology. In such a way, structural colored surfaces, nanostructured magnetic metamaterials, or self-sustained thermoelectric generators based on interconnected nanowires have been developed. Given that the nanostructures developed in this Thesis work have a direct application in the field of nanotechnology, and therefore this chapter will start with a brief introduction to it. Then, the state of the art in the fabrication of anodic alumina templates, which is at the core of all the developments of this work, will be described, with special attention to the different formation theories and most interesting structures developed to date, as well as an example of different applications. It is important to note that all the work presented in this Ph.D. Thesis is based on a deep understanding of the anodization process, its mechanisms, and the possibilities that it provides, and that is the reason why this is presented in detail. In the case of the different applications developed in this work, short introductions to structural coloring, magnetism, and thermoelectricity will be provided at the beginning of each of chapters 4, 5, and 6, respectively.

1.1. State of the art of the interconnected 3D micro- and nanostructures

Nanotechnology is present in almost every single aspect of our lives, on our phones, cars, TV's, computers, and all electronic devices we can think of. Also, it is used in cosmetics, food, and medicine. The fields of application of different nanotechnological developments are rapidly growing. We consume technology and we do it fast, with an increasing demand that grows every day, but we are also in a moment in human history where we need to cut down our energy consumption because we are exhausting our natural resources. So besides, looking for new and renewable energy sources, there is also the need for more efficient materials that will allow reducing the energy cost associated with our current rhythm of life.

Here, nanotechnology must further evolve to meet these new challenges. In this line, most recent nanotechnology advances cope with the development of novel fabrication strategies and shapes in which the materials can be nanostructured. Typically, nanostructured materials are defined by their space dimensionality as 2D, 1D, or 0D, which refers to 2D thin films where dimensionality is reduced along one space direction, its thickness. The next category, 1D is associated with nanowires with diameters in the nanometer range (the dimensionality here is reduced in two directions) and finally, when the size of the material is reduced in all its three dimensions, the generated nanostructure is known as 0D or quantum dots. However, triggered by the progress of new synthesis processes, more complex and hierarchical nanostructures in a three-dimensional configuration are beginning to be explored, some examples are shown in Figure 1.1. Figures 1.1a, 1.1b, and 1.1c show intricate 3D structures in wood-like piles [1], a three-dimensional array of spirals [2], and a bulky ball [2, 6], respectively; with sub-micrometer resolution fabricated by direct laser writing (DLW) technique over a photoresist, Then, the resulting 3D resists can be filled or coated with other materials, as in Figure 1.1c, which is coated with Co [6]. 3D periodic lattices can be obtained, for example, by interference lithography [3], as shown in Figure 1.1d., or by pulsed anodization of an aluminium substrate, Figure 1.1f (this work). 3D nanowires networks can be prepared inside perforated alumina membranes, like the one in Figure 1.1f, or employing ion track-etched polymer membranes [4], see Figure 1.1e. 3D printing in the nanometer scale is possible with a focused electron beam induced deposition (FEBID) [5],

Figures 1.1g and 1.1h correspond to Fe-Co nano-trees and nano-cubes grown by this technique. The underlying physics behind 3D nanostructures are still unknown, but they could be the key to fulfill the requirements for low energy technologies.
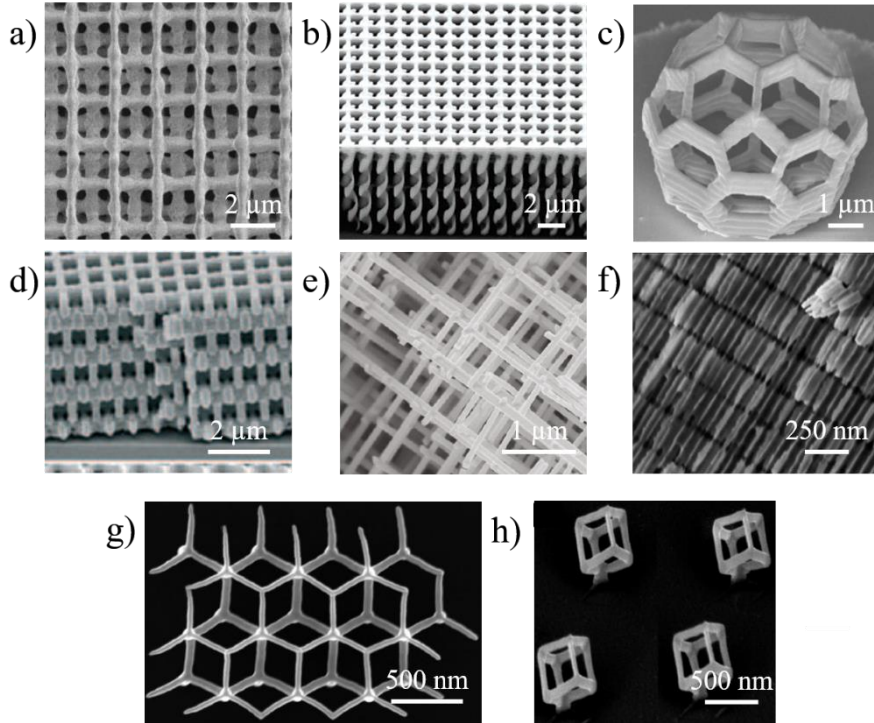
Figure 1.1. *Nanostructures in three-dimensional configuration: a), b) and c) three-dimensional nanostructures fabricated by direct laser writing (DLW) in the form of wood-like piles, a three-dimensional array of spirals, and a bulky ball, respectively. a) Reprinted with permission from reference [1]. Copyright © 2008 WILEY-VCH Verlag GmbH & Co. KGaA, Weinheim. b)and c) Reprinted with permission from reference [2]. Copyright © 2007, American Chemical Society d) 3D periodic lattice is grown employing interference lithography (IL). Reprinted with permission from reference [3]. Copyright © 2009 WILEY-VCH Verlag GmbH & Co. KGaA, Weinheim. e) 3D Nanowire networks prepared inside ion track-etched polymer membranes by electrodeposition technique (ED). Reprinted with permission from reference [4]. Copyright © 2011, American Chemical Society. f) Transversely perforated alumina membranes with 3D porous nanostructure obtained through anodization (this work) g) and h) Examples of the complex structures that have been synthesized with a focused electron beam induced deposition (FEBID): g) Fe-Co nano-tree and h) nano-cubes in the nanometer scale. Reprinted with permission from reference [5] Copyright © 2018, The Author(s)*

Among the different physical and chemical growth techniques that are available, in this thesis we have opted for a low-cost, highly efficient technology, based on the self-assembly process of anodic aluminium oxide

membranes (AAO). The fabrication process of the membranes employs an environmentally friendly aqueous solution, consisting of diluted sulfuric acid, none expensive materials (aluminium substrate), or complex equipment, just a power source. Overall, it is cost-effective and easily scalable to the industry. This technology is aligned with the requirements of efficiency and lower energy expenses.

1.2. Anodic aluminium oxide (AAO) membranes

Porous Anodic Aluminium Oxide -AAO- (also known as nanoporous alumina, Nanohole Alumina Arrays –NAA- or Nanoporous Anodized Alumina Platforms –NAAP-) has opened new opportunities in a wide range of fields, due to their great versatility. AAO membranes provide a cost-effective platform to obtain structures with a high density of ordering the pores with diameters in the order of nanometers and lengths that can go in the micrometer range. Since the published work of Masuda *et al*. in 1990 [7], where the fabrication process of highly ordered porous structured alumina membranes in oxalic acid was first reported, research has come a long way. New conditions under different anodization regimens have been explored in many different kinds of acidic electrolytes and experimental conditions (temperature, applied anodization potential, etc.) [8-19] that allow obtaining alumina membranes with pre-designed porous structures (pore diameter, inter-pore distance, porosity, length…) to fulfill a certain application. Possessing this high degree of tunability over the porous structure at the nanoscale level allows fine control of the optical properties displayed by the alumina films that can be exploited for sensing applications [20-26]. Also relevant is their high surface-to-volume ratio (associated with the pore density) that makes them appropriate vehicles for drug delivery applications [27-31]. These membranes can be further used as templates, for micro- and nano-structuration of different materials highly demanded in the nanotechnology field. Replication of the nanoporous structure can be achieved through different growth techniques such as electrochemical deposition (ED), chemical vapor deposition (CVD), Atomic Layer deposition (ALD), sputtering, among others. This way several distinct morphologies from solid nanowires [32-41], segmented nanowires of varying composition [42-44] or diameter [43, 45] hollowed tubular wires also referred to as nanotubes [46-54], nanocones [55], Y-branched wires [56-62], to 3D networks of interconnected nanowires [32, 63-68] can be obtained. Holey films [69-74], also known as antidote arrays, can be fabricated if deposition of a certain

material takes place only over the surface of the hollowed membrane, replicating this structure instead. Depending on the chosen material, different phenomena and interesting optical, electric, and magnetic properties have been observed in the above-mentioned shapes. Hence alumina membranes provide powerful platforms for studying the property changes occurring at the nanoscale.

1.2.1. Pore structure and formation mechanism

1.2.1.1. Pore nanostructure: structural parameters
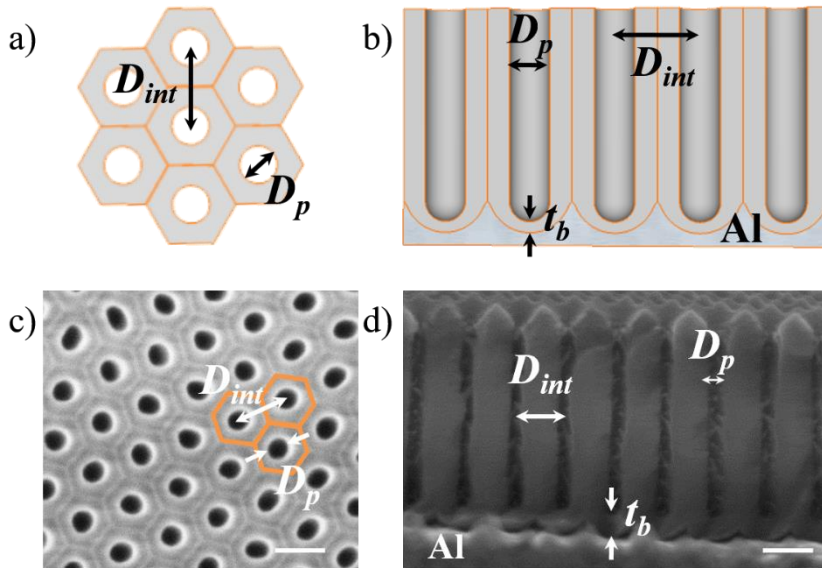
Figure 1.2. a) Schematic top view of 6 hexagonal pore unit cell arrangements. b) Lateral sketch view of an anodic oxide aluminum porous membrane. c) top and d) cross-section view SEM images of a lab-made alumina membrane (0.3 M Oxalic acid). Structural parameters of the alumina porous structure such as pore diameter (D_p), inter-pore distance, (D_{int}), and barrier layer thickness (t_b) are identified in all images. Scale bar 100 nm.

The fabrication process of porous alumina membranes is a well-known process, which consists of the electrochemical oxidation of the surface of an aluminium substrate, this process is also known as anodization. During anodization in an acidic medium (using acidic electrolytes such as oxalic, sulfuric, phosphoric, selenic, tartaric, malonic …) in which anodic oxide is slightly soluble, firstly a non-porous barrier oxide layer is formed when a certain potential (or current) is applied. Due to the increased solubility of this layer in an acidic environment, a porous anodic oxide layer starts to grow. In this system, the thickness of the barrier layer remains constant through the

whole process as a competition between aluminium oxide formation and re-dissolution of the oxide takes place [75, 76], accordingly to the following chemical reactions:

$$2Al^{3+}_{(ox)} + 3O^{2-}_{(ox)} \rightarrow Al_2O_3 \tag{1.1}$$

$$Al_2O_3 + 6H^+_{(aq)} \rightarrow 2Al^{3+}_{(aq)} + 3H_2O_{(l)} \tag{1.2}$$
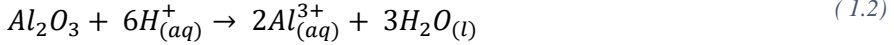
From the chemical point of view, the formation of anodic oxide occurs at the metal/oxide interface as described by the reaction *(1.2)* while the dissolution of the anodic alumina simultaneously occurs at the oxide/electrolyte interface, as in reaction *(1.1)*. Other reactions involved in the process are:

$$Al^{3+}_{(ox)} \rightarrow Al^{3+}_{(aq)} \tag{1.3}$$

$$2O^{2-}_{(ox)} \rightarrow O_{2(g)} + 4e^- \tag{1.4}$$

$$2H_2O_{(l)} \rightarrow H_3O^+_{(aq)} + OH^-_{(aq)} \tag{1.5}$$

Reaction *(1.3)* corresponds to the direct ejection of Al^{3+} ions from the metal surface towards the electrolyte, due to an applied electrical field. Reactions *(1.3)* and *(1.4)* reduce the efficiency of the anodization process. Both, dissolved Al^{3+} ions, according to equation *(1.4)*, and the ejected Al^{3+} ions, equation *(1.3)*, now present in the electrolytic solution, will form water-soluble complexes with the counter-anions, $[A^{-X}]$, of the different electrolytes. While reaction *(1.5)* is the dissociation of water molecules occurring at the oxide/electrolyte interface. O^{2-}/OH^- ions migrate inward toward the metal/oxide interface, under an electric field, providing new ions to form anodic oxide.

Under the right anodization conditions (such as temperature, anodization voltage/current, anodization time, electrolyte composition…) the porous alumina membrane self-organizes into a hexagonally closed packed pore structure, as shown in Figure 1.2. Figure 1.2a and 1.2c display, respectively, a top view sketch and an actual top-view SEM image of alumina grown in 0.3M sulfuric acid at 25 V and 0 °C. Figures 1.2b and 1.2d correspond to a lateral sketch view and cross-sectional SEM image. The most characteristic parameters of the porous structure, as indicated in Figure 1.2, are the pore diameter (D_p), inter-pore distance (D_{int}), which also refers to the cell size, and

barrier layer thickness (t_b). These structural parameters are directly linked to the anodizing conditions.
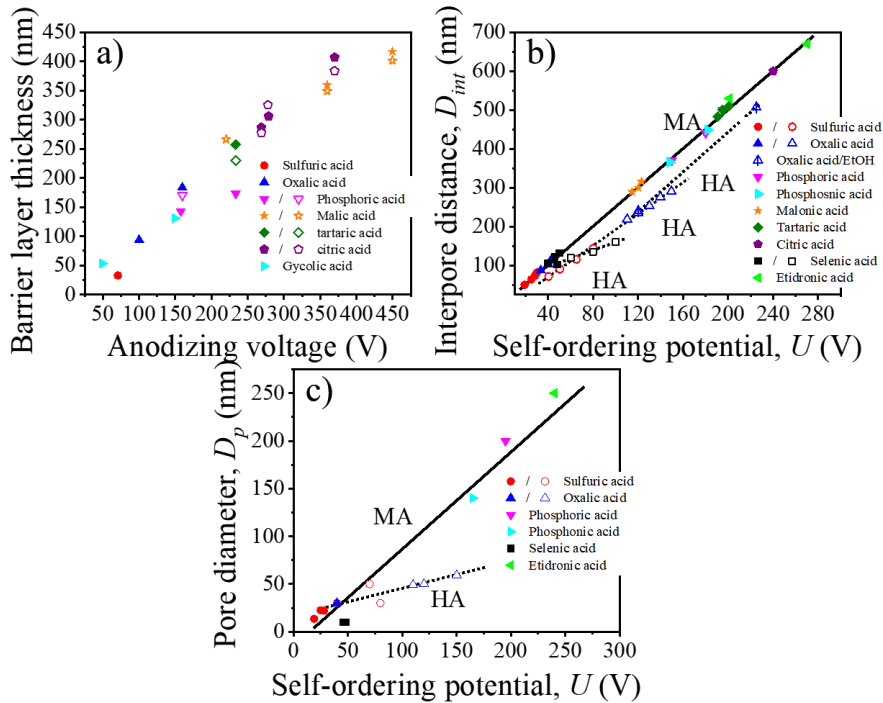
Figure 1.3. *a) Evolution of the barrier layer's thickness, t_b, as a function of the anodizing potential, U, in different acidic electrolytes [77]. Solid symbols measured values. Open symbols, calculated values from the half-thickness of the pore wall. b) and c) Evolution of the inter-pore distance, D_{int}, and pore diameter, D_P, respectively, with the applied potential, U, under MA (solid symbols) and HA (open symbols) conditions of self-ordering in different electrolytes. The black solid line and black dotted lines were added to guide the eye showing the linear correlation of the cell size (or inter-pore distance, D_{int}) and pore diameter with the anodizing potential (U) under MA and HA conditions, respectively. Data were taken from Table 1.1.*

Several authors have studied the dependence between t_b, D_{int}, and D_p with the anodizing potential (U), a linear relationship was found. Figure 1.3a, 1.3b, and 1.3c show the existing linear correlation of the t_b [77], D_{int} [78-80], and D_p [78], respectively, with U in various electrolytes and under different anodizing regimens of mild and hard anodization (see also, Table 1.1). Mild anodization conditions (MA) refer to anodization in a potential range below the breakdown potential of the forming oxide layer. Above this breakdown potential typically burning and cracking of the oxide, or an oxide formation with an increasing number of growing defects, occurs (hard anodization regimen, HA). Under mild anodization conditions there have been established empirical expressions

to define the linear relation of the D_{int}, and D_p to the anodizing potential, U, which are as follows:

$$D_p = \xi_p \cdot U = 1.29 \cdot U \qquad\qquad (1.6)$$

$$D_{int} = \xi_{MA} \cdot U = 2.5 \cdot U \qquad\qquad (1.7)$$

, where D_p and D_{int} are the pore diameter and interpore distance, ξ_p and ξ_{MA} are proportionality constants of the pore diameter and cell size under mild anodization conditions, respectively, with the applied potential (U).

Nevertheless, there is a discrepancy in the effect that temperature [78, 81-83] and electrolyte pH (electrolyte concentration) [78, 79, 84-86] have on both structural parameters. The major differences arise from comparing different electrolytic solutions. A more detailed explanation between the experimental conditions and the structural parameters from all the data that can be found in the literature is already discussed in several books [87, 88] and reviews [89].

The three most used acidic electrolytes are sulfuric, oxalic, and phosphoric. Studies of these three electrolytes have allowed ordered porous systems to be obtained in a wide range of conditions (temperature, concentration, and the mixture of the chemical species) and under two different regimes (potentiostatic or galvanostatic), from mild anodization (MA, low field-anodization regimen) to hard anodization (HA, high field-anodization regimen). Apart from those three, other acids have been also used, such as selenic (H_2SeO_4) [90-92], arsenic (H_3AsO_4) [17], phosphonic (H_3PO_3) [13], phosphonoacetic ($C_2H_5O_5P$) [14], chromic (H_2CrO_4) [93], sulfamic (NH_2SO_3H) [94], pyrophosphoric ($H_4P_2O_7$) [95], malonic ($C_3H_4O_4$) [96], tartaric ($C_4H_6O_6$) [15], citric ($C_6H_8O_7$) [80, 97] and etidronic ($C_2H_8O_7P_2$) [16] acids. Under these less known electrolytic solutions, the resulting alumina membranes display new cell parameters in terms of pore diameter and inter-pore distance that were not covered by the more traditional acids, as it is recorded in Table 1.1. There have been reported synthesized alumina membranes with pores as small as 8-10 nm of diameter [90] to several hundred nanometers [16, 98]. Interpore distance between neighboring pores ranges from 63-65 nm (smallest interpore distance obtained to date in sulfuric acid [99]) to around 1.4-2.0 µm (in a citric acid/ethylene glycol/phosphoric acid mixture solution [100]). The features of the porous structure of the alumina

membranes, then, could be selected to fulfill the requirements of many different applications.

***Table 1.1.** Structural parameters of ordered anodic oxide membranes obtained using different electrolytic solutions (single acids and mixed acidic solutions) and varying the anodizing conditions (temperature and applied potential).*

Single acids

Acid	Electrolyte concentration	Anodization regimen	Voltage/ Current density	Temperature	D_p (nm)	D_{int} (nm)	Ref.
Sulfuric	0.05-0.2 M	MA	30-28 V	0 °C	21-22	82-73	[86]
	0.3 M	MA	25 V	0 °C	20-25	63-65	[99]
	0.3 M	MA	25 V (0.3M, 10 min)	-1.5 to 1°C	15-30	78-114	[8]
		HA	40-80 V				
	10 % V/V	HA	40-70 V/ 160-200 mA/cm^{-2}	0 °C	30-50	90-130	[101]
	15% wt H$_2$SO$_4$/ 50% wt ethylene glycol	MA	19 V	-15 °C	12-15	50	[9]
Oxalic	0.3 M	MA	40 V	1 °C	30	100	[102]
	0.3 M	MA	40 V	1-2 °C	49-59	220-300	[10]
		HA	110-150 V				
	0.3-0.75 M (5-10% ethanol)	HA	120-225 V	-1-0 °C	50-60	240-507	[11]
Phosphoric	0.1-0.3 M	MA	195 V	0 °C	150-200	500	[98]-[79]
	0.25-0.5 M/ H$_2$O/EtOH	HA	195 V 150-400 mA/cm2	-10 to – 5 °C	140-80	380-320	[12]
Phosphonic	0.5 M	MA	150-180 V	0-10 °C	140	370-440	[13]
Phosphonoacetic	0.9 M	MA	205-210 V	10-15 °C		500-550	[14]
	0.3 M		225 V	10 °C			
Selenic	0.3 M	MA	46-48 V	0°C	10	102	[90-92]
	0.3 M	HA	60-100 V	0°C		120-160	[103]
Malonic	4 M	MA	120 V	5 °C		300	[15]
	0.3 M Oxalic	HA	110-140 V	5 °C			[96]
	1.67 M Malonic	MA	125-140 V	0 °C			
Citric	2 M	MA	240 V	20 °C		600	[80]
Tartaric	3 M	MA	195 V	5 °C		500	[15]
Etidronic	0.3 M	MA	210-270 V	20 °C	250	530-670	[16]
Arsenic	0.3 M	MA	320 V	0 °C	220	920	[17]

Mixture of acids							
Sulfuric + Oxalic acid	0.3 M + 0.3 M	MA	36 V	3 °C		73	[104]
	0.07-0.2 M Sulfuric + 0.4 M Oxalic	MA/HA	36-60 V	0 °C		69-115	[105]
Phosphoric + Oxalic acid	1% wt Phosphoric + 0.03-0.3 M Oxalic	MA	200-130 V	1 °C	130-53	500-300	[106]
	0.05-0.3 M Phosphoric + 0.3-0.4 M Oxalic	MA	35 V	0 °C		317-375	[107]
		HA	150-180 V				
	0.3 M Phosphoric + 0.1-0.3 M Oxalic	MA	70 V	<5 °C	110-119	520-700	[108]
		HA	230 (0.1 M Ox.)-360 V (0.3 M Ox.)				
Phosphoric + Citric acid	Citric acid/Ethylene glycol/Phosp. acid with different concentrations	HA	600-800 V	-2 °C		1400-2036	[100]

1.2.1.2. Pore formation and growth mechanism

The whole process can be divided into four stages. Each of them is associated with a step in the growth process of such membranes. Figure 1.4a shows a typical current density-time curve recorded during potentiostatic anodization conditions. The different stages are delimited by changes in the current density. The illustrations above portray the evolution of the undergrowing porous oxide film at each stage. Under galvanostatic conditions, in the profile of the recorded potential-time transient curve (not shown here), these same stages can be identified [109].

Stage I is delimited by the exponential decay of the current density and it's associated with the fast formation process of the oxide barrier layer, as the electrical resistance increases due to the insulator nature of the forming compact oxide layer. The final thickness of the oxide barrier layer is linearly dependent on the anodizing potential, as is shown in Figure 1.3a. This dependence is known as the anodization ratio, $AR = t_b/U$ and takes different values under different anodization conditions, $AR_{MA} = 1.14\text{-}1.20$ nm V^{-1} (for MA regimens) [78, 110-114] and $AR_{HA} = 0.6\text{-}1.0$ nm V^{-1} (HA regimen) [8, 10, 12, 77].
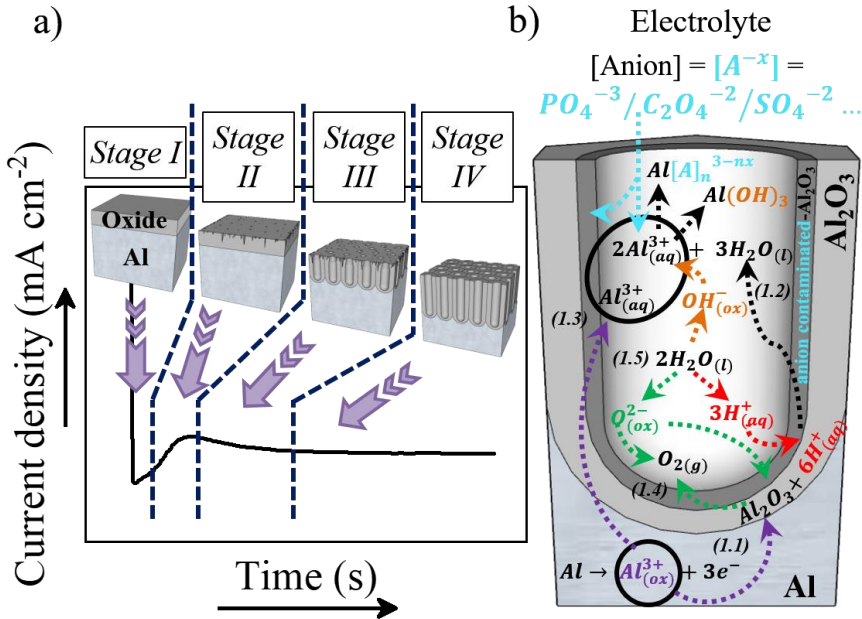
Figure 1.4. *a) Profile of the current density-time curve recorded during potentiostatic anodization of a lab-made AAO alumina membrane prepared in 0.3 M H_2SO_4 at 25 V. The above-inserted illustrations show the changes occurring at the different stages, from the formation of the non-porous oxide barrier layer (stage I) to the development of pores in an ordered hexagonal arrangement (stage IV). Going through several intermediate states, the generation of defects and cracks in the surface of the oxide barrier layer (stage II) where the current will accumulate giving place to the nucleation pore sites, acting as precursors for the initiation growth of bigger pores (stage III). b) Representation of the chemical reactions taking place during the anodization process: Purple arrows point the route of the metallic aluminium of the substrate as it is oxidized, towards the formation of Al_2O_3 or the direct ejection of the oxidized Al^{3+} ions into the electrolyte, corresponding to reactions (1.1) and (1.3), respectively. Green arrows point to the inward migration of O^{2-} species to form new Al_2O_3 (reaction (1.1)) from the dissociation of water molecules, according to the reaction (1.5), and indicates the generation of oxygen bubbles as $O_{2(g)}$ is released, described by the reaction (1.4). The red arrows mark the dissociation of water into H^+ ions (reaction (1.5)) and the role played by such H^+ ions in the redissolution of the already formed Al_2O_3, as shown in reaction (1.1). The orange arrows show the dissociation of water into OH^- ions (reaction (1.5)) that later react with the Al^{3+} species present in the solution. The black arrows point out the re-dissolution of Al_2O_3, as in reaction (1.2), and the formation of Al-based soluble complexes. Blue arrows mark the inward migration of the counter-anions from the bulk electrolyte that binds Al^{3+} ions in the solution, to form water-soluble complexes and their incorporation to the Al_2O_3 of the outer walls of the pores.*

Stage II starts with the increase of the current density until a local maximum is reached. This maximum is associated with the breakdown of the oxide barrier layer and the actual development of an incipient disordered

porous structure. Two main theories have been proposed to try to explain the pore nucleation mechanism occurring at this stage: The field-assisted model and the stress-driven mechanism. In the *field-assisted* model, developed by O'Sullivan and Wood [78], it is suggested that pore nucleation points emerge at the local imperfections on the barrier layer where current accumulates leading to a non-homogeneous growth of this layer. The s*tress-driven mechanism* was developed by Shimizu and Thompson [115]. They defend that stress is the key factor for the evolution of pores. Stress originates at the metal/oxide interface because of volume expansion at this interface as the metal substrate is being oxidized. This tensile stress is responsible, in first place, for the local cracking of the anodic oxide film over protuberances or ridges found in the metal surface (due to imperfections or impurities of the aluminium substrate). Then, high local current density occurs at the cracked sites, and ions are consumed from the aluminium base to heal these regions, resulting in non-uniform film growth. Both theories are not excluding, but complementary.

At *Stage III,* the current density decreases until the final steady state is reached and the current density stabilizes *Stage IV*. At this point, the thickness of the barrier layer (t_b) is kept constant, due to the balance of the reactions (*1.1*) and (*1.2*), and the porous structure grows in thickness; while the density of pores is reduced, disordered pores start to merge and pores parallel to each other and perpendicular to the surface are favoured instead. This could be explained using the '*average field model'* developed by O'Sullivan and Wood [78]. At first, pores will grow with different pore sizes experiencing different electric fields and thus different dissolution rates. Through merging and self-arrangement of the pores, the electrical field experienced by each pore will balance to the same average electric field. Under this average field, the equilibrium of the growth rate is achieved for all pores. Later, Su *et al.* [116] presented a mathematical model supporting the equi-field strength empirical model, described by O'Sullivan, but also including both the oxide dissolution (*reaction 1.2,* black arrows in Figure 1.4b) and oxygen migration rates and in which the latter, determined by the water dissociation rate (*reaction 1.5*, as illustrated by the green arrows in Figure 1.4b), plays a key role in the final porosity (the pore to cell size ratio). However, some experimental studies employing [18]O isotope tracers show no significant oxide dissolution occurring during steady-state pore formation [117, 118]. The recession of the oxide-solution interface to keep the thickness of the barrier layer (t_b) at a constant value, according to the anodization ratio, had to be attributed to other

phenomena. Under this new perspective, the direct cation ejection mechanism gains relevance [117-120], in this scenario, the free volume left by the ejection of Al^{3+} ions (purple arrow corresponding to *reaction 1.3* of Figure 1.4b) has to be compensated by an inward movement of the oxide at the oxide-solution interface.

The formation of porous alumina and self-alignment of the pores in a closed-packed pattern was also associated with a stress-relieving process due to plastic deformation during anodic oxide growth. Jessensky [102] and Li [121] stated that stress is the driving force responsible for this alignment, due to repulsive forces between neighboring pores. Further on, Skeldon *et al.* [122, 123] proposed a flow mechanism where the thickness of the barrier layer (t_b) is kept constant by the flow of oxide materials from the base of the pore towards the cell boundaries. This flow model is also supported by a stress-driven transport theoretical model developed by Hebert and Houser [124-126]. In which, the authors concluded that the stress field driving the flow originates from volume expansion at the metal/oxide interface, different migration rates of O^{2-}/OH^- species and Al^{3+} ions, and incorporation of acidic anionic species from the electrolyte solution into the oxide (at the oxide-solution interface, a light blue arrow pointing towards this interface in Figure 1.4b).

In short, at *Stage IV* all the different *reactions 1.1-1.5* that are involved in the growth process of porous type alumina and is displayed in Figure 1.4b, reach their steady-state value. A dynamic equilibrium is established between oxide formation and oxide removal at metal-oxide and oxide solution interfaces, respectively. This equilibrium has been studied under different perspectives to understand the mechanism that leads to pore formation and the steady-state growth stage: Joule's heat-induced dissolution at the pore base [81, 110, 127, 128], field-assisted oxide dissolution [78, 127, 129], and more recently, the stress-induced plastic flow model [122, 124-126, 130-136]. Nevertheless, there is still research being done to fully understand how the different phenomena affect the actual formation mechanism and self-ordering of the pores, such as volume expansion [137-139] and anion incorporation from the electrolyte solution [140, 141]. Both seem to linearly depend on the applied anodizing voltage, whereas the latter, at least in the particular case of sulfur incorporation, seems to increase the plasticity of the oxide since the breakdown limit of the oxide before cracking under mechanical stress is increased [141]. This can open new regimens under high stress (due to higher

volume expansion of the oxide) for the self-ordering formation of nanoporous alumina.

Another model related to the generation of the pores, the oxygen bubble mold model, accounts for the effect that the oxygen bubbles that are produced as a side reaction during anodization (*reaction 1.4*), have on the morphology of the anodic oxide layer [142, 143]. As it will be seen in section 1.2.2., apart from pores with parallel walls, different pore-wall morphologies can be obtained, such as serrated walls [144, 145] or diameter modulated pores (also called bamboo-like structures) [146], for instance, and these morphologies can be understood under the oxygen bubble mold model. As hinted by its name, this model considers the oxygen generated while the oxidation is taking place during the anodization. Then, the generated oxygen bubbles are presented as molds for the formation of a semi-spherical barrier layer at the bottom of the pores. This model is also related to the previous one because the plastic flow of the produced oxide is enhanced by the high-pressure areas under the oxygen bubbles, where there is also a higher electric field. Then, there is a plastic flow from the bottom of the pores towards the pore walls favored by the bubbles.

1.2.2. Morphologies of the porous structure

Comprehending the self-assembling process of the pores helps to develop new procedures (such as pulsing between MA/HA regimens, or pre-patterning of the aluminium substrate, among others) under different anodization conditions (of voltage, temperature, electrolytic solution) that allow obtaining pores with different morphologies and novel pore architectures, as of in-depth modulation of the diameter pore. In this section, we will review some of the most singular pore geometries that have been achieved to date.

1.2.2.1. Branched nanoporous structures

Branching of stem pores can be achieved through two different approaches: steady-state and non-steady-state anodization. In the former, the anodizing voltage is decreased accordingly to the equal-area model, which states that the total pore area of the template is invariant, hence branching of the stem pore into *n* smaller in diameter pores satisfices the relation,

$$d_2/d_1 = 1/\sqrt{n} \qquad\qquad (1.8)$$

, being d_1 and d_2 the diameter of the stem pore and the diameter of smaller branched pores, respectively. And where n is the number of smaller pores in which the main stem pore divides, while considering the conservation of the pore area. Then, from the linear relationship between the pore diameter with the anodizing potential (see section 1.2.1.a., *equation 1.6*), and considering the equal-area model, the anodizing voltage should be decreased by a factor of $1/\sqrt{n}$. To obtain n Y-junctions the voltage is systematically reduced in $1/\sqrt{n}$ steps. . Each step will be extended over time until the steady state of the current density is reached under the new anodizing conditions. To reduce the duration of these steps, we can follow different anodization routes: one is to perform a chemical etching [147-150] between branching steps to reduce the barrier layer according to $AR = t_b/U$ (where $AR_{MA} = 1.14$-1.20 nm V^{-1}, for MA regimens, and $AR_{HA} = 0.6$-1.0 nm V^{-1}, HA regimen). Another option is to change the electrolyte solution at each step to suit the new anodizing conditions [147, 148, 150, 151], reckoning that, for example, each of the acids works best in a certain voltage range, as listed in Table 1.1.

In particular, it is worth mentioning that hierarchical multi-branched pores in succeeding tiers have been successfully fabricated if etching of the barrier layer is performed between each branching step [148]. Figure 1.5a shows cross-sectional and top (insets) views of a three-tiered branched pore structure. The fabrication process goes as follows: 1st anodization in 0.3 M phosphoric acid at 130 V for 30 min and a subsequent 50 min chemical etching step, followed by a 2nd anodization in 0.15 M oxalic acid at 80 V for 3.5 min and a 90 min chemical etching step and finally, the 3rd anodization in 0.3M oxalic acid at 50 V for 15 min and a 40 min chemical etching step. Other authors also defend the need to add a chemical etching step of the barrier layer before variations of the anodizing voltage to eliminate the competitive growth of the branched pores. Competition between stem pores or branched pores occurs due to the non-uniform dissolution of the barrier layer during the different anodizing steps and non-uniform field strength distribution at the pore base. Then, the pore growth rate of certain pores (or branched pores) takes over the others. The etching of the barrier layer enables to reach the steady-state growth more rapidly under the new anodizing conditions, thus avoiding the non-uniform dissolution of this barrier layer occurring during the long periods that take to reach the new steady-state when no previous etching is performed [147].
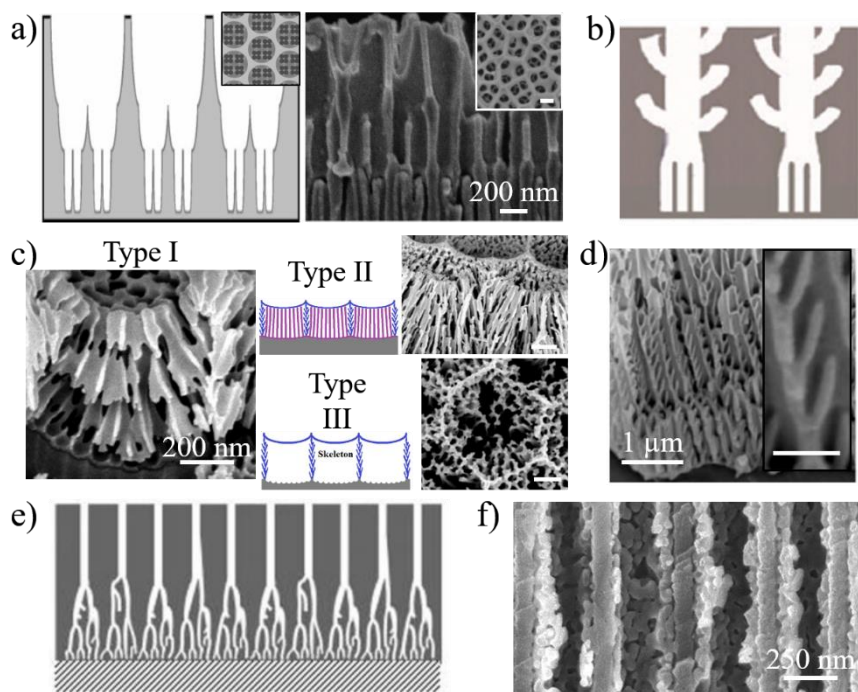
Figure 1.5. *a) Schematic illustration and actual SEM images, to the left and the right, respectively, of multi-branched pores fabricated in succeeding tiers. Insets correspond to a top view image of such structure. Reprinted with permission from [148]. Copyright © 2008 WILEY-VCH Verlag GmbH & Co. KGaA, Weinheim b) Sketch of a tree-like hyper-branched porous structure by alternating between voltage to current control anodization. Reprinted with permission from [153]. Copyright © The Royal Society of Chemistry 2009. c) SEM image of an interconnected branched porous AAO film fabricated by applying a periodic anodization voltage on the patterned aluminium surface in 0.3 M oxalic acid electrolyte solution, followed by a 35 min etching step (type 1 structure). Schematic diagrams and the corresponding SEM images of the type 2 structure of AAO nanowires and type 3 supporting AAO skeleton structure. Reprinted with permission from [155]. Copyright © 2016 The Electrochemical Society. d) SEM micrograph showing the cross-section view of serrated nanopores. Inset, magnified image of one of them. Reprinted with permission from [142]. Copyright © 2008, Springer-Verlag. e) Schematic illustration of the tree-like branched pores obtained through non-steady-state anodization. Reprinted with permission from [156]. Copyright © 2007, The Royal Society of Chemistry. f) Cross view SEM image of macropores with smaller mesopores all along the pore walls. Reprinted with permission from [157]. Copyright © 2017 Elsevier Ltd. All rights reserved.*

Opposite to the voltage-control method described above, Guo *et al*. [152] reported a current-control method for the fabrication of highly homogeneous triple-branching pores where the homogeneity of the branching pores is improved by controlling the applied current against the reduction of the

applied potential. More complex branched structures have been grown by alternating voltage and current control anodizing steps [153], which consist of hyper-branched alumina membranes with tree-like branches coming from the trunk of the pore that ends in multi-tiered branches, as illustrated in the sketch image in Figure 1.5b.

Zakeri and co-workers [154], in parallel, proposed a model where branching of pores occurs over non-flat aluminium surfaces and without the need of reducing the anodizing voltage through the curving and subsequent merging of the growing pores over edges, notches, and curved sites.

More recently, in 2016 Jin *et al*. [155] developed three different types of complex branched structures by combining steady-state growth of branched pores on pre-patterned curved aluminum substrates, where tree-like porous structures are formed, as previously described by Zakeri *et al*., at the boundaries of the pattern cells. See Figure 1.5c: Type 1, 3D interconnected branched structure; type 2, self-supported AAO nanowires structure, and type 3, which is what authors called supporting AAO skeleton structure. To obtain 3D interconnected branched pores (type 1 structure), a periodic anodizing potential was applied alternating between 50-30 V in 0.3M oxalic acid, followed by a 35 min etching treatment. Types 2 and 3, were grown under constant voltage (30 and 40 V) and different etching times 31-33 min (AAO nanowires are formed) and 43 min for a complete dissolution of such nanowires, respectively.

Serrated branched porous structures (Figure 1.5d) associated with oxygen evolution when applying different voltage steps have also been reported by several authors [142, 144, 145]. The growth of serrated pores in the oblique direction along the vertical walls of the pore channels (inset image in Figure 1.5d) cannot be assessed by field-assisted dissolution theory at the pore bottom of perpendicular pores (concerning the aluminium substrate) due to geometric considerations. Therefore, the formation mechanism of serrated pores combines the previously proposed field-assisted flow model of Skeldon *et al*. [122, 123] with the oxygen bubble mold effect. During anodization, oxygen bubbles trapped within the oxide barrier layer are generated, and current density accumulates around them. As a result, Al_2O_3 formation is promoted at these local points where the field strength is increased, a protuberance is formed, and the oxygen is released from the oxide. Then, at the steady-state growth stage, protuberances are pushed towards the vertical walls by oxide flow deformation. However, this mechanism is only enhanced

under certain conditions: at elevated anodizing temperatures at which the increase of the current density induces higher oxygen evolution and when the Al substrate is placed vertically in the electrochemical cell, which seems to promote the formation of serrated branched pores aligned on one side of the walls of the vertical channels.

In the case of a non-steady-state, the anodizing potential is exponentially decreased, and potential reduction steps are applied before the steady stage could be reached at each anodizing step. Transient current versus time curves show a toothed-like profile. Current drops as the applied potential are reduced and then starts to increase with time. However, the next potential reduction step will be applied before the current stabilization is achieved.

Cheng *et al.* [156] proposed a specific mechanism for the formation of branched pores under the conditions described above. They stated that when the anodization process is kept in a non-steady state, the oxide formation and dissolution rates never reach an equilibrium balance and negative charges (coming from oxygen-containing species) will tend to accumulate in the oxide layer up to a threshold accumulative charge. Then, discharging of the negatively charged oxide layer will occur, leading to the generation of non-uniform current pathways running through the oxide. Field-assisted dissolution is induced this way, giving as a result formation of branched pores. Therefore, the pore diameter of the branched pores is not proportional to the anodizing potential with a root or tree-like form, Figure 1.5e.

In addition to the electrical field effect, the authors also pay attention to the role played by mechanical stress. One specific morphological characteristic of this kind of branched pores is their uneven morphology, where some nodes could be found along with individual pores. Furthermore, when branching of a pore takes place, the stem pore will always grow into two pores smaller in diameter. This was explained because of the strong repulsive forces between neighboring pores. Repulsive forces, due to space limitation, keep down the ramification of a pore into only two branches, if they manage to overcome such forces. If not, a node appears. In this competitive branching pore formation mechanism, pores suddenly change direction, looking for space to grow and deviate from the perpendicular direction concerning the substrate.

A slightly different concept of the branched structure was presented in 2018 by Hashimoto *et al.* [157], consisting of a macroporous structure in which the pore walls were full of smaller mesopores, see Figure 1.5f. The

anodization process was carried out in phosphoric acid and then, the membrane is subjected to a heat treatment at 1400 °C. The latter produces the formation of aluminum phosphate nanoparticles that were segregated from the alpha-alumina matrix formed during the annealing. Then, these nanoparticles were dissolved in concentrated hydrochloric acid, giving rise to the combination of the straight macropores (with diameters around 220 nm) with mesopores of around 20-80 nm in diameter present inside the macropore walls.

All the branched structures described in this section could be later used for the fabrication of branched nanowires (NWs) and nanotubes (NTs) for several practical applications in different fields, namely electronics, optics, energy harvesting, and biotechnology. More details of the actual applications of Y-branched NWs and NTs will be described in more detail in section 1.2.3.

1.2.2.2. Nanopores with modulated diameters

In-depth modulation of the diameter along the length of the pore is produced employing different synthetic routes, such as alternating between different electrolytes [151] or modifying its viscosity with the incorporation of additives (i.e. ethylene glycol) [158], combining constant anodization and chemical etchings [159] or using hard anodization conditions that characterized by high anodizing voltages [160, 161]. Of these strategies to tune the diameter of the pores as they are being formed, the most popular and successful have been switching between different acidic baths, or, if the anodization is performed employing the same electrolyte, varying the applied potential. In the former approach, nano-funnels and inverted nano-funnels were obtained by anodizing firstly in 5 wt% phosphoric acid followed by anodization in 0.015 M oxalic acid and vice versa approach [151], top and bottom SEM images in Figure 1.6a, respectively. In phosphoric acid the diameter of the pores is 85 nm but the solution is changed to oxalic the diameter reduces to 55 nm, the dotted line shows the change in pore diameter. The latter can be carried out alternating between periods of mild anodization and hard anodization, this technique is known as pulsed anodization [162], giving, as a result, a MA/HA layered structure, see Figure 1.6b. In which, the MA and HA layers possess different properties, concerning their pore diameter, porosity, and refractive index [162, 163]. This method provides fine control over the pore size and the specific location of the modulations of the diameter. Such structures are currently being widely used as photonic structures, as we will further discuss in Chapter 3.
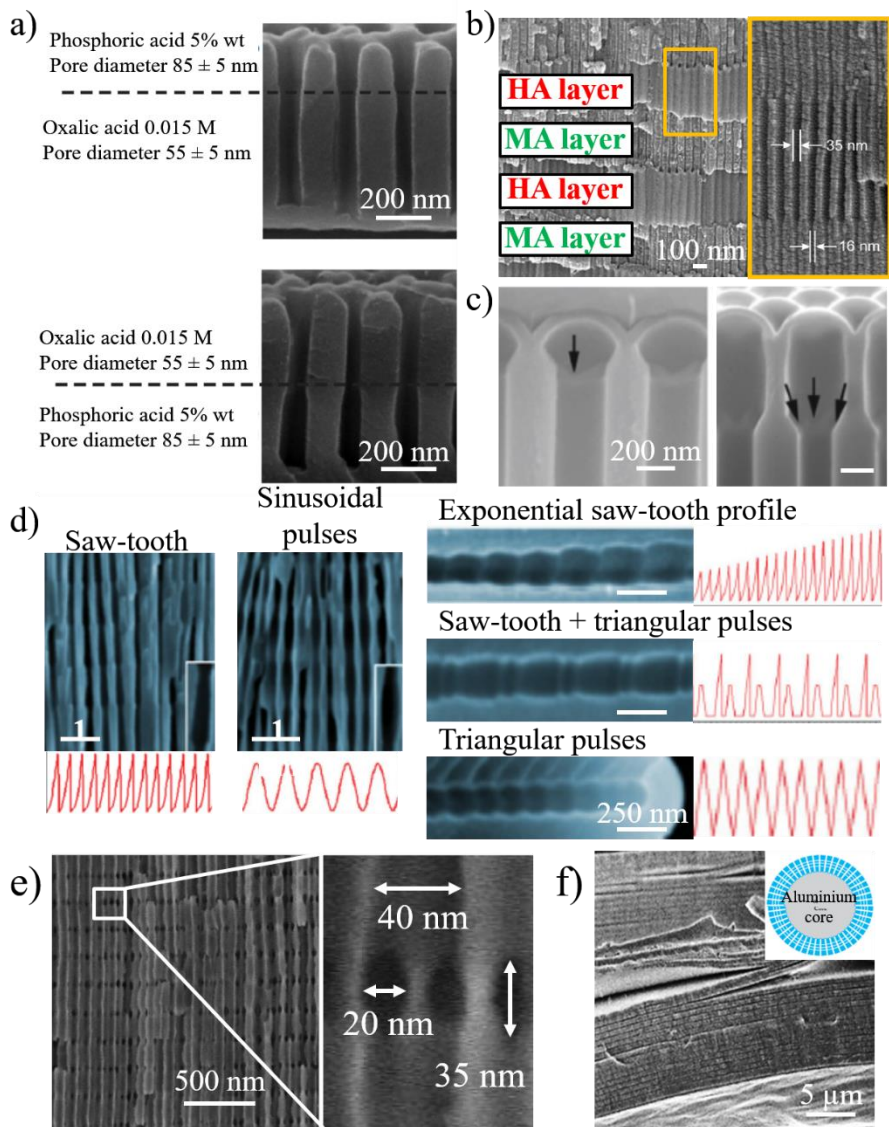
Figure 1.6. a) Nano-funnels and inverted nano-funnels, top, and bottom SEM images, respectively. They are formed by anodizing firstly in 5 wt% phosphoric acid followed by anodization in 0.015 M oxalic acid and vice versa. The pore spacing is 200 nm and the dotted line shows the change in pore diameter. Reprinted with permission from [151]. Copyright © 2007 WILEY-VCH Verlag GmbH & Co. KGaA, Weinheim. b) SEM cross-sectional view of AAO with modulated pore diameters by pulsed anodization in 0.3 M sulfuric acid at 1°C. Each cycle consisted of an MA pulse (25 V for 180 s) and an HA pulse (35 V and 0.5 s). Inset, magnification of the image around the area marked by the rectangle. Reprinted with permission from [162]. Copyright © 2011 Elsevier Ltd. All rights reserved. c) Cross-sectional SEM micrographs of bottle-shaped pore channels with two sections of significantly differential pore diameters after

an annealing treatment at 500 °C, followed by re-anodization in phosphoric acid up to a specific current density (of 0.5 mA/cm2 and 6 mA/cm2, respectively) and then etching for 32 min. Reprinted with permission from [164]. d) Controlling the shape of AAO modulation by cyclic anodization. Current-time curves and corresponding SEM images of AAO pore structures fabricated by galvanostatic anodization in 0.1 M phosphoric acid at -1 °C using different current signals: (1) exponential saw-toothed-like profile giving, as a result, an asymmetrical bottle-neck shaped pores. (2) Symmetric sinusoidal current signals showing pore segments with spherical shapes. The combination of (3) asymmetrical current signal with an exponential saw-toothed like the profile of increasing amplitude, (4) alternating asymmetrical (saw-toothed like a profile) and symmetric (triangular) current signals, and (5) a final series of symmetrical triangle pulses for the fabrication of AAO with more complex pore architectures. Reprinted with permission from [165]. Copyright © 2009 Wiley-VCH Verlag GmbH & Co. KGaA, Weinheim. e) 3D porous structure fabricated by a voltage-controlled pulsed anodization in 0.3 M Sulfuric acid. Enlarged view of the area marked with b with a square in which longitudinal pores (diameter = 40 nm) and the transversal pores (diameter = 20-35 nm) can be distinguished. Reprinted with permission from [166]. Copyright © 2014, Nature Publishing Group, a division of Macmillan Publishers Limited. All Rights Reserved. f) 3D porous structure fabricated over a cylindrical aluminium wire. Inset, the schematic cartoon of the 3D AAO formed around the Al wire. Reprinted with permission from [167]. Copyright © 2016 by the authors; licensee MDPI, Basel, Switzerland.

Furthermore, controlling the profile of the periodic pulsed signals, meaning the amplitude and period of the applied pulse, the shape of the pores can also be modulated, and pores with the desired geometry can be fabricated. Hence voltage or current pulses with tooth, sinusoidal, triangle, or square profiles result in different pore geometries. This process is known as cyclic anodization and differs from the pulsed anodization technique in a slower transition from MA anodization conditions to HA anodization that allows better control over the shape of the modulated pores [163, 165]. Figure 1.6d shows modulated pores with different shapes fabricated by cyclic anodization processes. When asymmetric current pulses with an exponential toothed-like profile are applied, asymmetric pores are also obtained with asymmetrical bottle-neck type geometry (left image). As expected, under symmetrical sinusoidal pulses (center image), the resulting pores present a symmetric spherical shape. Inset images show in more detail the different features of the modulated pores obtained by the different profile periodic pulses that appear underneath each of them. Finally, a more complex multilayer pore structure with different geometries can be obtained by combining tooth-like and triangular pulses, as is shown in the right image in Figure 1.6d.

Cyclic anodization, during which the anodizing voltage (or current) is gradually increased up to HA conditions, is advised when using oxalic and phosphoric electrolytes, due to the long recovery times until the current

density stabilizes as the applied potential is increased [149, 168]. The forming oxide barrier layer is thicker in phosphoric acid and oxalic acid solutions than sulfuric electrolytes, hence if pulsed anodization is used, where the transition between MA and HA regimens happens at a faster rate, a current steady state is not reached during the applied HA pulses and the changes of the anodizing voltage (or current) do not result into an actual modulation of the pore structure for the former cases. The barrier oxide layer of sulfuric AAO membranes is thin enough, so control over the pore geometry could be attained through pulse anodization.

In both cases, pulsed anodization and cyclic anodization, the thickness of each segment can be controlled by the duration of each of the pulses. However, the mechanism behind the change of the geometry of the modulated pores is yet not well understood. It seems that the key factor is the difference between oxide formation and oxide dissolution rates as the anodizing conditions are varied (HA/MA anodization regimens) and the electric field that generates under each regimen. Comparing the curvature of the barrier layer formed during the different stages of a cyclic anodization process (HA, MA and the transient time in between) from SEM images taken at each of them, it was observed that during HA conditions the barrier layer possesses more of an ellipsoidal shape, while at the other two stages the barrier layer has a more circular geometry. These experimental findings indicate that the different formation and dissolution rates at each of the different stages of the periodical pulses indeed affect the shape and morphology of the resulting pores [165].

Other combinations of anodization conditions, etching, annealing, etc. have been also explored to give rise to pore morphologies such as bottle-shaped pores in the base of the pores, like in reference [164]. During this process, the prior annealing treatment reduces the etching rate of the pore walls while that of the barrier layer is enhanced by the subsequent re-anodization processes, and the preferred chemical etching around this oxide layer (probably due to structural changes induced by the annealing treatment), gives as a result, the generation of scalloped pored tips at the bottom of narrower channels (bottle-shaped like, like the one represented in Figure 1.6c).

Another approach consists of temperature modulated hard anodization, which was developed by Bayat and co-workers [169]. In this process, the current density, and hence pore diameters, were varied by temperature

modulation under hard anodization conditions. Anodization was carried out in 0.075 M oxalic acid solution containing 10 v/v% ethanol at -4 °C, and 130 V as starting potential. After 10 minutes the anodizing voltage was gradually increased to 230 V, and at this potential, the anodization was extended for 1 h. During this time, the temperature was periodically increased, which in turn caused an increment of the current density, and then lowered down again back to the steady state. By this method, cylindrical pores with modulated diameters were successfully fabricated, with narrow segmented pores of 47 nm in diameter and the widest segments of 130 nm.

1.2.2.3. 3D porous structures

These structures provide a further step to the modulated nanoporous structures, given that the fabrication principle is similar, that is, a periodic change in the anodization conditions switching between MA to HA by either pulsed or cyclic anodization. Nevertheless, in this case, precise control over the anodization parameters is required to obtain a 3D interconnected porous structure, in which the longitudinal pores are connected to other 6-neighboring pores through transversal nanochannels. The etching times must be precisely adjusted so that selective chemical dissolution at certain positions along the pore channels, corresponding to the HA pulses, is achieved. At the same time, excessive etching must be avoided, which would revert to the collapse of the whole porous structure. The higher content of impurities and less density of the HA layers make them less chemically stable against chemical etching compared to MA layers hence selective etching of HA layers is accomplished.

In 2009, 3D nanoporous structures (grown in 0.1 M phosphoric acid using cyclic anodization under galvanostatic mode) were fabricated by Losic and co-workers [170], as shown in Figure 1.1f, combining longitudinal nanopores of around 250 nm in diameter and transversal nanochannels with dimensions of 60-100 nm in diameter, located periodically along the length of the former. This way the porosity of the alumina membranes was significantly increased. Later in 2014, Martin *et al*. [166] developed a pulsed anodization controlling-voltage procedure in which 3D nanoporous networks with longitudinal pore diameters of 45-50 nm and transversal pores of 25-30 nm diameters were synthesized in 0.3 M sulfuric acid electrolyte (Figure 1.6e). Of the two kinds of perforated 3D AAO membranes, the reduced dimensions of the pores that were obtained in sulfuric acid by Martin *et al*., make them more suitable for nanotechnology applications.

Following this approach, these structures have been even fabricated in cylindrical aluminium wires [167], see Figure 1.6f, which demonstrates the good reproducibility and consistency of the method.

1.2.2.4. Pre-patterned structures on the alumina surface
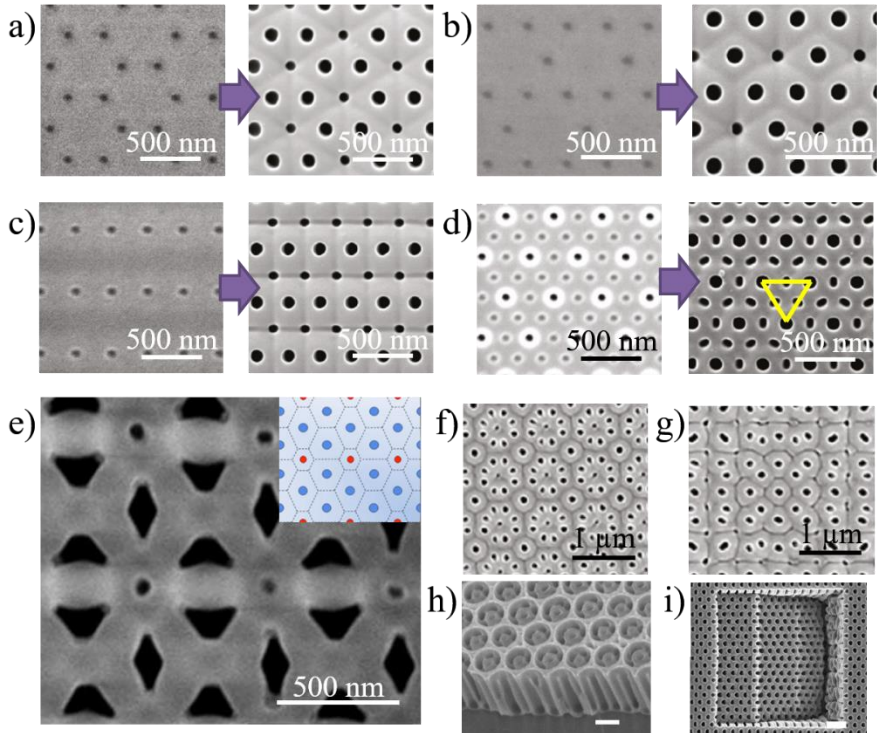
Figure 1.7. Images to the left correspond to FIB patterned concaves with a) graphite, c) hexagonal, and e) rectangular lattice structure, the interpore distance between concaves is 300 nm in all cases. To the right, are the corresponding SEM images after anodization in 0.3 M phosphoric acid at 20 mA with a steady-state potential of 140 V. d) Alternating FIB pattern with 200 nm interpore distance; the larger concave size is 65 nm and the smaller concave size is 45 nm, image in the left side. The right-side image corresponds to the cell geometry after the anodization in 0.3 M phosphoric acid at 20 mA with a steady-state potential of 140 V. The connecting lines between the bigger circular pores show the direction along with the growth of the smaller in the middle of the two is restricted. Reprinted with permission from [171]. Copyright © 2011, American Chemical Society. e) SEM image of hybrid triangle-diamond patterned porous template (with a 300 nm periodicity), upon a 30 min anodization at 120 V in a 0.3 M H_3PO_4 electrolyte. The top-right inset image shows a schematic representation of the corresponding triangle-diamond pattern tiling scheme, where a large, blue dot represents sites included in the prepattern process and the small red dots indicate locations at which compensated pores will appear. Dashed lines define the location of the cell wall formation. Reprinted with permission from [172]. Rights managed by AIP Publishing. f) and g SEM

images of the porous surface of alumina with Moiré pattern created from overlapping two square patterns with the same interpore distance (350 nm) and two square patterns with different interpore distances (400 nm and 500 nm), respectively. The nanoindentations were performed with a rotational angle of f) 36.9° and g) 0°, the subsequent anodization was carried out under 20 mA constant current at 0° for 2 min, in 0.3 M phosphoric acid. Reprinted with permission from [173]. Copyright © 2011, American Chemical Society. h) SEM image of a hierarchical AAO structure by nanosphere lithography (NSL) technique. The period of the pre-patterned aluminium substrate is 680 nm. Reprinted with permission from [174]. Copyright © 2012 WILEY-VCH Verlag GmbH & Co. KGaA, Weinheim. i) SEM image of anodized nanopore arrays across a stair-case-shaped surface. The interpore distance between nanopores is 200 nm. Reprinted with permission from [175]. Copyright © 2011 Elsevier Ltd. All rights reserved.

A completely different strategy consists of pre-patterning of the surface of the aluminium substrate before the anodization process, which typically produces long-range, highly ordered nanopores, reducing the number of anodizing steps to achieve perfect order. Moreover, the typical hexagonal geometry of the unit cell can be altered to produce new morphologies with pores in a square and triangular arrangement.

Pre-patterning of the aluminium surface can be carried out by two different methods through a direct approach or an indirect one. Direct indentation methods include the use of focus ion beam (FIB) lithography [171, 173, 175-177], or the scanning probe of an AFM [178, 179] to generate an indention on the Al surface, interference lithography [180], reactive ion etching (RIE) [181, 182], and also through the combination of lithographic processes and resins [183, 184] or employing AAO and PMMA as masks [172, 185] followed by wet chemical etching. Indirect impression techniques are based on imprinting molds [174, 186-189] employing, for example, nanoimprint lithography technology. A monodomain porous structure could be of relevance for certain applications in photonics [190-194] and magnetic recording media [195]. For this goal, however, the first approach results time-consuming and expensive, while the second route has a limitation of the area of the fabricated mold of 1 mm^2 for imprinting.

Regarding how the pore can be shaped through this approach, it has been established that what determines the geometry of the pore cell (in, for example, a square, triangular, hexagonal, or even diamond arrange) and hence, the morphology of the pore itself, is the initial arrangement of the pre-patterned concave pits over the Al substrate guiding the initiation of pores, but not the shape of the indented pits.

In particular, when a FIB pattern with a graphite lattice and a 300 nm interpore distance is used, then the oxide walls develop in a triangular shape (see Figure 1.7a, the FIB pattern corresponds to the SEM image to the left, while the image to the right shows the final geometry of the alumina cell), if the pattern used has a hexagonal arrangement with some missing sites but the same interpore distance (Figure 1.7b, to the left) then the shape of the visible oxide walls is diamond (Figure 1.7b, right image). A final example of a rectangular arranged pattern of holes with 300 nm for the long and $300\sqrt{3}$ nm for the short interpore distance is shown in the left in Figure 1.7c, which produces also a rectangular arrangement of the pores after anodization (right image in Figure 1.7c). The SEM images corroborate that the final arrangement of the pores is only dependent on the arrangement of the pattern [171]. Another recent development addresses FIB patterning over uneven surfaces [175], Figures 1.7i. The order of the nanopore array is well maintained all along the uneven surfaces, however, there is some pore shape deformation at the edges due to the absence of a flat surface.

It is also worth mentioning that more complex arrays based on Moiré patterns, which consist of the superposition of hexagonal patterns with a rotation angle, with several different interpore distances have been reproduced over the alumina surface by nanoimprinting lithographic techniques [173], as in Figure 1.7f and 1.7g. We must keep in mind, however, that in all cases the non-hexagonal arrangement could only be maintained during a certain anodization time before rearrangement of the pores occurs in a hexagonal pattern, limiting the thickness of the membrane.

In general, the introduction of indentations over the aluminium surface, acting as nucleation sites, guides the growth and development of the pores, as well as the geometry of the unit cell. However, nucleation of pores at the edges of the cell boundaries can be propitiated under certain conditions, so that if the interpore distance between neighboring pores is sufficiently large cell boundaries become visible and new pores can be formed at the cell junctions of the imprinted pattern. This phenomenon occurs in the three different examples presented in Figures 1.7a, 1.7b, and 1.7c, where the smaller pores appearing in the SEM images on the right side, are not present in the FIB pattern that was used in each case, images on the left side. The common factor in the three cases is the interpore distance between indented pits of 300 nm (long interpore distance in the rectangular pattern, along which the smaller pores arise), which seems to be enough distance for the development of these

new pores. In such a case, the electric field at the bottom of the imprinted concaves defines the size of the pore cell while the mechanical stress guides the growth direction of the new pores forming at the cell junctions. This way, not only non-hexagonal cells can be generated, but also non-spherical pore shapes are produced depending on the stress field experienced at the cell boundaries. Hence, elongated, elliptical, and triangular smaller pores are generated depending on their surroundings; the bigger pores grow faster and will confine and restrict the growth of the former ones. More complex patterns could be created with both triangular and diamond shape pores as in Figure 1.7e when an array of non-regular hexagonal polygons (inset in Figure 1.7e) is employed. In these nonequilibrium arrangements, the hexagonal cell is partially compressed leading to the formation of diamond, circular, and triangular pores. This also applies to the smaller pores in alternating size patterns, as in Figure 1.7d, where two different sized pits of 65 and 45 nm were imprinted at a 200 nm interpore distance over an Al substrate by FIB (FIB pattern image on the left of the Figure 1.7d). After anodization, the larger pores present a spherical shape with a diameter of 105 nm while smaller pores grow with an elongated shape along the direction that is not restricted by the presence of the bigger pores (see SEM image to the right in Figure 1.7d). The long axis of the pores is 95 nm and the short axis is 50 nm, for the latter the growth in the direction between two bigger pores is cut short due to the much faster growth of the oxide layer of the larger pores thus resulting in such elongated pore shape. On the other hand, circular pores are favored when the neighboring concave patterns surrounding a pit have a symmetrical distribution (of distance and sizes). Also, if the interpore distance of the patterned concave reaches the optimal value to allow the complete development of the pore, the generated pores develop a round shape [196]. Moreover, as the interpore distance is further increased the area between the cell boundaries of neighboring pores becomes too broad and new non-pre-patterned pores can form [196, 197], as mentioned before. The self-formation mechanism of these pores was first studied by Masuda [187] using a hexagonal pattern with a missing hole; however, after the anodization process, a complete repair of the hexagonal arrangement with no missing pores was accomplished, in what the author described as a self-compensating healing process. The growth and complete development of such pores could also be explained accordingly to the equifield strength model [116], as proposed by several authors [171, 196]. But more importantly, the self-compensating mechanism can be used to overcome the resolution limit of the technology

employing lithographic techniques and etching treatments, to produce the stamps and molds, in the case of using indirect indentation methods, as proposed in references [196, 198, 199]. Hence, nanosphere lithography emerges as a promising technique to solve the resolution problem of conventional lithography, by selecting the appropriate size of the spheres. Molding patterns using spheres in the range between 13-500 nm in diameter and different interpore distances have been successfully achieved through this method [174, 200, 201]. In this case, hierarchical nanoporous structures, like the one shown in Figure 1.7h with a multi-periodic porous structure, were prepared by the NSL (nanosphere lithography) method.

1.2.3. Properties of the nanoporous alumina structures and their applications

AAO membranes provide versatile tools for the development of future technologies, with many different applications in a wide variety of fields. One of their main advantages is their low production cost, which makes alumina-based devices cheaper and more easily scalable to industrial production than nanostructures fabricated by other techniques, such as lithography, for instance. Table 1.2 summarizes the different pore shapes with which alumina can be obtained, their direct application in several scientific fields, and their uses as templates for the nanostructuration of other materials. In this section, we revise the latter two.
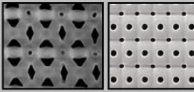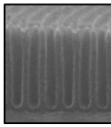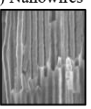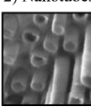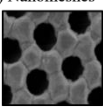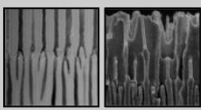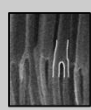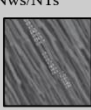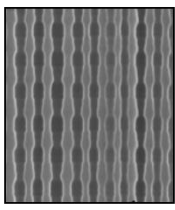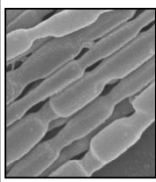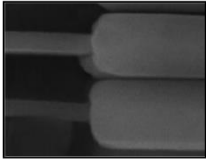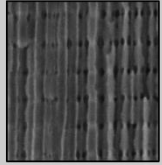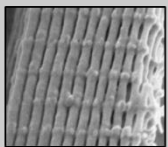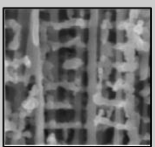
In the previous section, we have shown that many different pore architectures can be achieved through this technology in a controlled way. The high surface area to volume ratio of such membranes is a highly desirable property for drug delivery [202], sensing, and biosensing [24, 25, 203] applications. Showing some advantages such as a controlled drug release that can be sustained over long periods, with no observed bursting effects (where high doses of the load are released in an early stage), chemical stability of the alumina membranes, and the bonus of the possibility of functionalizing the surface to promote the selective release (a review on this application can be found in [202]). Additionally, there has been reported dependence on the total drug load and diffusion kinetics of the subsequent drug release with pore geometry [27]. Three different structures were studied: straight pores, nano funnel consisting of different layers with decreasing pore diameters (from top to bottom), and inverted nano-funnel. The first two show a linear relationship between the amounts of drug-loaded with pore volume. The latter showed a

higher degree of loaded amount of drug per unit volume and a slower release rate of the drug associated with the bottle-neck geometry of the pores and smaller pore diameter of the top layer, which hinders the diffusion of the drug out of the alumina while favoring drug loading. Inverted nano-funnels are adequate for long-term release drug systems. However, if higher release rates are required, then straight pore structures are more appropriate. Also, higher release rates have been achieved, reducing the diameter, d, of the pores at the top surface by adding a polymer layer ($d < 5$ nm). The main challenge in this field is to be able to extend the time-release after 3 months [204], even though there are some promising works [28] this goal is yet to be realized.

Other strategies are the aforementioned chemical tuning of the alumina surface (i.e. hydrophobic or hydrophilic functional groups can alter the water affinity of the loaded drug and its release rate) [204, 205]. The influence of the pH media has also been investigated by researchers [31]. More novel intelligent drug release approaches are based on induced changes of the alumina structures to external stimuli (change in the pH, inducing electromagnetic fields, etc.) to have better control over the way the drug is released and when, and the exact amount that is required in each particular situation. For example, if the AAO is coated with a polymer, polymerization, and depolymerization of this top layer could be controlled by an applied external field through electrochemical polymerization. In return, the opening and closing of the pores are controlled through an external electric field [29]. There is also been reported the addition of iron particles to trigger the release of the load whenever a magnetic field is applied [204]. More recently, a photoresponse transport controlled of molecules process has been developed, where the alumina was modified with certain peptides that are sensitive to light exposure undergoing reversible isomerism transformations. This way the transport of molecules can be switched on and off by an optical stimulus [30]. Finally, taking advantage of their high surface to volume ratio and the varied available morphologies achievable, there are also studies on the application of nanoporous alumina for tissue engineering, providing large areas of hydrophilic or hydrophobic surfaces, depending on the application, for cell proliferation, tissue migration, etc [206].

Another important property of the nanoporous alumina is that the adsorption on its surface is very sensitive to the morphology and structural features of the membrane such as the pore diameters, the roughness of the top surface layer, etc. In the same way, the adsorption of different substances

Table 1.2. *Summary of the different morphologies with which the alumina membranes could be obtained (straight pores, branched pores, modulated or interconnected pores) and possible modifications of the pore shape and geometry, the structures that can be grown by several deposition techniques when acting as templates and the direct applications of such membranes accordingly to the different morphologies of the alumina.*

Morphology	Example	Uses as template			Uses as grown
Pre-patterned guided porous structure*		1) Square -dot arrays**	2) Triangular NTs***	3) Highly ordered cylinders****	Photonic devices
Ordered nanoporous structure●		1) Nanowires	2) Nanotubes ●●	3) Nanomeshes ●●●	Structural coloration: Fabry Pérot Biosensors Adsorption
Branched structure○		1) Y-branched Nws or NTs ○○	2) Multi branched Nws or NTs ○○	3) Hierrachically branched Nws/NTs ○○○	Drug delivery Biosensors
Modulated in diameter nanopores◊		Modulated Nws or NTs◊◊			Structural coloration: DBR Photonic crystals Optical microcavities Graded index filters Biosensors
3D nanoporous structure†		3D Nanowire -networks††			Structural coloration: Distributed Bragg Reflector Photonic crystals Biosensors

along the pore walls is affected by the shape and structural properties of the vertical channels (modulation in the diameter, length, roughness of the pores, etc., see reference [214]. These studies are quite relevant for their use as biosensors, where the pores should be activated to detect certain molecules, for instance. Also, this property can be exploited for applications such as humidity sensors [215]. A further step in these studies is the fabrication of superhydrophobic surfaces by fabricating a highly rough structure with the combination of hard anodization and mild anodization, protecting the material from corrosion, bacteria growth, etc. in a cheap way easy to be produced in big areas [216].

In the optics field, the alumina membrane is understood as a photonic crystal, where one can control the propagation of light across the membrane by the engineering of the porous structure [217-226]. For instance, in the simplest case, the position of the photonic bandgap is tuned with the interpore distance or with the pore diameter, if the former is kept constant [219, 220]. In this context, the development of more complex anodization processes to gain control over the in-depth modulation of the porous structure of the alumina such as pulsed and cyclic anodization techniques provides a new means in the control and modulation of light. Hence, most recent and advanced photonic crystal structures that have been reported in the literature are based on branched [227-229], modulated [162, 163, 230-235], or 3D-nanoporous anodic alumina [22]. The photonic response of these structures, from simple straight pores to other more complex pore architectures (as the ones shown in Figure 1.6), will be extensively described in chapter 3 of this thesis, which copes with the photonic crystal properties of the alumina and their possible applications, dealing in particular with the specific case of the perforated 3D nanoporous AAOs.

Another application of the alumina that we explore in chapters 4 and 5 of the thesis, is their use as templates. These membranes constitute reliable platforms for the nanostructuration of all kinds of different materials with a high degree of control over the final shape of the material being able to obtain solid nanowires [34, 42, 44, 211, 236-240], hollowed nanotubular wires [46, 47, 49-52, 149, 236, 241-247], non-continuous films of antidots arrays [69, 70, 72, 74, 248-250], branched nanowires [59, 211, 236, 251], modulated (in

diameter) nanowires [43, 45, 169, 252] or even, 3D interconnected nanowire networks [32, 63, 65, 66] see Table 1.2. Which can be fabricated employing different deposition techniques such as ED, CVD, ALD, etc., or in some cases by direct infiltration of the material (i.e. polymers). The resulting nanostructures have many different applications depending on the filling or deposited material, but also on the dimensions and structural parameters of the synthesized structures within the nanometer scale, such as nanowire/nanotube diameter or size of the hole of the antidot films (corresponding to the pore diameter), interdistance between neighboring wires/tubes or interdistance between antidots (interpore distance of the original alumina template), the length of the wires and tubes or the thickness of the antidot film. In addition, the distance between transverse connections in the 3D networks, is a parameter that can be modified as desired during the fabrication process. These nanostructures open new possibilities and ways to tailor the magnetic [45, 47, 49, 65, 252-260], electrical [46, 64, 237, 244, 251, 261-266], optical [50, 267], etc. properties from bulk to nano, in the design of next-generation devices and improvement of the existing technologies.

Among all the different structures that one can obtain, we have decided to study the properties of 3D nanowire networks made of Ni and Co, to explore new functionalities in the magnetic field (chapter 4), and also Bi_2Te_3 3D networks have been grown for their application in thermoelectrics, looking to improve the thermoelectric performance of such material (chapter 5). The fabrication of these structures has been possible due to the recent development of the perforated 3D AAO templates, described in section 1.2.2.

2. Chapter 2: Experimental techniques and characterization

This chapter starts with a detailed explanation of the fabrication techniques employed in this work (Section 2.1). Firstly, the anodization procedure and subsequent etching steps for the growth of conventional 1D-AAO and 3D-AAO membranes is presented in Section 2.11. Secondly, electron beam evaporation technique used to fabricate conductive layers on the templates will be introduced in Section 2.1.2, followed by a description of the electrodeposition technique which was employed to synthesize 1D nanowires and 3D nano-networks, Section 2.1.3. Then, this will be followed by a brief description of the different techniques used during the morphological, structural, and compositional characterization of such structures (Section 2.2). Finally, in a separated section, Section 2.3, the systems employed in the characterization of the optical, electrical, and magnetic physical properties of the 1D nanowires and 3D nano-networks, will be introduced.

2.1. Fabrication techniques

2.1.1. Anodization process: Anodic Aluminium Oxide (AAO) membranes, fabrication method

2.1.1.1. Conventional 1D-AAO membranes

Well-ordered 1D alumina membranes consisting of only longitudinal pores were fabricated during this thesis to be used as templates for the growth of nanowires by electrochemical deposition. Self-ordering of the porous structure is achieved through a two-step anodization process, as first reported by Masuda *et al*. [7, 268] and illustrated in Figure 2.1. The fabrication process of the membranes was carried out under mild anodization conditions at a constant applied voltage of 25 V, using a 0.3 M sulfuric acid solution diluted in deionized water as the electrolytic bath. The temperature of the bath was fixed at 0 °C. These are the optimized conditions for 0.3 M H_2SO_4 [99]. During this process, a first anodization step is performed under the conditions described above for 24 h. After this long anodization period, the self-arrangement of the pores at the metal/oxide interface is achieved.

Table 2.1. Anodization conditions used for the growth of 1D alumina membranes and their corresponding structural parameters pore diameter (Dp), inter-pore distance (Dint), and barrier layer thickness (tb).

Acid	Electrolyte concentration (M)	Anodization regimen	Applied voltage (V)	Temperature (°C)	Pore diameter, D_p (nm)	Interpore distance, D_{int} (nm)	Barrier layer thickness, t_b (nm)
Sulfuric (H_2SO_4)	0.3	MA	25	0	19-21	63-65	22-23

The end of this step is the removal of the oxide porous layer formed by chemical etching in 6 wt. %H_3PO_4 and 1.8 wt. %CrO_3 mixed solution, to ensure the complete dissolution of the membranes they should be kept immersed in the cited solution for 12 to 24 h. As a result, we are left with just the remaining aluminum substrate which in its surface presents a hexagonal pattern structure that will facilitate the growth of highly ordered pores in the direction normal to the substrate during the second anodization step. This second anodization is carried out following the same procedure; however, the anodization time was reduced to only 6 to 12 h depending on the required

thickness of the membranes. The structural parameters of the final alumina regarding t_b, D_{int}, and D_p, were 22-23, 63-65, and 19-21 nm, as recorded in table 2.1. These values were experimentally measured from the SEM images of the actual samples, see Figure 1.2 in chapter 1. In particular, the barrier layer thickness was taken from the cross-sectional SEM image in Figure 1.2d. While the inter-pore distance and diameter pore were obtained from the SEM top image of an alumina (as in Figure 1.2c). The measured values of both parameters, D_{int} =63-65 nm and D_p =19-21 nm (for an alumina grown at 25 V), are in good agreement with the empirical equations *(1.6)* and *(1.7)* that describe the linear relation of the D_{int}, and D_p with the anodizing potential U, respectively.
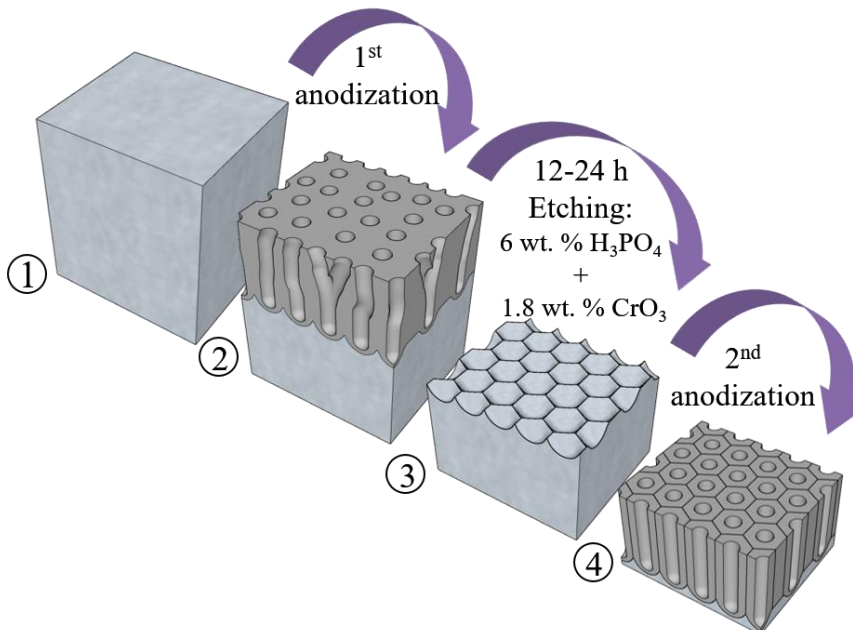
Figure 2.1. Schematic sketch of the steps involved in the two-anodization process carried out in our samples and originally developed by Masuda et al. [7,99] to obtain a higher order in nanoporous alumina.

2.1.1.2. 3D AAO membranes

This thesis is mainly focused on the study of 3D nano-networks, 3DNNs, consisting of transversely interconnected nanowires that have been grown in a new type of alumina membranes, here called 3D AAOs. The most remarkable feature of the 3D AAO membranes is the addition of transversal pore channels interconnecting the porous structure of the 1D AAOs, described in the previous section. Now, every vertical pore is transversely connected to

its closest 6 neighbour pores. This 3D porous structure extends in the three space directions (x, y, z), as its name indicates. The way the transversal pores are introduced into the structure is by modifying the second anodization step. In this case, instead of applying a constant voltage, pulsed anodization is performed, alternating longer pulses at a lower potential of 25 V with shorter ones of 33 V, higher voltage. For that, the current provided by the power source was limited to 0.14 A, which corresponds to a current density of $2.85 \cdot 10^{-2}$ A/cm^2 for an anodized aluminium surface of 4.91 cm^2. Pulsed anodization was carried out using the same electrolyte concentration and temperature of the bath, 0.3 M H_2SO_4 at 0 °C, as in potentiostatic anodization conditions.

In Figure 2.2, Mild constant anodization and Mild/Hard pulsed anodization are compared. Figure 2.2a shows the applied voltage signal at a constant potential in MA conditions ($U_{MA} = 25$ V) for the growth of 1D AAO with straight porous structure, corresponding to the SEM image in Figure 2.2c, and its respective current density transient curve, as recorded during the second anodization step. Figure 2.2b shows the voltage profile of pulsed anodization, switching HA pulses, fixed at $U_{HA} = 33$ V and during a certain time, $t_{HA} = 2$ s, with MA pulses of $U_{MA} = 25$ V and a certain duration, t_{MA}. The duration of the MA pulses was varied along this thesis for different proposes from 100 s up to 540 s. For higher stability of such transversely perforated membranes mild anodization at 25 V is performed at the beginning and the end of pulsed anodization for 800 s, before the first HA pulse and after the last one, t_i and t_f, respectively. The total duration of the pulsed anodization was adapted depending on the required thickness of the 3D AAO template (normally, 6-6.5 h resulting in a thickness of 20-30 µm or 3D AAOs with a thickness of 50-60 µm were grown for 12-14 h in this thesis). In this graph, N is the number of HA pulses and depends on t_{MA} and the total thickness of the 3D AAO (or total anodization time). Underneath, the recorded current density-time curve during pulsed anodization can be found.

During this pulsed anodization, the thickness of each segment can be controlled by the duration of each of the applied pulses, as indicated in the insert image in Figure 2.2d, where the correlation between the duration of the MA and HA pulses (t_{MA} and t_{HA}, respectively) and the thickness of the MA and HA layer is shown. Also, the 800s initial (t_i) or final (t_f) MA pulse is shown in this SEM image (Figure 2.2d). Table 2.2 compares the anodization conditions

used to grow 1D and 3D alumina templates, and the structural parameters of the as-grown membranes.

In this step, after the pulsed anodization, the transversal pores are not opened; this is achieved afterwards through chemical etching. The etching process would be explained in detail in the following section (section 2.1.2.1). Alternating between MA/HA pulses produces a variation of the wall thickness or, in other words, modulation of the pore diameter, however, the mechanism behind is yet not well understood. It seems that the key factor is the difference between the oxide formation and oxide dissolution rates in the two regimens, MA and HA. HA anodization is associated with large evolution of heat as compared to MA, and accelerating oxide dissolution rates, which favors thinning of the pore wall structure [11, 165, 269]. Moreover, the higher content of impurities (incorporation of the anionic species present in the electrolyte into the pore walls is favoured under HA conditions [166, 170]) and less density of the HA layers make them less chemically stable against chemical etching compared to MA layers, hence, selective etching of HA layers is accomplished.

44

Table 2.2. *Anodization conditions used during MA anodization and MA/HA anodization, and structural parameters of 1D AAOs and 3D AAOs.*

Anodization conditions and structural parameters	1D AAO		3D AAO	
[H_2SO_3] (M)	0.3		0.3	
Temperature (°C)	0		0	
Anodization regimen	MA		MA	HA
Applied voltage (V)	25		25	33
Anodization pulses	-		t_{MA} = 100-540 s	t_{HA} (s) = 2 s
Thickness of MA/HA layers			MA layer = 80-720 nm	HA layer = 35-40 nm
Pore diameter, D_p (nm)	19-21		19-21	
Interpore distance, D_{int} (nm)	63-65		63-65	
Barrier layer thickness, t_b (nm)	22-23		22-23	
Anodization time (h)	6	12	6	12
Total thickness (µm)	30	60	30	60

2.1.2. Post treatments of the alumina membranes

2.1.2.1. Etching procedure

An etching treatment must be performed on the as-fabricated 3D AAO's to reveal their 3D porous structure. During this process the etching times must be precisely adjusted so that selective chemical dissolution at certain positions along the vertical pore channels, corresponding to the HA pulses, is achieved while avoiding over-etching, which would revert in the collapse of 3D AAO. A completely open 3D porous alumina membrane is shown in Figure 2.2d after an etching treatment.

The etching procedure consists of several steps. First, removal of the remaining aluminum substrate is accomplished using an $HCl/CuCl_2$ solution in an iced bath to slow down the dissolution rate of the aluminum, which affords more control over the process and thus, avoids further etching of the alumina membrane. This is followed by chemical etching of the initial oxide barrier layer in a 10%wt H_3PO_4 diluted solution for 8-14 min, depending on the total thickness of the alumina membrane, at 30 °C. Finally, the samples are immersed in a similar but less concentrated solution, 5%wt H_3PO_4, also at 30 °C to reveal the transversal pores. Etching times were varied as a function of the thickness of the AAO, from 20-25 min for the thinnest AAOs (30 µm) up to 50-55 min for the thickest of 60 µm.

Table 2.3. *Etching times and final structural parameters of 1D AAOs and 3D AAOs.*

Etching parameters		1D AAO	3D AAO
Etching time in 10%wt H_3PO_4 (min)	Total thickness 30 μm	8	8
	Total thickness 60 μm	14	14
Etching time in 5%wt H_3PO_4 (min)	Total thickness 30 μm	20-25	20-25
	Total thickness 60 μm	50-55	50-55
Etching temperature (°C)		30	30
Structural parameters after the etching treatment		1D AAO	3D AAO
Pore diameter, D_p (nm)		45-50	45-50
Transversal pore dimensions (nm)		-	Length = 30 nm
			Width = 15-20 nm

After the etching, the walls of the vertical pores are also etched but to a lesser extent, thus the diameter of these vertical pores was increased from the characteristic 19-21 nm in diameter of the as anodized 1D AAO, in 0.3 M H_2SO_4 at 25 V, up to a diameter of 45-55 nm in the case of 3D AAOs. For this reason, 1D AAO membranes were also etched, to increase the diameter pore up to 45-55 nm. So the nanowires grown using either template would have the same pore diameter.

The transversal pores present an elongated shape, thus having different dimensions along the vertical (or length of the pore) and transversal (width of the pore) direction. The former being the longest of around 30 nm while the latter is the shortest one with 15-20 nm. Table 2.3 summarizes the etching times and the final structural parameters of the 1D and 3D alumina after the etching was performed in both kinds of alumina.

In this thesis, it was found that by immersing the samples vertically to the bottom of the beaker to avoid obstructing one side of the AAO membrane, the homogeneity of the etching was improved. However, above certain thickness (> 60 μm) homogeneity along the whole membrane could not be achieved by any means, finding zones where the transversal pores were not opened yet or on the contrary, that were excessively etched.

The 3D AAOs and 1D AAOs described in sections 2.1.1.2 and 2.1.1.1, respectively, would be filled by an electrochemical process to produce nanostructures. Further details of the deposition process of the different materials (on one hand magnetic ones Ni, Co, different Ni/Co alloys, and on the other hand, semiconductor materials with thermoelectric properties as Bi_2Te_3) grown in this thesis are given in the following section. However, before electrodeposition can be performed, both kinds of membranes must be metalized. Electrochemical deposition occurs over a conductive surface, but anodic alumina oxide is a non-conductive dielectric material, hence evaporation with a metallic material is required, this is next described.

2.1.2.2. Thin-film electron beam evaporation

The substrates used in this thesis (Si substrate, and 1D and 3D AAO templates) to grow the above-mentioned materials (in the form of films, 1D nanowires, and 3D nano-networks, respectively) were metalized using electron beam evaporation technique, in which an electron beam is emitted from a charged tungsten filament and directed towards a target of the metallic material of our choice. The target heats up, as it is being hit by electrons, until its transformation into the gaseous phase. The evaporated material precipitates and deposits, covering any surface around the vacuum chamber where the process takes place. The substrate must be introduced into this chamber and located within a reaching distance from the target.

In all cases, one side of the different substrates was evaporated with 5 nm of chromium (Cr) and 150 nm of gold (Au) resulting in, from bottom to top: Si substrate/5 nm Cr/150 nm Au, 150 nm Au/5 nm Cr/30-60 µm 1D AAO template and 150 nm Au/5 nm Cr/30-60 µm 3D AAO template. Once the working electrode is prepared, the evaporated layer of Au on the alumina templates is only accessible from the vertical pores.

Further on, before the experimental determination of the thermal conductivity of bismuth telluride samples measured by the photoacoustic technique, the samples have to be coated with an 80 nm Titanium layer, which was also deposited using the electron beam technique.

2.1.3. Chemical electrodeposition technique

The electrochemical deposition process entails the reduction of the metallic ions contained in an electrolytic solution to accumulate over the surface of a

conductive or semiconductive substrate, through electron transfer [270], according to the following reaction:

$$M^{z+}_{solución} + ze \rightarrow M_{red}$$ (2.1)

This process is assisted by an electric field generated between two electrodes immersed in the electrolyte, those being:

(1) The conductive substrate acting as a working electrode (WE) and over which deposition of the ions in solution takes place.

(2) The counter-electrode (CE), where oxidation of the electrochemical species, to maintain the neutral charge of the solution, occurs. During this thesis, a platinum mesh was used as a counter-electrode in all deposition processes.

A third electrode is added, an Ag/AgCl reference electrode (RE) with a stable and well-known electrochemical potential, so the established potential between the WE and CE can be measured. The three of them composed a three-electrode electrochemical cell system (see Figure 2.3).

Since the 70 s, electrodeposition has been widely used in the industry, more in particular in the automotive sector for coatings [271]. In the last years, however, it has been gaining relevance as a technique for the growth of nanowires. Electrodeposition offers multiple advantages over other more complex and expensive physical or chemical techniques, such as molecular beam epitaxy (MBE) or epitaxial growth by pulsed laser deposition (PLD), among others [272, 273]. Some of them are the simplicity and low cost of the system that only requires a three-electrode cell, an electrolyte of the desired material, and a power source. The process can take place at room temperature and in air conditions, depending on the material, without the need for low temperatures or vacuum. It is a highly versatile method since virtually any material can be grown using this technique and non-planar complex shapes can be fully coated [274]. In this thesis, it has been proved as a valid technique to fill the transversal channels of the 3D AAO membranes, as the electrolyte fills the 3D porous structure of such membranes when immersed in the solution. Moreover, high control over the quality of the grown material (thickness, chemical composition, crystallite size, crystallographic

orientation, ...) can be achieved during the deposition process by optimization of the deposition parameters such as temperature, pH, selected solvent and additives, applied potential/current, deposition time, stirring, cell dimensions and cell configuration (area of the WE, distance between the WE to the CE). The most important variables affecting the electrodeposition process are listed in Figure 2.3.

2.1.3.1. Electrodeposition process

Three electrode cell

| **External variables** Temperature, pH | **Cell configuration** Dimensions, distance between WE and CE |

I

WE
- Substrate
- Shape/Geometry
- Area
- Cleaningness

V

Electrolyte
- Type of solvent (aqueous, organic)
- Concentration
- Ionic species

RE

Power source variables
- Deposition tecnique (constant, pulsed, potentiostatic, galvanostatic...)
- Applied potential
- Applied current
- Deposition time

WE

Mass transfer limiting factors
- By diffusion/ migartion/convection
- Surface
- Distance to WE
- Concentration

CE

Figure 2.3. Sketch of the three-electrode cell configuration used in most experiments of this thesis. Ag/AgCl was used as the reference electrode (RE), Pt mesh employed as the counter-electrode (CE), and a 3DAAO membrane as the working electrode (WE). The experimental parameters that control the deposition are recorded.

Under an electric field when working at the equilibrium potential of the cell (*equation 2.2*), segregation of charges is induced on the surface of the substrate (WE) in contact with the electrolyte, and an interface is formed between both. At this interface, the working electrode acting as the cathode is negatively charged towards which the positively charged cations in the electrolyte are electrostatically attracted, forming a double layer of charged particles, called the Helmholtz double-layer [275, 276], see Figure 2.4a. Then,

under a certain overpotential (an applied voltage above the equilibrium potential), cations enter the discharged region, in close vicinity to the WE surface, where they receive electrons and are reduced to atoms, as illustrate in Figure 2.4b. As atoms, they are strongly attached to the cathode surface (WE), at the Inner Helmholtz diffusion layer (IHP). It was found that as the distance to this surface increases the electric potential experienced by the cations in the electrolyte linearly decreases, until a limiting point called the Outer Helmholtz diffusion layer (OHP), around this layer cations are still solvated. Passed this last region, the potential decreases exponentially entering a diffusion layer, made of freer ions that move in the electrolyte under the influence of the electric attraction, electrolytic concentration, and thermal motion. Forming a three-layer model as described by Grahame [277], (see Figure 2.4).

Through Nernst general equation, giving the reduction potential of the species in dissolution, the thermodynamic potential of the electrochemical cell at equilibrium, which corresponds to the situation illustrated in Figure 2.4a, can be known:

$$E = E^0 - \frac{RT}{nF} \ln a$$

(2.2)

, where E is the cell potential, E^0 the standard reduction potential for reaction (2.1) versus the standard hydrogen electrode (SHE), R the gas constant (8.3143 J/Kmol), T the absolute temperature (K), n the valence change or the valence number of the metal element, F the Faraday constant and a the activity of the metal ion, which can be approximated to the concentration of the metal ion in the electrolyte. The voltage difference between the equilibrium potential of the cell and the actual deposition potential is known as the over-potential. The way to explore the best-suited deposition potential in each case is through cyclic voltammetry. This technique allows us to study the different reduction/oxidation reactions taking place in the electrolyte.

i)   *Pulsed electrodeposition*

The deposition mechanism during the field-assisted reduction/oxidation of the chemical species in dissolution can be divided into five steps (Figure 2.4c):

(1) Electric transport migration of the oxidized species at the CE towards the WE-electrolyte interface. An electric field is generated between both electrodes.
(2) Adsorption to the WE electrode surface.

50

(3) Charge transfer of electrons from the WE and reduction of the electrolytic species, when the applied potential reaches the reduction potential.

(4) Diffusion of the atoms attached to the WE across its surfaces until finding other atoms where they start to grow forming atomic clusters, this is known as a nucleation site.
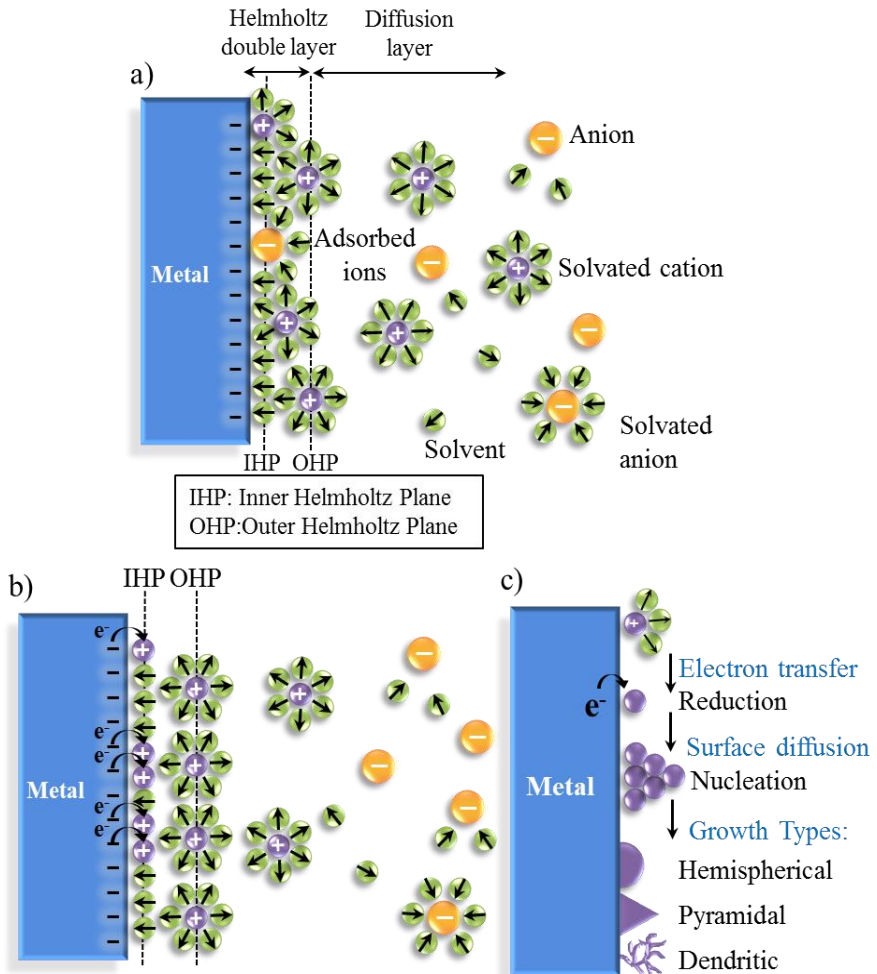
Figure 2.4. a) Three-layer model at thermodynamic equilibrium, without applying external voltage.b) Electron transfer from the metallic surface electrode to the absorbed ions at the IHP, under an external applied potential. This illustrates the reduction half reaction of ions at the cathode. c) Steps of the deposition process: 1) electric transport of the ionic species towards the WE-electrolyte interface, 2) adsorption of the ions on the WE surface, 3) charge transfer of electrons, 4) diffusion of the reduced atoms across the surface of the WE until arriving at a growing site. Then, as nucleation begins 5) the material can grow with different morphologies (i.e. hemispherical, pyramidal, dendritic…).

(5) Further growth and organization of the atoms within a certain crystallographic order and morphology.

During deposition, the kinetics of the redox reaction (step 3) could limit the deposition rate at the WE electrode; this is known as a charge transfer limiting process. This occurs at low reduction potential regimens. The mass transfer rate (step 1) dominates the deposition process at high overpotentials as a function of the electrolyte concentration at the WE-electrolyte interface, which is limited by the migration, diffusion, and convection rates. To avoid the latter case, electrodeposition was performed switching the potentiostatic mode (at a certain applied voltage, for a time on of 1s, $t_{on} = 1s$) with the galvanostatic mode, this is known as pulsing or pulsed electrodeposition. As deposition occurs the ions are retrieved from the solution and the electrolyte concentration at the electrolyte/WE interface is exhausted. During the galvanostatic pulse, the current circulating in the system is set to zero for 0.1 s time off ($t_{off} = 0.1$ s). The established potential between the electrodes, at zero current, is the open circuit potential at which the system is at equilibrium and allows it to relax. This way the exhausted electrolyte concentration at the WE-electrolyte interface can recover before the next potentiostatic pulse by diffusion of the ionic species from the bulk electrolyte towards this interface. The applied potential versus Ag/AgCl in the potentiostatic part of the pulses was determined by a cyclic voltammetry (CV) curve performed before each deposition. A bi-potentiostat (Autolab PGSTAT 302) was used with the customized software Nova 1.10 to obtain the cyclic voltammograms and to control the potenciostatic/galvanostatic pulses.

ii) *Cyclic voltammetry*

Cyclic voltammetry (CV) studies allow observing the charge transfer processes associated with the oxidation/reduction reactions of the electrolytic species. Figure 2.5 illustrates a cyclic voltammogram of $Bi^{3+}/HTeO_2^+$ species. In this case, the CV is performed by a cyclic sweep of the potential between two set voltage values, of negative voltage and positive voltage, while measuring the current that develops in the electrochemical cell. Scans are taken starting from the open circuit potential (OCP), at which the system is at its equilibrium potential, according to Nernst equation *2.2*, with no current circulating through the cell. Under an applied voltage, the equilibrium position shifts and the current begins to flow. Thus, the equilibrium between the

concentration of reduced and oxidized species is altered. First, a forward negative scan is carried out until the extreme negative potential is reached; this potential is higher, in absolute terms than the reduction potential to ensure the reduction of the chemical species. The resulting current is called the cathodic current (i_{pc}), along this cathodic branch (marked by the orange arrows in the graph) the reduction peak (E_{pc}) of the ionic species is located, and around this peak (peak A in Figure 2.5) deposition over the WE surface takes place. Then, (the direction of the potential sweep is switched) the potential is ramped back up in the opposite direction towards positive voltages, well above the positive oxidation potential, before returning to the initial OCP potential, allowing the system to relax. The positive branch of the cyclic voltammetry curve (indicated by the red arrows in Figure 2.5) measures the anodic current (i_{pa}) during the oxidation reaction. At the oxidation peak (E_{pa}), desorption of the deposited species occurs as they are being oxidized and re-dissolved into the electrolyte. The reduction and oxidation reactions reach a peak and the current density decreases, due to the depletion of ions at the WE surface. Then, a diffusion control mechanism is established.

$$3HTeO_2^+ + 2Bi^{3+} + 18e^- + 9H^+ \leftrightarrow Bi_2Te_3(s) + 6H_2O$$
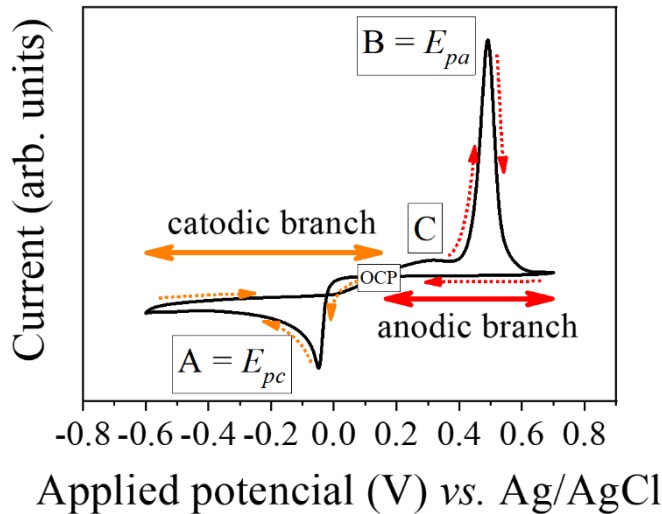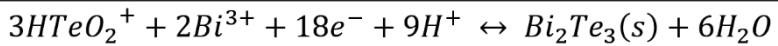
Figure 2.5. An example of the cyclic voltammetry of $Bi^{3+}/HTeO_2^+$ solution obtained in this PhD thesis. Peak A corresponds to the co-deposition reduction potential (E_{pc}) of both species to form Bi_2Te_3. Peak B is associated with the direct oxidation potential (E_{pa}) of Bi_2Te_3 according to the general equation above. Peak C has been assigned as a minor oxidation peak of Bi^{3+} to Bi [430].

2.1.4. Preparation of the filled alumina membranes for experimental measurements

To fully characterize the nanowires, and 3D nano-networks, some experimental techniques require preparation of the sample, from complete removal of the supporting substrate to mechanical polishing or chemical etching to partially expose the surface of the material. The techniques used to prepare them will be described in this section.

2.1.4.1. Dissolution of the alumina membrane

Some techniques, such as TEM and t-EBS, both used in this thesis, require the material to be freestanding to perform their topographical and structural characterization, as it was done in our case for the 3D nanowire networks. Hence the supporting 3D AAO embedding matrix was left to dissolve for 24-48 h, in 6 wt. %H_3PO_4 and 1.8 wt. %CrO_3 mixed solution. Afterwards, the freestanding interconnected nanowires were filtered using a Kitasato flask with the help of the vacuum, while washed with water and ethanol repeatedly. Once clean, the nanowires were recovered from the filter paper and kept in suspension in ethanol. A few drops are cast over TEM grids and after the ethanol has evaporated the freestanding 3D nano-networks can be measured.

2.1.4.2. Exposing the surface of the nanowires

As in the case of Bi_2Te_3 films, for the characterization of the Bi_2Te_3 3DNNs, the gold layer has to be removed, entirely or partially, depending on the technique. The interconnections between the longitudinal nanowires allow using the same experimental techniques as the ones used to measure the properties of bulk materials or films. For example, the electrical conductivity of a 3D Bi_2Te_3 nano-network can be measured much in the same way as in films, since the electrical current runs along the nanowires, but also from one nanowire to the next as they are interconnected. It is, however, required to eliminate the Au and Cr layers and expose the nanowires to be able to add electrical contacts.

The nanowires were exposed by two different approaches, see Figure 2.6a: mechanical polishing of the alumina from the side of the gold and chromium layer or selective chemical etching of both, the Au first and then the Cr layer.
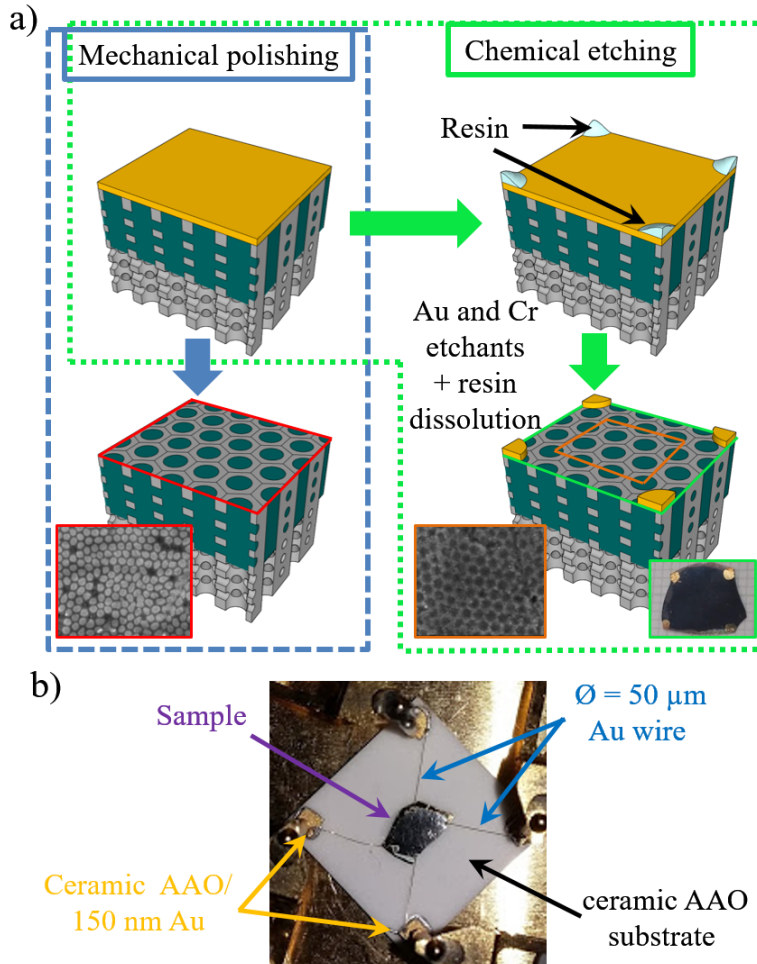
Figure 2.6. *a) Sample preparation through mechanical polishing and chemical etching. Inset images on the left side provide a microscopic view of the samples after the removal of the Au and Cr layers by the two different approaches. On the right side, the inset corresponds to a macroscopic photo of a sample after chemical etching of the Au and Cr that leaves four gold pads at the corners of the square for electrically contacting the sample. b) The macroscopic image of a polished sample that was electrically contacted at the corners.*

i)   *Mechanical polishing of Au and Cr*

Samples are first glued to a metallic holder by the opposite side of the Au layer. Then, the Au layer and the 5 nm Cr layer were polished away using a polishing cloth along with alumina powders of different particle sizes: 5 µm, 1 µm, 0.3 µm, and 0.05 µm. Polishing in that order, from the largest to the smallest powder size, the roughness of the polished surface is reduced down

to 50-20 nm. In Figure 2.6a, the inset marked in red shows an SEM image of the exposed nanowires after mechanical polishing of the Au and Cr layers.

ii)   Selective chemical etching of Au and Cr

For the characterization of the electrical properties of the 3D Bi_2Te_3 nano-networks, the samples have to be electrically contacted. Nail polish was employed to cover a small area at the corners of a squared cut sample, to protect the gold for the etching, see illustration of this etching process in Figure 2.6a. The remaining gold pads at the corners, as the ones shown in the inset macroscopic image (boxed in green), can be used later to contact the sample.

The Au is first selectively removed using a potassium iodine (KI) and iodine (I_2) solution in water, in 1:4:4 I_2:KI:H_2O ratio. And the Cr, the Cr etchant consists of 0.5 M potassium permanganate ($KMnO_2$) and 0.5 M sodium hydroxide (NaOH), compatible with Bi_2Te_3. Samples were suspended on the etching solutions for 1 min and 30 s, respectively. The side of Au and Cr layers is the side in contact with the solution. Samples are rinsed with water after the etching and finally with acetone to remove the nail polished at the corners of the sample. An SEM photo of the etched gold side of the alumina revealing the nanowires is displayed in the inset image inside the orange box of Figure 2.6a.

2.1.4.3. Electrical contacts

The four gold pads left untouched at the corner of the samples are used to contact the nanowires electrically. The gold reduces the electrical resistance of the electrical contacts as compared to directly contacting over the exposed surface of the nanowires (through mechanical polishing or chemical etching). Moreover, this gold layer is in electrical contact with the nanowires, given that it was the metallic layer from which the nanowires grew in the first place. Then, a gold wire with a diameter of 50 µm is attached at one end to the remaining gold at the edges of the sample and to its other end to 2x2 mm^2 of ceramic alumina evaporated with 5 nm Cr and 150 nm Au. The silver epoxy paste was used to glue the gold wires, leaving it to cure at 50 °C (to avoid evaporation of tellurium from the 3D Bi_2Te_3 nano-networks embedded in the alumina matrix) for 1-2 h. The squared ceramic alumina pads as well as the sample (from the side where there wasn't gold) were previously fixed to the

same ceramic alumina substrate or a glass substrate. An actual photo of an electrically contacted sample is supplied in Figure 2.6b.

2.2. Structural characterization techniques

2.2.1. Scanning electron microscopy (SEM)

The morphology and topography of the different structures (AAO membranes, films, nanowires, and 3D nano-networks) grown in this thesis were assessed in further detail by scanning electron microscopy (SEM), using a high-resolution SEM Verios 460, from FEI, with a resolution down to 10 nm. SEM provides three-dimensional–like topographical information of bulk specimens on nanometer resolution. SEM images have great resolution and depth of field, for which SEM is being widely used as a surface analysis tool [278].

SEM functions by focusing a relatively high-energy electron beam (typically, 1-100 keV) on a specimen that is under vacuum. This interaction results in numerous emitted signals: low-energy secondary electrons, backscattered electrons, X-ray emission, etc.[278, 279] From the secondary electron (SE) emission, an image of the surface morphology of the sample under observation can be reconstructed. Backscattered electrons (BSE) provide a compositional contrast image. This last signal would be of use when looking at nanowires and 3D nanowire networks still embedded in 1D AAO and 3D AAO membranes, respectively. The high contrast between the electrically isolating AAO and the conductive filling is highly useful to determine the filling rate of the membrane, the front growth, and other properties.

Normally, SEM analysis of non-conductive materials, such as the alumina membranes studied in this thesis, requires a previous metallization of the sample to minimize negative charge accumulation from the electron beam. This could be avoided in the HR-SEM (which requires the immersion lense mode and employs working distances below 4 mm, at high vacuum, between $1 \cdot 10^{-6}$ and $5 \cdot 10^{-7}$ mbar) used in this work by working at low accelerating voltages. For the non-conductive alumina membranes, in particular, the optimum conditions were 1.13-1.3 kV voltage and a current value of 0.25 pA. Short acquisition times from 100-300 ns that reduce the time exposure of the sample to the electron beam while SEM micrographs are taken, thus reducing the charge accumulation, are employed. To make up for the reduction of the

acquisition time, scan interlace and high integration number of frames, up to 75, were applied to improve image resolution.

However, when conductive nanowires and 3D nano-networks (still embedded in the alumina matrix or dissolved) were examined under SEM the acquisition parameters were varied. A higher accelerating voltage of 2 kV and a 0.5 pA current are required to obtain a high enough BSE signal for compositional contrast imaging. Longer acquisition times are used (10-30 µs) in combination with just 1 frame integration providing great topographic details.

2.2.2. Energy dispersive X-Ray Spectroscopy (EDX)

As mentioned above, the SEM electron beam also stimulates the emission of X-Rays by dislodging inner shell electrons, which are then replaced by an outer shell electron. As the outer shell electron fills the inner shell, the energy difference is emitted as an X-Ray. Each element produces a characteristic X-Ray signal, allowing the compositional analysis of the sample [280].

EDX spectroscopy was employed to determine the chemical composition of 3D Ni-Co alloys and study the stoichiometry of Bismuth telluride films and 3D nano-networks. Measurements were carried out with a Hitachi S-3000 N SEM, assuming a 5% error in the atomic % value. Compositional analysis was performed employing high voltage conditions, 20 kV and a working distance of 15 mm. This service was provided by the SIdI department (Servicio Interdepartamental de Investigación) of Universidad Autónoma de Madrid, (Spain).

2.2.3. Transmission electron backscattered diffraction (t-EBSD)

t-EBSD is based on the detection of the transmitted Kikuchi electrons [281] in a scanning electron microscope (SEM). The sample specimen must be electron transparent, and hence the thickness of the sample is a critical parameter to the resolution of t-EBSD measurements, which must stay within a reasonable range so that electron transparency is maintained. Furthermore, the sample must be placed horizontally or tilted backward from the detector [282]. Sample preparation was executed, accordingly, by dispersing 3D nanowires (that are 50-55 nm in diameter) over TEM grids after the dissolution of the AAO (described in section 2.1.4.2).

The bandwidth of Kikuchi diffraction lines agrees with Bragg's Law (see reaction *2.3*) so that a crystallographic study can be performed [281]. Then, the reconstructed image of the Kikuchi lines provides local information on the crystallographic structure of the sample with spatial resolution down to 5-10 nm [283, 284] but allowing the mapping of larger areas than under TEM observation. This is a useful technique to carry out a thorough statistical analysis of nanostructured materials. In this thesis, we look into the crystal orientation along the transversal connections between longitudinal nanowires (with sizes of 35 nm in height and 15-20 nm in width).

The t-EBSD measurements were performed in a Lyra dual-beam SEM-FIB (focused ion beam) instrument (TESCAN). The t-EBSD scans were taken using a 30 kV, 5 nA beam, with step sizes of 5-15 nm. t-EBSD measurements and analysis were done by Xavier Maeder at EMPA institute (Swiss Federal Laboratories for Materials Science and Technology) in Switzerland.

2.2.4. Transmission electron microscope (TEM)

TEM is the most complete technique in microscopy, providing topographical imaging, compositional analysis, and crystallographic information. Contrary to SEM, TEM microscopy measures both the electrons that are emitted forward and those transmitted through the sample. Using higher accelerating voltages than in SEM, in the range of 100-300 kV, the spatial resolution is improved down to 0.1-0.2 nm [285].

TEM microscopy possesses two working modes: a bright field and a dark field mode. The former only uses transmitted electrons to form TEM images, whilst the scattered electrons are blocked. In dark-field TEM the scattered electrons are the ones that are selected, and the electrons passing through the sample would be now excluded. Electrons suffer more scattering when interacting with heavier atoms than lighter ones. So that heavy atoms appear darker in bright field images, but brighter in dark field mode. Something similar occurs in the crystalline samples, where electrons are strongly diffracted, giving a darker contrast, if bright field mode is employed and crystallographic information can be lost. Hence, using darkfield mode is more reliable to study the crystal structure of the samples.

In this thesis, TEM characterization of 3D Bi_2Te_3 nanowire networks was performed to corroborate the stoichiometry of the nanowires and to study not only the crystal preferred orientation of the longitudinal nanowires, but also

to obtain local information of the crystal orientation at the location of the transversal interconnections along the nanowires. TEM analysis was carried out using an FEI Tecnai and an FEI Titan low-base HR-STEM, located at Laboratorio de Microscopía Avanzadas in Universidad de Zaragoza, (Spain).

2.2.5. TEM tomography

Electron tomographic imaging in TEM has also been performed. This tool allows generating a 3D reconstruction of the sample from 2D images, opening the field to 3D imaging. This technique was employed to obtain a reconstruction of the actual structure and morphology of the 3D nano-networks that have been grown in this thesis.

Electron tomography experiments were conducted in a Titan Themis at 200 KeV, retrieving the reconstructions from 15 to 30 projections by means of a TV minimization algorithm run in Matlab. The alignment of the projections prior to reconstruction was carried out in the Thermofisher Inspect 3D software and TomoJ plugin of the ImageJ software. The reconstructed volumes and visualization were done in the thermofisher Avizo software.

2.2.6. X-Ray diffraction (XRD)

The crystal structure of the different materials (Ni, Co, and Bi_2Te_3) grown in this thesis through electrochemical deposition was investigated by X-Ray Diffraction (XRD) in the range of $2\theta = 20\text{-}100°$. A Philips X'pert PANalytical diffractometer was employed, with Cu K_α radiation, and $\lambda = 0.15418$ nm. The system is available at the Instituto the Micro y Nanotecnología (IMN-CSIC), located in Madrid (Spain).

This technique is based on the interaction of the incident X-ray radiation with the crystal lattice of the samples, according to Bragg's Law equation.

$$n\lambda = 2d\sin\theta$$

(2.3)

, where λ is the wavelength of the incident beam, n only takes values of integer numbers ($n = 1, 2, ...$), d is the distance between the atom planes within the crystal, and θ is the angle of the beam with respect to the planes of the material. As the X-rays are scattered by the atoms disposed of in a periodical arrange, this equation is satisfied at certain angles where the interference is constructively producing a diffraction signal. Constructive interference, in turn, only takes place if the path difference, given by the second term of the

equation, is a multiple of the wavelength (first term). During XRD, λ of the incident radiation is known, while θ angles at which diffraction occurs are measured, giving a diffraction pattern of varying intensities. Then, each diffraction peak can be directly linked to a distance d between crystal planes characteristic of the crystal structure of the material. The different intensities of the peaks can be related to the crystal orientation of the material [286].

2.2.7. Raman spectroscopy

Raman spectroscopy measures the vibrational modes of the molecules composing the sample. So the chemical composition of the material can be evaluated by identifying its molecular/atomic bonds. EDX and compositional TEM results were further corroborated by Raman, regarding the desired 2:3 Bi:Te stoichiometry of the electrodeposited 3D nano-networks. Moreover, Raman spectroscopy gives information about the strain on the sample.

Table 2.4. Raman measurement conditions for the characterization of Bi_2Te_3 nanowire networks.

Measurement range (cm^{-1})	Magnification (%)	Diameter of the pinhole (μm)	Optic density (%)	Acquisition time (s)	Integration number
10-200	x100	100	10	20	5

A laser is used as incident light; as the photons hit the sample they gain or lose energy from this interaction. Photons inelastically scattered from the sample are detected, and the difference of energy is measured. This frequency shift, also called the Raman shift, is associated with the vibrational mode of a specific molecular bond. Raman shifts were measured with a Jobin-Yvon LabRam HR, confocal micro-Raman system, using an Nd:YAG laser ($\lambda = 532$ nm). This equipment belongs to our research group (FINDER) which can be found at the Instituto the Micro y Nanotecnología (IMN-CSIC), Madrid (Spain).

The samples can be measured along the length of the nanowires (after cutting the sample and exposing the lateral view of the structure) or in top-view. For the latter, certain preparation was required; samples were mechanically polished until the surface of the nanowires was exposed (see section 2.1.4.2.1). During the measurements, Bi_2Te_3 could be heated by the laser causing a not desired change of composition, as Tellurium starts to

evaporate at 80 °C, but the intensity of the incident laser was kept lower than that needed to heat them, by decreasing the power reaching the sample. Our Raman system was coupled with an optical microscope. The polished surface of the sample (or the cross section view of the nanowires) was systematically checked after each measurement to evaluate any burns or damages due to the laser source. A compromise was to be reached between the resolution of the peaks and not damaging the sample. So the experimental parameters (optic density, acquisition time, and integration) had to be adjusted specifically, the optimized parameters for Bi_2Te_3 are recorded in Table 2.4.

2.3. Physical properties characterization

2.3.1. Optical characterization

2.3.1.1. Spectrophotometry

This technique measures the capability of a material to reflect or absorb (transmit) light at different wavelengths, by measuring the intensity of the reflected or absorbed (transmitted) light beam. Moreover, the refractive index of a sample can be extracted from the reflectance, absorbance, or transmittance data.

In this thesis, the optical properties of the empty 3D AAO membranes were studied. These types of alumina could be understood as a Bragg reflector material composed of two layers, with different refractive indexes, that are periodically alternated, as will be fully explained in chapter 3.2. Corresponding to the MA layer of lower porosity and the HA layer with a higher porosity %. As the thickness of the MA layer was varied, the effective refractive index of the whole 3D alumina is also modified, thus affecting its optical properties. These variations could be perceived with the naked eye by changes in the color of the 3D AAO templates, the change of color is associated with the interaction with light. Hence, the reflectance spectra of different 3D AAO membranes grown with fixed MA layer thickness from 100 up to 622 nm were taken. Reflectance measurements were carried out with a PerkinElmer-Lambda 950 UV/VIS spectrophotometer using the Universal Reflectance Accessory (URA) module, between 200 and 800 nm in wavelength, with incident angles of illumination and detection, with respect to the surface of the sample, of 30°, 45°, and 82° (82° being the closest to the case of normal incidence at which the equipment could measure). Measurements were repeated between 300 and 800 nm with an Agilent Cary

5000 UV/vis spectrophotometer using the integrating sphere. The systems were calibrated before the measurements. A non-reflective (black cardboard) was employed as reference zero before data acquisition. Both systems are found at Instituto de Cerámica y Vidrio (ICV-CSIC) located in Madrid, (Spain).

2.3.2. Magnetic characterization

2.3.2.1. Vibrating Sample Magnetometer (VSM)
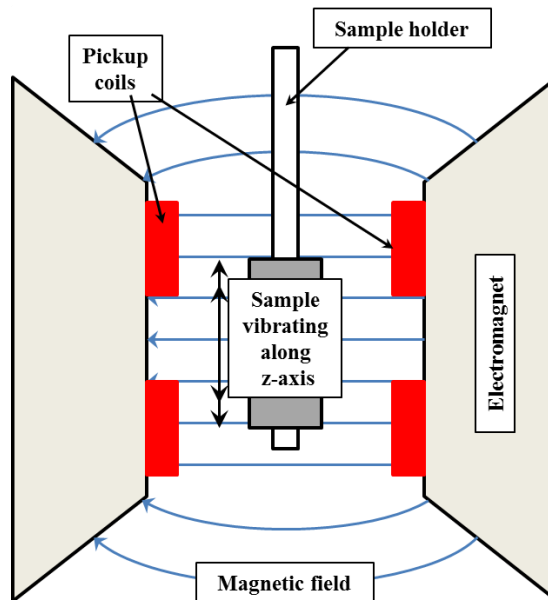
Figure 2.7. The configuration of the Vibrating Sample Magnetometer (VSM) measurement system.

A vibrating sample magnetometer operates under the principle of electromagnetic induction, in which a changing magnetic field generates an electrical current in a coil. The induced current in the coil is described by Faraday's law of Induction [287]:

$$\varepsilon = -N\frac{\Delta\Phi}{\Delta t} \qquad (2.4)$$

, where ε is the induced electromotive force measured as a voltage, which is strengthened by the number of turns or loops of the coil, N. $\Delta\Phi$ is the change in the magnetic flux in a time Δt.

Experimentally the sample is placed in between two electromagnets and mounted in a moving sample holder, as shown in Figure 2.7. The magnetic sample is magnetized under a constant magnetic field and then the holder is moved up and down in the vertical direction, making the sample vibrate. The magnetic dipole of the sample generates a surrounding stray magnetic field, then, as the sample is vibrated the stray field fluctuates. The fluctuations of this stray field are sensed by a set of pick-up coils as an induced voltage that is proportional to the sample's magnetic moment. During the measurements, the sample is brought under different magnetic fields and the magnetization value is measured at each field.

From VSM measurements different types of curves were obtained:

i)   *Mayor Cyclic Hysteresis Loops*
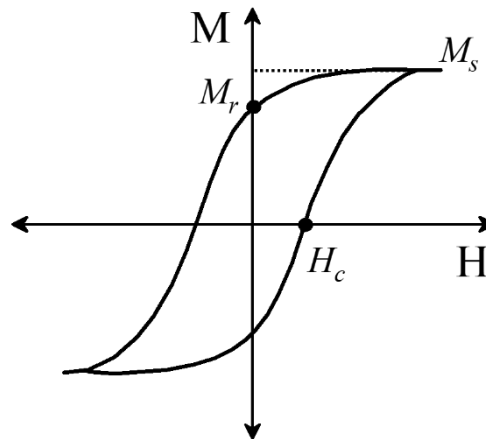
Figure 2.8. *Cyclic hysteresis curve.*

Mayor hysteresis curves were taken by a sweep of the external magnetic field (H) as the magnetization (M) of the sample is recorded. H is increased/decreased until positive/negative saturation magnetization (M_S). Mayor cyclic hysteresis curves allow studying the magnetic behavior of a whole magnetic system, some important parameters that can be extracted from these curves are magnetic saturation (M_s), coercive field (H_c), and remanence (M_{rs}). The magnetic saturation field corresponds to the alignment of all the magnetic moments with the external field when the magnetic flux in the sample reaches a constant value. The value of the external field H at which the material is demagnetized, meaning its magnetization is brought to zero, is called coercive force, H_c. It measures the needed strength to demagnetize a sample. The remanence is the magnetization left behind in the sample once

the applied external field is removed. It measures the magnetic memory of the material.

Measurements were performed by Dr. Sandra Ruiz Gómez and Dr. Lucas Pérez from the Universidad Co mplutense de Madrid (Spain), using a 7304 LakeShore vibrating sample magnetometer. Magnetic hysteresis curves were taken using a magnetic field of up to 10 000 Oe (1 T) at RT. The samples were rotated in the field to measure magnetization processes with the applied field parallel to the plane (IP, x-axis) and along the wires i.e., OOP, z-axis.

ii) *First Magnetization Curves*

First magnetization curves are taken from an almost null magnetized state of the sample up to magnetic saturation, providing valuable information about the initial magnetization processes. Measurements were performed by Dr. Ruy Sanz González at Instituto Nacional de Técnica Aeroespacial (INTA), Madrid (Spain). Using a vibrating sample magnetometer (VSM, model Microsense EZ-7). First magnetization curves were measured from 0 to a saturating magnetic field of 16 kOe and at different angles 0º, 30º, 60º and 90º. But, previously, samples were submitted to a demagnetization process. This process consisted in the exposition to magnetic field, from 1.5 to 0 T, with alternate polarity.

iii) *First Order Reversal Curves (FORC)*

The magnetic characterization of the samples was completed with FORC measurements. If from the major Hysteresis curves one obtains information about the global magnetic properties of the system, then FORC provides local information. In particular, it is suggested that the coercive field of individual NWs can be determined, as well as the demagnetization field between neighboring NWs in an array. Also, some insights into the magnetization reversal processes involving domain wall propagation in NWs can be gained.

FORC measurements consist of a set of minor hysteresis curves that are taken covering the area inside the major hysteric curve (see Figure 2.9). Each of them is called a hysteron [288] and is defined by a critical coercive field (H_c) and a critical interaction field (H_u). Measurements begin from positive saturation magnetization down to lower reversible fields, to switch down the magnetization of some hysterons depending upon their coercive and interaction field. Then the field is increased again up to saturation.
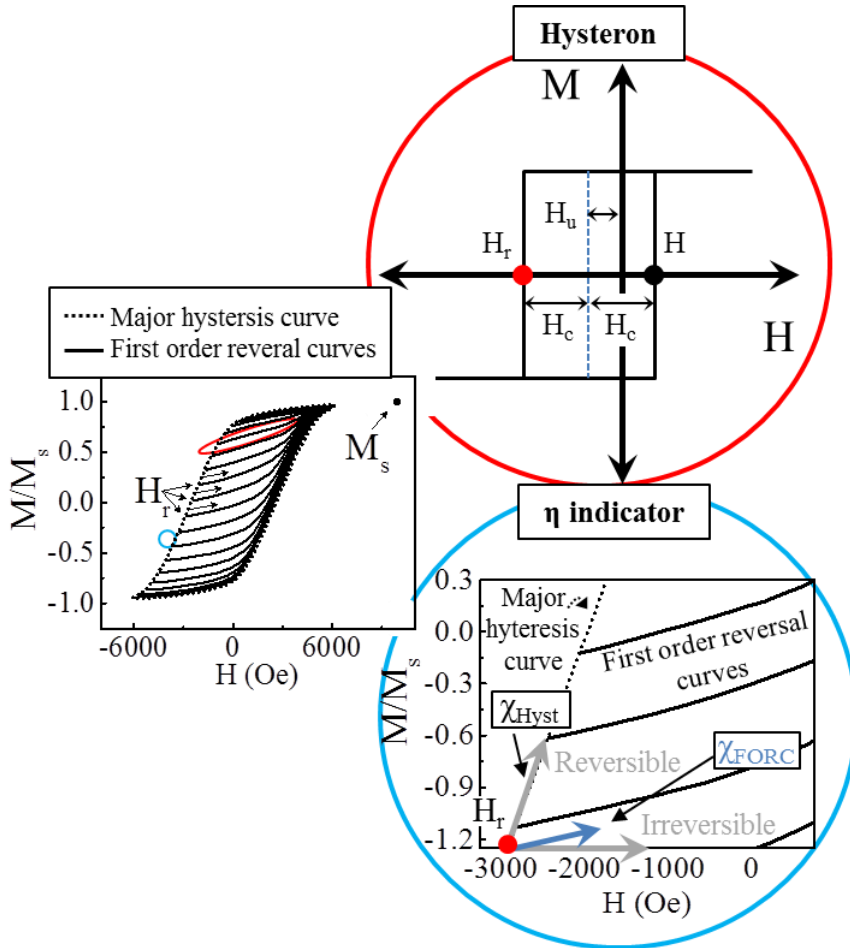
Figure 2.9. *Set of FORCs. A hysteron defined by a critical coercive field, H_c, and interaction field, H_u. The reversibility indicator, η, of individual hysterons is obtained from the slope of the hysteron divided by the slope of the mayor hysteresis curve at H_r of each hysteron.*

The difference of magnetization between the applied field and the reversal field is directly proportional to the number of hysterons that are switched back up. Thus the FORC distribution relates to the distribution of hysterons and can be obtained by applying the second-order derivative of the magnetization [289], as stated by the following expression,

$$p(H_r, H) = -\frac{\partial^2 M(H_r, H)}{\partial H_r, H}$$

(2.5)

, where $p(H_r, H)$ is the FORC distribution number of hysterons switched back up at H_r (reversal field of each particular hysteron) as a function of the

external field H. The term on the right side of the equation is the second-order derivate of the magnetization (M) of a set of hysterons starting at different H_r. Afterwards, a change of coordinates is also required to define the coercive (H_c) and interaction field axis (H_u),

$$H_C = \frac{H - H_r}{2} \quad and \quad H_u = \frac{H + H_r}{2}$$

(2.6)

On the other hand, the reversibility of the process can be extracted from the slope of the minor curves at the reversal field, numerator term of the equation, $\chi_{FORC}(H = H_r)$, normalized by the slope of the major hysteresis curve branch at the reversal field, $\chi_{Hyst}(H = H_r)$. Giving a reversibility indicator, η, of the magnetization process.

$$\eta(H = H_r) = \frac{\chi_{FORC}(H = H_r)}{\chi_{Hyst}(H = H_r)}$$

(2.7)

It is a fully reversible process when this indicator is 1, matching the slope of the major hysteresis curve, whilst a 0 value indicates the irreversibility of the process, as indicated in Figure 2.9.

A VSM, model Microsense EZ-7, was used for these measurements under a maximum magnetic field of 16 kOe. The acquisition covered ±2500 Oe region, and up to 100 reversal curves with 50 Oe field spacing were measured. Measurements were performed by Dr. Ruy Sanz González at Instituto Nacional de Técnica Aeroespacial (INTA), Madrid (Spain).

The magnetic characterization of the 3DNNs does not require any further sample preparation, the nanowires and 3D interconnected nanowires were fully characterized still embedded in the original 1D and 3D AAO templates, respectively.

2.3.3. Thermoelectric characterization

Section 5.2. describes the nanostructuration of Bi_2Te_3 in the form of films and 3D nanowire networks. The characterization of the thermoelectric efficiency of this material involves the determination of the Seebeck coefficient (S), electrical transport properties (in particular, the electrical conductivity, σ), and thermal conductivity (κ) of the different nanostructured samples. According to the expression of the figure of merit, ZT, that

determines the thermoelectric performance of thermoelectric materials [290, 291],

$$ZT = \frac{\sigma S^2}{\kappa} T, \qquad where \ \kappa = \kappa_{ph} + \kappa_e \qquad (2.8)$$

In this equation σ is the electrical conductivity, S is the Seebeck coefficient and κ is the thermal conductivity of the sample. The κ is composed by the contribution to heat dissipation by phonons, κ_{ph}, and electrons, κ_e.

2.3.3.1. Electrical conductivity, σ
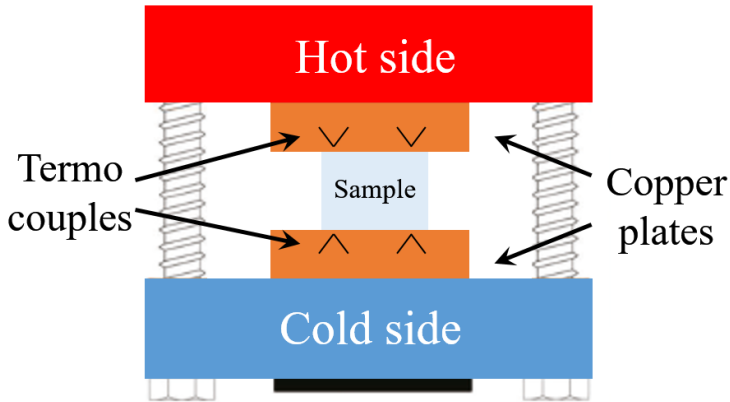
i)   *Out-of-plane σ*

Figure 2.10. *Out of plane measurement system.*

The out of plane electrical conductivity, in the direction parallel to the longitudinal Bi$_2$Te$_3$ nanowires of the 3DNNs, was measured in a lab-made system consisting of two moving cooper blocks, which are electrically connected. As the sample is sandwiched between the two blocks (see Figure 2.10) an external current is injected from one cooper block to another and through the sample, in the direction of the longitudinal nanowires while recording the generated voltage between opposite ends of the nanowires. In this set up the resistance along the nanowires is obtained from the slope of the recorded *I-V* curves. The current load was varied from 0 and up to 5 mA with a step size of 0.5 mA, at RT conditions. But previously, to ensure good Ohmic contact between the nanowires extremities and the cooper surface, both sides of the filled alumina membrane were polished following the procedure in section 2.1.4.2.1, until nanowires were exposed from both sides of the sample.

Out of plane measurements were performed during a brief stay at the Jean Lamour Insitute in Metz (France).

ii)   *In-plane σ*

The characterization of the electric transport properties, such as electrical resistance (ρ), electrical conductivity (σ), and carrier concentration, along the in plane direction was carried out using: a commercial Hall system, and a lab-made Hall system, based on the same principle, the Hall Effect [292, 293].
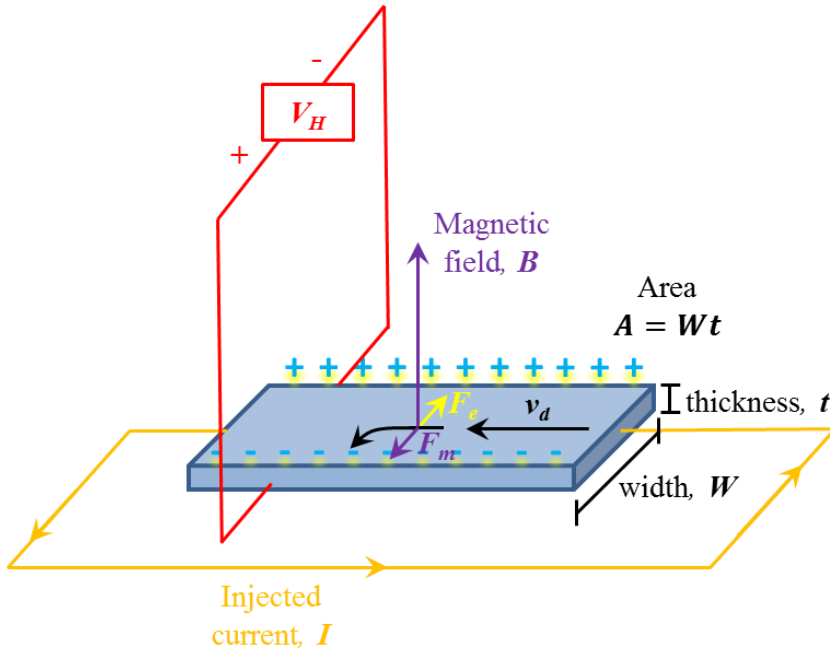
Figure 2.11. A diagram illustrating the Hall Effect.

The Hall Effect is a consequence of the Lorentz force (F_m) [287] acting upon electrons (holes) moving across a conductor or semiconductor material when placed under a magnetic field perpendicular (B) to the injected current (I) that propels electron (hole) motion, as illustrated in Figure 2.11. In this setup, the Lorentz force (F_m) is defined by

$$F_m = qv_dB \ \ where \ v_d = I/Anq \tag{2.9}$$

In this equation F_m is the Lorentz force, proportional to the perpendicular magnetic field B, the charge of the carries q, and the drift velocity of the charge carriers, v_d. In turn, the moving velocity of the charge carriers depends on the

injected current I, the sectional area of sample A, the charge q, and the density n of the charge carriers.

Then, F_m can be rewritten as

$$F_m = IB/nA \qquad\qquad (2.10)$$

This force causes the electrons (holes) to deviate from their 'straight' path towards one side of the conductor/semiconductor, producing an accumulation of charge at the sides. To balance the buildup charge, electrons (holes) move towards the positively (negatively) charged side, generating a measurable voltage in the direction perpendicular to the injected current, known as the Hall voltage.

$$F_m = F_e = V_H q/W \qquad\qquad (2.11)$$

, where F_e is the electric force that rises to balance out the accumulation of charge acting in the opposite direction to the F_m. V_H is the measurable Hall voltage generated from the F_e. And W is the width of the sample.

The advantage of using a Hall measurement system is that, aside from the electrical resistivity and conductivity of the sample, the carrier concentration can be also determined. Since the carrier concentration is proportional to the transverse Hall voltage, according to

$$V_H = IB/qnt \qquad\qquad (2.12)$$

, which is obtained by inserting equation *2.11* in *2.12* and solving V_H. In equation *2.12* the V_H is inversely proportional to the thickness (t) of the measured sample.

Measurements are carried out by the van der Pauw method [294], which employs a four-point probe placed at the edges of the sample. This configuration reduces any effects due to the irregular shape of the sample providing an average resistivity value. A DC is injected between adjacent probes (i.e. 1-2, I_{12}) while the voltage is measured between two opposite points (i.e.4-3, V_{43}). There are 8 possible measurement configurations, as shown in Figure 2.12, which introduces a geometrical correction factor. The sample is rotated before each measurement, forcing the current through different

entrance points, and then measurements are repeated while the polarity of the injected current is switched.
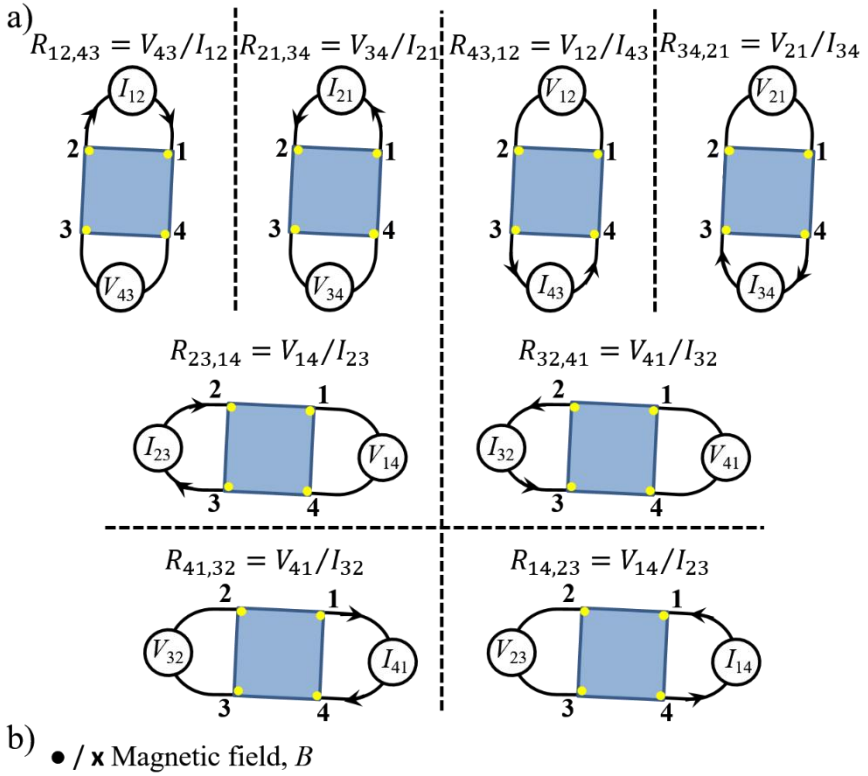
Figure 2.12. *a) Experimental configurations used for the determination of resistance R_A and R_B, and b) voltage hall, V_H, using the van der Pauw method.*

The 8 resulting values of resistance can be grouped in just two, R_A and R_B, according to

$$R_A = \frac{R_{21,34} + R_{12,43} + R_{43,12} + R_{34,21}}{4} \qquad (2.13)$$

$$R_B = \frac{R_{32,41} + R_{23,14} + R_{14,23} + R_{41,32}}{4} \qquad (2.14)$$

From the characteristic resistances R_A and R_B, the average sheet resistance R_S of the sample can be obtained by numerically solving the van der Pauw equation through iteration

$$e^{-\pi R_A/R_S} + e^{-\pi R_B/R_S} = 1 \qquad\qquad (2.15)$$

Then the resistivity, ρ, is given by

$$\rho = R_S \cdot d \qquad\qquad (2.16)$$

For which the thickness, d, of sample must be known.

In this technique, if the area of the contacts is small enough compared to the total area of the sample, the contribution to the resistance from the electrical contacts can be neglected [295, 296]. Another requirement is that samples must be continuous, without holes, and the width of the samples must be at least one order of magnitude higher than its thickness [297, 298].

Experiments in this configuration were also performed under a magnetic field, then, as a current is injected across the sample a transversal V_H is generated due to the Hall Effect (see Figure 2.12b)

Before determining the resistivity and the hall mobility of the samples, *I vs. V* curves were measured to establish the optimum current range at which the samples show Ohmic behavior. Accordingly, 3DNNs were measured using an applied current between 100-500 µA, and RT conditions. The electrical characterization was carried out employing an HMS-5000 Ecopia Hall Effect Measurement System operating at 0.548 T, which belongs to our group and is located at Instituto the Micro y Nanotecnología (IMN-CSIC), Madrid (Spain).

The experimental results were double-checked using a lab-made Hall system reaching 0.9 T. The sample was placed inside a closed-cycle Janis cryostat, through which cold helium vapor is pumped to lower the temperature of the sample, and situated between two magnetic coils providing the magnetic field. Measurements were carried out by Dr. Eric García Hemme and Dr. David Pastor at Dpto. Física Aplicada III (Electricidad y Electrónica), Facultad de Ciencias Físicas, Universidad Complutense de Madrid (Spain).

Further on, bismuth telluride is known to present a topological insulator behavior at low temperature regimes, allowing only surface state conduction. Under this prerogative, the magneto transport properties of this material when nanostructured in the form of a 3D nanowire network was investigated. Sheet resistance was recorded while reducing the temperature down to 1.8 K. Once the temperature of the sample was stabilized at 1.8 K, the resistance was measured as a function of the increasing magnetic field, applied at several angles (0, 12.86, 25.72, 38.58, 51.43, 64.29, 77.15 and 90.01 ° with respect to the normal of the sample). For which the sample was rotated inside the holder. Magnetoresistance measurements were done by Dr. Nicolas Pérez using a ppms, found in Leibniz Institute for Solis State and Materials Research (IFW), Dresden (Germany).

The same sample preparation as the ones employed for the determination of the Seebeck coefficient was followed.

2.3.3.2. Seebeck coefficient, *S*

This coefficient measures the generated voltage across the sample due to an applied temperature gradient, as defined by the following expression:

$$S = \frac{\Delta V}{\Delta T}$$

(2.17)

, in which ΔT is de temperature difference between the two ends of the sample and ΔV is the induced thermoelectric voltage across the sample.

i) *Out-of-plane S*

The determination of the Seebeck coefficient in the out of plane direction (along the length of the longitudinal nanowires of the 3D networks) was performed employing the same set up described for the measurement of the out of plane electrical conductivity (see. Figure 2.10), with some minor modifications. In this case, the cooper blocks will act as thermocouples, while one side is heat up and the other cooled down. The temperature in the cold side is controlled by running water flowing in and out of the cooper block. Whereas the temperature at the hot side is rise by injecting an increasing current, from 10 up to 200 mA (step size 38 mA), in the copper block. Measurements were performed by establishing a temperature gradient across the sample up to 4 ºC and recording the generated out voltage.

ii)   <u>*In-plane S*</u>
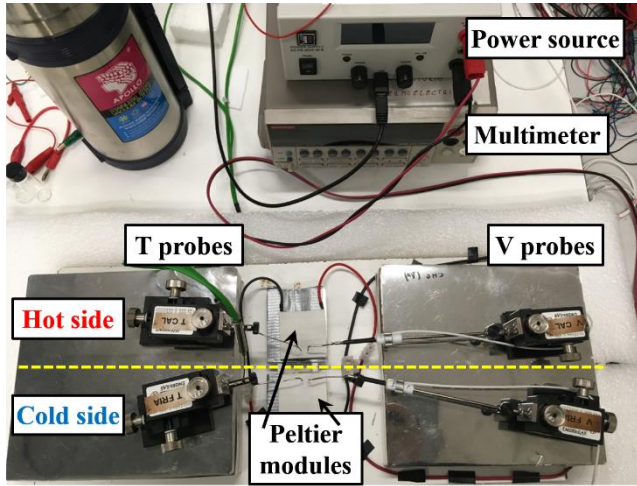
Figure 2.13. *Displays the set-up system for the determination of the Seebeck coefficient, composed of an external power supply, a multimeter, two Peltier modules, and 4 thermo-resistive probes.*

This parameter was measured in a lab-made system (mounted by a person of our research group) operating at room temperature conditions; the configuration of such a system is shown in Figure 2.13. This setup consists of two Peltier modules that transfer the heat generated at the module, to a sample placed between both modules, due to an applied voltage, according to the Peltier effect. The applied voltage is controlled through the injection of current using an external power source (power supply EA-PS 2042-06B). Then, as the sample, in contact with the Pelriers, is heated and cooled down at each of its ends, a measurable voltage is produced. This temperature gradient and the subsequently induced voltage are measured with four thermosensitive and metallic probes connected to a multimeter (2000 multimeter Keithley). The probes must be situated at the ends of the sample. Inserting the recorded values of ΔV vs. ΔT in the above equation (reaction *2.10*) the Seebeck coefficient can be calculated. The set-up is available at Instituto the Micro y Nanotecnología (IMN-CSIC), Madrid (Spain).

Before performing the measurements, certain sample preparation is required, as was explained before. The gold and chromium layers at the bottom of the sample have to be removed, see section 2.1.4.1. Afterwards, the samples were electrically contacted as explained in section 2.1.4.3.

2.3.3.3. Thermal conductivity, κ

i) <u>*Out-of-plane κ*</u>

The out-of-plane thermal conductivity of 3D Bi_2Te_3 nano-networks was obtained by the Photoacoustic technique.

In this technique, the sample is mounted in a specific photoacoustic cell with fixed dimensions [299]. The sample must be large enough to cover the opening of the cell (~over 4 mm in diameter) and an 80 nm Ti layer is previously deposited on top of it to act as a transducer

During the measurements, the sample is periodically heated with a laser, and due to the thermoelastic expansion and compression of the sample, an acoustic wave is emitted and recorded with a microphone. The phase shift between the initial radiation and the generated acoustic signal measures the thermal diffusivity, α, of the material. Hence, the κ has to be calculated from the following expression, knowing beforehand the density (ρ_{vol}) and specific heat of the sample (C_p):

$$\kappa = \alpha \cdot C_p \cdot \rho_{vol} \qquad \qquad (2.18)$$

Then, certain data treatment is required depending on the type of sample under study. In this thesis, the 3D Bi_2Te_3 networks of interconnected nanowires were measured while embedded in the 3D AAO templates, thus the value of the thermal conductivity is an effective thermal conductivity value, with the contribution of both the nanostructured Bi_2Te_3 as well as the AAO matrix. Accordingly, a multilayered model had to be considered in order to extract the thermal diffusivity of the 'problem' layer, which corresponds to the filled region of the 3DAAO with Bi_2Te_3. In particular, this model consists of three different layers: the titanium film, the region filled by Bi_2Te_3 (that is, alumina and bismuth telluride) and the empty region of the 3DAOO membrane, (alumina and air). From each layer it is required to know its thickness, the density and the specific heat. In the case of the 3D NN region and the 3D AAO region, effective medium theory was used to obtain both the density and the specific heat. The specific values of these parameters are recorded in Table 2.5.

In this table, the skeletal density refers to the density intrinsic to the material; the data given for the skeletal density of air and bulk Bi_2Te_3 were taken from the literature [299, 300]. In the case of the 3D alumina, the density

was experimentally measured by Archimedes' method, giving 2.770 g·cm^{-3} [301] which is in good agreement with the skeletal density of sulfuric alumina membranes [87, 302]. The specific heat of bulk Bi_2Te_3 could be found in [300].

Table 2.5. *Parameters used for the PA data fitting*

Material	Specific heat $C_{p(mat)}$, $(J·g^{-1}K^{-1})$	Skeletal density ρ_{mat}, $(g·cm^{-3})$	Ref.
3D Alumina	0.885	2.770	[301]
Air	1.007	1.176	[299]
Bi_2Te_3 (Bulk)	0.165	7.600	[300]
LAYER 1: 3DAAO filled with air			
	3D porosisty (%)	Composite Specific heat $C_{p(air)}$, $(J·g^{-1}K^{-1})$	Composite density ρ_{3DAAO}, $(g·cm^{-3})$	Composite thermal conductivity κ_{3DAAO}, (calculated) $(W·m^{-1}·K^{-1})$
3DAAO220	70.6	0.971	1.645	0.170
3DAAO350	68.5	0.969	1.678	0.220
3DAAO680	66.7	0.966	1.707	0.296
LAYER 2: 3DAAO filled with Bi_2Te_3			
	3D porosisty (%)	Composite Specific heat $C_{p(air)}$, $(J·g^{-1}K^{-1})$	Composite Density ρ_{3DNNs}, $(g·cm^{-3})$
3DNN220	70.6	0.377	6.180
3DNN350	68.5	0.392	6.079
3DNN680	66.7	0.405	5.992

For the 3D alumina membranes the specific heat capacity was found to be 0.885 J·g^{-1}K^{-1}, as reported in the thesis of B. Abad [299]. This value is in between to that of the non-porous aluminum oxide, around 0.800 J·g^{-1}K^{-1}, and the specific heat capacity of air, $C_{p(air)} = 1.007$ J·g^{-1}K^{-1}. Also, we have individually calculated the specific heat capacity of each of the three alumina templates employed in this chapter, 3DAAO220, 3DAAO350 and

3DAAO680, by applying the Effective Medium Theory (EMT) to this parameter

$$C_{P(3DAAO)} = (1 - x)C_{p(Al_2O_3)} + (x)C_{p(air)} \qquad (2.19)$$

, where x is the total porosity of the 3D alumina membrane, which was obtained by modelling the geometry of the 3DNNs with different P in COMSOL (see Figure 5.15a) and using the actual structural parameters of samples 3DNN220, 3DNN350, and 3DNN680, recorded in table 5.5.

Introducing the corresponding values of the porosity calculated for 3DAAO220, 3DAAO350and 3DAAO680 into *equation 2.20* we obtained $C_{P(3DAAO220)} = 0.971$, $C_{P(3DAAO350)} = 0.969$, and $\qquad C_{P(3DAAO680)}$ $= 0.966$ J·g^{-1}K^{-1}, which are also found in table 5.9.

These calculations were repeated in the case of the 3DAAO filled with Bi$_2$Te$_3$ substituting the value of the $C_{p(air)}$ by that of bulk Bi$_2$Te$_3$, $C_{p(Bi_2Te_3)} =$ 0.165 J·g^{-1}K^{-1}, in *equation 2.20*.

In a similar way, the density of the composite, consisting of the alumina filled with air or Bi$_2$TE$_3$, can be calculated applying,

$$\rho_{(3DAAO)} = (1 - x)\rho_{(Al_2O_3)} + (x)\rho_{(air)} \qquad (2.20)$$

or

$$\rho_{(3DNNs)} = (1 - x)\rho_{(Al_2O_3)} + (x)\rho_{(Bi_2Te_3)} \qquad (2.21)$$

, respectively.

Aside from that, the thermal conductivity of the Ti layer and that of the 3DAAO region are also required. The former has a fixed value of 21.9 W·m^{-1}·K^{-1} [299]. Whereas, the effective thermal conductivity of the 3DAAO region was calculated using COMSOL (detailed explanation is provided in appendix C), simulations were performed considering three 3DAAOs with different P, as recorded also in Table 2.5. Hence, the only unknown variable is the effective thermal conductivity of the 3DNN region, which can be extracted from the fitting between the measured frequency phase shift and all the known variables in table 2.5 that satisfies *equation 2.18*.

The system was built from the star by Begoña Abad while she developed her PhD Thesis in our group. The photoacoustic measurements were carried

out by Dr. Olga Caballero at Instituto the Micro y Nanotecnología (IMN-CSIC), Madrid (Spain).

3. Optical properties of 3D AAO membranes

In this chapter, the photonic behaviour of empty 3D AAO membranes was investigated for their exploitation as photonic sensors. This chapter is structured in three sections, starting with a brief summary of the state of the art and precedents of different photonic applications of AAO's (section 3.1), followed by the experimental results obtained in this Thesis for the 3D AAO membranes (section 3.2) and finishing with the conclusions extracted from these experiments, section 3.3.

3.1. Alumina membranes for photonic applications
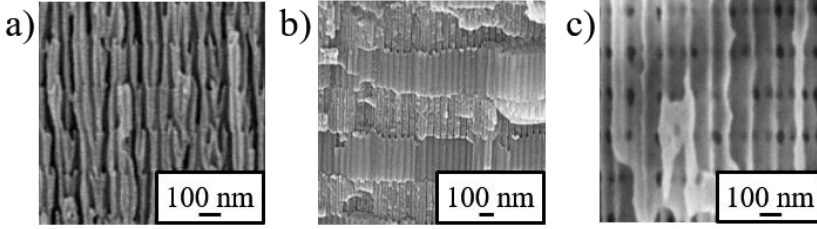
Figure 3.1. *Possible morphologies of the alumina membrane by pulsed/cyclic anodization: a) branched structure. Reprinted with permission from [142]. Copyright © 2008, Springer-Verlag, b) pore modulated. Reprinted with permission from [162]. Copyright © 2011 Elsevier Ltd. All rights reserved.and c) perforated 3D structure (fabricated in this thesis).*

The fabrication of photonic crystals based on anodic alumina templates represents a step forward in the control and modulation of light. This method has several advantages over others, being cost-competitive, fully scalable, and relatively simple to implement [76, 224, 225]. The pioneering work of Masuda and coworkers demonstrated the feasibility of structural engineering of nanoporous alumina for the fabrication of 2D photonic crystals [226], which can be treated as a composite material consisting of an alumina matrix filled with air (determined by the porosity percentage of the AAO). In this two-medium system the effective refractive index of the AAO membrane, n_i is defined by the sum of the aluminum oxide, n_{AAO} and air , n_{air}, (or any other medium filling the pores) refractive indexes in different proportions, depending on the fraction of skeletal aluminum oxide and porosity, p, that compose the alumina template, this is the effective medium theory

$$n_i = (1 - p) \cdot n_{AAO} + p \cdot n_{air} \qquad (3.1)$$

By exploding the tunability of the effective medium of such membranes one can control the way light is propagated across the porous AAO structure, according to the Bragg equation

$$\sum_i 2n_i \cdot d_i \cdot \cos \theta_i = m \cdot \lambda \qquad (3.2)$$

, which establishes a clear relationship between the effective refractive index, n_i and the wavelength of the reflected light at a given angle, generating a certain coloration. The reflection of light is defined by the reflection angle, θ_i and the wavelength, λ associated with the refractive peak that gives the observed colour. d_i is the thickness, and m is the order number. The suffix i

stands for the different dielectric layers with different refractive indexes of which the alumina membrane can be composed, as it will be seen in the next sections 3.1.1, 3.1.2 and 3.1.3. It is also worth mentioning that the latter two parameters, and thus the structural coloration, are angle-dependent on the incident light (section 3.2.3).

Masuda *et al*. [226] reported a modulation of the position at which a photonic bandgap appears: by controlling the interpore distance in thin alumina membranes, a redshift was observed as the cell size (that is, the interpore distance) was increased. Further control over the position of the photonic bandgap could be achieved by the widening of the pores through chemical etching while the interpore distance is kept constant. In this case, a blue shift of the photonic emission was recorded. In this study, the different modifications of the band-gap were produced by the variation of the refractive effective index of the AAO layer, according to the effective medium theory. Varying either, the diameter of the pores or the density of pores, the porosity changes and so it does the proportion of air of the alumina composite, modifying the effective index and thus, the Bragg condition.

Such optical structures with uniform effective refractive index are known as Fabry-Perot interferometers, which work on the basis of Fabry-Perot interference occurring at the Al metal/AAO film and air/AAO film interfaces. However, there is a threshold thickness of around 2 µm above which this interference is not observed [303] as all the incident light will be absorbed by the porous membrane. Regardless of the film thickness limitation for Fabry-Perot interference, the way light interferes at the different interfaces can be modulated to produce coloration with a high degree of tunability, by two means: controlling the depth of the pore channels (or total thickness of the oxide layer within the limiting range) [217, 218] or by tuning the porosity (changing the pore diameter or interpore distance while one of the two is fixed) [219, 220]. These structures can act as sensing platforms, due to changes of the effective index of the two-medium composite alumina as a function of the filling material (which could be any filling substance, from solids to liquids and gases) with a characteristic refractive index. Furthermore, if a metal layer is evaporated over the porous membrane, the obtained structural coloration is enhanced. In this case, changes of the filling medium could be perceived even with the naked eye by the improved colorimetric sensitivity of these metal-AAO/Al films [219, 220].

More recently, their performance as chemical sensing platforms was tested by Ferro *et al*. [20] in a study that evaluates the Fabry-Perot interference spectra of AAO films as a function of glucose concentration through photoluminescence measurements, combined with other multivariate analytical data processing techniques. Interferometric reflectance spectroscopy also allows detecting other more complex molecules (proteins, enzymes, DNA…) or even virus, and living cell detection (tumor cells) in nanoporous alumina.
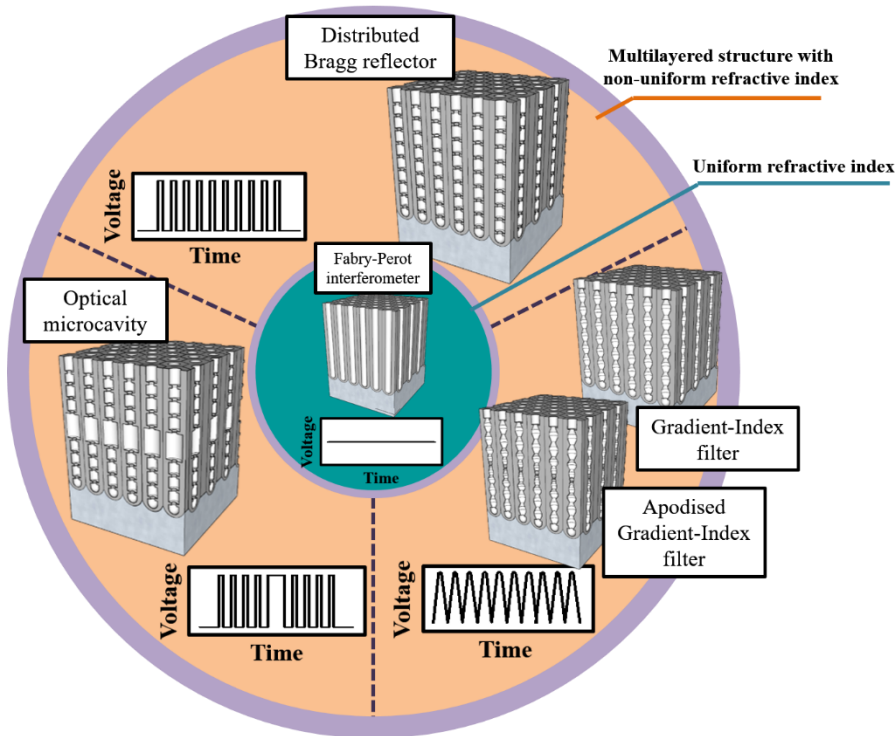
Figure 3.2. *Diagram of the different photonic crystal structure built up from alumina membranes: Fabry-Perot interferometer based on straight pores with a uniform refractive index. If pulsed or cyclic anodization is applied, more complex multilayered structures are obtained with control over in-depth pore modulation, which results in a non-uniform refractive index. This control can generate different photonic structures such as distributed Bragg reflectors, optical microcavities, and gradient-index filters or apodised gradient -index filters.*

Additionally, the structural coloration of AAO could be employed for writing and labelling applications as well as anti-counterfeiting and data encryption storage applications with small micrometric resolution on large surface areas up to the centimeter scale [220].

However, these proposals based on straight pore channels soon showed to have geometric limiting factors (limiting the range of the structural parameters with which alumina membranes could be fabricated; interpore distance, pore diameter, porosity, thickness…) and therefore, their versatility is too low for most practical applications.

From this point, the development of more complex anodization processes allowed gaining control over the in-depth modulation of the porous structure of the alumina, such as pulsed and cyclic anodization techniques, resulting in branched, modulated or 3D nanoporous anodic alumina (see Figure 3.1), providing a higher degree of tunability of the possible applications. In the case of nanoporous structures with non-homogeneous diameters along the depth of the pores (branched [222], modulated nanopores [221, 222], or even 3D nano-structures [223]), the oscillatory optical response of such structures is based on the interference of light reflected through a multilayer nanoporous structure of alternating layers of low porosity (MA layers) and high porosity (HA layers) with higher and lower refractive indexes, respectively (Figure 2.2d, section 2.1.1.2). High porosity layers would correspond to wider pore segments (see Figure 3.1b) in the case of modulated nanopores. Regarding 3D porous structures, high porosity layers are associated with the transversal nanochannels interconnecting the longitudinal pores (see Figure 3.1c) with a porosity that can reach up to 91 % compared to the longitudinal pores of around 50 - 55 % porosity (low porosity layer). Thus, the refractive index of each layer is defined by the fraction of alumina filled with air and it changes as a function of its corresponding porosity.

In particular, four different photonic crystal structures could be generated with this porosity variation method: distributed Bragg reflectors, optical microcavities, gradient index filters or apodised gradient index filters, as illustrated in Figure 3.2.

3.1.1. Distributed Bragg reflectors

Distributed Bragg reflectors are fabricated through periodic pulses resulting in a stack layered structure of high and low porosity (low and high refractive indexes, respectively). Applying the Bragg reflection law *(equation 3.2),* by tuning the different refractive indexes of the layers, the location of the optical bandgap can be tailored to fulfill certain requirements for specific applications. Pulsed anodization alternating between MA and HA regimens has been intensely used in the fabrication of Bragg stacked reflectors based on

MA/HA layered AAO by several authors [162, 163, 166, 168], where the phonic response was modulated by the length of the MA segment (or duration of the MA pulse) followed by subsequent chemical etching of the HA layer. Another approach consist of carrying out cyclic or pulsed anodization within MA regimen, where the applied voltage is reduced systematically by a factor or $1/\sqrt{n}$. Under such conditions, an n-branched porous alumina structure is formed (see Figure 3.1a). Then, as the voltage is restored to the initial anodization voltage only one of the branched channels will continue to grow to undergo a new branching process. In these layered structures, layer 1 is the main stem pore, with a characteristic d_1 thickness and n_1 refractive index and layer 2 consists of branched smaller pores with a d_2 layer thickness and n_2 refractive index. Then, according to Bragg reflection law *(equation 3.2)* varying d_1/n_1 or/and d_2/n_2 of each respective layer, the locations of the photonic bandgaps can be tuned across the UV-VIS-NIR spectrum [231] depending on the desired applications.

Photonic heterostuctures, based on the above mentioned Bragg reflectors AAO's, have been fabricated, generating two different (first-order) photonic band gaps, PC1 and PC2 [230, 304]. The disposition of such bands can be specifically tailored, creating overlapped (which produce a huge prohibited photonic bandgap as a way to reduce reflection losses), staggered and splitted photonic bandgaps. In the former cases, the separation between splitting bandgaps could be tuned for filtering applications, with control over permitted passbands and multichannel transmissions.

Photonic crystal heterostuctures based on 3D porous alumina networks where the periodicity of the high and low porosity layer (layers of low and high refractive index, respectively) is systematically altered, as the thickness of such layers is gradually reduced, have proved to enhance the optical sensibility four-fold (translate into a change of color) due to induced resonant interference [22].

Additionally, due to the porous nature of such anodic oxide membranes, the refractive index of the initial metamaterial composed of a porous alumina structure filled by air will be drastically changed by wetting it in water (or any other liquid or gas), since the filling of the pores with a different substance will change the effective index of the layers, as it was the case with the Fabry-Perot interferometers. This change in the effective refractive index results in a shift of the reflection peaks and hence different colorimetric responses due

to environmental changes. This process is reversible and therefore it can be easily implemented for the fabrication of colorimetric sensors to detect certain substances [67, 305]. There has been experimentally observed a redshift of the photonic stopband of porous alumina photonic crystals based on the distributed Bragg reflector structures described above and a decrease of the intensity in the transmission spectra with exposure time and increasing concentration of different substances from liquids (of increasing refractive indexes water, ethyl alcohol, ethylene glycol, and glycerol, for instance) [306] to gases (ethanol, methanol, acetone and toluene [307, 308]). Based on this sensitivity towards changes in the effective medium, more sophisticated BRs-AAO sensors have been developed for the detection of specific molecules, as in the case of vitamin C [309] or particles, as mercury ions, Hg^{2+} [23].

In this thesis, different Bragg reflector structures were fabricated based on the perforated 3D AAO membranes to prove the ability of the method to reproduce any color of the palette (see section 3.2). Furthermore, the increase of the surface to volume ratio in these types of membranes, due to the presence of transversal channels, can be of great use in sensing applications as highly sensitive colorimetric sensors can be produced for their implementation in many fields from environmental monitoring, color filtering, food safety, homeland security, anticounterfeiting, and healthcare.

3.1.2. Optical microcavities

Another structure with great interest from the photonic point of view are those that permit trapping certain wavelengths within them, such as optical waveguides. To mimic this behaviour, a microcavity section can be fabricated between two Bragg stacked reflectors for the confinement of light, by introducing a central high voltage pulse of a certain duration. The length of the cavities is adjusted by varying the duration time of the central pulse. This microcavity can cause constructive or destructive interference depending if the Bragg reflectors at each side of it are applied in-phase or with a phase shift, producing type I or type II optical microcavities [232]. In the former case, by optimization of the length of the resonant cavity, resonant peaks appear at positions corresponding to the different order resonant peaks associated with the Bragg reflector structure. In the latter, the phase shift between the two Bragg reflectors translates into a shift of the refractive index of the bottom distributed Bragg reflector (DBR) structure.

Both types of microcavities offer great versatility in the way that resonant peaks and stop bands are tuned across the UV-visible and near-infrared spectra. Moreover, the specifically added resonant peaks are narrower and the energy transmission of such peaks is enhanced, compared to the actual photonic stop bands of the distributed Bragg reflectors, thus the performance (higher sensitivity and quality factor Q) of such photonic structures is improved [22, 232, 310].

3.1.3. Gradient index-filters and apodised gradient index filters

In the fabrication of gradient index optical filters (GIF) or apodised gradient-index filters, pulses with a sinusoidal profile are what define the geometry of the pores within the structures. The difference between both methods is the introduction of a mathematical function, in the latter case, to produce a change in the original sinusoidal profile that aims to enhance the photonic crystal quality of the structure. In this way, narrower and more intense photonic stop bands are achieved [233]. In both cases, however, the time between sinusoidal pulses allows tuning of the location of permitted and forbidden bands across the UV-VIS to NIR spectra [22, 233-235].

Such gradient-index filters have proved to be useful for sensing applications [22, 311, 312]. Several studies show that engineering the porous alumina structure can improve the sensibility to certain molecules (i.e. detention of different concentration levels of D-glucose, as the sensibility of the GIF structure towards changes of the refractive index were enhanced, 4.93 nm/M, the detention limit was lower down to 0.01 M [311]). Moreover, the functionalization of the alumina surface further improves the sensing capability of the alumina gradient filters. For example, thiol-modified surface AAO-GIFs were developed with increase sensibility to Hg^{2+} [312]. Increasing the complexity of the functionalizing agents using amino acids, or proteins, more specific detection systems to vitamins and drugs [313, 314] were designed.

Another interesting application, making use of more complex AAO-GIFs systems with tuned located narrow peaks through multiple-sinusoidal anodization (MSPA, consisting of the combination of multiple sinusoidal waves), was proposed by Santos *et al.* for optical encoding information within the porous alumina structure based on a color barcode system [235].

A different application of alumina porous membranes with gradient refractive index structures is the development of anti-reflective films. In this case, the refractive index of the photonic crystal structure is gradually reduced in a layered structure, by changing the pore diameter and length, from a value close to the refractive index of the aluminum substrate down to a value matching that of the refractive index of air. The resulting graded refractive index layered structure shows a broad transmission band, up to 85° angle of the light incidence, and hence the reflectance of the porous alumina membrane was greatly suppressed, having omnidirectional properties. This is important to suppress the energy losses in the form of reflected light, as it happens at the interfaces between different media having different refractive indices, for instance in solar cells [315].

3.2. Experimental results: modulation of light in 3D AAO Bragg refractors.

In this thesis, different Bragg reflectors were produced with specific periodic 3D internal porous structures via pulsed anodization of an aluminium substrate, see Table 3.1. The anodization method allows covering large surface areas in the range of cm^2 and the possibility to increase it to industry standards up to m^2, but with internal resolution down to the nanometer scale. Thus, providing high control over the photonic response of the 3D AAOs, which present strong coloration depending on their internal nanoporous structure. The colorimetric optical response of the fabricated structures is formed as a result of the destructive and constructive interference of light reflected from the multiple interfaces along the 3D alumina membranes consisting of a stack MA/HA layered structure of different porosity, as illustrated in Figure 3.3. The MA layer is formed only by longitudinal pores constituting the low porosity layer (d_2) marked in Figure 3.3 by the green dashed lines. The HA layer is associated to the high porosity layer (d_1), consisting of both longitudinal and transverse pores (area delimited by orange dotted lines in Figure 3.3).

In turn, the 3D alumina samples are characterized by the effective refractive indices of high and low porosity layers, n_1 and n_2, respectively. Then, knowing the porosities of the different layers and inserting the porosity value of each layer d_1 and d_2 in equation *3.1*, we obtain n_1 and n_2. And, along with Bragg's law (equation *3.2*), the interaction with light could be tuned, for instance, by varying the thickness of the low porosity layer, d_2, while the

thickness of the high porosity layer is set to a constant value. Figure 3.3 exemplifies the structural color formation mechanism in these 3D AAO membranes. Varying d_2 alters the way light is reflected from the samples. The wavelength with which light is reflected from each of the samples can be directly associated with a certain color in the UV-VIS spectrum. Inset images on the right-up corner in Figure 3.3, show the corresponding colors to the 3D AAOs with different d_2 thicknesses: $d_2 = 198$ nm gives a green coloration to the fabricated 3D AAO (Figure 3.3a), and as this magnitude is further increased, $d_2 = 413$ nm (Figure 3.3b) produces a yellow coloration and $d_2 = 701$ nm (Figure 3.3c) a pink one.
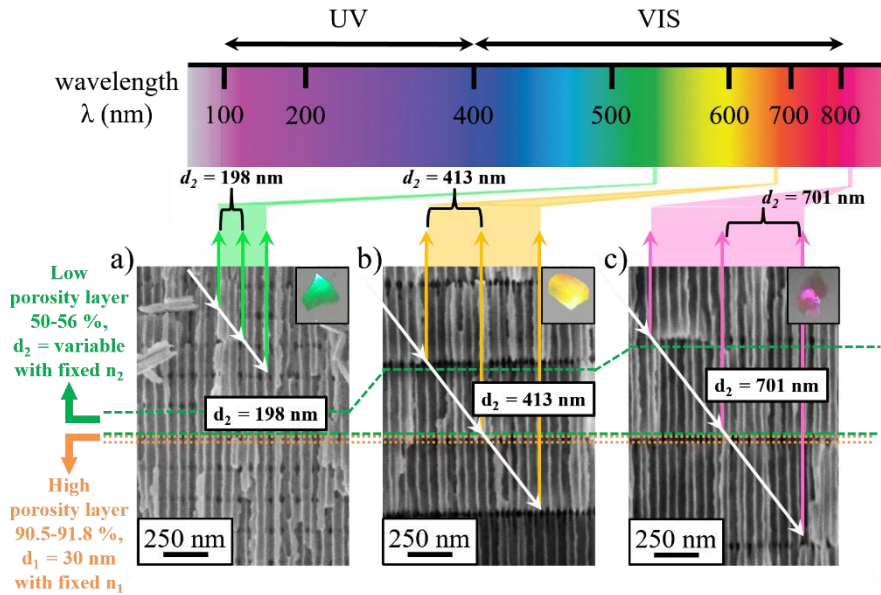
Figure 3.3. Cross-sectional SEM images of 3D AAO membranes with varying d_2 layer thickness: a) 198, b) 413 and c) 701 nm. Insets images in the right up corner show macroscopic photographs of samples with their characteristic coloration. The green dashed lines delimit the thickness of the low porosity layer (or MA pulse), d_2, formed by the longitudinal pores. The dotted orange lines mark the high porosity layer, composed of longitudinal and transverse pores, with fixed thickness, d_1, by the $t_{HA} = 2$ s HA pulse.

The periodic features of these metamaterial structures make them tunable as to cover the whole gamut of visible colors [223]. Hence, in this PhD Thesis they were investigated as promising candidates for the fabrication of colorimetric sensors and for colouring applications.

3.2.1. 3D AAO distributed Bragg reflectors structure

$$d_2 = 16.89904 + 0.76363 \cdot t_{MA}$$

$$R^2 = 0.99353$$
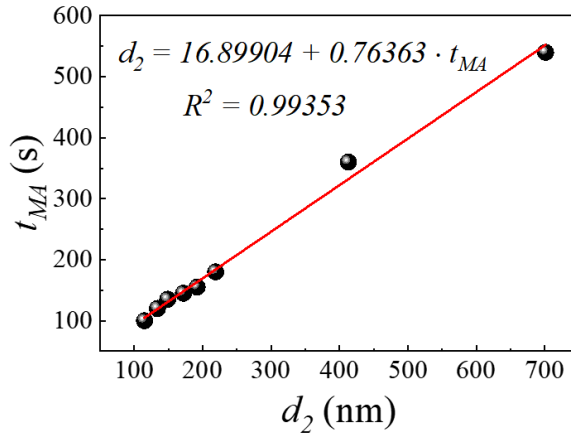
Figure 3.4. Linear fit found between the experimental duration of the applied MA pulses in seconds and the thickness of this layer (or low porosity layer), d_2, measured in nm. The equation governing the linear relationship between these parameters with a determination coefficient of $R^2 = 0.994$ is shown along with the plotted data.

Experimentally, the thickness of the d_2 layer is determined by the duration of the MA pulses during the fabrication of the AAOs, as explained in section 2.1.1.2 (see Figure 2.2b and 2.2d). The 3D AAO membranes are labeled after the parameter d_2. The thickness of the layer with transverse pores, d_1, is controlled by the short 2 s duration of the applied HA pulses. Following this procedure, several samples were fabricated applying a 100 s, 120s, 135 s, 145 s, 155 s, 180 s, 360 s, and 540 s duration MA pulses. Those were alternated with a 2 s HA pulse. After the required etching treatments (see section 2.1.2.1), the thickness of the resulting d_2 and d_1 layers was experimentally measured from the SEM photographs taken of each of the 3D alumina samples. In all cases, the d_1 layer thickness was fixed at an approximated value of 30 nm, corresponding to the length of the transversal pore in the vertical direction. The porosity percentage of the low porosity layer was extracted from top view SEM images from each of the samples using the ImageJ software, and it was calculated to be around 50-56 %. The porosity of the high porosity layer was approximated to a value of 90.5-90.8 %. This value was obtained from a sketch of the vertical and transverse channels seen from above, and taking in consideration the real dimensions of such 3D alumina membranes.

As it can be seen in Figure 3.4, the relationship between the parameters varied in these experiments, that is, the duration of the MA pulse (s) and

thickness of the resulting layer d_2 measured in nanometers, corresponds to a linear fit. Furthermore, the effect of the total thickness of the alumina membranes on the observed colors and optical properties of the alumina was also studied. To this end, two different sets of samples were grown, one of them with a total thickness of 30 µm and a second set with an increased total thickness of 90 µm. Those results will be discussed in the following sections.

Table 3.1. Structural parameters of the 3D AAO samples and their corresponding reflectance band structure (measured with an angle of incidence and detection of 82° from the surface of the sample) and the observable coloration.

Structural parameters	3DAAO							
	#1	#2	#3	#4	#5	#6	#7	#8
t_{MA} (s)	100	120	135	145	155	180	360	540
d_2 (nm)	115	134	149	172	198	219	413	701
Porosity d_2 layer (%)	50-56	50-56	50-56	50-56	50-56	50-56	50-56	50-56
t_{HA} (s)	2	2	2	2	2	2	2	2
d_1 (nm)	31	27	25	28	31	31	28	31
Porosity d_1 layer (%)	90.8	90.5	90.5	90.7	90.8	90.8	90.7	90.8
Period, $d_1 + d_2$ (nm)	146	169	174	200	229	250	441	732
Measured peak position	3D AAO115	3D AAO134	3D AAO149	3D AAO172	3D AAO198	3D AAO219	3D AAO413	3D AAO701
5th order							244	353
4th order							300	437
3rd order						210	396	581
2nd order	208	222	236	248	282	294	590	
1st order	386	426	452	474	550	590		
Color	white	violet	blue	cyan	green	red	yellow	pink

3.2.2. Photonic response as a function of the d_2 layer thickness
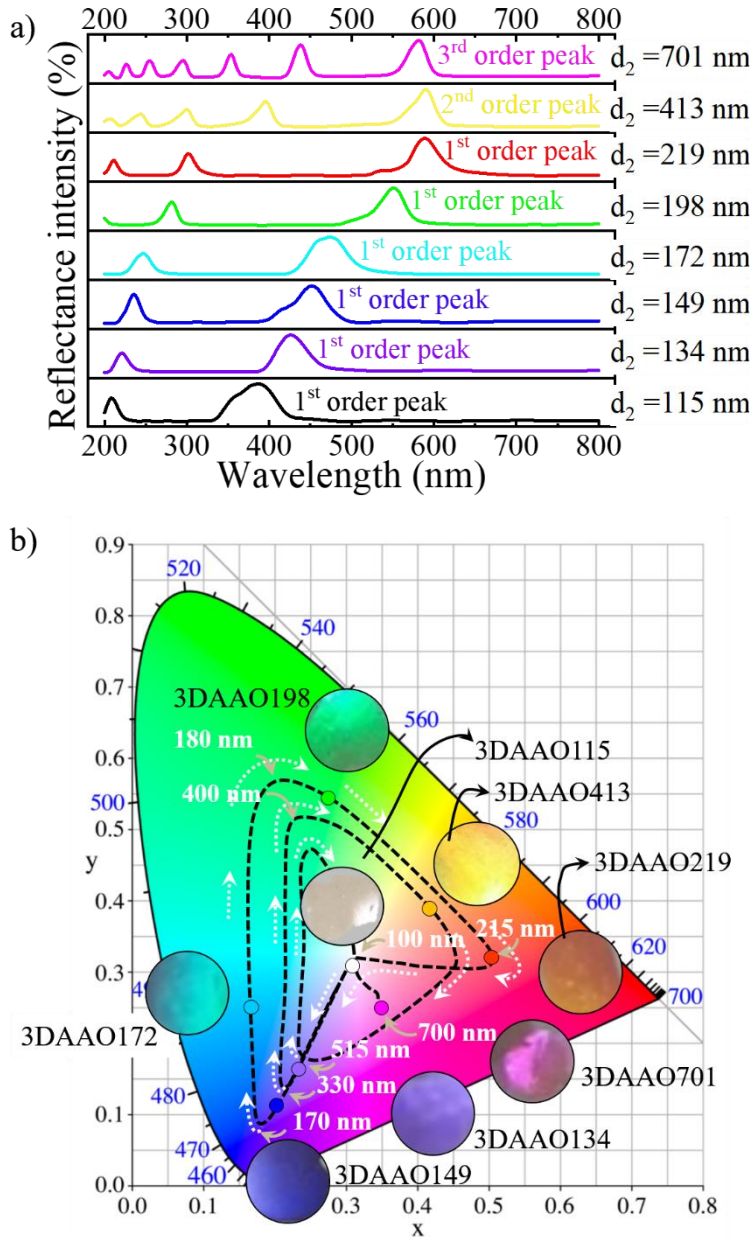
Figure 3.5. a) Reflectance spectra for 3DAAO membranes in table 3.1, associated to d_2 thickness between 115 nm and 701 nm. b) CIE color diagram in which the different 3DAAO samples are located according to their color, which is given by their characteristic multi band reflectance. The black curve represents the evolution of color in the 3D AAO's as a function of

the low porosity layer, d₂, as theoretically predicted by our color model (Appendix A). Experimental samples, shown as an insert in round pictures, perfectly fit into the predicted model curve. For better comprehension, the model color evolution follows the direction indicated by the white dotted arrows. While the solid arrows show the scale along the black curve in terms of the increase of d₂.

The optical and colorimetric response as a function of the thickness of the layer d_2 was investigated through reflectivity measurements, carried out using an UV/VIS spectrophotometer (from 200-800 nm measurable range) coupled with the Universal Reflectance Accessory (URA). Samples were measured with an incidence and observation angle of 82° with respect to the sample surface. To convert the reflectance spectra into the color associated to each structurer, we used the CIE color space chromaticity diagram, introduced in 1931 by the International Commission on Illumination (CIE) [316]. And then, we compared the given color by the CIE with the color perceived with the eye on the alumina membrane, to corroborate that both match. Table 3.1, records the structural parameters of the fabricated samples and their corresponding reflectance peaks and the observed color at 82° angle of incidence and detection.

Reflection occurs at certain wavelengths associated with the formation of photonic band gaps where light propagation through the material is forbidden. The reflectance spectra measured at near normal angle (82° to the sample surface) of samples 3DAAO115, 3DAAO134, 3DAAO149, 3DAAO172, 3DAAO198, 3DAAO219, 3DAAO413, and 3DAAO701 are plotted together in Figure 3.5a, presents a multi band structure characteristic of the internal structure of each sample. Starting from sample 3DAAO115 with the smallest d_2 value, the first-order reflection band appears below the visible frequency range, which explains the absence of coloration of the sample (labeled as white). As the thickness of layer d_2 was increased, the reflection band structure red-shifts, moving through the visible range and into the near infrared, first towards violet and blue coloration in samples 3DAAO134, 3DAAO149, and 3DAAO172, then, evolving into green (sample 3DAAO198) and finally red, in samples 3DAAO219, 3DAAO413, and 3DAAO701. Thus, the first order peaks of the multiband reflectance spectra of samples 3DAAO413 and 3DAAO701 could not be observed, appearing outside the measurable range of the spectrophotometer, and do not contribute to the formation of color detectable by the human eye because they are far beyond the visible range. According to our model (in Appendix A) the first measurable peaks of samples 3DAAO413 and 3DAAO701 correspond to second and third order peaks,

respectively. Then, the color coordinates, based on the experimental spectra of all the 3DAAO samples, were calculated employing *equations A.3 and A.4* of *Appendix A*, and represented within the CIE color diagram; see Figure 3.5b. Each colored dot corresponds to a certain 3DAAO, which were given the same color as their respective coloration (i.e. blue dot corresponds to sample 3DAAO149, which presents blue coloration). These colors are clearly perceived by the naked eye and are shown in the optical photographs of the 3DAAO membranes, which were taken at an angle normal to the sample surface, perfectly matching the assigned color by the CIE diagram. The black dotted curve shows the predicted evolution of colors as the low porosity layer thickness, d_2, is continuously increased, the white dotted arrows indicated the direction to be followed and solid white arrows show the scale around the black dotted curve in terms of the low porosity thickness, d_2, according to the model show in Appendix A.
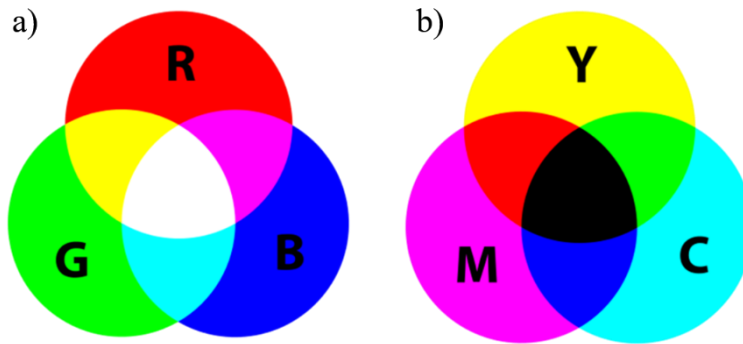
Figure 3.6. *a) Structural or additive and b) pigment or subtractive color mixing diagrams. The former is based on the RGB color model, in which the three primary colors red, green and blue, are added together in various ways to reproduce a broad array of colors. On the contrary, the primary colors of the subtractive system are the opposites of red, green and blue, which happen to be cyan, magenta and yellow (CMY). The sum of primary pigments colors yields black, while the addition of structural reflectance-based colors gives white.*

Samples were design to reflect the light within a given wavelength range with the goal in mind to engineer the whole gamut of colors in the visible spectrum, based on the predictions made by a model for structural color formation in these periodic 3D AAO templates (see Appendix A) developed in a collaborative work between the Department of Mechanical Engineering at the Massachusetts Institute of Technology (MIT) and our group at the IMN (Instituto de Micro y Nanotecnología, CNM-CSIC) that gave as a result publication in the ACS Photonics Journal [301]. According to this model, any

color could be accessible through this technology by previously selecting the appropriate thickness of the low porosity layer. However, the experimental parameter that we directly control is the duration of the MA pulse, t_{MA}, hence the relationship between the t_{MA} and d_2 was analyzed, see Figure 3.4. A linear behavior was observed with a fitting coefficient $R^2 = 0.994$, given by the following expression:

$$t_{MA} = 16.90 + 0.76 \cdot d_2 \qquad\qquad (3.2)$$

Introducing the d_2 value predicted by the color model in this equation, the t_{MA} pulse that is necessary to apply, in order to generate the corresponding photonic crystal structure, can be extracted.

This model also helped to better explain the color formation mechanism in these periodic mesoporous structures. Showing that as d_2 is increased, the predicted color converges towards white at certain values of d_2. This is a result of additive color formation [317-319] due to the reflection within multiple forbidden frequency bands, in contrast to the pigment color formation mechanism, also known as subtractive coloring. Pigments produce black color if mixed, owing to additive absorbance of mixed single-color substances, using cyan, magenta and yellow as primary colors (CMY color model) [320-322], as illustrated in Figure 3.6b. In turn, mixing of reflected light of different wavelengths spanning the whole visible spectrum yields white color, based on the RGB (red, green, blue) color mixing model, Figure 3.6a.

3.2.3. Photonic response as a function of the incidence/detection angle: 82 °, 45 ° and 30 °

The 3D AAO-DBRs are iridescent meaning that their photonic response is angle dependent of light incidence. In this case, a blue shift can be detected by the naked eye in the change of coloration of the samples as the observation angle is reduced (with respect to the surface of the sample) while the sample is being rotated. This blue shift was also experimentally measured from an observation angle near to the normal to the sample, 82° with respect the sample surface, to lower angles, 45° and 30° from the sample surface, see Table 3.2.

In Figure 3.7a, sample 3DAAO134 is shown. This sample presents coloration above an oblique viewed angle of 45° with respect to the sample surface, becoming transparent at a 45° and lower angles. This is due to the

blue shift of the reflectance band as the observation angle is reduced. In this case, the first order peaks of the reflectance spectra of this sample measured at 45° and 30° angle appear out of the visible spectrum range, at 392 and 356 nm, respectively.
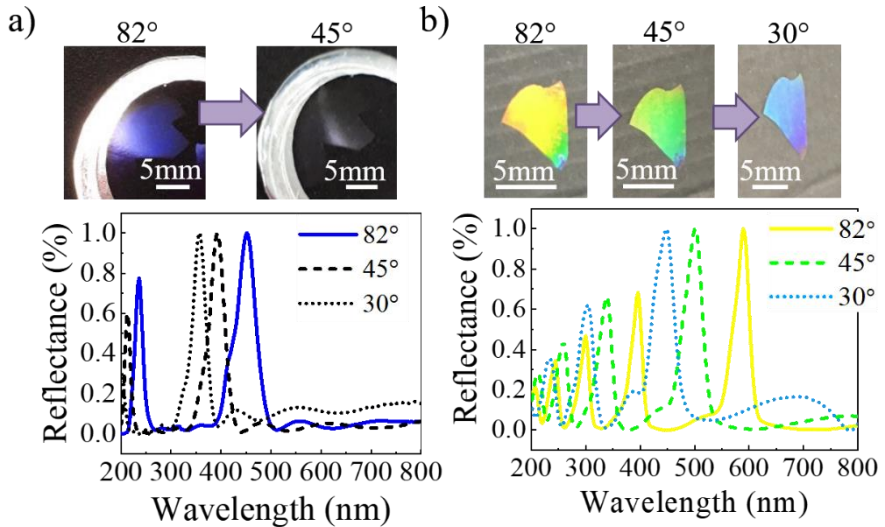
Figure 3.7. Experimental demonstration of the dependence of the photonic response and change of coloration with the incidence or detection angle. a) Photographs of the fabricated sample 3DAAO134 at normal viewing angle of 82°, displaying blue color and at an oblique angle of 45 ° from the sample surface, at which the sample exhibits no color. Underneath, the measured reflectance spectra under near normal illumination (in blue), 45° (black dashed line) and 30° (black dotted line) are shown. At 45 ° and 30 ° the reflectance bands are blue-shifted below the visible range, corroborating the loss of coloration observed in sample 3DAAO134. b) Photographs of sample 3DAAO413 taken at 82°, 45° and 30° show the change color of this sample from yellow, to green and blue, respectively. Below, the reflectance spectra at 82° (yellow line), 45° (green line) and 30° (blue line). In this case, the observed blue shift occurs within the visible spectrum range

Figure 3.7b shows the change of color of sample 3DAAO413 from a yellow coloration if viewed at 82° degrees (near to the normal surface), to green if the angle is reduced to 45° and then, it shifts to blue at a viewed angle of 30° (with respect to the sample surface). Correspondingly, the measured spectra at 45° and 30° are blue-shifted with respect to the reflectance band taken at a viewed angle of 82°. For this sample, the first order peak at 45° appears at 502 nm, in the same range as sample 3DAAO198 measured at 82° (first order peak at 490 nm) for which a green coloration was predicted. This first order peak is further blue shifted at an observation angle of 30° to at a wavelength of 448 nm, which gives a blue color to the sample comparable to

the coloration and reflectance structure of sample 3DAAO149 (when measured at an angle close to the normal to the sample surface).

Table 3.2. Reflectance band structure of the different 3DAAO membranes as a function of the angle of incidence, 82°, 45° and 30°.

3DAAO	Measured peak position														
	1st order			2nd order			3rd order			4th order			5th order		
	82 (°)	45 (°)	30 (°)	82 (°)	45 (°)	30 (°)	82 (°)	45 (°)	30 (°)	82 (°)	45 (°)	30 (°)	82 (°)	45 (°)	30 (°)
3DAAO115	386	330	298	208											
3DAAO134	426	364	326	222	196										
3DAAO149	452	392	356	236	212										
3DAAO172	474	396	348	248	216										
3DAAO198	550	416	368	282	220	204									
3DAAO219	590	412	340	294	212		210								
3DAAO413		502	448	590	338	304	396	260	234	300	212		244		
3DAAO701			628		720	424	581	482	324	437	366	262	353	296	224

3.2.4. Photonic response as a function of the total thickness of the AAO3D membranes

The effect of the total thickness of the alumina membranes on the observed colors and optical properties of the alumina was also studied. To this end, two different sets of samples were grown, one with total thickness of 30 µm and a second one with increased total thickness of 90 µm. It was observed that the total thickness of the alumina does not affect its color, as expected, given that the structure is not changed and therefore, the Bragg condition is not modified. But higher thicknesses increase the color intensity of the sample, if the homogeneity across the sample is maintained. The calculated reflectance spectra of sample 3DAAO701 with increasing number of repeating layers, (N = 30, 60 and 150 d_2 layers), shows an increase of the reflectance intensity, see Figure 3.8a. This could be corroborated by comparing the intensity of the measured spectra, as shown in Figure 3.8b, for a sample grown applying a 100s duration MA pulse, labeled as 3DAAO115. In this plot, it is observed an increase of the intensity reflectance with the number of repeating MA layers, from N = 291 to N = 947 layers, corresponding to a total thickness of 30 and 90 µm, respectively.

The calculated results do not take into account possible imperfections due the fabrication process, affecting the uniformity of the transverse pore

dimensions, variations in the layer thickness, etc. Experimentally, however, samples are not completely perfect or homogeneous; these imperfections are more noticeable as the total thickness is increased. In Figure 3.8b, there is a slight displacement of the reflection peak due to a difference in the actual thickness of the MA layer, d_2. Despite of using the same $t_{MA} = 100$ s, the thinner sample presented a d_2 thickness of 115 nm, while for the thicker sample d_2 was reduced to 95 nm. Thicker samples require longer etching times in order to open the transverse pores which also causes an over-etching, see section 2.1.2.1, hence, resulting in the thinning of the MA layer.
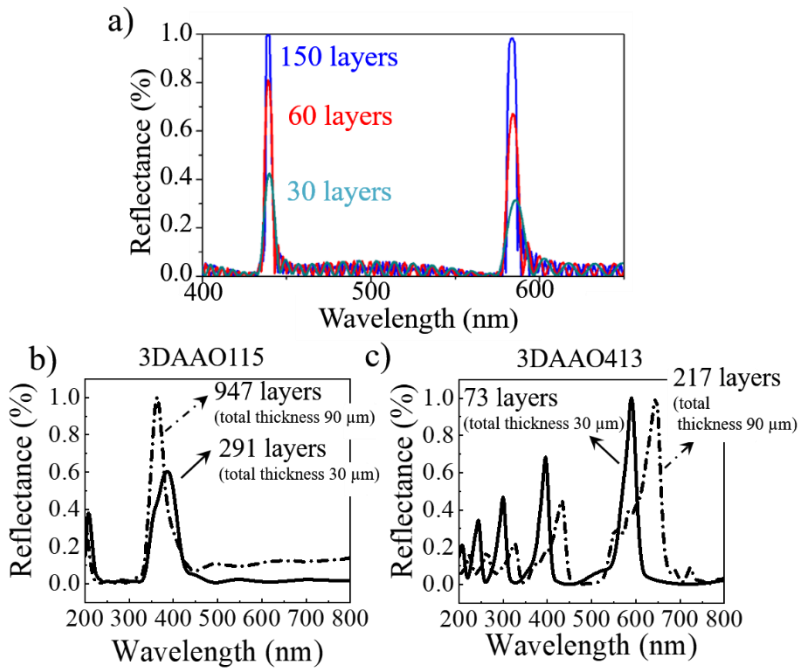
Figure 3.8. Dependence of the photonic response with the thickness of the 3D AAO membrane. a) Calculated reflectance spectra for sample 3DAAO701 with increasing number of d_2 layers, N (N =30, 60 and 150), hence, increasing total thickness. Typical for Bragg interference mechanism in periodic solids, the reflectance bands become more pronounced with the increase of the structure thickness, while their spectral positions remain virtually unchanged. b) Experimental reflectance spectra of sample 3DAAO115 with a total thickness of 30 μm in black and in green for an equivalent sample with 90 μm thickness. The increase of the intensity of the reflectance peaks is also experimentally observed as predicted, however, the reflectance peaks are slightly displaced due to the higher number of imperfections that are found along thicker membranes. c) Normalized spectra for sample 3DAAO413 with 30 μm (black) and 90 μm (green) total thicknesses are plotted together. The displacement of the reflectance peaks was more accused in this sample as the total thickness is increased, also featuring a broadening of the spectral peaks with multiple shoulders.

Moreover, for longer MA pulses, the uniformity across the sample could not be guaranteed as the total thickness is increased to 90 µm. Sample AA3D7 with a 30 µm thickness presents a homogeneous d_2 average value of 410 nm across the whole alumina membrane, fabricated applying a $t_{MA} = 360$ s. The same $t_{MA} = 360$ was used to grow another sample with increased thickness of 90 µm. After analyzing the SEM images of the microstructure of this second sample, it was found that the d_2 layer thickness varied from 391 to 460 nm. This inhomogeneity of the microstructure results in a broadening of the spectral peaks (see Figure 3.8c, in green), featuring multiple shoulders and a more pronounce displacement of the reflectance band, according to the variation of the d_2 layer thickness, when compared to the thinner example of sample 3DAAO413, which is represented by the black curve in Figure 3.8c.

Nevertheless, given the price of fabricating these distributed Bragg sensors, their stability and their easiness in tunability when compared to other fabrication techniques, makes these platforms a very attractive alternative for a great number of applications.

3.2.5. Photonic response as a function of environmental changes: colorimetric sensors.

As a direct application of the photonic response with a colorimetric transduction that can be easily perceived by the naked eye, these 3D AOO-BDRs are proposed in this thesis as colorimetric sensors for the detection of environmental changes. Due to the porous nature of the membranes, as it has been already explained, depending on the media filling the pores, the way light propagates through them changes, because the effective refractive index changes. This translates into a shift of the reflection bands, which in turn produces an observable change of coloration. With the knowledge acquired from section 3.2.2., the colorimetric read out can be engineered in the form of color appearing or disappearing (switching from transparent to colorful) or by ensuring a distinctive change of color to certain substances, from liquids to gases.

Sample 3DAAO115 with its reflectance band appearing in the ultraviolet region (at all collected angles) and thus being transparent to the human eye (Figure 3.9c), when immersed in water displays a blue color, as shown in Figure 3.9d. This change of color is associated with a red-shift of the reflection peaks moving into the blue part of the visible spectrum as the pores are filled with water, with higher refractive index ($n = 1.33$) than air ($n = 1.00$). This

red-shift could not be measured; however, it was theoretically predicted by the color model, see Figure 3.9a. Another example is the color change of sample 3DAAO701 with the greatest d_2 thickness was also predicted in this work (Figure 3.9b), showing a strong contrast coloration going from pink to green as the sample was wetted (see Figure 3.9e and 3.9f, respectively).
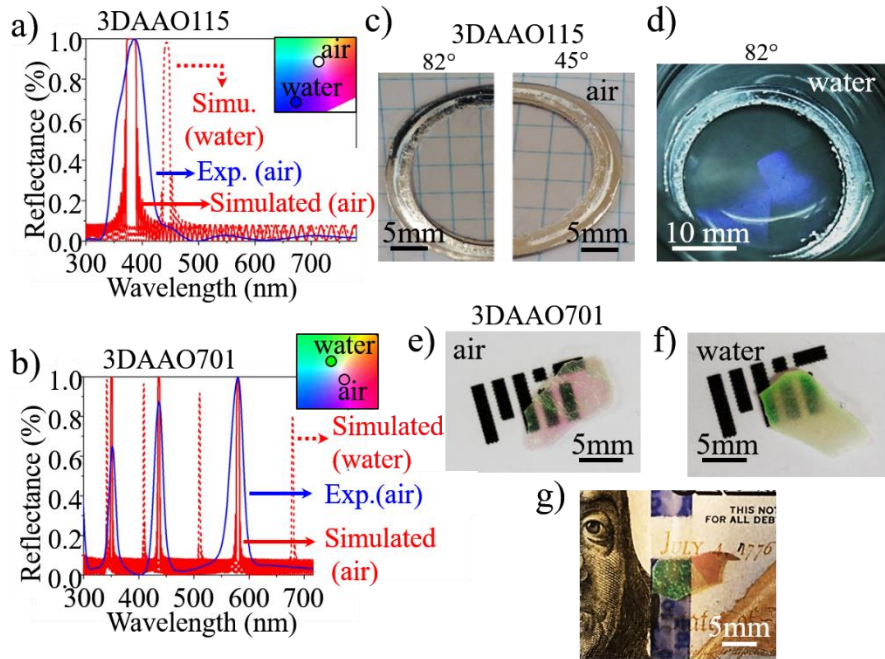
Figure 3.9. Colorimetric sensing with porous 3D AAO's. a) and b) Experimental (solid blue) and predicted (solid red) reflectance spectra of sample 3DAAO115 and 3DAAO701, respectively, at almost normal incidence (82° to the sample surface). The dashed red line shows the predicted spectral shift upon sample immersion in water. Inset images show the color change of the samples in air and water on the CIE color diagram. c) Photographs of sample 3DAAO115 in air taken from an 82° and 45 ° angles, showing in both cases no coloration. d) Photograph of 3DAAO115 submerged in water, displaying a blue color. e) and f) Photographs of sample 3DAAO701 in air (pink color) and water (green color). g) Color change of sample 3DAAO701 on the different textures of a 100 US dollar bill.

A last experiment was performed with this sample 3DAAO701 by placing it over a 100 US dollar currency bill as shown in Figure 3.9g. The sample was specifically situated between two surfaces of the note with different color/compositions. The portion of the sample 3DAAO701 that was on top of a purple stripe prominently changed its perceived color from pink to green. The part of the spectrum reflected from the substrate propagates back through the sample, mixing with the reflection from the Bragg reflector structure of

this particular sample, 3DAAO701, to produce a color variation. This feature makes our structures potentially useful for security, anti-counterfeiting, camouflage detection, and food safety applications [323-325]. They can also help to discriminate meta-materials exhibiting colors indistinguishable by a naked eye [326].

3.3. Concluding remarks: optical properties of 3D-AAOs.

On the one hand, these transversally perforated membranes show higher color saturation compared to branched or modulated Bragg reflectors mentioned in section 3.1.1, even after the removal of the aluminium substrate. On the other, color engineering due to Fabry-Perot interference in thin films of porous alumina presents certain limitations, as it was stated in the previous section 3.1. Structures with two-dimensional internal periodic order, typically exhibit only one refection band, tunable through the visible spectrum via variation of the structural parameters. Those being the thickness of the film, but that should be always kept below 2 µm, and the porosity, which can be altered to some extent by changing the pore diameter or interpore distance. In contrast, the colorimetric response of 3D porous anodized alumina structures studied in this thesis is based in a multilayer Bragg diffractor, with the layers defined by the different porosities of the MA and HA layers. Thanks to the high control over the fabrication of the 3D-AAOs, the thickness of the MA layer can be finely controlled, and thus distributed Bragg diffractors with one or multiple reflection bands can be engineered (see Figure3.5). As it has been shown in this chapter, this allows tuning of their structural color within the full range accessible by standard red, green, blue (RGB) display technologies, which can be directly exploited as color printing technique, or in the creation of color filters for security applications. Moreover, the nanoporous 3D structure of the samples enables fast and easy penetration of liquids and gases throughout the sample volume, which produces a change in their perceived color. It has been shown also the high color sensitivity to environmental changes, which can be easily detected by the naked eye, for the design of colorimetric sensors based on this technology.

It is clear that this PhD work opens a new path for more sophisticated sensors for the detection of certain molecules, proteins and cells that can be fabricated by functionalizing the 3D AAO internal surfaces [21, 23-25, 203, 309, 312-314], or they can be employed as drug delivery platforms [27, 202, 204, 205],

due to the chemical stability and biocompatibility of the alumina, with the bonus of the increased surface to volume ratio that is achieved in these 3D membranes, which a priori should increase the sensibility of the detector and the drug loading capacity as compared to that registered in 2D alumina porous systems (in section 3.1).

4. Magnetic properties of 3D Ni, 3DCo, and 3D Ni$_{1-x}$Co$_x$ alloy nano-networks.

In this chapter, 3D nanoporous alumina membranes with three different periodicities (t_{MA} = 180, 360, and 540 s) were filled with different magnetic materials: nickel (Ni), cobalt (Co), and alloys of both. Single electrochemical deposition of each material, but also co-deposition of Ni and Co elements were performed for the growth of 3D Ni or 3D Co nano-networks (3DNNs) and 3DNN of Ni-Co alloys.

The chapter is structured as follows: First, an introduction to 3D magnetism is given in section 4.1. Then, the deposition process is briefly described (section 4.2). After the structural and morphological characteristics of the resulting magnetic 3DNNs are presented (section 4.3), the research on the magnetic properties of the nanostructures is shown (section 4.4).

4.1. Introduction: Nanomagnetism

Thanks to the advances in synthesis process at nanoscale, Nanomagnetism arises as vibrant field due to its application in critical fields as for data storage, biomedicine¸ among others. In these systems, the classical properties of magnets, such as magnetic domains, domain walls, transition zones, etc. are completely modified by the reduced size, which varies their dynamics, distribution, and behaviour [327-329]. The development of new synthesis strategies, along with the evolution of the available technology at the nanoscale, has shifted the research paradigm from nanoestructures arranged in planar systems, towards a new regimen: 3D nanostructures distributed in complex 3D geometries [330-333]. 3D magnetic nano-systems provide a completely new context for the study of fundamental magnetism. Also, 3D magnetic nano-systems open the possibility to achieve higher control over the magnetization process, for example, in discrete magnetic states, which is not available in classical magnets [331]. More details on the latest advances in magnetic nanostructures can be found in *Appendix B*.

In this work, I have synthesized a novel kind 3D magnetic nanostructures and studied their possibilities and magnetic behavior. These consist of longitudinal nanowires (perpendicular to the plane of the alumina template) that are transversally interconnected to their six-closest neighbors (see inset image in Figure 4.2d) by transversal nanochannels (TCs). In these 3D magnetic nano-networks, each component (longitudinal and transverse connections) has different dimensions, (see Table 4.2). This geometry with a somewhat scaffold design constitutes a truly 3D network extending in the three space dimensions. The 3D geometry of the networks adds extra degrees of freedom to tune the magnetic properties and provides an excellent platform to dip into the field of 3D nanomagnetism. Firstly, by considering the TCs along the length of the nanowires, present in our 3NNs, as pinning sites for domain wall motion, which modify the domain wall dynamics and incorporate additional interacting elements to the 1D NW arrays. Secondly, due to the local interactions among NW-NW, NW-TC and TC-TC. These interactions depend on the geometry of the 3DNN. Thus, if the geometry is varied, the global magnetic response of the system changes. All these will be studied in the following sections through experimental measurements (hysteresis loops, first magnetization curves, and first-order reversal curves (FORC) diagrams), along with micromagnetic simulations to understand the different behaviors found.

4.2. Pulsed electrodeposition of Ni and Co

4.2.1. Single element deposition of Ni and Co
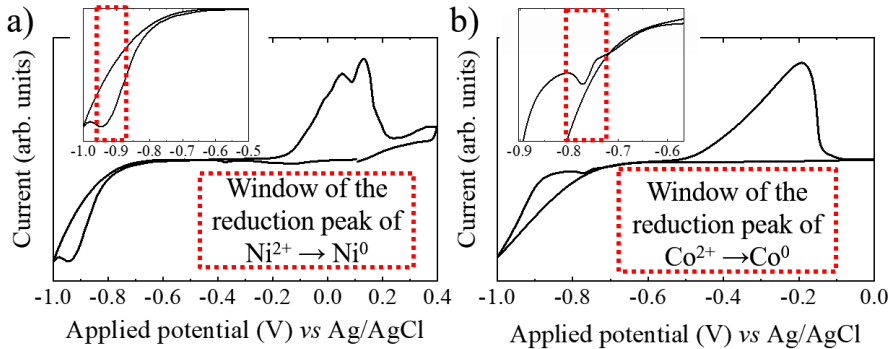
Figure 4.1. Cyclic voltammetry of a) Ni and b) Co. Inset images show the reduction potential window for each material.

The fabrication of 3D Ni and Co single element nano-networks (3DNNs) was carried out via pulsed electrodeposition into 3D AAO templates with a fixed distance between TCs, which will be named *P*. Electrodeposition was performed on three different nanoporous templates with three different transverse channels distance, fixed at around: 240, 440, and 680 nm. The corresponding 3D AAO templates were fabricated by applying a 180, 360, and 540 s MA pulse; hence the resulting 3D nano-networks were labelled as 3DNN220, 3DNN440, and 3DNN680, after the distance *P* of the 3D nano-networks. The objective of this study was to discern the role played by the transverse connections, specially placed every 220, 440, or 680 nm along the nanowires, in the magnetic behaviour of the nano-networks. As a means of comparison, straight 1D nanowires (Nws) of Ni and Co were also grown, using lab-made 1D AAOs in sulphuric acid, as described in section 2.1.1.1. In summary, two sets of samples were grown: one made of Ni and another one of Co, consisting of 1D Nws and 3DNN of *P* = 220, 440, and 680 nm.

Ni and Co were electrodeposited separately, from 0.75 M $NiSO_4·6H_2O$, 0.02 M $NiCl_2·6H_2O$, 0.4 M H_3BO_3, and 0.016 M of saccharine, and 0.1M $CoSO_4·7H_2O$ and 0.4 M H_3BO_3 electrolytic baths, respectively. In this study, the deposition potential of Ni and Co metals was determined by cyclic

voltammetry curves (in Figure 4.1a, Ni and 4.1b, Co) where the cathode was a Si substrate coated with a 5 nm Cr and 150 nm Au layers.

Single element electrodeposition of Ni was carried out at -0.9 V versus Ag/AgCl at 45 °C, as reported in the literature. The deposition potential of Ni is close to the voltage at which electrolysis of water takes place (around 1 V, see Figure 4.1a), hence, deposition was performed at a lower potential of   -0.9 V to avoid hydrogen evolution occurring at the WE electrode surface. Co deposition was performed at -0.8 V versus Ag/AgCl in room temperature (RT) conditions, according to the deposition potential found in the cyclic voltammetry curve in Figure 4.1b. The voltage pulse was applied for a $t_{on} = 1$s, followed by a zero-current pulsed of 0.1 s (t_{off}). The electrodeposition was performed for a total duration time of 2-4 h. In all cases, the longitudinal nanowires were 10-20 µm in length, having a diameter of 55 ± 5 nm, while 3D nano-networks additionally present transversal interconnections between neighbor nanowires with an ellipsoidal shape, in the form of a disc of 35-40 nm in height and 25-30 nm in width, see Table 4.2. The dimensions of the transversal pore channels are slightly increased during electrochemical deposition, due to the acidic aqueous solution in which the Ni and Co species are dissolved.

4.2.2. Co-deposition of Ni and Co

The effect of the composition on the magnetic properties of the 3D nano-networks was also investigated. In this case, the geometry of the nano-networks was set at $P = 680$ nm (3DNN680), while the composition was varied from sample to sample. Several Ni-Co alloys were grown with 0%, 33%, 54%, 91% and 100% Co content. The 0% and 100% (that is, purely Ni and purely Co samples, respectively) were added to compare the magnetic properties of the alloys with the 3DNN680 of the previous experiment.

Table 4.1. The different Ni and Co baths used in the Ph.D. work with the nominal ratios used, and the final film composition in at % of Ni and Co.

Ni/Co bath ratio	Ni at%	Co at%	Co_xNi_{1-x} alloys
4:1	66.94	33.06	$Co_{0.33}Ni_{0.67}$
3:2	45.02	54.98	$Co_{0.55}Ni_{0.45}$
1:4	8.29	91.71	$Co_{0.92}Ni_{0.08}$

Co-deposition of Ni and Co was performed to grow Co_xNi_{1-x} alloys. The applied deposition potential was set at the highest deposition potential of the two, that being - 0.9 V, to avoid depletion of the material with a higher deposition potential, in this case, Ni. The Co percentage in the alloy was then varied by mixing the selected Ni and Co electrolytic baths, employed in the former experiments, in different ratios, as recorded in Table 4.1. Temperature deposition was fixed at 45 °C.

4.3.   Morphological, compositional, and structural characterization of magnetic 1D nanowires and 3D nano-networks.

4.3.1. Morphological characterization

i)   <u>SEM</u>

The geometry and quality of the electrodeposited 1DNW and 3DNN were analysed by SEM imaging (see Figure 4.2). In particular, Figure 4.2a shows a Ni 1DNW array electrodeposited inside a sulphuric AAO membrane with an enlarged diameter pore of 45-55 nm as a result of the etching treatment (section 2.1.2.1). Thus, having the same diameter as the longitudinal NWs of the 3DNN. The diameter of the longitudinal pores could be experimentally measured from the top-view SEM images of the samples (inset image in Figure 4.2a) after mechanical polishing of the gold side of the AAO, as described in section 2.1.4.3.1, to expose the nanowires. Cross-sectional SEM images of Ni 3DNN composed of $\phi =50 \pm 5$ nm longitudinal wires transversally interconnected at every 220 and 680 nm, labelled as 3DNN220 and 3DNN680, are displayed in Figure 4.2b and 4.2c, respectively. The green dashed lines mark the location of the TCs along the nanowires. The inset image in Figure 4.2b corresponds to zoom in of the 3DNN at the area enclosed by the yellow square, showing these TCs in greater detail. TCs present an elongated shape reproducing the ellipsoidal shape of the transversal pores produced by a quadratic HA pulse. The dotted orange lines were added to highlight the shape of the connections, which are characterized by two different distances: a short average distance of 15-20 nm and a long distance of 30-40 nm. The side panels in Figures 4.2a (sketch of 1DNWs), 4.2b, and 4.2c (sketches of 3DNN220 and 3DNN680, respectively) were incorporated to help describe the geometry of the 3DNN compared to traditional 1DNWs.

The Co 3DNN and 1DNWs (not shown here) present an analogous morphology as the Ni ones. All Ni-Co alloys were also observed under SEM and showed a geometry equivalent to Ni 3DNN680 samples (Figure 4.2c).
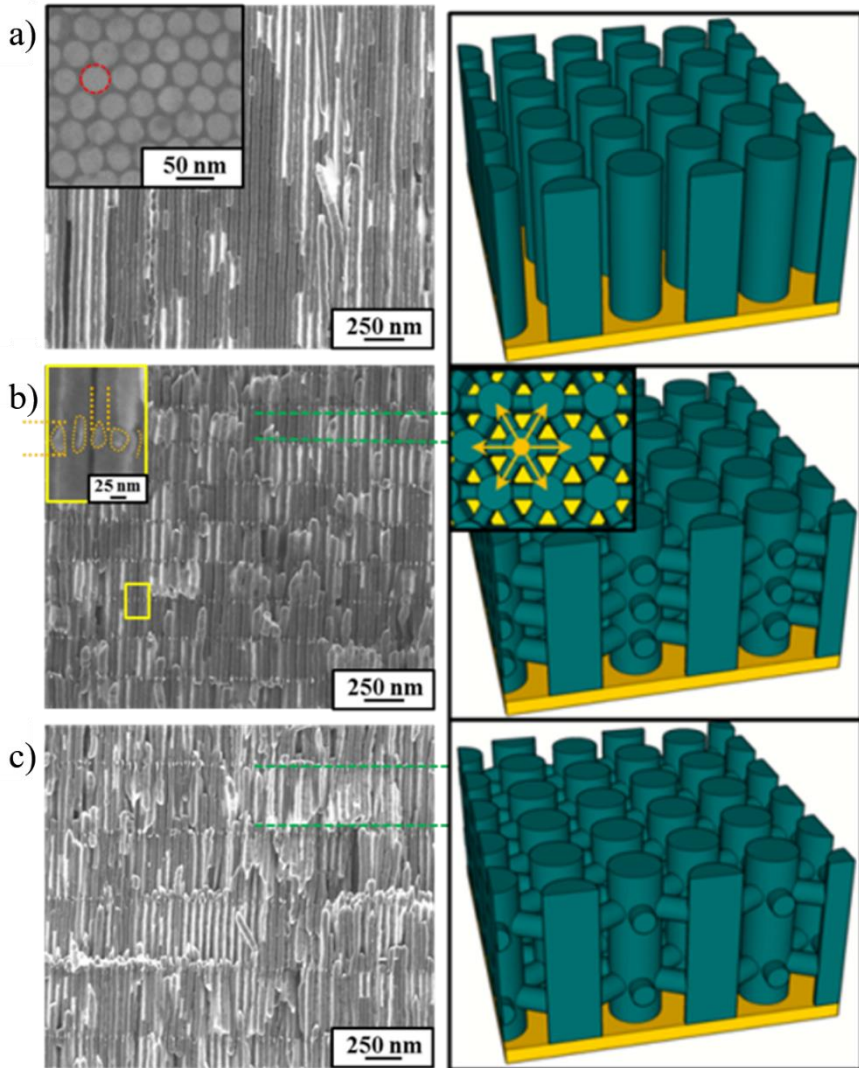
Figure 4.2. *Left side SEM micrographs of the cross-section of Ni: a) 1DNW, b) 3DNN220 and c) 3DNN680. The green dashed lines indicate the presence of TCs along 3DNN220 and 3DNN680. Insets in a) and b) correspond to a top view SEM photo of the nanowires and to an enlarged image of the TCs around the area marked with a yellow rectangle, respectively. The orange dotted lines were added to help visualize the ellipsoidal shape of TCs, with a smaller width and larger length. Right side, schematic drawings of samples a) 1DNW, b) 3DNN220 and c) 3DNN680. The inset represents the 3DNNs looking from the top.*

The specific dimensions of the nanowires in the array and 3DNN extracted from these SEM images are recorded in Table 4.2. It is worth noting that the synthesis method includes the use of acid etching, both in anodization and during the opening of the transversal pores for extended periods. Therefore, the diameter of the nanowires and dimensions of the TCs, given in Table 4.2, are statistically averaged values that may suffer small deviations ($\pm$ 5 nm diameter *vs.* tens µm length).

Table 4.2. *Dimensions of the 1D nanowire arrays and 3D nano-networks.*

Sample name	Nanowire diameter, ϕ (nm)	Distance between neighbouring Nws, D_{int} (nm)	Distance between transversal connection, P (nm)	Dimensions of the transverse connections		Nanowire length, L (µm)	Crystallite size, τ (nm)
				Long length (nm)	Short length (nm)		
Ni samples							
1DNw	53	65	--	--	--	25	48
3DNN680	52	64	680	35-40	15-20	11	22
3DNN440	53	64	440	35-40	15-20	24	32
3DNN220	54	61	220	35-40	15-20	5	36
Co samples							
1DNw	48	66	--	--	--	24	52
3DNN680	52	64	650	35-40	15-20	10	106
3DNN440	51	68	438	35-40	15-20	27	120
3DNN180	55	65	230	35-40	15-20	28	56
Ni-Co alloys							
70Ni30Co-3DNN680	50	65	670	35-40	15-20	56	--
45Ni55Co-3DNN680	52	66	677	35-40	15-20	58	--
10Ni90Co-3DNN680	49	67	696	35-40	15-20	59	--

ii)   TEM tomography

SEM imaging does not allow us to appreciate the full geometry of the 3DNN, in which nanowires are disposed in a hexagonal arrange and thus, transversal connections follow the same radial configuration where a single nanowire is connected to its 6-closest neighbour wires in the hexagonal

arrangement, as shown in the inset top view sketch of the 3DNN of Figure 4.2d and indicated by the orange arrows. Hence, tomography measurements were performed to reconstruct the 3DNN structure from 2D images of the dissolved nanowires, taken in a TEM (see Figure 4.3).
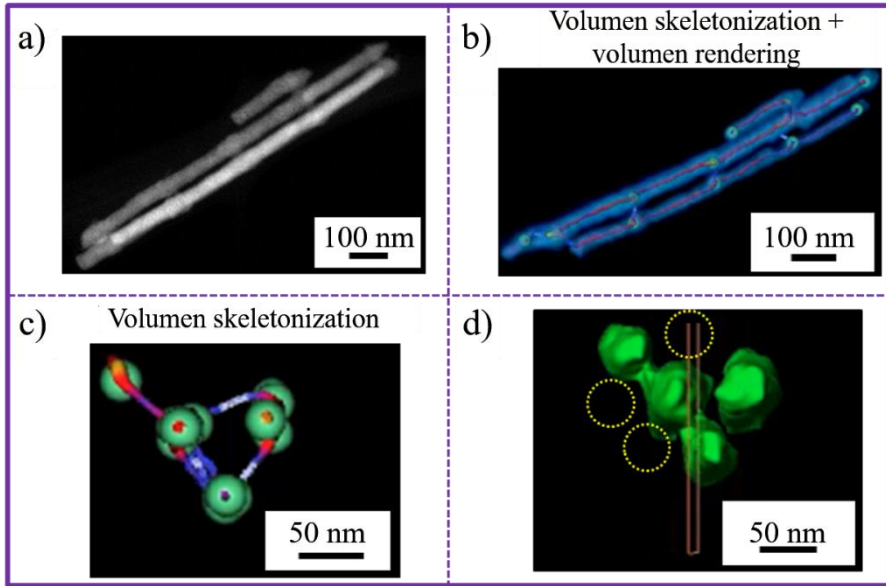
Figure 4.3. a) TEM image of two nanowires interconnected at every 220 nm. b) Volume skeletonization and volume rendering of a). c) and d) top view perspective of the 3D skeleton and complete 3D volume reconstruction of the TEM image a), respectively. The yellow circles in d) indicate the missing nanowires surrounding the one at the center of the hexagonal arrangement.

Figure 4.3a shows the 2D TEM image taken as a reference for the reconstruction of the 3DNN. By making several transversal cuts of the initial 2D image, a recreation of the skeletal structure of the 3DNN is obtained, as shown in Figure 4.3b, which can also be observed and modelled from the top view perspective, Figure 4.3c. Then, with specific software, a 3D model of the structure can be built. Figure 4.3d corresponds to the full reconstruction of the initial SEM image in Figure 4.3a from a top view perspective. In this last image, we can better appreciate the connectivity of the nanowires to their neighbours. The yellow dashed circles indicate the vacated spots that missing nanowires should occupy in the hexagonal arrangement of the alumina template. During sample preparation, the dissolved interconnected nanowires have to be sonicated to isolate a small number of them, and that is the reason why there are missing nanowires. Otherwise, if there were a high number of nanowires to measure, electrons wouldn't be able to pass through the sample

specimen and reach the detector to obtain TEM images and the reconstruction of the 3D image will not be possible.

4.3.2. Compositional analysis

i)   Energy–dispersive X-ray spectroscopy (EDX)

EDX analysis was performed on the different alloys to determine the Co and Ni percentage in each sample, for which, measurements were taken in different areas along a cross-sectional cut of the 3DNN680 samples with varying composition, while still embedded in the alumina matrix. The conditions employed during the measurements are listed in section 2.2.3. The composition of the different alloys as a function of the Ni:Co ratio in the electrolytic bath is recorded in Table 4.1.

4.3.3. Structural characterization

i)   X-Ray diffraction (XRD)

The crystal structure of the Ni, Co, and Ni-Co samples was studied by XRD. The y-axis corresponding to the intensity of the diffraction peaks is expressed in a logarithmic scale to enhance the lower intensity peaks and confirm the absence of possible impurities due to the oxidation of Ni or Co. Figure 4.4a shows the diffraction patterns of the Ni samples with different morphologies, grown as 1D NWs, 3DNN5680, 3DNN440, and 3DNN220, from bottom to top. In all cases, the different Ni samples present a polycrystalline structure, as indicated by the presence of multiple diffraction maxima. The peaks were located at a 2θ angle of 44.54, 51.89, 76.45, and 93.04° correspond to the (111), (200), (220), and (311) diffraction planes in a face-centered cubic (FCC) arrangement (marked with green dotted lines). The crystalline structure of the Ni nanowires is not affected by the presence (or absence) of transversal connections, suggesting that there is no dependence between the crystalline structure with which the Ni was grown and the imposed geometry of different nanostructures.

Looking at the Co set of samples, shown in Figure 4.4b, it can be concluded that the Co 1DNWs and all the Co 3DNN (3DNN680, 3DNN440, and 3DNN220) present the same polycrystalline structure. The peaks marked by the orange dashed lines are associated with the (100), (110), and (200)

direction of a hexagonal closed packed (HCP) crystal structure, appearing at 41.59, 75.90, and 90.49°, respectively.
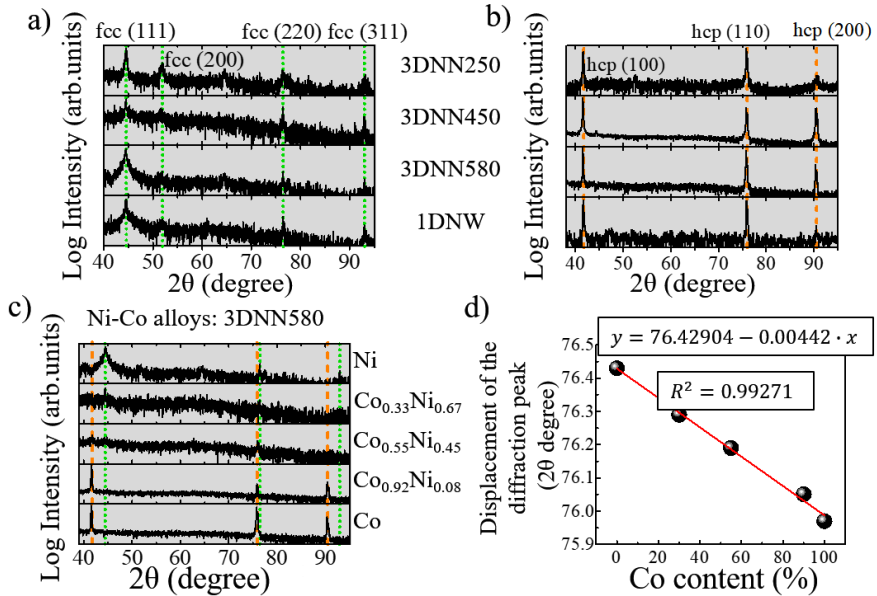
Figure 4.4. XRD diffraction spectra of 1DNW and 3DNNs with different P = 680, 440, and 220 nm, corresponding to 3DNN680, 3DNN440, and 3DNN220, from bottom to top made of a) Ni and b) Co. The XRD pattern is taken from the reference pattern JCPDS-ICDD-00-004-0850 for Ni FCC (green dotted lines), ICDD 00-005-0727 for HCP Co (orange dashed lines) c) XRD diffraction patterns of 3DNNs Co_xNi_{1-x} alloys with fixed geometry P = 680 nm (3DNN680). 100% Co, 90% Co, 55% Co, 30% Co and 0% Co, from bottom to top. Ni diffraction peaks are marked in green, the Co ones are orange. d) Evolution of the (110)HCP and (220)-FCC peak, corresponding to Co and Ni, respectively, as a function of the Co % in the alloy.

In Figure 4.4c, the diffraction patterns of the Ni-Co 3DNN680 alloys are compared, (from bottom to top: 100, 90, 55, 30, and 0% Co content in the alloys) while the morphology of the 3DNN was fixed by setting the distance between transverse connections at around 680 ± 5 nm. The 100% Ni and 100% Co 3DNN680 samples were also included in the graph as reference samples that allow analyzing the evolution of the diffraction patterns as the composition was varied. The green solid lines correspond to Ni FCC peaks while the orange solid lines indicate the location of the Co HCP and FCC peaks. The 100% Co-3DNN680 sample, previously analyzed, shows four characteristic peaks: (100) HCP, (110) HCP, and (200) HCP. The equivalent 3D nano-network composed of 100% Ni presents an FCC structure with no preferred crystal orientation, in which the crystal growth lies along different directions: (111), (200), (220), and (311). As the Co content is gradually

decreased, the Co peaks are substituted by the Ni ones. In the case of the 90% Co alloys, all the Co peaks are still present and none of the Ni ones could be found. Then, when the Co content was reduced to 55% the intensity of the (100) HCP-Co peak drastically decreases, and (200) HCP-Co completely disappears. At the same time, a small peak starts to evolve at 44.54° that was associated with the (111) FCC-Ni peak. If the Co content was further reduced to only 30%, the main (100) HCP-Co peak is suppressed while the (111) FCC-Ni peak continues gaining in intensity. We also noticed that, as the Co content decreases, the (110) HCP-Co peak, found at 75.90° for 100% Co, is continuously displaced towards higher 2θ values until almost reaching 76.45°, the angle at which the (220) FCC-Ni peak is located (Figure 4.4d). This plot allows evaluating more clearly the complete evolution of the crystal structure in the alloys by just looking at the displacement of the (110) HCP-Co diffraction peak. The position of the peak follows a linear trend with the Co content so that its position can be predicted for a certain alloy composition according to the expression shown in the graph.

The crystallite size of the different Ni and Co samples was also extracted from the XRD diffractograms of Figure 4.4 by applying the Scherrer equation that relates the broadening of the XRD peaks with the size of the crystallites and goes as follows

$$\tau = \frac{K\lambda}{\beta \cos \theta}$$

(4.1)

In which, τ is the size of the oriented crystalline domains, K is a dimensionless shape factor that takes a value close to unity, in this thesis a $K = 0.94$ value was employed. λ is the X-ray wavelength, XRD measurements were carried using Cu Kα radiation with a characteristic $\lambda = 1.54$ Å. β corresponds to broaden or full width of the peak measured at half maximum (FWHM) and should be given in radians. θ is the Bragg angle of the corresponding peak, which must be expressed in radians.

For the determination of the crystallite size of the Ni 1DNws and Ni 3DNN, the diffraction peak associated with the FCC (111) direction was analysed. In the case of Co, the HCP (100) peak was chosen for the analysis. The obtained results are recorded in Table 4.2.

A more local study of the crystallographic structure of the 1D NWs and 3DNNs was carried out through transmission electron backscattered diffraction (t-EBSD) on the Ni samples. This technique has allowed us to map the crystal structure along a single Ni nanowire (see Figure 4.5a) and in a bunch of interconnected nanowires from a 3DNN, Figure 4.5b, corresponding to the Ni 3DNN220 sample. The colour mapping of the nanowires in 4. 5a and 5b show a polycrystalline structure, in good agreement with XRD results. However, with this technique, we can appreciate the crystal structure of the nanowires in higher detail, and we observed that most grains present equal crystal orientation but are displayed with a 60° rotation angle around the (111) plane of the FCC crystal structure, forming sigma three (Σ3) twin boundaries that produce mirror symmetry between grains.

Measurements were performed on transmission mode requiring certain sample preparation. The Ni samples labelled as 1DNW and 3DNN220 had to be previously dissolved, and the resulting nanowire suspension was spread over a TEM grid as described in section 2.1.4.1.

iii)   <u>TEM</u>

On the other hand, a fraction of the Co 3DNN220 sample was prepared for TEM measurements, Figure 4.5c to 4.5d. TEM analysis was performed at two distinct locations of the 3DNN220 sample: 1, along a nanowire, and 2, at the union between two interconnected nanowires, as indicated in Figure 4.5c.

Then, once we have selected a particularly isolated nanowire we have measured the region at the center of the nanowire and the border, see Figure 4.5d. The HR-TEM image and FFT pattern in the orange box, corresponding to the area at the center of the nanowire, displays the preferred crystal growth of Co with (100) plane and, hence, the *c*-axis is aligned perpendicular to the length of the nanowires. The measured lattice space was 2.16 Å which corresponds to the distance between (100) planes. All of it seems to confirm the XRD results in Figure 4.5b.

Nevertheless, as we move towards the border of the nanowires we found the presence of some oxide. In the FFT pattern (red box) we observed other diffraction spots, along with those associated to (100) plane Co-HCP, that were assigned to the (111) direction of CoO rock salt. This indicates that

without the protection of the alumina membrane, the nanowires are more prone to experience oxidation being in closer contact with the oxygen present in the air and the ethanol suspension, and they end up covered with a thin outer layer of Co oxide.
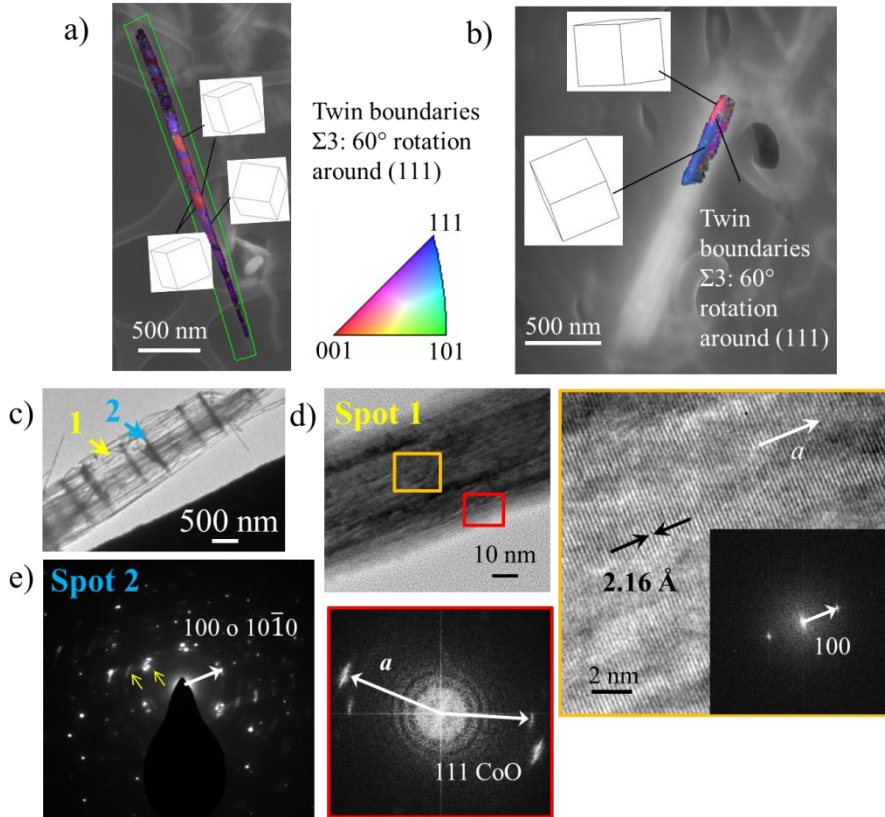
Figure 4.5. SEM images and t-EBSD orientation maps of a) a single Ni nanowire and b) a bunch of interconnected nanowires from sample 3DNN220. The colors of the t-EBSD orientation maps indicate the crystal orientation along the wires, these colors associate to the color scale triangle that is defined by the (001), (010), and (111) crystal planes of the FCC structure. c) Bright-field TEM image of dissolved interconnected Co nanowires (3DNN220). Numbers 1 and 2 indicate the positions where local measurements were performed. d) At spot 1, low magnification image along a nanowire. TEM analysis was carried out in two zones of the nanowire, at its center (orange rectangle) and the borders (red rectangle). The image boxed in orange is a high magnification TEM photograph at the center of the nanowire, where the inset shows its corresponding FFT diffraction pattern. Boxed in red, the FFT diffraction pattern at the border of the nanowire. e) SAED diffraction pattern taken at the union between two interconnected nanowires, Spot 2 in c).

In Figure 4.5e, the SAED pattern taken at the intersection between two nanowires reveals a hexagonal diffraction pattern that contains the basal planes of the HCP structure, meaning that the c-axis is now located parallel to the NW axis but perpendicular to the TCs.

Final remarks, from the characterization of the crystalline structure of Ni and Co performed by several techniques we can conclude that Ni 3DNNs were grown with FCC polycrystalline structure. The crystallite size of the Ni sample according to XRD analysis is similar to the average diameter of the TCs of the nano-networks, however, t-EBSD measurements have allowed us to observe that some crystal grains extend up to several hundred nanometers (> 200 nm) along the length of longitudinal nanowires. Most of the time the boundary between two grains with different orientations appears at the intersection between the longitudinal NWs and the TCs, forming a sigma three (Σ3) twin boundaries that produce mirror symmetry between grains. On the other hand, Co 3DNNs present HCP polycrystalline structure, possessing a certain texture along the (100) plane. Prove of this is the bigger crystallite sizes around 100 nm that were calculated using the (100)-HCP peak from X-ray diffractograms of the different Co samples. But, furthermore, TEM measurements confirm the existence of regions of those sizes with nearly epitaxial growth along the (100) and where the *c*-axis of the HCP crystal structure is perpendicular to the nanowires long length.

4.4.   Characterization of magnetic properties of the 1D nanowire arrays and 3D nano-networks.

In this section, the effect of geometry and composition on the magnetic properties of these nanostructures will be discussed. Here, we present the study of the influence of the different parameters of the resulting 3DNN. On the one hand, the effect of changes in geometry was first analyzed by modifying the distance between the TCs, that is, *P*. The effect of *P* was evaluated in two different scenarios: soft magnets (Ni) and permanent magnets (Co).

On the other hand, the dependence of the magnetic behavior as a function of the composition of the different alloys when fixing the geometry was also investigated.

4.4.1. Effect of the geometry

3DNN are studied as promising structures with tunable magnetic properties just by varying the distance between the TCs distributed along the length of the nanowire. As it has been previously discussed in this thesis, this distance can be modified during the second anodization step by changing the duration of the mild anodization pulse, as described in section 2.1.1.2.

The effect of the geometry was studied in a set of 3DNN with different TC distances (3DNN220, 3DNN440, and 3DNN680) of two different materials, namely Ni and Co. Their magnetic characterization includes the analysis of the hysteresis loops, the first magnetization curves under different angles of applied magnetic fields, and FORC diagrams, measured along the length of the nanowire and in the transverse direction of the NW axis. During the experiments, the out-of-plane (OOP) direction was defined as the direction parallel to the NWs and the in-plane (IP) direction as the perpendicular one, which is parallel to the plane of the transverse interconnections. It is also worth mentioning that the analyzed samples were small pieces of areas in the order of some mm^2, obtained from larger samples ($\sim cm^2$ in size). These pieces presented an irregular macroscopic shape due to the cutting process. Therefore, the assessment of mass or volume of the samples will induce errors with a high degree of indetermination margins. To try to counteract this effect, all the samples' results have been normalized to their saturation magnetization, and to ease the inter-comparison between different nanostructures.

4.4.1.1. 1D Ni NWs and 3D Ni nano-networks

1D NWs and next-generation 3DNN are highly magnetic interactive systems, where the composition, crystalline, and geometrical structure of the NWs and transverse connections play critical roles [65, 331].

Firstly, the composition and crystalline anisotropy resulting from the wet chemistry synthesis method and filling of the alumina template should be taken into account. From the previous section, it can be concluded that in the case of nickel, both 1D Nws and 3DNN, independently of the presence or absence of transverse connections, were grown with a face-centered cubic (FCC) crystalline structure. In all cases, they presented the main signal ascribed to the (111) crystallographic plane, which corresponds to the lowest magnetocrystalline energy. Additional minor signals ascribed to the (220)

direction, with the highest magnetocrystalline energy, and (200) plane were also detected on all samples (see Figure 4.4a). The mean crystallite size, obtained from XRD diffractograms and calculated using the Scherrer equation, gave results compatible with the dimensions of the longitudinal nanowires and the transverse connections (see Table 4.2). Thus, it is plausible to assume that the main part of Ni composing the NWs as well as the transversal connections is polycrystalline with a preferential (111) texture. Getting to this conclusion is of great importance to discern which is the role played by the magnetocrystalline energy term on the magnetic behaviour of the nanostructures synthesised in this thesis and helps to interpret the magnetic measurements.

Secondly, the shape magnetic anisotropy term should be dominant in nanowire systems due to the low dimensionality of the NWs. In this case, the aspect ratio (length/diameter), and nanowire inter-distance in the array are determinants of the final properties. In addition, the distribution and shape of the transversal connections present in the 3DNNs will contribute to this shape anisotropy term. Assuming a hexagonal cell with perfect geometry we have been able to calculate The approximate (nominal) volume ratio, R_v, of NW, V_{NW}, and transversal connections (TCs), V_{TC}, for each of the samples was calculated, considering a hexagonal cell with perfect geometry, as expressed by the following equations,

$$V_{NW}(nm^3) = \frac{3}{6} \cdot \pi \cdot r_{NW}{}^2 \cdot P$$

$$\text{(4.2)}$$

$$V_{TC}(nm^3) = \frac{3}{2} \cdot \pi \cdot r_{TC}{}^2 \cdot (D_{Int-NW} - \phi)$$

$$\text{(4.3)}$$

$$R_V = \frac{V_{TC}}{V_{NW}}$$

$$\text{(4.4)}$$

The first expression corresponds to the volume that the NWs occupy assuming a cylindrical shape. The volume of the cylinder is given by $V = \pi r^2 \cdot h$, where r is the radius of the cylinder and h is the height. In our case, r is substituted by the radius of the nanowire ($\phi/2$), r_{NW}, and the height is determined by P. The volume fraction of the transversal connections corresponds to the volume of the TCs approximated to smaller cylinders as expressed in *equation 4.3*. An average homogeneous radius of $r_{TC} = 28/2$ nm was assumed for the transversal connections, while their height was

delimited by the space that physically separated two neighboring wires, or wall thickness of the alumina membrane, which is given by the difference of the distance between nanowires from center-center, D_{int-NW}, and the NW's diameter, ϕ. The result of this difference throws a value of 15 nm.

Then, according to these expressions, the transversal connections represent 2.1, 2.6, and 4.6 % of the total volume of the 3DNNs for the 3DNN680, 3D440, and 3DNN220 samples, respectively. However, it must be kept in mind that this is only an approximation. Transverse connections present an ellipsoidal shape and when they connect, SEM imaging reveals that the radius (or diameter) of the TC constrains at the connecting point between NWs. It is also worth noting that in these arrangements the distance between transverse connections of the same plane is much smaller than the distance between connections located at different levels along the NWS axis, ≈5 nm *vs.* > 220 nm. Thus, (dipolar) interactions between TC and NW of the same level will be more intense compared to those from TC and NW from adjacent levels. All these specific details of the geometry of the 3DNNs should be taken into consideration when analyzing the different magnetic measurements.

i)   Major hysteresis curves

Major hysteresis loops measured in a VSM (see conditions in section 2.3.2) are presented in Figure 4.6 First, we investigated the magnetic properties of the different planes that constitute the 3D nano-networks. For this, hysteresis loops were measured with the magnetic field applied along the in-plane (IP) direction at several angles, Φ, but always within the plane, as defined by the sketch image in Figure 4.6a. As it can be seen in the plot, the hysteresis loops measured in different IP directions, corresponding to $\Phi = 0, 30, 45, 60,$ and 90°, are the same within the experimental error. The enlargement of the central part of the hysteresis curves shown in the inset of the figure further proves that there are no differences between the measured curves, not even in the low field region.

The represented IP measurements in Figure 4.6a correspond to the Ni sample 3DNN220. When IP measurements were performed on Ni samples 3DNN360 and 3DNN540 the same behavior was observed, with the only difference of the square shape of the IP loops that varied for the different 3D nano-networks. This suggests that the 3DNN does not show any magnetic anisotropy in the plane, which is somehow expected due to the geometry of the nano-networks. Although they are composed of locally ordered hexagonal

structures and therefore, there are non-equivalent directions in the plane, giving rise to certain anisotropy, the macroscopic samples are constituted by randomly distributed oriented regions, also called domains. For this reason, the possible IP magnetic anisotropy contributions average to zero when measuring the macroscopic behavior of the whole structure. Therefore, only one IP curve will be considered for each sample in future measurements.
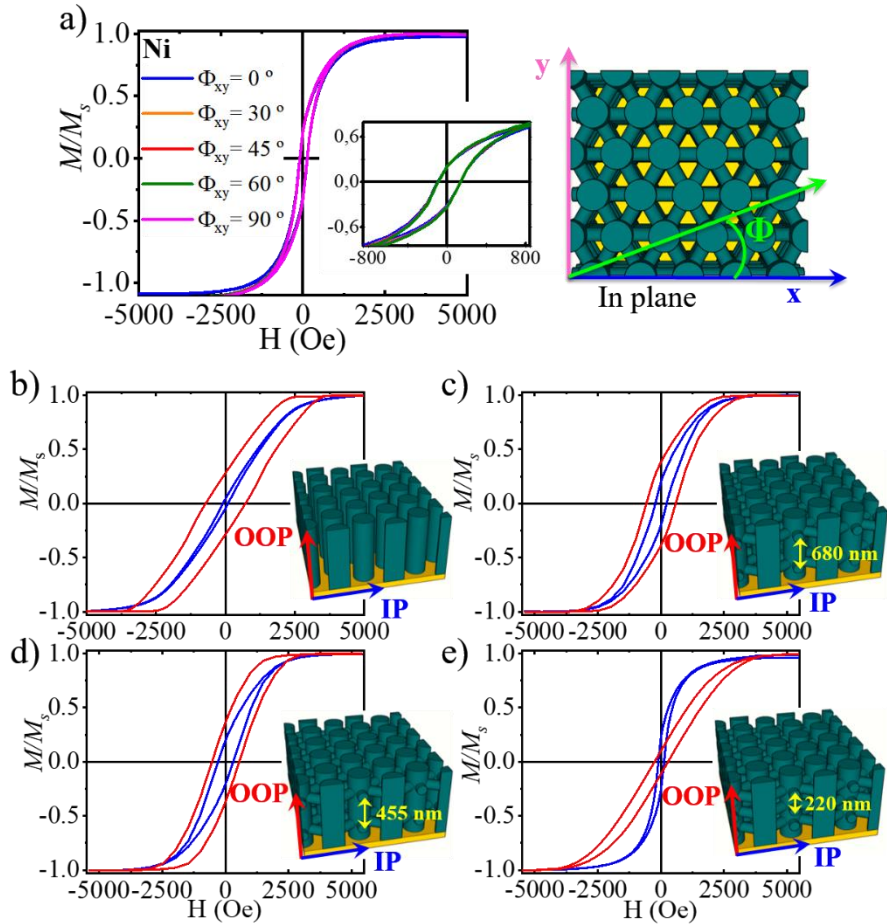
Figure 4.6. *a) Hysteresis loops measured with the magnetic field applied in different directions along the plane (IP direction) of Ni 3DNN220. The insets show an enlargement of the central part of the hysteresis loops, respectively. The drawing to the right represents a schematic top view of a 3DNN, corresponding to the XY plane (IP direction) along which the magnetic field was applied during the measurements. Hysteresis loops measured along the OOP direction. b) Ni 1DNW, c) Ni 3DNN680, d) Ni 3DNN440 and e) Ni 3DNN220. The inset drawings present a sketch of the sample configuration for each case. The arrows for IP and OOP axis show the different directions along which an external magnetic field is applied during the experiments.*

Taking these results into account, in the following, we will focus on analyzing the differences in the magnetic properties measured IP and OOP. To this end, in Figure 4.6b, 4.6c, 4.6d, and 4.6e the OOP (blue) and IP (red) hysteresis curves were plotted together, corresponding to the Ni samples: 1DNW, 3DNN680, 3DNN440, and 3DNN220, respectively.

In general terms, high aspect ratio NW arrays exhibit an easy axis along the NW's length, governed by the shape anisotropy, regardless of the magnetostatic dipolar interactions between neighboring nanowires generating a magnetic field that opposes the parallel magnetization of the array [334]. In good agreement with the literature, in the case of 1D Ni nanowires (Figure 4.6b), the coercive field is almost zero in the IP direction, pointing out to a hard magnetization axis. On the other hand, the coercive field is larger in the OOP direction (parallel to the wire axis), typical behavior of an easy axis. When comparing the magnetic behavior of the 1DNW sample with that of our Ni 3DNNs, one can observe that upon reducing the distance P (Figure 4.6c, 4.6d, and 4.6e) the anisotropy increases in the IP direction, and the magnetization easy axes progressively changes from an out-of-plane easy axis to an in-plane easy magnetization direction. Probably, due to the higher magnetostatic interactions experience by TCs situated at different levels as the distance between them is reduced.

For the largest distance between TCs (P = 680 nm), corresponding to Figure 4.6c, the system tends to the behavior found in 1DNWs array, with an easy axis along the OOP direction. As this distance is reduced to 440 nm, the 3DNN440 sample behavior changes to an almost isotropic magnetic response (Figure 4.6d) until the magnetization is completely reversed, as can be seen in Figure 4.6e for sample 3DNN220 with transverse connections located at every 220 nm, where the easy axis lies in the IP direction whereas the OOP becomes a hard magnetization direction.

The experimental values of coercive (H_c), and remanence fields (Mr/M_s) extracted from the hysteresis curves obtained in the IP and OOP configurations and recorded in Table 4.3, corroborates the effective rotation of the easy axis from the axial to the transverse direction. While the values of coercivity, H_C^H, measured in the IP direction do not show a clear trend when reducing the distance between consecutive transversal connections along the NWs length, the H_C^H in the OOP direction is drastically reduced from 580 Oe to 215 Oe. If IP remanence in the form of M_r/M_s is compared, this coefficient

notably increases due to the presence of transverse connections. The smaller the distance, the higher the value of M_r/M_s, reaching 4 times the value of the 1DNWs for the 3DNN220 sample. However, the OOP M_r/M_s presents a maximum for the 3DNN680 sample that is 4 folds that of the 3DNN220 one. These results point out that the presence of transversal interconnections between nanowires tends to stabilize the magnetic anisotropy in the IP direction (even if their relative volumes, V_R, of TC are below 5%). From these results, the distance between connections, or from another point of view the V_R of TC/NW, seems to play a major role in the OOP magnetization, since, when compared to 1D NWs, 3DNN680 and 3DNN440 almost doubles the value of the remanence and the 3DNN220 divides it by two, while decreasing by three the coercive field compared to 1DNW. In this case, we associate the observed effect to a high interaction field due to nanowire magnetostatic interactions between the longitudinal NWs and the transverse connections, which modify completely the interaction fields inside the system.

Table 4.3. *Experimental values of the coercive field,* H_c^H, *remanence,* M_r/M_s, *and the external field,* H, *at which* M_s *of the sample is achieved, as obtained from the major hysteresis loops.*

Ni samples	P (nm) / L (μm)	Coercive field, H_c^H (Oe)		Remanence, M_r/M_s		H at M_s (Oe)	
		IP	OOP	IP	OOP	IP	OOP
		(⊥to NW axis)	(∥ to NW axis)	(⊥to NW axis)	(∥ to NW axis)	(⊥to NW axis)	(∥ to NW xis)
1DNw	None /24	110±1	680±3	0.06±0.01	0.26±0.01	>5000	4100
3DNN 680	680 / 11	220±1	580±3	0.20±0.01	0.39±0.01	4417	3973
3DNN 440	440 / 25	320±3	586±3	0.19±0.01	0.35±0.01	4739	4492
3DNN 220	220 / 5	106±1	215±1	0.24±0.01	0.10±0.01	5409	6229

These experimental findings were compared to micromagnetic models with the aid of micromagnetic simulations using the OOMF code, see *Appendix B.1* for more detailed information. The 3DNN structures were simulated considering a simplified geometry, as it is schematically shown in Figures 4.7a. Figures 4.7b to 4.7d show IP (blue) and OOP (red) simulated hysteresis loops while varying the distance between the transverse planes of material in Figure 4.7a from $P = 10$ to 500 nm. The evolution of the simulated hysteresis loops when the field is applied along the length of the nanowires (OOP) or in the direction of the planes (IP) shows the same evolution as the one observed in the experimental measurements. For the shortest set distance

between planes (10 nm, Figure 4.7b), the easy and hard axes are reversed if compared to non-interconnected 1DNWs. Then, when the distance separating the planes increases, the easy magnetization axis moves from the IP to the OOP direction. Another important feature shown in the simulations is that the isotropic symmetric configuration is obtained when the distance between transversal planes is set to only 50 nm (Figure 4.7d), in which both directions are magnetically equivalent, with no clear easy axis of magnetization, that is, the 3D Ni nano-network becomes isotropic magnetic meta-material. It should be noted that the simulations do not include thermal effects or impurities, they consist of a simplified model of the real structures and therefore, the magnetic energy needed for magnetization reversal is higher than in the experimental results. Due to this, the distance between transversal planes and transversal connections in both cases, simulations, and experiments, are different, however, these simplified models are enough to qualitatively confirm the magnetic behavior of the 3D nano-networks.
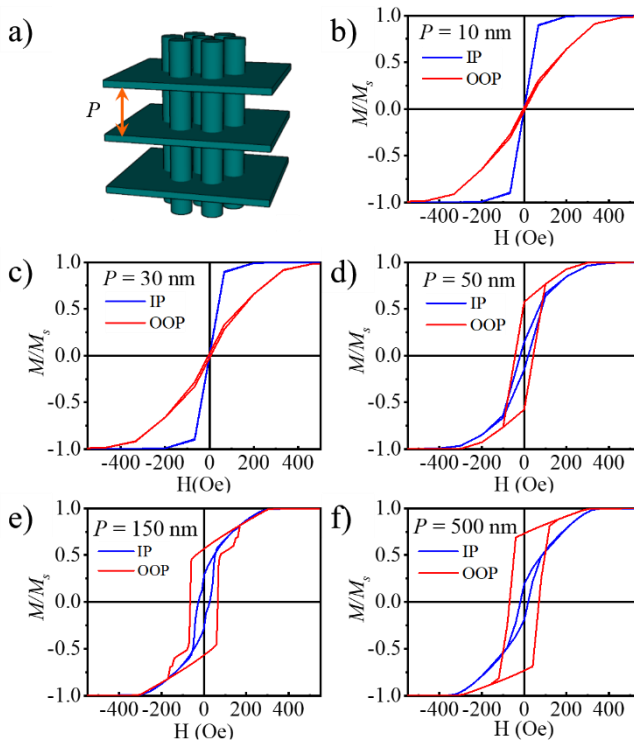
Figure 4.7. *a) Simplified geometry used for the micromagnetic simulations of the 3DNNs. Evolution of the simulated hysteresis loops with P: b) 10 nm c) 30 nm d) 50 nm e) 150 nm and f) 500 nm. When the field is applied IP the hysteresis loops are represented in blue, whereas the OOP direction is plotted in red.*

ii) First Magnetization Curves

The hysteresis loops provide information about the magnetic evolution of the system from saturated states in the direction of the external applied magnetic field. The measurement of the first magnetization curves provides information about the initial magnetization processes involved from (quasi) null magnetized state to magnetic saturation along the field direction. These measurements consisted of the magnetization of the samples, from a demagnetized state, under a magnetic field applied at 0º, 30º, 60º, and 90º. Due to the particular geometrical constitution of the nanostructures, two consecutive AC de-magnetization processes were applied to prevent as much as possible the possible effects of previous remanence magnetizations, i.e. the sample is kept in a remanent state, coming from the saturation along the previous measurement direction, by applying an AC de-magnetization process along that direction. Then, and before performing the next measurement along a new different direction, another AC de-magnetization process was applied to begin the measurement from an ideally demagnetized state in that direction.
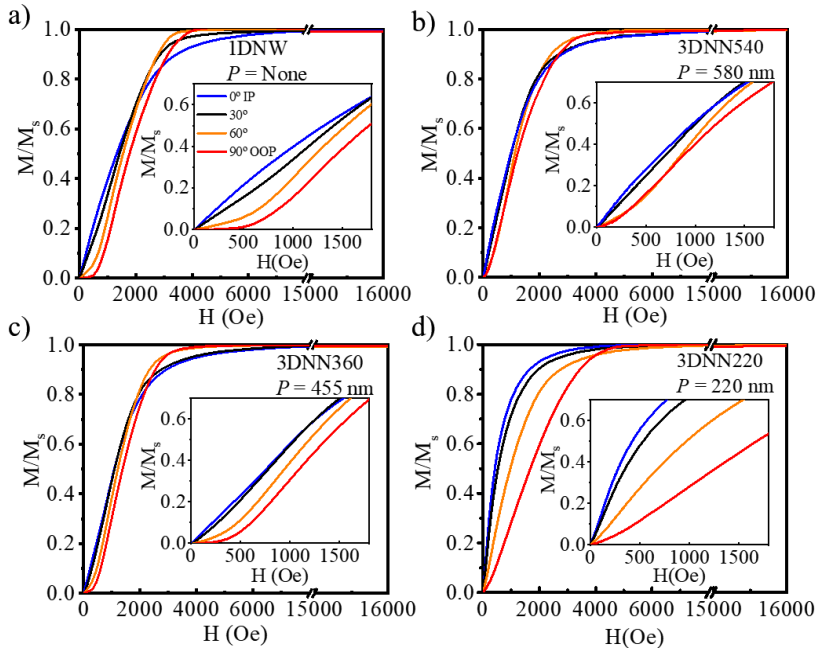
Figure 4.8. *First magnetization curves of the different geometries studied in this work: a) 1DNW, b)3DNN680, c) 3DNN440 and d) 3DNN220 at different angles of the applied field from in-plane to out plane configuration, 0°(IP, blue plane), 30° (blackline), 60° (orange line) and 90° (OOP, red line).*

The first magnetization curves, shown in Figures 4.8a, 4.8c, 4.8e, and 4.8g correspond to Ni 1DNW, 3DNN680, 3DNN440, and 3DNN220, respectively, reveal notorious changes in the evolution of these systems from a non-magnetized state. For all the samples, OOP initial magnetization is strongly hindered by NWs dipolar magnetostatic interaction acting as a demagnetization field, as a result, initial IP magnetization is higher for all the samples. However, as the applied magnetic field is increased this trend is reversed in all the samples but for the 3DNN220 sample, for which the IP direction is the easy magnetization within the whole field range. This is in good agreement with the conclusions extracted from the major cyclic hysteresis curves of each of the samples.

iii)   *First Order Reversal Curves (FORC)*

Previous measurements (hysteresis loops and first magnetization curves) revealed changes of the magnetic anisotropy as a function of the geometry of the 3DNNs, however, the subjacent magnetization reversal and magnetic interactions in these systems remain unclear. Then, to get an insight into the underlying magnetization dynamics of the 3D nanowire networks, FORC diagrams were obtained. Based on the classical Presiach model, FORC analysis models the hysteresis as a set of independent mathematical hysterons [288, 289, 335]. Each hysteron is characterized by their coercivity, H_C^F, and bias field H_U. Hysterons provide statistical information about the magnetic behavior of the whole system and at the same time, they allow to de-convolute some of the individual magnetic characteristics from the interaction field among the whole array. Nevertheless, FORC signatures are strongly dependent on each component of the array magnetization and the macroscopic homogeneity characteristics of the samples, such as border effects. FORC technique and details on its analysis can be found in section 2.3.2. Before calculating the density function according to *equation 2.5*, magnetization values were normalized by *Ms* of each sample, and thus, intensities are relative for each sample. The FORC distribution is represented using a coordinated system defined by H_C and H_U after applying *equation 2.6*. Hence, the resulting diagrams provide the representation of hysterons, which should be carefully analyzed to offer a proper physical interpretation. Taking into account this, H_C^F is then an indicator for the energy required for achieving this specific magnetization change, but not necessarily a true coercive field [336]. Hence, FORC measurements need to be accompanied by micromagnetic simulations

that help to correlate the information extracted from the FORC distributions with a certain physical phenomenon.

FORC measurements were performed on: Ni 1DNW, 3DNN220, and 3DNN440, which present different magnetic anisotropy: easy OOP magnetization direction, easy IP magnetization and almost isotropic OOP/IP magnetization, respectively. In this study, we have compared local magnetic interactions and magnetization reversal in a system with and without TCs.

Sample 1DNW consists of straight longitudinal nanowires of 25 µm with no TCs. Whereas, the 3DNN220 sample was composed of 20 interconnecting layers with a separating distance of 220 nm, which corresponds to the total length of 5 µm. Sample 3DNN440 has a characteristic P of 440 nm and a longer total length of 24 µm, which can fit up to 50 TCs. The resulting FORC diagrams for OOP and IP orientation are presented in Figures 4.9 to 4.11 along with the corresponding micromagnetic simulations. The color scale bar represents the normalized density of the FORC distribution, this scale is truncated at zero (meaning that the response variable cannot have a value of 0) to ease the interpretation. 3D micromagnetic simulations were carried out by employing MuMax3.10 [337], see *Appendix B.2*.

Ni 1DNW

As it has been observed in ferromagnetic nanowire arrays [335, 338-344], the OOP FORC diagram of the 1DNW sample (Figure 4.9a) presents a T-shape with an elongated distribution along the H_U axis, or interaction field distribution (IFD), with an interaction field value at saturation > 2000 Oe, and a less prominent ridge along the coercive field axis or the coercive field distribution (CFD) [345-347]. The main H_U distribution (IFD) is typically associated with strong magnetostatic interactions between the magnetic nanowires in the array, but CFB can be caused by different factors such as the nanowire diameter and length distributions.

Also, we should note that the profile of the IFD distribution is not homogeneous, as it is composed by up to 3 different local maxima, see Figure 4.9a. The most intense one is located at $H_C^F = 600$ Oe and $H_U = 650$ Oe, the second is centered at $H_C^F = 650$ Oe and $H_U = 450$ Oe and the third is situated at $H_C^F = 400$ Oe and $H_U = 875$ Oe. For Ni nanowires with a diameter ≥ 40 nm, it is typically accepted that magnetization reversal occurs through the nucleation and propagation of a vortex domain wall from the NW extremities

[253]. However, the presence of such peaks at different *Hc* and *Hu* fields point towards the existence of DW pining along the NWs length.
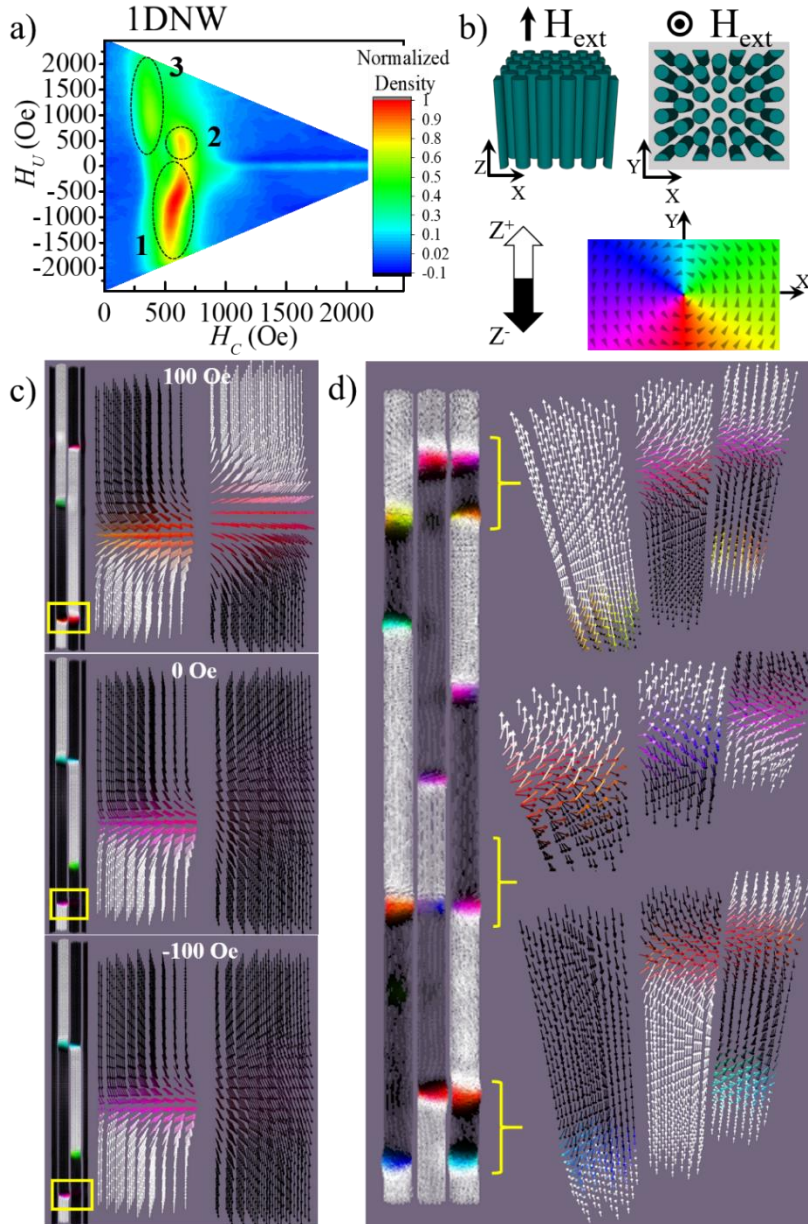
Figure 4.9. *Study of local interactions in 1DNW in the presence of an external magnetic field (Hext) applied in the OOP direction. a) FORC diagram. b) Sketch of the 1DNW sample from the cross and top views. Color map of the magnetization direction along the XY plane. White arrows pointing up and black arrows pointing down correspond to the alignment of the spins*

This behavior was further corroborated by micromagnetic simulations, performed as described in *Appendix B.2*. The OOP simulations in Figure 4.9c show that multiple transverse domain walls have nucleated along the 1D nanowires. These transverse domain walls interact with neighboring NWs, even acting as pinning centers, while they propagate from the nanowires extremities. As the NWs break in magnetic multi-domains during the magnetization reversal (even at the demagnetized state, see Figure 4.9c, Ni NWs still exhibit a multi-domain structure along their length), the generation of domains separated by domain walls justifies the peaks observed in the experimental FORC distribution shown in Figure 4.9a. More in particular, we suggest that our second peak (H_C^F = 650 Oe, Hu = 450 Oe) corresponds to the complete magnetization reversal of some Ni NWs, while the other peaks are associated with the partial magnetization reversal of the NWs.

When the external magnetic field was applied perpendicular to the wire axis or along the hard magnetization axis, the obtained 1DNW IP FORC diagram (Figure 4.10a) is consistent with the results reported in the literature [335, 339, 348], where a nearly reversible magnetization process by coherent rotation has been suggested. In particular, the IP FORC of 1DNW shows 2 irreversibly peaks with a narrow distribution along the H_U axis. The less intense peak is located at H_C^F = 50 Oe. And the more intense and broad peak is centered at H_C^F = 250 Oe, with an interaction field value at saturation of ≈ 300 Oe that is considerably smaller than the values observed for the OOP direction.

Looking at the IP simulations (Figure 4.9b), we can confirm that the magnetization reversal process is mainly driven by coherent rotation. But, here again, NWs split also into magnetic domains, separated by domain walls. Contrary to the observed DWs in the OOP configuration, DWs in the IP geometry stand and do not propagate along de NW with the external applied magnetic field. Then, simulations suggest that the observed features in the corresponding IP FORC diagram (Figure 4.10a) could be related to the presence of these DWs. For instance, we suggest that the reversible distribution corresponds to the coherent rotation of the domains, while the

irreversible distribution, observed at $H_C{}^F$ = 250 Oe, reflects the generation/annihilation of DWs.
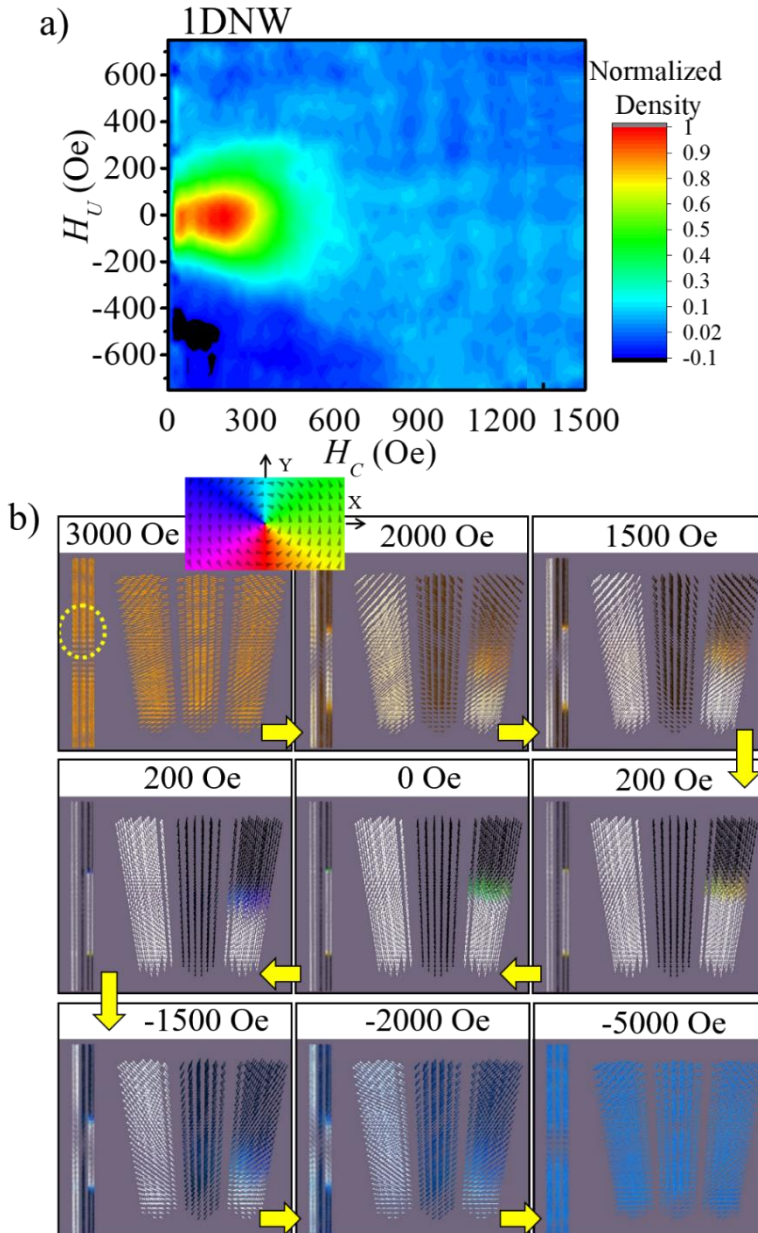
Figure 4.10. *a) IP FORC diagram of Ni 1DNW sample. The inset image shows the direction of the external applied (H_{ext}) in the XY plane (IP direction perpendicular to the NWs in the array). b) Simulated IP magnetization reversal of Ni 1DNW. The red circle on the left panel denotes the magnified areas in the right panels*

3DNN220

Regarding the Ni 3DNN220 sample, with the smallest separation between TCs (P = 220 nm), in which the magnetization easy axis has switched from parallel (OOP direction) to perpendicular (IP) to the NWs (see Figure 4.6). The OOP FORC distribution (Figure 4.11a), instead of a T-shape, presents an elongated shape along the H_U axis (with a strong interaction field > 2000 Oe and no CFD ridge), that has noticeable shifted towards a lower value of H_C field axis, which now is located at H_C^F = 325 Oe. As it was recently discussed by Pierrot *et al.* [347], the shape of the distribution along the interaction field axis (IFD) can constitute a criterion to distinguish the interaction regime acting over the sample. For example, regarding the magnetostatic dipolar interactions among NWs, a stronger dipolar field is generated between NWs located at the center of the array than between those at the edges of the sample. These are known as border effects and contribute to the inhomogeneity of the total magnetic field acting over the nanowires. An IFD flat profile, like that observed for 3DNN220, was linked to a homogeneous interaction magnetic field, in opposition to the OOP FORC distribution with a maxima at H_C^F = 650 Oe and Hu = 450 Oe, which was associated to the complete magnetization reversal of the Ni nanowires. Therefore, we suggest that when the TCs are placed this close, the interactions between TCs of different levels contribute to the homogeneity of the magnetostatic interaction field, generated within the sample.

On the other hand, micromagnetic simulations reveal further details about the OOP magnetization reversal mechanism. The OOP magnetization reversal begins from the saturated state (white arrows in our case), see Figure 4.11b Then, as the external magnetic field is reduced, TCs start to rotate their magnetization to the IP configuration, meanwhile, the NW segments (or the NW limited by two consecutive TCs) keep their magnetization OOP (see Figure 4.11c with H_{ext} = 1600 Oe). At this point, we observe that the IP magnetization at each TC level is still homogeneous, with all magnetic moments pointing in one direction. Although this direction is different for every level, we should note that the magnetization direction at each level is not random and shows an in-plane rotation from one TC to the next one, but of a different level. The IP magnetization of the TC levels adopts a *corkscrew*-like configuration along the NWs axes (see the central panel in Figure 4.11c) confirming the presence of a significant magnetostatic coupling between the TCs placed at a 220 nm distance.
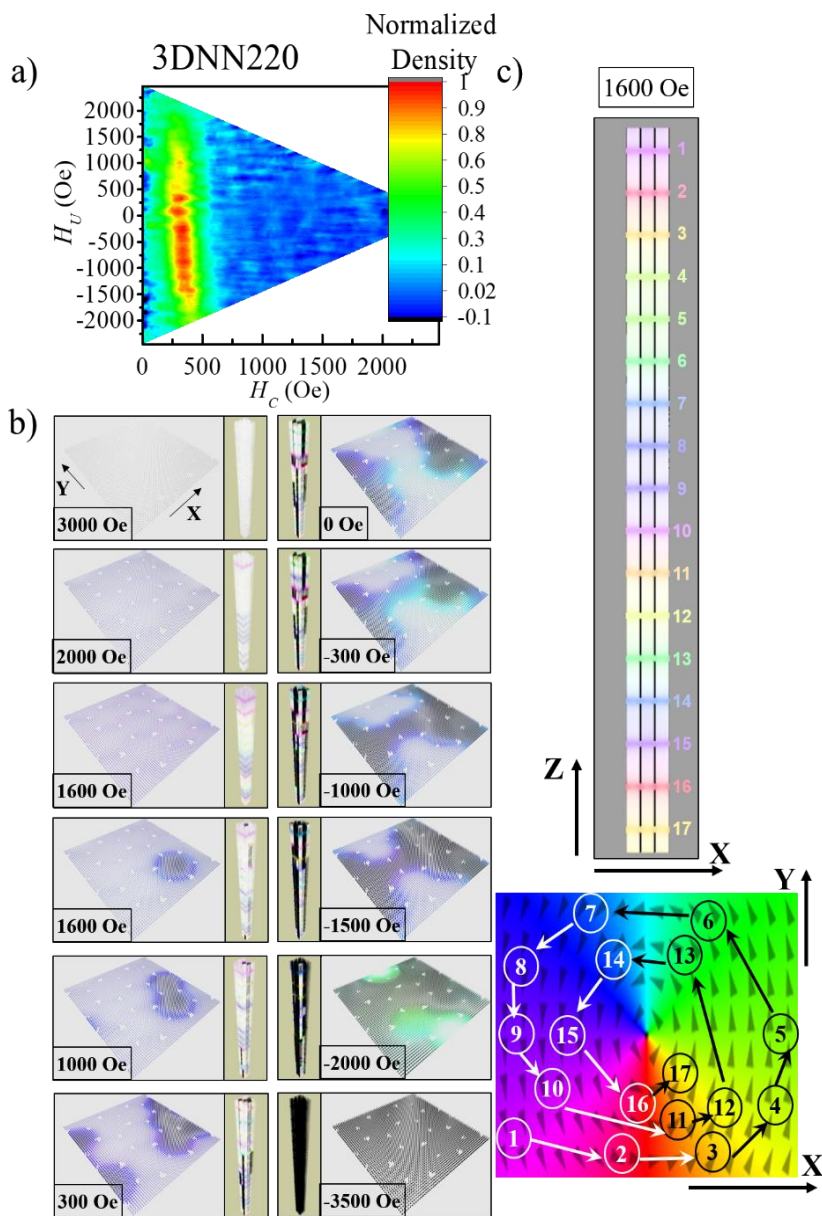
Figure 4.11. a) *OOP FORC diagram of Ni 3DNN220. b) Simulated OOP magnetization reversal sequence of 3DNN220. Each panel shows the dependence of the magnetic configuration with the externally applied field and it is composed of a 3D view of the whole sample and the top-view (XY plane) of the 9th TC level. c) Cross-section view (XZ plane) of the whole sample at H = 0.16 T is represented at the center of the figure showing the TC corkscrew configuration. Each level is denoted by a colored number that relates to the numbers in the color map (magnetic direction) at the bottom.*

130

By continuing to reduce the externally applied magnetic field, the magnetization of the NWs segments rotates from OOP to the IP direction at the intersection between NWs segments and TCs, meanwhile, the central part of the segmented NWs keeps the OOP orientation. This stage remains until the OOP magnetization reversal of some NWs segments is abruptly achieved (occurring at H_{ext} = 1500 Oe, Figure 4.11b). Contrary to what is usually observed in ferromagnetic 1DNWs, where the OOP reversal process starts at the NWs extremities, this event first starts with IP rotation at the NWs segments/TCs intersections followed by full magnetization reversal of the segments, which occurs anywhere along the NW and in any wire of the array. Once a NW segment reverses, the magnetization configuration inside the two related TC levels changes from the IP homogenous orientation to a more complex OOP/IP configuration.

The complexity of the magnetization reversal process can be directly linked to the FORC diagram of the sample. In particular, we claim that our OOP FORC distribution elongating along the H_U axis (Figure 4.11a), is formed by multiple overlapping peaks. These peaks correspond to multiple switching events, occurring at different interaction fields but at the same H_C. Therefore, we suggest that these irreversible events correspond to the complete magnetization reversal of the NW segments.

The IP FORC distribution of 3DNN220 (Figure 4.12a) presents a peak at H_C^F = 50 Oe and a lobe through H_C^F and negative H_U axes. This type of lobe has not been observed in 1DNW (Figure 4.10a), but it was previously reported in a Ni antidot array under the influence of non-cylindrical Ni nanopillars [349], Fe regular antidots [350] as well as in an artificial spin ice system [351]. Usually, this lobe, also called "left-bending boomerang", points out the nucleation and abrupt propagation of domain walls [351], such as those generated at the intersection between TCs and NWs.

Regarding IP micromagnetic simulations of the 3DNN220 (Figure 4.12b), they provide a magnetization reversal process by coherent rotation. In this case, when IP magnetic field was reduced from saturation field, the NW's segments, mainly placed at the center of the sample, initiate an OOP magnetization rotation; meanwhile, TCs maintain their IP magnetization. This OOP rotation begins at the middle of the NW segments and propagates towards the interconnections between NWs and TCs. Due to the effective in-plane anisotropy of the sample (see Figure 4.6c) the TCs mostly maintained their initial IP magnetization at saturation (rotating uniformly). Only when the

applied magnetic field is set to 0 Oe, at the remanence state, the TCs acquire a completely different IP configuration than the one at saturation. Then, as the magnetic field is applied again but in the opposite direction, the TCs accommodates their IP magnetization according to the direction of the applied field until reaching full saturation in the opposite IP direction. However, part of the TCs suffer an abrupt IP magnetization reversal at low fields right after the 0 Oe situation. This is followed by the subsequent IP magnetization rotation of the segments until the whole sample is saturated. In this case, the NWs segments localized at the extremities of an entire nanowire are the first ones to initiate their IP magnetization rotation.
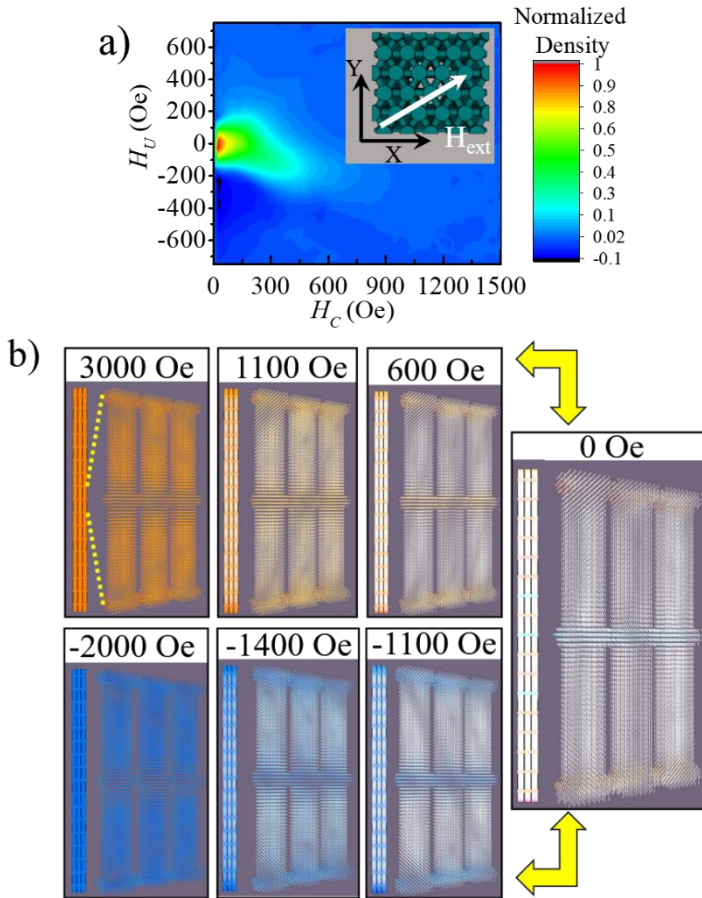
Figure 4.12. a) OOP FORC diagram of Ni 3DNN220. Inset indicates the direction of H_{ext} applied along the XY plane (in-plane direction of the 3DDNN220). b) Simulated IP magnetization reversal sequence of sample 3DNN220 for different magnetic applied fields. For each panel: the left side is a cross view of the 3 central nanowires; on the right, it is a detailed view of the sections between the levels 8th, 9th, and 10th.

This IP simulated magnetization reversal mechanism is compatible with the measured IP FORC for 3DNN220 (Figure 4.12a). The FORC distribution observed at low H_C and H_U is related to the magnetization reversal of the NW segments. Meanwhile, the observed lobe could be related to the abrupt IP magnetization reversal stage of the TCs combined with the segments.

3DNN440
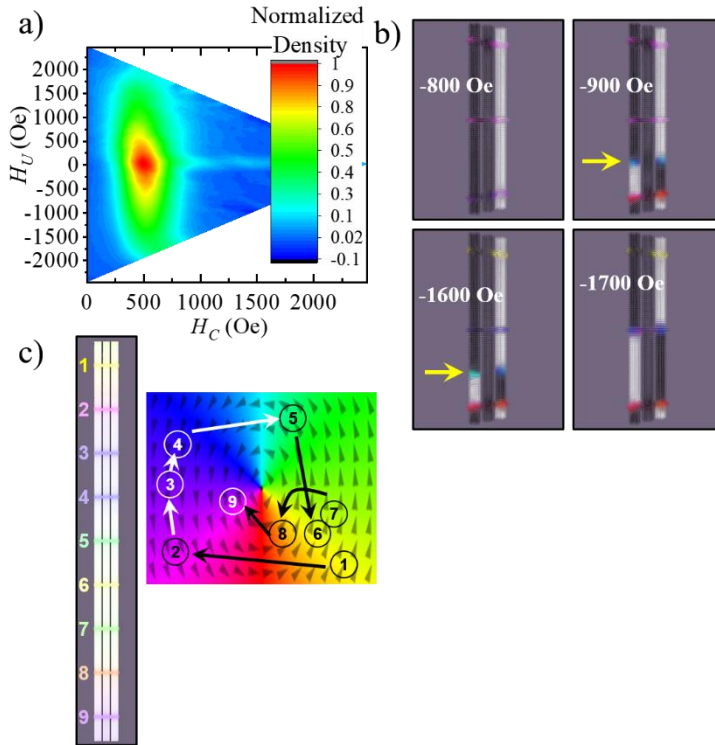
Figure 4.13. *a) OOP FORC diagram of 3DNN445. b) Cross-section images of the simulated OOP magnetization reversal of 3DNN445 as a function of the external applied magnetic field. c) The cross-section view (XZ plane) of the whole sample at H = 0.20 T and showing the IP configuration of the TC levels. Each level is denoted by a colored number that relates to the numbers in the color map (magnetic direction) at the right hand.*

If the distance P was increased up to 440 nm, corresponding to sample 3DNN440, the OOP FORC distribution of 3DNN445 (Figure 4.13a) presents a T-shape structure with an elongated distribution along H_U axis (IFD) and a less prominent ridge along the coercive field axis (CFD), as for nanowires. Figure 4.13a also shows that the distribution along the H_U axis is counter-clockwise tilting and a single peak is located at $H_C^F = 520$ Oe and centered on

the H_U axis. Similar OOP FORC distributions have been reported for shorter and less interacting nanowire arrays [340, 342-344, 352-354].

The OOP micromagnetic simulations have confirmed that TCs act as nucleation sites for magnetization reversal see Figure 4.13b. Interestingly, it was also shown that the segments (of 440 nm) in 3DNN440 are long enough to sustain their division in magnetic domains during the magnetization reversal, as marked by the arrows in Figure 4.13b. Therefore, the 3DNN440 magnetization reversal would be a hybrid process between those of 1DNW and 3DNN220. In addition, the *corkscrew*-like configuration of the IP magnetization at the TC levels is not as evident as in the 3DNN220 sample, suggesting that the magnetostatic coupling between adjacent TC levels is reduced when *P* increases from 220 to 440 nm (Figure 4.13c).
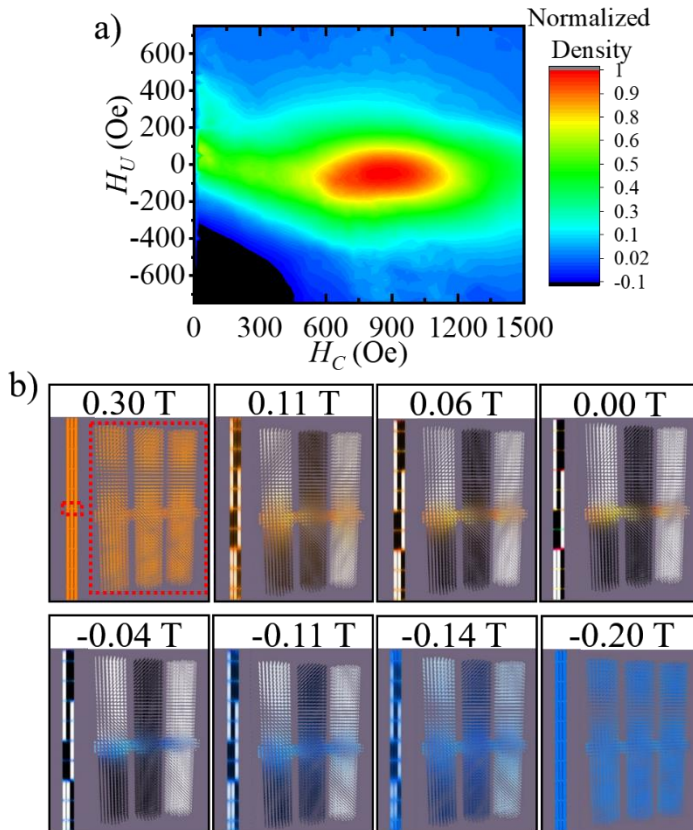
Figure 4.14. *a) IP FORC diagram and b) simulated IP magnetization reversal of sample 3DNN445.*

When P increases to 440 nm (3DNN440), the IP magnetic response diverges markedly from that of the shorter period. The IP FORC diagram of 3DNN440 (Figure 4.14a) presents two irreversible peaks which are mainly located along the H_C axis. While the less intense peak is centered again at Hc^F = 50 Oe, the more intense one has shifted up to H_C^F = 845 Oe. Like in nanowire arrays, this second peak confirms an interaction field value of $\approx$ 300 Oe but the distribution is broader along the coercive field axis (> 600 Oe) meaning a broad population of coercivities or switching events. By comparing with nanowire arrays, this second distribution is directly associated with the presence of TCs.

On the other hand, the IP micromagnetic simulations of 3DNN440, in Figure 4.14b, show that the NWs segments are fully magnetized, they do not break into magnetic domains, pointing to any of the OOP directions during the reversal process, while DWs are formed at the TCs. Consequently, the broad distribution in the FORC diagram (Figure 4.14a), at high H_C, must be related to the irreversible process that is the magnetization reversal of the NWs segments. The broader distribution along the coercive field axis is justified by the fact that the magnetization switching of the NWs segments occurs throughout the whole magnetization reversal process of the sample and as long as the sample is not saturated.

In conclusion, FORC measurement provides clear evidence of the existence of strong dipolar interactions ($\geq$ 2000 Oe) among the densely packed nanowires (diameter/inter-wire distance ratio = 55/65) in 1DNW and 3DNNs which are responsible for the generation of interactions between DWs in 1DNW and segments in 3DNN450. However, the interactions within the array are notoriously affected by the presence of TCs. Micromagnetic simulations have allowed us to depict what is the role of the TCs in the magnetic response of the 3DNNs. Therefore, we can suggest first that TCs behave as pinning sites for the magnetic domain walls. But, also, as the period between TCs is reduced to a short enough distance the TCs of different levels are coupled, which generates additional magnetostatic interactions in the sample.

In the OOP configuration, the distance between TCs control the effective length for the generation of multiple magnetic domains along the nanowire. NW segments are monodomains and TCs behave like good pinning sites for the magnetic domain walls when P is short enough like it occurred in the 3D nanowire network with P = 220 nm. Larger P are not efficient for avoiding the splitting in multi-domains (sample 3DNN440), which also happened in the

case of 1D Ni NWs. Even more, our model predicts the generations of a particular global ordered magnetization state (corkscrew-like configuration) during the magnetization reversal for 3DNN220. This state is worse defined for longer *P*, as in 3DNN440.

Meanwhile, for the IP configuration, the magnetization reversal mechanism takes place mainly through the coherent rotation for both conventional nanowires and 3D nanowire networks. In 1D NWs static DW nucleates and divide NW in domains. Then, these domains reverse their magnetizacion by a coherent rotation mechanism. IP reversal magnetization of the 3DNNs is controlled by TC and follows a more complex evolution. For *P* = 220 nm the existence of these DW in the segments, and their interactions, can not be extracted from FORC analysis and it is not observed in the performed simulations. However, for *P* = 440 nm the existence of these DW is congruent with FORC results but it is not observed in the performed simulations. Therefore periodicity of TC (P) limits the effective length of NW to sustain the generation of these DW within the segments and thus their magnetic response.

4.4.1.2. 1D Co NWs and 3D Co nano-networks

In contrast to Ni, bulk Co with an HCP crystalline structure, HCP-Co, has a strong uniaxial anisotropy along its crystallographic c-axis. Moreover, it has been reported that for HCP-Co nanowires with a diameter above 40 nm the hexagonal c-axis sits perpendicular to the wire axis [336, 355-357]. Hence, opposing shape anisotropy. Both terms are of the same order of magnitude, the magnetocrystalline anisotropy of bulk HCP-Co is $K_{HCP} = 4.3 \cdot 10^5$ J/m^3, which is just slightly smaller than the shape anisotropy constant of the nanowires, $K_s = 6.57\ 3 \cdot 10^5$ J/m^3.

As observed from the XRD diffractograms of the 1DNW Co sample and all of the Co 3DNNs (in section 4.3.1) and TEM analysis of 3DNN220, the crystal structure of the NWs and TCs is polycrystalline consisting of an HCP phase with preferred crystal orientation along the (100) plane and the c-axis perpendicular to the NWs. Considering the dimensions of our nanowires (diameter ~55 nm) and their crystal structure, the magnetic behavior of the Co nanowires and nano-networks will be determined by the competition between two different anisotropy axes, one located in the direction perpendicular to the wires (magnetocrystalline anisotropy) and the other parallel to the nanowires (shape anisotropy).

Concerning the geometrical aspects of the Co 1DNWs and Co 3DNNs (listed in Table 4.2), the structure and morphology of the Co samples are homologous to the Ni ones. The same volume fraction of V_{TCs} to V_{NW} was established in the 3DNNs, where the TCs correspond to 2.1, 2.6, and 4.6 % of the total volume in the 3DNN680, 3DNN440, and 3DNN220 samples, respectively.

i) *Major hysteresis curves*
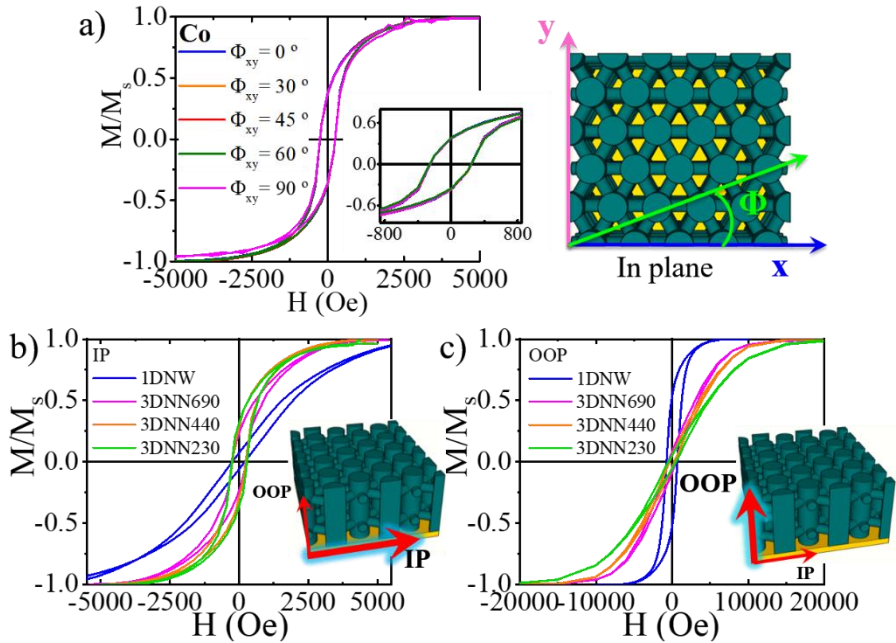
Figure 4.15. *a) Hysteresis loops measured with the magnetic field applied in different directions along the IP direction of Co 3DNN18. The inset shows an enlargement of the central part of the hysteresis loops. The drawing on the right side represents a schematic top view of a 3D nano-network, corresponding to the XY plane (IP direction) along which the magnetic field was applied during measurements. b) IP hysteresis loops and c) OOP hysteresis loops of Co 1DNW and all 3DNNs (3DNN540 3DNN360 and 3DNN180) plotted together.*

Co nanowires in the array are disposed in a hexagonal arrangement, but due to the absence of long-range order in the alumina templates any IP magnetic anisotropy averages to zero, in the same way of what happened in the Ni samples. Figure 4.15a, which shows the hysteresis loops measured with the magnetic field applied in different directions along the plane of the Co sample 3DNN220, corroborates this statement.

Figures 4.15b to 4.15c show the evolution of the anisotropy magnetization in the Co 3DNNs, measured in the IP and OOP direction, respectively. In the inset images, the direction of the measurements with respect to the structure of the 3DNNs is indicated by the red arrows and accentuated in blue. Again, the magnetization easy axes also change progressively from an IP easy axis to an OOP easy magnetization direction when increasing $P,$ the distance between consecutive TC levels. The change of the magnetization is much more pronounced in this case since all the Co 3DNN present already an IP easy axis compared to the OOP magnetization direction of the Co 1DNWs. This highlights the relevance of the magnetocrystalline anisotropy, whereas, for the Ni 3DNN, the IP preferential magnetization was not observed until a reduced P distance of 220 nm, the contribution of the magnetocrystalline term to the in-plane magnetization in the Co 3DNN fixes this direction as the favourable magnetic axis. The difference in the magnetic behaviour of the Ni and Co 3DNN nanostructures is explained by the larger shape anisotropy of Co due to its higher saturation magnetization ($M_{SCo} = 1400 \cdot 10^3$ A/m $vs.$ M_{SNi} $490 \cdot 10^3$ A/m), and thus the effect of the presence of transverse interconnections is more evident. But also, the contribution from the magnetocrystalline anisotropy, acting in the same direction as the TCs, helps to understand the magnetic behavior of the Co 3DNNs.

Table 4.4. *Experimental values of the coercive field, H_C^H, remance, M_r/M_s and the external field, H, at which M_s of the sample is achieved, as obtained from the mayor hysteresis loops.*

Co samples	P (nm) / L (µm)	Coercive field, H_c^H (Oe)		Remanence, M_r/M_s		H at M_s (Oe)	
		IP	OOP	IP	OOP	IP	OOP
		(⊥ to NW axis)	(‖ to NW axis)	(⊥ to NW axis)	(‖ to NW axis)	(⊥ to NW axis)	(‖ to NW xis)
1DNW	None / 24	225±5	712±4	0.07±0.01	0.53±0.01	8169	6380
3DNN690	688 / 10	242±6	480±7	0.24±0.01	0.09±0.01	4935	20400
3DNN440	438 / 27	243±6	350±5	0.29±0.01	0.05±0.01	4770	28503
3DNN230	233 / 28	274±5	490±6	0.34±0.01	0.06±0.01	4681	30300

In the Co 1DNW sample, the magnetocrystalline anisotropy alone cannot switch the OOP easy axis of the non-interconnected nanowires. It was found that for small nanowire diameters (~ 50 nm or below) the shape anisotropy is reinforced [358]. All these facts point towards an OOP easy magnetization direction.

Quantitatively, the values of Table 4.4 show a significant reduction of the H_C value measured in the OOP direction between that of the Co 1DNW and the Co 3DNN690 with the highest P distance, being H_C 712 Oe and 480 Oe,

respectively. The squareness ratio of the hysteresis curves follows the same trend when the magnetization is along the OOP, decreasing by a factor of almost 6 from 0.53 down to 0.09, while the squareness of the cycle in the IP direction increases by a factor of 3 from 0.07 up to 0.24. The saturation field in the OOP direction greatly increases from 6380 up to 20400 Oe and reduces along the IP direction from 8170 down to 4935 Oe. Further reducing the P distance of the 3DNNs does not dramatically change their magnetic behavior. Only the squareness ratio of the cycles along the IP was further altered, increasing from 0.24 up to 0.34 when the P value of the 3DNN was decreased from 690 nm distance between TCs down to 230 nm.
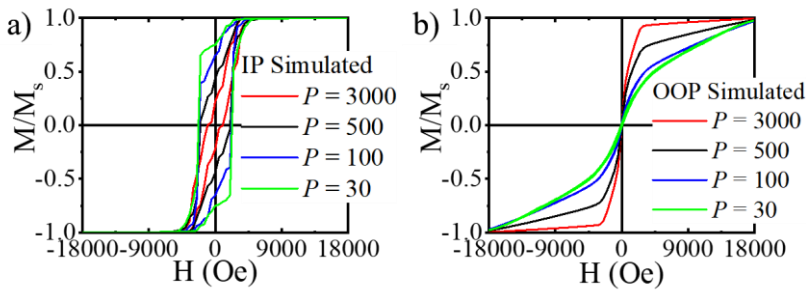
Figure 4.16. *a) IP and b) OOP micromagnetic simulations carried out in the case of Co 3DNNs with P = 30, 100, 500, and 3000 nm.*

The experimental results were supported by micromagnetic simulations. During the simulations, the saturation magnetization was set at $1400 \cdot 10^3$ A/m for Co and the additional contribution of anisotropy within the IP direction was also included, for which magnetocrystalline term corresponding to HCP Co has been taken as $K_1 = 4.3 \cdot 10^5$ J/m^3. In the case of Co, higher P was simulated to find the appropriate distance between transverse connections at which the OOP is an easy axis, P = 30, 100, 500, 3000 nm. Figure 4.16a corresponds to the IP simulated loops, and Figure 4.16b represents the OOP simulations. The simulations gave a P = 3000 nm to observe an easy axis along the length of the nanowires.

4.4.2. Effect of the composition

After studying the effect of the geometry of the 3DNNs fabricated in two different magnetic materials (Ni and Co), we can conclude that there is a clear relationship between the magnetization and the geometry (when changing the inter-distance P of the 3DNNs). To describe this behavior we can use the following equation that takes into account the shape anisotropy

$$K_{shape} = \frac{1}{2}\mu_0 N M_S^2$$

where N is the demagnetizing factor, which depends only on the shape of the studied sample, μ_0 is the vacuum permeability and M_S is the saturation magnetization.

Equation 4.6 establishes a clear link between shape anisotropy and saturation magnetization that opens the possibility to further investigate the magnetic behaviour when keeping the morphology constant (K_{shape}) but changing the saturation magnetization. This was achieved by growing 3D CoNi alloys, from 0% up to 100% Co content, with a separation distance between transversal connections of 680 nm, as described in section 4.2.2.   A P = 680 nm distance was chosen, given that the results obtained for this configuration show a change of the easy axis from the OOP to the IP direction depending on the material, Ni or Co. In other words, at the selected distance the corresponding Ni and Co 3DNN680 samples have different easy magnetization directions.

4.4.2.1. 3D CoNi interconnected networks

i)   Major hysteresis curves

Hysteresis loops measured for all samples in the IP direction are shown in Figure 4.17a. Apart from small differences, due mainly to the small
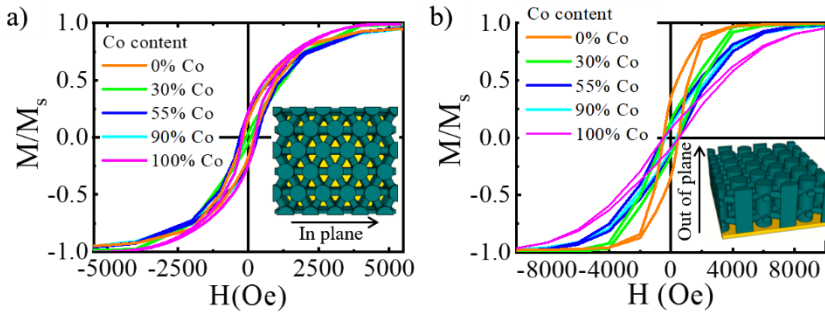
Figure 4.17. *Hysteresis loops measured for different Co$_x$Ni$_{1-x}$ 3DNNs with the applied field in the a) IP and b) OOP directions.*

misalignment of the sample in the magnetometer, the magnetic behaviour of the samples is the same. Hysteresis loops have been normalized for comparison. However, when measuring in the OOP direction (Figure 4.17b),

a clear difference in saturation field is observed. Saturation magnetization increases with the Co content in the alloy. When increasing saturation magnetization, anisotropy, which is governed by shape anisotropy, increases, making necessary a larger field to fully saturate the structure.

The same conclusions can be drawn from the *Hc*, *Ms,* and *Mr/Ms* experimental values (Table 4.5). Starting with a 100% Ni content (0 % Co content), the easy magnetization axis is set along the OOP direction, showing a higher coercive field (478 Oe) in this direction than in the IP direction (195 Oe). Saturation of the sample is reached at the lower applied field (7740 Oe) in the OOP and the squareness (0.34) of the hysteresis loop is twice that of the IP direction (0.17). Then, as the Co percentage is increased there is a progressive reduction of the coercive field along the OOP while the IP coercive field increases. This was also observed when analyzing the squareness ratio and from these values, we can conclude that the magnetization easy axis changes from an out-of-plane direction to an in-plane direction when the Co content reaches 55%. In such a case, the OOP squareness ratio was already lower than that in the IP direction, being 0.14 and 0.21, respectively.

Table 4.5. *Experimental values of the coercive field,* H_C^H, *remance,* M_r/M_s, *and the external field, H, at which* M_s *of the sample is achieved, as obtained from the mayor hysteresis loops of the CoNi 3DNN540 alloys.*

% Co content	P (nm)	Coercive field, $H_c{}^H$ (Oe)		Remanence, M_r/M_s		H at M_s (Oe)	
		IP	OOP	IP	OOP	IP	OOP
		(⊥to NW axis)	(∥ to NW axis)	(⊥to NW axis)	(∥ to NW axis)	(⊥to NW axis)	(∥ to NW xis)
0	680	220±5	580±4	0.20±0.01	0.39±0.01	4417	3973
30	680	79±6	448±7	0.05±0.01	0.15±0.01	5384	8255
55	680	309±6	511±5	0.21±0.01	0.14±0.01	4912	15037
90	680	209±5	360±6	0.21±0.01	0.10±0.01	4636	20097
100	680	242±6	480±7	0.24±0.01	0.09±0.01	4935	20400

The saturation magnetization experiences the opposite phenomena. OOP saturation magnetization increases as does the magnetic field required to saturate the sample, but along the IP direction, it decreases when increasing the Co content in the 3DNN680. All this corresponds to the OOP becoming a hard magnetization direction as the content of Co increases.
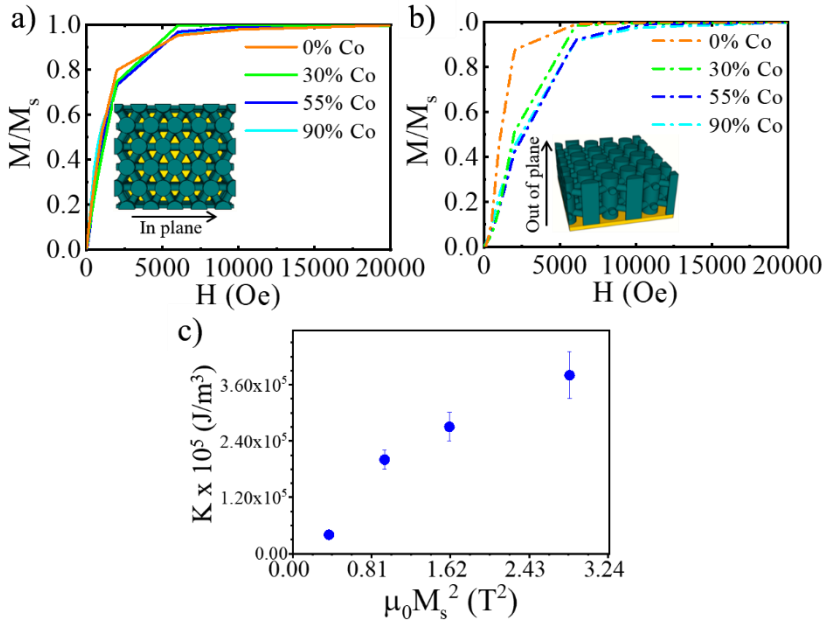
Figure 4.18. a) Hysteresis loops measured for different CoxNi1-x 3DNNs with the applied field in the a) IP and b) OOP directions. c) Anisotropy energy, calculated by numerical integration from the measured first magnetization curves as a function of $(\mu_0 M_s)^2$.

The first magnetization curves of the alloys were also measured. In Figure 4.18a, IP magnetization curves of the alloys are plotted together, along this direction, no dramatic changes were observed with the increase of the Co content. However, when the field is applied at the OOP direction, then the alignment of the magnetization parallel to the Nws axis is hindered by the Co increase. The OOP magnetization curve of the 100 % Ni 3DNN680 sample, corresponding to the orange dash-dotted line in Figure 4.18b, is higher than in any of the alloys, this sample is, therefore, easier magnetized in the OOP direction than any of the 3D nano-networks containing a low or high Co %.

Another interesting piece of information that can be extracted from the first magnetization curves is the anisotropy energy. The anisotropy energy can be calculated by integrating the first magnetization curves, measured after demagnetizing the samples in an oscillating magnetic field and then increasing the magnetic field in the OOP direction upon saturation. If the shape anisotropy is the main contribution to the total anisotropy energy, from *Equation 4.6*, a dependence on $(\mu_0 M_S)^2$ is expected. The calculated values of

anisotropy energy have been plotted as a function of $(\mu_0 M_S)^2$ in Figure 4.18c, where M_S was estimated from the composition and values of saturation magnetization of Co and Ni, according to the following expression,

$$M_{s\,alloy} = \left((1 - f_{Co})M_{s\,Ni} + (f_{Co})M_{s\,Co}\right)$$

(4.7)

in which f_{Co} is the fraction of Co present in the alloy. $M_{s\,Ni}$ and $M_{s\,Co}$ are the saturation magnetization of Ni and Co, which were taken as $490 \cdot 10^3$ and $1400 \cdot 10^3$ A/m. After the unit conversion from A/m to T (tesla), the corresponding values of saturation magnetization are $M_{s\,Ni} = 0.62$ and $M_{s\,Co} = 1.76$ T. The anisotropy energy, K, extracted from the OOP first magnetization curves shown in Figure 4.18b and the saturation magnetization, M_s, of the different alloys calculated employing *equation 4.7* are recorded in Table 4.6.

Although more energy terms should be considered for a better fitting, there is an almost linear relationship between both magnitudes, showing that shape anisotropy is the most important contribution to the total anisotropy energy of these 3D structures, making possible a full control of anisotropy just by choosing the appropriate composition for the same P inter-distance. Nevertheless, it is important to remark that this approximation is valid for thin NWs, where axial configuration of magnetization is expected. For thicker wires, different configuration of magnetic domains, with orthoradial components, would appear, introducing new contributions of the total anisotropy energy [260].

Table 4.6. *Calculated values of the anisotropy energy, K, of the Co_xNi_{1-x} 3DNN540 samples employing equation 4.7.*

P (nm)	% Co content	f_{Co}	$(f_{Co})M_{s\,Co}$ (T)	1- f_{Co}	$(1-f_{Co})M_{s\,Ni}$ (T)	$M_{s\,alloy}$ (T)	$M_{s\,alloy}^2$ (T²)	$K \cdot 10^4$ (A/m)	$K \cdot 10^5$ (J/m³)
680	0	0.00	0.00	1.00	0.62	0.62	0.38	6.63	0.41
680	30	0.30	0.53	0.70	0.43	0.96	0.92	20.63	1.98
680	55	0.55	0.97	0.45	0.28	1.24	1.55	21.31	2.65
680	90	0.90	1.58	0.10	0.06	1.64	2.71	22.55	3.71

This control of magnetization processes by changing the composition is particularly interesting since it has been recently shown that changes in composition can lead to full control of magnetization processes in NWs [359, 360]. Even more, the introduction of local changes in the composition in NWs,

in which magnetization processes are fully controlled by magnetostatic interactions, can introduce topologically protected magnetic structures, very interesting from both the theoretical and application point of view[361].

4.5.   Concluding remarks: Magnetic 3D nano-networks (3DNNs).

In conclusion, we have grown magnetic 3D NW interconnected networks, in which spacing and composition can be designed to obtain the desired magnetic anisotropy and coercivity. The 3D NW network can be described as vertical NWs interconnected by transversal NWs connecting each NW with its closest neighbors. The interconnections can be spaced along the NW length at will. We have demonstrated, that for a given material, we can tune the magnetic properties just by tuning the interconnection distances of the 3D network. The possibility of controlling magnetic anisotropy in 3Dstructures paves the way for the introduction of these newstructures in 3D devices, opening new opportunities for thedevelopment of 3D memories, portable magnetic tags, 3D oscillators, etc. In addition, the tunability of our structures, where magnetization can befinely controlled with composition and by tailoring the interconnection distance, is rather easy to implement. All this without forgetting that it is possible to have free-standing (without collapsing) 3D interconnected NW networks that can be easily handled with tweezers as in bulk, resulting in a very interesting material with additional advantages and with the possibility to be applied in macroscopic devices.

More in detail, FORC measurements and micromagnetic simulations reveal that TCs play a capital role and give rise to a complex landscape of magnetic behavior within the Ni 3D Nano-Networks (3DNNs). Our results confirm that TCs act like pinning sites for the magnetic domain walls and they contribute to the global homogeneity of the magnetostatic dipolar field acting over the sample. In particular, in the OOP configuration, TCs control the effective length for the generation of multiple magnetic domains along a nanowire. NW segments are monodomains and TCs behave like good pinning sites for the magnetic domain walls when P is short enough, like in 3DNN255. Larger P are not efficient for the correct pinning of DWs and the NW segments splits in multi-domains, like in 3DNN445 and as it was previously described for the Ni nanowire array. Evenmore, our model predicts the generation of a particular global ordered magnetization state (*corkscrew*-like state) during

magnetization reversal for 3DNN255. This state is worse defined for larger P (3DNN445).

We believe that the obtained results provide a deeper understanding of the magnetic behavior of these novel nanostructures with well-controlled and tuned magnetic properties through the introduction of several levels/periods of TCs. Moreover, the validated framework of magnetization dynamics, based on the generation/annihilation and interaction of DWs, paves the way for controlling DWs on new ways of logic computation and sensing or even for the future designing *a-la-carte* of magnetic metamaterials by the combination of different materials and/or periods within the same 3D nanonetwork.

5. Thermoelectric properties of 3D Bi$_2$Te$_3$ nano-networks.

This chapter deals with the nanostructuration of a well-known thermoelectric material, Bi$_2$Te$_3$, in the form of 3D nanowire networks, 3DNNs. The different aspects of this investigation are divided into several sections.

Firstly, Section 5.1. presents the latest achievements of nanostructured bismuth telluride materials in the field of thermoelectricity. Then, the description of the fabrication process and the characterization of the morphology, composition, and crystalline structure of the resulting Bi$_2$Te$_3$ networks can be found in section 5.2. The thermoelectric performance of Bismuth Telluride, nanostructured in such a novel way, is presented in section 5.3. The chapter closes with a final section of conclusions (section 5.4), where the validation and advantages of this approach are discussed.

5.1. Introduction: Thermoelectricity. Bismuth telluride, a good thermoelectric material.

5.1.1. State-of-the-art of thermoelectricity

Briefly, thermoelectric materials are those capable to convert a thermal gradient directly into electrical energy, and vice versa, which allows for power generation or on the other way around, cooling applications and refrigerators. The fundamental principles behind thermoelectricity were separately described by Seebeck, Peltier, and Thomson [290] (more details about the working principles behind thermoelectricity are given in *Appendix C.1.1*).

The main problem that thermoelectricity encounters for its application in everyday devices, is its low efficiency, which is defined by the figure of merit, zT, of the material (see *equation C.5.1* in *Appendix C.2*). Different approximations have been studied lately to increase it [362-365]. One of those approaches is nanostructuring, which has become the most popular since in 1993, Dresselhaus theoretically predicted that by reducing the dimensions of the material its thermoelectric performance could be increased well above the unit, $zT \gg 1$, for 2D (films) and 1D (nanowires) systems. But more accused in the latter [265]. In such low dimensional systems, quantum effects arise, which can modify the transport properties observed in bulk. In general, reducing the dimensionality of the system increases the surface-to-volume ratio, causing higher phonon dispersion due to the increased number of interfaces. However, in the theory proposed by Dresselhaus [265, 266], the most relevant changes were those related to the configuration of the electronic structure when quantum confinement was reached. As a consequence, electronic bands split into localized and discrete energy states. This, in turn, can result in semimetal-semiconductor transitions [366] and thus, affecting the electrical conductivity and Seebeck coefficient of the material. Nowadays, the limit of quantum confinement has not been reached, and most of the experimental results that have shown an increase of the zT in these structures are based on the decrease of thermal conductivity. Nevertheless, there are still efforts to overcome such limits and produce much more efficient structures.

Nanowire engineering aims to decouple the parameters involved in the figure of merit to obtain phonon-glass electron-crystal behavior. In this case, electron conductivity is enhanced along the length of the wire through free electron motion in this direction (transition from semimetal to semi-conductor

behaviour) and phonon scattering is increased in the direction perpendicular to that, due to the presence of the surface of the nanowires, which reduces the thermal conductivity [367]. This can be achieved since normally both electrons and phonons suffer collision events or scattering processes at significantly different characteristic distances; in most materials, the mean free path of phonons (in the range of hundred nanometers) is higher than that of the electrons (usually in the order of tens of nanometers), and therefore, the scattering of phonons with the surface of the nanowires increases their scattering without affecting much the electrons. Furthermore, the Seebeck coefficient can be further improved due to the increase in the density of states at the Fermi level, as a result of the reduction of the dimensionality. Nevertheless, the diameters required to experimentally observe such an enhancement of the S are too small for most of the interesting materials, being below the lowest limit that can be achieved through AAO based technology or other nanowire fabrication methods (i.e. to fulfill this requirement, bismuth telluride nanowires with diameters of 1 nm are needed). Still, it is possible to use nanowire structures of thermoelectric materials employing alumina membranes as templates to improve their thermoelectric figure of merit, zT, through an increase of σ [368] or a reduction of κ [367-370]. In particular, the latter approach has yielded more successful results to date.

Other phenomena, such as topological insulator effects, associated with the appearance of electron surface states, can emerge in low dimensional structures such as nanowires made of certain thermoelectric materials, as Bi_2Te_3 [33, 237, 371]. These effects have provided some of the latest breakthroughs in the field of thermoelectricity, both from the experimental and theoretical points of view

In this thesis, we investigated a different way of nanostructuring that diverges from traditional 1D nanowire arrays, inspired by the previous work of Martin *et al.*[166] and Chapter 3 in this thesis. We studied the thermoelectric performance of 3D nano-networks, which are composed of 1D nanowires interconnected along the transversal direction. In these structures electrons may flow in the three space directions (z, x, y), that is, not only along the length of the nanowire but also from one nanowire to the next through the transverse interconnections. However, the conduction of phonons through the transversal connections is expected to be hindered due to the reduced dimensions of the connections, even smaller than the diameter of the nanowires. In such networks, the impact over the Seebeck coefficient is not

straightforward and we should wait to comment on the experimental results. We have selected Bi_2Te_3 for its already good thermoelectric performance at RT.

5.1.2. Bismuth telluride, Bi_2Te_3

Figure 5.1. a) Crystal structure of Bi_2Te_3 with hexagonal unit cell formed by Te(1)-Bi-Te(2)-Bi-Te(1) quintuplets stacked along [0001] direction. b) Representation of the crystal structure of Bi_2Te_3 from the(0001) basal plane.

Bismuth telluride is one of the most well-known and studied materials for thermoelectric applications in room temperature conditions [265, 372-374]. It is one of the thermoelectric materials found in commercially available TE Peltier modules, as the n-type leg component.

This semiconductor possesses a narrow band gap, of 0.15 eV [375, 376], and a rhombohedral crystal structure with space group R-3m and hexagonal unit cell. In this structure, the atoms of Te and Bi, are disposed of in different monoatomic layers, in which atoms are covalently bonded. A single unit cell is composed of five layers in the following sequence -Te(1)-Bi-Te(2)-Bi-Te(1), stacked along the *c*-axis and forming what is called a quintuplet, as shown in Figure 5.1a. The bonds that are formed between atomic sheets are of two different types. The Te-Te bonding between consecutive Te(1) layers that

belong to different quintuplets is produced by weak van der Waals forces. The type of bond forming between Bi and Te(1) is covalent, however, the Bi-Te(2) bond between Bi and Te(2) atoms presents some ionic contribution.

The different natures of the bondings that one can encounter depending on the direction we move along the crystal structure, defined by the *a*, *b* (Figure 5.1b), and *c*-axis (Figure 5.1a), result in a highly anisotropic behaviour. This anisotropy translates to the transport properties of the material as well, affecting, in particular, the thermal and electrical conductivities [377-380]. The Seebeck coefficient is, however, an isotropic magnitude [379, 380]. Along the *c*-axis, the presence of weak interaction forces between quintuplets reduces the thermal and electrical conductivity, giving place to *zT* of 0.31, at room temperature (RT) for bulk single-crystal Bi_2Te_3 (see Table 5.1). As for the direction perpendicular to the *c*-axis, characterized by strong covalent bonds, the electrical conductivity is enhanced, but so is the thermal conductivity of the material. Nevertheless, the gain in the electrical conductivity makes that the best thermoelectric performance is found in the direction of the Bi and Te planes, with a *zT* value of 0.78 at RT.

Table 5.1. *Thermoelectric properties of Bi_2Te_3 from bulk to nano.*

	Sample	Crystal growth direction	Size (nm)	$\sigma_{\parallel c}$ (S/m)	$\sigma_{\perp c}$	$S_{\parallel c}$ (μV/K)	$S_{\perp c}$	$PF_{\parallel c}$ (mW/mK²)	$PF_{\perp c}$	$\kappa_{\parallel c}$ (W/mK)	$\kappa_{\perp c}$	$ZT_{\parallel c}$	$ZT_{\perp c}$	T (K)	Growth technique	Year	Ref
Bulk Bi_2Te_3	Single crystal n-type $Bi_{1.8}Te_{3.2}$	-	-	2.00·10⁴	1.00·10⁵	-216	-240	0.93	5.76	1.01	2.02	0.27	0.86	298	Bridgman solidification method	1988	[381]
	Single crystal p-type $Bi_{2.3}Te_{2.7}$	-	-	-	1.82·10⁵	-	162	-	4.72	-	2.06	-	0.69	298	Bridgman solidification method	1988	[381]
	Single crystal n-type Bi_2Te_3	-	-	1.85·10⁴	1.00·10⁵	-240	-240	1.06	5.76	1.00	2.20	0.31	0.78	298	-	2010	[379]
Bulk Bi_2Te_3	Polycrystalline n-type Bi_2Te_3	-		$\sigma_{mix\parallel c\ and \perp c}$ (S/m)		$S_{mix\parallel c\ and \perp c}$ (μV/K)		$PF_{mix\parallel c\ and \perp c}$ (mW/mK²)		$\kappa_{mix\parallel c\ and \perp c}$ (W/mK)		$zT_{mix\parallel c\ and \perp c}$		300	Standard solid-state reaction	2006	[382]
				6.91·10⁴		-170		1.9		-		-					
Bulk Bi_2Te_3	Polycr. n-type B_2Te_3	015 texture	–	0.12·10⁴		-125		0.19·10⁻¹		-		-		300	-	2009	[383]

150

	Sample	Crystal growth direction	Particle/grain size (nm)	$\sigma_{\parallel c}$	$\sigma_{\perp c}$ (S/m)	$S_{\parallel c}$	$S_{\perp c}$ (µV/K)	$PF_{\parallel c}$	$PF_{\perp c}$ (mW/mK²)	$\kappa_{\parallel c}$	$\kappa_{\perp c}$ (W/mK)	$ZT_{\parallel c}$	$ZT_{\perp c}$	T (K)	Growth technique	Year	Ref
Nanostructured bulk Bi₂Te₃	Polycrystalline n-type Bi₂Te₃ nanopart.	00l (F = 0.67) texture	≤ 1000	-	1.25·10⁵	-	-160	-	3.10	-	1.12	-	1.18	423	Mechanical alloying + SPS	2008	[384]
	Single crystal n-type Bi₂Te₃ nanopart.	015	30	$\sigma_{mix\parallel c\ and\perp c}$ (S/m) 5.00·10⁴		$S_{mix\parallel c\ and\perp c}$ (µV/K) -155		$PF_{mix\parallel c\ and\perp c}$ (mW/mK²) 1.20		$\kappa_{mix\parallel c\ and\perp c}$ (W/mK) 0.60		$zT_{mix\parallel c\ and\perp c}$ 0.94		398	Ball milling + Cold press +Temp. sintering	2009	[385]
	Single crystal n-type Bi₂Te₃ nanopart.	015	60	0.50·10⁴		-91		0.04		0.5		0.03		300	Chemical alloying + annealing and pressing	2009	[383]
	Single crystal n-type Bi₂Te₃ nanoplates	110	L = 50 - 1200 Thickness = 5- 20	1.30·10⁵		-185		4.45		1.23		1.1		300	Wet chemical synthesis + Cold compactation	2012	[386]
	Polycrystalline n-type Bi₂Te₃ nanopart.	015 texture	90	1.90·10⁵		- 120		2.75		0.84		1.1		340	Chemical alloying + SPS	2012	[387]
	Polycrystalline n-type Bi₂Te₃ nanopart.	015 texture	10-30	0.77·10⁵		-80		0.49		0.80		0.32		300	Chemical alloying + SPS	2009	[388]
	Polycrystalline n-type Bi₂Te₃ nanopart.	015 texture	300-500	1.15·10⁵		-117		1.57		0.94		0.50 (max ~ 0.68 at 423 K)		298	Chemical alloying + SPS	2011	[389]
	Polycrystalline n-type Bi₂Te₃ nanopart.	-	1200	0.83·10⁵		-150		1.87		1.23		0.46		300	Chemical alloying + Hot pressing	2005	[390]
	Polycrystalline n-type Bi₂Te₃ nanopart.	015 texture	20	0.83·10⁵		-176		2.50		2		0.38		300	Chemical alloying + FAST	2013	[391]
	Polycrystalline n-type Bi₂.₄₂Te₂.₅₈ nano-platellets	015 texture	= 500 900 Thickness = 15	1.54·10²		-135		0.28·10⁻²		0.27		0.003		298	Chemical alloying + pressing	2017	[392]
	Polycrystalline n-type Bi₂Te₃ nanostring	015 texture	= 20 - 50 L = 500	5.08·10²		-172		0.15·10⁻¹		0.29		0.015		298	Hydrothermal method + SPS	2010	[393]

	Sample	Crystal growth direction	Diameter, d /Length, L (nm)	$\sigma_{mix\parallel c}$ $_{and\perp c}$ (S/m)	$S_{mix\parallel c}$ $_{and\perp c}$ (μV/K)	$PF_{mix\parallel c}$ $_{and\perp c}$ (mW/mK^2)	$\kappa_{mix\parallel c}$ $_{and\perp c}$ (W/mK)	$zT_{mix\parallel c}$ $_{and\perp c}$	T (K)	Growth technique	Year	Ref
	Polycrystalline n-type Bi_2Te_3 nanoflowers	015 texture	L = 300 Thickness = 10 - 30	$3.64 \cdot 10^4$	-154	0.86	~ 0.53	0.70	453	Hydrothermal method + pressing	2012	[394]
	n-type Bi_2Te_3 nanotubes + powder	015	d = 30 - 100 L > 1000	$1.30 \cdot 10^5$	-130	0.22	1.00	0.70 (max ~ 1.1 at 450 K)	300	Hydroth. method + Milling + Hot pressing	2005	[395]
	Single crystal n-type Bi_2Te_3 nanorods	015	d = 27 – 80 L= 210 - 520	$6.00 \cdot 10^2$	-100	$0.60 \cdot 10^{-2}$	-	-	298	Wet chemical synthesis	2006	[396]
Nanocomposite	Polycrystalline n-type Bi_2Te_3 nanorods + graphene oxide	015 texture	d = 408 L = 2400	$0.42 \cdot 10^4$	-187	0.15	0.15	0.29	298	Hydrothermal synthesis + annealing	2019	[397]
	Polycrystalline n-type Bi_2Te_3 nanowires + graphene	015 texture	d = 15 L = 1000	$2.84 \cdot 10^4$	-132	0.49	0.7	0.21	300	Wet chemical synthesis + sinitering	2015	[398]
	Polycrystalline n-type Bi_2Te_3 nanowires + graphene	015 texture	d = 15-20 L = 1000	$2.15 \cdot 10^4$	-180	0.70	0.5	0.41	300	Wet chemical synthesis + sinitering	2016	[399]
	Polycrystalline n-type Bi_2Te_3 + graphene quantum dots	015 texture	-	$4.10 \cdot 10^4$	-147	0.89	0.69	0.55	425	Wet chemical synthesis + SPS	2017	[400]
	Poly-crystalline n-type Bi_2Te_3 powder + grahene	015 texture	100 - 1000	$2.65 \cdot 10^4$	-154	0.63	0.56	0.33	300	Ball milling + sintering	2016	[399]

	Sample	Crystal growth direction	Thickness (nm)	$\sigma_{\parallel c}$	$\sigma_{\perp c}$ (S/m)	$S_{\parallel c}$	$S_{\perp c}$ (µV/K)	$PF_{\parallel c}$	$PF_{\perp c}$ (mW/mK²)	$\kappa_{\parallel c}$	$\kappa_{\perp c}$ (W/mK)	$ZT_{\parallel c}$	$ZT_{\perp c}$	T (K)	Growth techniq.	Year	Ref
Films	Single crystal n-type Bi$_2$Te$_3$	001	1000	-	1.10·10^5	-	-167	-	2.80	-	1.87	-	0.45	300	MBE	2006	[401]
	Single crystal n-type Bi$_2$Te$_3$	001	1000	-	5.32·10^4	-	-208	-	2.30	-	-	-	-	300	Co-evaporat.	2008	[402]
	Single crysta n-type Bi$_2$Te$_3$	110	4500 ± 300	6.7·10^4	3.2·10^5	-58	-50	0.23	0.80	1.2	2.4	0.06	0.10	300	Electro-deposition	2016	[380]
	Polycrystall. n-ty pe Bi$_2$Te$_3$	001	1000	-	5.49·10^4	-	-128	-	0.90	-	-	-	-	300	Co-sputt.	2006	[403]
	Polycrystall. n-type Bi$_{2.17}$Te$_{2.83}$	110	2000-3000	6.91·10^4	-	-146	-	1.47	-	-	-	-	-	300	Electro-deposition	2016	[404]
	Poly-crystall. n-type Bi$_2$Te$_3$	110	600·10^3	4.00·10^4	-	-200	-	1.60	-	-	-	-	-	300	Electro-deposition	2016	[405]
	Polycrystall. n-type Bi$_2$Te$_3$	001	700	-	7.69·10^4	-	-228	-	3.99	-	-	-	-	300	Co-evaporat.	2002	[406]
	Polycrystall. n-type Bi$_2$Te$_3$	001	-	-	1.11·10^5	-	-210	-	4.90	-	-	-	-	300	MOCVD	1999	[407]
	Polycrystall. n-type Bi$_2$Te$_3$	001	800-1200	-	7.50·10^4	-	-150	-	1.69	-	-	-	-	300	Sputt.	2020	[408]
	Polycrystall. n-type Bi$_2$Te$_3$	001	20·10^3	-	2.45·10^5	-	- 40	-	0.39	-	-	-	-	300	Sputt.	2016	[409]
	Polycrystall. n-type Bi$_3$Te$_1$	001	300	~7.70·10^3	~4.00·10^4	~-116	~-123	~0.11	~0.62	-	-	-	-	300	Sputt.	2017	[410]
	Polycrystall. n-type Bi$_1$Te$_3$	0015	700	-	7.69·10^4	-	-226	-	3.99	-	-	-	-	300	Co-evapor.	2001	[411]
	Polycrystall. p-type Bi$_1$Te$_2$	0015	720	-	3.12·10^5	-	80	-	2.05	-	-	-	-	300	Co-evapor.	2001	[411]

	Sample	Crysal growth direction	Thickness (nm)	$\sigma_{mix\,\parallel c\,and\,\perp c}$ (S/m)	$S_{mix\,\parallel c\,and\,\perp c}$ (µV/K)	$PF_{mix\,\parallel c\,and\,\perp c}$ (mW/mK²)	$\kappa_{mix\,\parallel c\,and\,\perp c}$ (W/mK)	$zT_{mix\,\parallel c\,and\,\perp c}$	T (K)	Growth techni.	Year	Ref
Films	Polycrystalline n-type Bi$_2$Te$_3$ (Te rich)	-	20·10^3	6.10·10^4	-160	1.57	-	-	300	Co-evaporat.	2004	[412]
	Polycrystalline n-type Bi$_2$Te$_3$	006/015	350 ± 5	7.10·10^4	-75	0.40	-	-	300	Sputt.	2009	[413]

	Sample	Crysal growth direct.	Thickness (nm)	$\sigma_{mix\parallel c\ and\perp c}$ (S/m)	$S_{mix\parallel c\ and\perp c}$ (µV/K)	$PF_{mix\parallel c\ and\perp c}$ (mW/mK^2)	$\kappa_{mix\parallel c\ and\perp c}$ (W/mK)	$zT_{mix\parallel c\ and\perp c}$	T (K)	Growth techni.	Year	Ref
Films	Polycrystall. n-type Bi$_2$Te$_3$	-	10 000	$1.20\cdot10^5$	-80	0.86	-	-	300	Electro-deposition	2010	[414]
	Polycrystall. n-type Bi$_{2.17}$Te$_{2.83}$	006/015	1500	$1.84\cdot10^5$	-70	0.88	-	-	300	Sputtering	2011	[415]
	Polycrystall. n-type Bi$_2$Te$_3$	015	$20\cdot10^3$	~ $7.00\cdot10^4$	~ -55	~ 0.20	-	-	300	Sputtering	2016	[409]
	Polycrystall. n-type Bi$_2$Te$_3$	-	1000	~ $3.80\cdot10^4$	~ -90	0.31	-	-	300	Sputtering	2018	[416]

	Sample	Crystal growth direction	Thickness (nm)	$\sigma_{\parallel c}$	$\sigma_{\perp c}$ (S/m)	$S_{\parallel c}$	$S_{\perp c}$ (µV/K)	$PF_{\parallel c}$	$PF_{\perp c}$ (mW/mK^2)	$\kappa_{\parallel c}$	$\kappa_{\perp c}$ (W/mK)	$ZT_{\parallel c}$	$ZT_{\perp c}$	T (K)	Growth techniq.	Year	Ref
Nanowires	p-type Bi$_2$Te$_3$	110	$d=40$ nm $L_{NW}=15$ µm	-	~ $4.17\cdot10^4$	-	13	-	~ $0.62\cdot10^{-2}$	-	-	-	-	300	Electro-deposit.	2008	[417]
	Single crystal n-type Bi$_1$Te$_1$	110	$d=81$ nm	-	~ $5.00\cdot10^4$	-	-30	-	~ $0.45\cdot10^{-1}$	-	1	-	0.01	300	Electro-deposit.	2005	[418]
	Single crystal n-type Bi$_2$Te$_3$	100	$d=$ 50-55 nm	-	~ $2.15\cdot10^5$	~ -70	~ -50	-	0.58	1.4	3.0	-	0.06	300	Electro-deposit.	2009	[419]
	n-type Bi$_2$Te$_3$	110	$d=64$ nm	-	$2.20\cdot10^4$	-	-120	-	0.32	-	-	-	-	300	VLS	2013	[420]
	n-type Bi$_2$Te$_3$	110	$d=280$ nm $L_{NW}=12.5$ µm	-	$1.30\cdot10^5$	-	-41	-	0.22	-	0.9	-	0.08	300	Electro-deposit.	2014	[421]
			$d=187$ nm $L_{NW}=11.3$ µm	-	$2.30\cdot10^5$	-	-45	-	0.47	-	2.0	-	0.07				

	Sample	Crystal growth Direct.	Thickness (nm)	$\sigma_{\parallel c}$	$\sigma_{\perp c}$ (S/m)	$S_{\parallel c}$	$S_{\perp c}$ (µV/K)	$PF_{\parallel c}$	$PF_{\perp c}$ (mW/mK²)	$\kappa_{\parallel c}$	$\kappa_{\perp c}$ (W/mK)	$ZT_{\parallel c}$	$ZT_{\perp c}$	T (K)	Growth techniq.	Year	Ref
Nanowires	n-type Bi$_2$Te$_3$	110	d = 67 nm L_{NW} = 15 µm	-	2.00·10^5	-	-98	-	1.90	-	2.6	-	0.22	300	Electro-deposit.	2014	[422]
	n-type Bi$_2$Te$_3$	110	d = 75 nm L_{NW} = 15 µm	-	7.50·10^4	-	-143	-	1.50	-	1.4	-	0.32		Electro-deposit.	2014	[422]
	n-type Bi$_2$Te$_3$	110	d = 120 nm L_{NW} = 20 µm	-	2.30·10^5	-	-65	-	0.97	-	0.75	-	0.45 (0.90)	300 (350)	Electro-deposit.	2010	[414]
	Sample	Crysal growth direct.	Thickness (nm)	$\sigma_{mix\,\parallel c\;and\perp c}$ (S/m)		$S_{mix\,\parallel c\;and\perp c}$ (µV/K)		$PF_{mix\,\parallel c\;and\perp c}$ (mW/mK²)		$\kappa_{mix\,\parallel c\;and\perp c}$ (W/mK)		$zT_{mix\,\parallel c\;and\perp c}$		T (K)	Growth techni.	Year	Ref
	n-type Bi$_2$Te$_3$	-	d = 50 nm L_{NW} = 25 µm	1.69·10^5		-53		0.47		-		-		300	Electro-deposit.	2010	[423]

♦ The given values corresponding to the direction parallel to the c-axis were calculated from the experimental measurements performed along the perpendicular direction to the c-axis in [381].

SPS spark plasma sintering
FAST field-assisted sintering
VLS vapour-liquid-solid method
MBE Molecular beam epitaxy
MOCVD metal-organic chemical vapour deposition

There has been intensive work looking for ways to increase its figure of merit above the reported value for the material in bulk. In Table 5.1, the thermoelectric properties for nanostructured bismuth telluride in the form of nanoparticles, thin films, nanowires, nanorods, among others, are collected and compared to the actual values of the bulk material and nanocomposite bulk Bi$_2$Te$_3$. A common fact was observed when analysing the effect of nanostructuration (regardless of the final shape) over the thermal conductivity of Bi$_2$Te$_3$, which in all cases results in a significant reduction of this parameter compared to bulk.

5.2. Growth of Bi$_2$Te$_3$ via electrochemical deposition

As has been discussed above, bulk Bi$_2$Te$_3$ is a good thermoelectric material with certain crystal anisotropy. Hence, its thermoelectric properties vary depending on the crystal orientation [379, 380]. As it has been previously

reported by C. V. Manzano *et al.* [240, 380, 424], when fabricated by electrochemical deposition, the quality, and crystal structure of the material can be controlled as desired through an optimization of the electrodeposition parameters.

In particular, pulsed electrodeposition favours a more homogenous growth with smaller grain sizes, as the process is switched off for the duration of the pulsed applied at zero current density. During this zero current density time, the system is left to rest, after ions are deposited and removed from the solution at the WE-electrolyte interface, and recovered, as the chemical species at the electrode interface are replaced by new ones that diffuse or migrate from other parts of the solution. Whereas, when the process is turned back on for the application of the potentionstatic pulses, the deposition potential determines, to a large extent, the crystal orientation of the deposited grains. Other important parameters to consider that were also investigated in this thesis are the temperature at which the deposition of the material is carried and the influence of the substrate. Even though the electrochemical conditions for the growth of Bi_2Te_3 in the form of films and 1D nanowires were previously evaluated in the literature [34, 240, 414, 417, 425-428], there is no report on the growth of 3D nano-networks (3DNNs) that employ transversally perforated 3D AAOs as templates. Due to the importance of the substrate, the deposition conditions of these networks can differ from what was previously established. In this regard, cyclic voltammetry curves help to localize the reduction and oxidation potentials of the ionic species in dissolution.

5.2.1. Cyclic voltammetry study

CVs measurements were performed on different working electrodes, consisting of a silicon substrate, and two different kinds of alumina templates (1D AAOs and 3D AAOs) evaporated with a layer of chromium (5 nm) and gold (150 m thickness), to evaluate the best deposition conditions of Bi_2Te_3 in the form of films, 1D nanowires, and 3D nanowire networks, respectively. The electrolyte solution was the same in all the cases, using 0.90×10^{-2} M Bi^{3+}, 1×10^{-2} M $HTeO_2^+$, and 1 M HNO_3. Cyclic voltammograms were carried out in the above-mentioned electrolyte solution, at 0 °C, with a scan rate of 10 mV·s^{-1} over a potential range between −1.0 to 1.0 V applied potential vs. Ag/AgCl in the case of gold over a silicon substrate, and −0.6 to 0.6 V applied potential vs. Ag/AgCl when 1D AAO and 3D AAO membranes were used as templates.

156
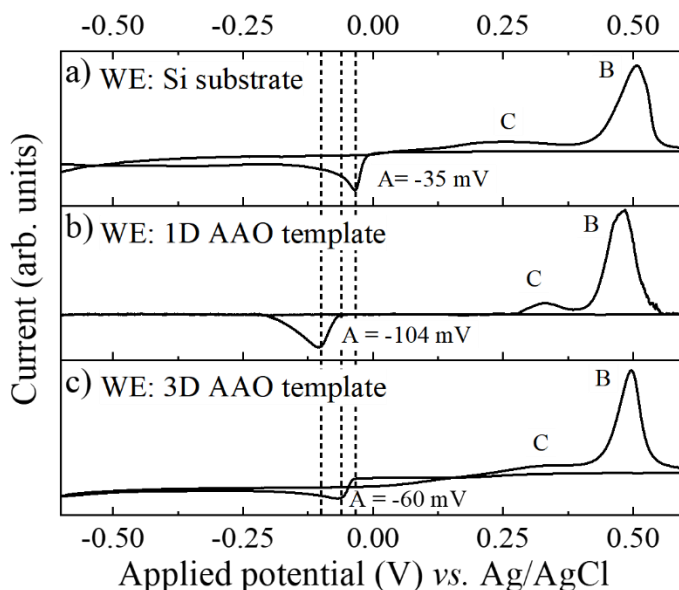
Figure 5.2. Cyclic voltammetries measured with three WE configurations: a) Si/Au substrate, b) 1D AAO/Au template and c) 3D AAO/Au template. From -0.6 to 0.6 V with a scan rate of 10 mV/s. the electrolyte consisted of 0.90×10^{-2} M Bi^{3+}, 1×10^{-2} M $HTeO_2^{+}$, and 1 M HNO_3 at 0 °C

In all cases (see Figure 5.2a, 5.2b, and 5.2c), three peaks could be identified, labeled as *A*, *B*, and *C*. Peaks *A* and *B* are associated with the direct reduction potential of $Bi^{3+}/HTeO_2^{+}$ to form Bi_2Te_3 and the reversible oxidation reaction and dissolution of Bi_2Te_3, respectively. Meanwhile, the smaller peak *C* has been assigned as a minor oxidation side reaction of Bi^{3+} to Bi [429]. Focusing on the reduction peak *A* of $Bi^{3+}/HTeO_2^{+}$ species, around which deposition occurs, a displacement of this peak is observed depending on the type of WE used. If, the material is grown as a film over a silicon substrate, the reduction of $Bi^{3+}/HTeO_2^{+}$ species takes place at a negative potential of -35 mV (corresponding to peak *A* in Figure 5. 2a). When 1D AAO is employed as WE, the reduction peak reaches the highest negative values (> -100 mV), see Figure 5.2b. This could be due to the hampered migration of ions along the narrow porous structure (45-55 nm diameter pores) of such membranes before reaching the Au layer at the bottom side of the template, where deposition starts. However, when a 3D AAO is used as a working electrode, the reduction peak appears at an intermediate voltage value of around −60 mV, (peak *A* in Figure 5.2c). Taking into account that both templates, 1D AAO and 3D AAO, have the same pore diameter for the longitudinal pores, that is, 45-55 nm, it has to be the presence of the transversal nanochannels in our 3D AAO

membranes that facilitates the migration of the ions through this kind of alumina matrix. As a consequence, the reduction of the species in dissolution takes place at a less negative potential than the voltage at which the reduction peak of $Bi^{3+}/HTeO_2^+$ species appears when using conventional 1D AAO templates.
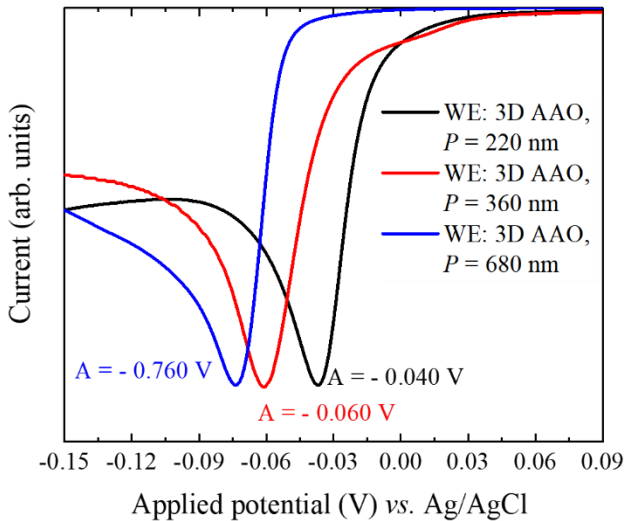
Figure 5.3. Cyclic voltammetry curves performed over a three different 3DAAO templates: 3DAAO220 (black curve) characterized by P = 220 in nm, 3DAAO350 (red curved) corresponding to P = 350 nm and 3DAAO540 (blue curved) with P = 680 nm.

It is worth mentioning that the position of the reduction peak *A* on 3D AAO templates could experience some displacement in the range of -100 to -35 mV, marked by the other two substrates, depending on the distance between the transversal pores in the alumina, *P*. The CV showing a reduction peak at -60 mV, Figure 5.3, was performed on a 3D alumina characterized by a *P* distance of around 350 nm. As *P* is increased to 680 nm, the reduction potential shifts towards smaller (more negative) voltages around -0.70 V. On the contrary, if *P* is reduced (*P* = 220 nm) the peak moves towards higher (less negative) potentials to a value that is close to -35 mV, which corresponds to the reduction potential of $Bi^{3+}/HTeO_2^+$ species on a Si substrate. Figure 5.5 shows a zoom around the reduction peak for three different 3D AAOs with *P* = 220 (black curve), 350 (red), and 680 nm (blue line), which better illustrates the displacement of the peak as a function of *P*. This corroborates our hypothesis that ion migration is favored across such perforated membranes compared to regular 1D AAOs. Moreover, it indicates that reducing the distance *P* further

enhances this migration and that it could be hindered if the transverse channels are set too far apart.

5.2.2. Pulsed electrodeposition

5.2.2.1. Deposition potential

During pulsed electrodeposition, the conditions are switched between potentiostatic and galvanostatic modes. The latter consists of applying a zero current while the former is performed at a certain voltage. The deposition potential employed at the potentiostatic pulses is one of the most important parameters that influence the proportion in which Bi and Te are present in the alloy (that is, the final composition) as well as the crystal growth direction of the material.

As explained in section 5.2.1, voltammetry measurements allow identifying the simultaneous reduction potential of Bi^{3+} and $HTeO_2^+$ species, which narrows down the voltage range to obtain Bi_2Te_3. Accordingly, to find the optimum deposition potential, pulsed electrodeposition was carried out at several voltages around this peak while other deposition parameters such as the deposition temperature, and the duration of the potentiostatic (*time on*, t_{on}) and galvanostatic (*time off*, t_{off}) pulses, were fixed. Samples were grown by pulsed electrodeposition using a *time on* of $t_{on} = 1$s for the potentiostatic pulse and a $t_{off} = 0.1$ s (*time off*) while pulsing at zero current density. The *time on/time off* ratio was maintained at 10. The temperature of the electrolyte was kept at 2 °C.

Experiments were first performed over a Si substrate, cut in small pieces of several centimeters in size. Up to four different samples were grown under different voltages. The deposition potential was varied from a negative value of - 20 mV (site 1), towards positive and higher voltages of 15, 40, and 50 mV, corresponding to sites 3, 4, and 5. EDX and XRD analysis of the samples, as recorded in table 5.3, show the evolution of the composition and crystal structure of the bismuth telluride films with the applied deposition voltage. It was observed that at a negative deposition potential of - 0.020 V, close to the reduction peak located at - 0.035 V, the film is Bismuth rich with a polycrystalline structure and preferably oriented along the (015) direction. Applying a positive voltage of 0.015 V, the Bi excess is reduced and the preferred crystal direction stops being the (015), starting to switch towards the (110) crystal plane. As the deposition voltage is increased in the range of 0.04

to 0.05 V, the obtained films present the desired stoichiometry, corresponding to a Bi/Te ratio of 2/3. In these films, the crystal growth is aligned to the (110) direction, which is perpendicular to the c-axis of the Bi_2Te_3 crystal structure and, hence, the c-axis lies in the substrate plane. While the presence of the (015) peak in the films is almost negligible. As we saw in section 5.1.2, for bismuth telluride, the direction perpendicular to the c-axis is associated with the best thermoelectric performance (see Table 5.1), and therefore, it is the desired one for our applications.

Then, we reproduced these experiments on a 3D AAO membrane (evaporated with 5 nm Cr and 180 nm Au layers) as our working electrode. For that, we selected a 3D alumina template, characterized by a periodic distance between transversal pores of around 220 nm (P = 220 nm), cut in 5 smaller pieces (of a few mm^2 of size). As mentioned in the previous section 5.2.1., the substrate has a great influence on the electrodeposition process, altering the reduction voltage of the chemical species in dissolution. The reduction peak for this particular 3D AAO with P = 220 nm, labeled as 3DAAO220, (corresponding to a 3D AAO fabricated applying a t_{MA} = 180 s) is located in the range of – 30 to – 40 mV, which matches the reduction voltage (- 35 mV) of the Bi^{3+} and $HTeO_2^+$ species on the experiments performed over a Si substrate (Figure 5.2a.) so that both sets of experiments are comparable. Hence, depositions were performed employing similar voltages - 0.016, 0.003, 0.023, 0.037, and 0.055 V, associated with sites 1, 2, 3, 4, and 5 along the reduction peak in Figure 5.6.

EDX measurements of the resulting 3DNNs, also recorded in Table 5.2, reveal changes of the composition with the deposition potential, following the trend found for the deposit of films. At low voltages, Bi rich nanowires were produced. A Bi-rich phase, $Bi_{2.06}Te_{2.94}$, is obtained at 0.003 V (site-2) but the Bi excess, in this case, was less compared to the Bi content in a film grown at 0.015 V (site-3), even though the latter was grown at a more positive potential. At the next deposition voltage, 0.023 V (site-3) the nanowires are nearly stoichiometric in a Bi:Te ratio of 1.98:3.02. Then, as we move towards higher and more positive deposition potentials the desired 2:3 stoichiometry was achieved, site-4, corresponding to Bi_2Te_3 3DNN220 grown at 0.037V. Films deposited at 0.04 V (site-4) also possess this stoichiometry. In these experiments, the further increase of the deposition voltage up to 0.050 V did not produce any changes in the composition. However, for 3D nanowires fabricated at a similar potential, 0.055 V (site-5), the composition again

deviates from the desired stoichiometry (Bi:Te = 2:3) and the obtained 3DNN220 were tellurium rich, $Bi_{1.88}Te_{3.12}$.

Table 5.2. Fabrication parameters, structural and chemical characterization of Bi/Te thin films, and 3D Bi/Te nanowire networks fabricated by pulsed deposition.

WE: Si (100) wafer	Applied voltage (V)	Difference applied voltage, ΔV (mV)	Composition	Bi/Te ratio	Texture coefficient ($TC_{(hkl)}$) (hkl)				Growth rate (nm/min)
					(015)	(110)	(205)	(125)	
Site-1	-0.020	15	$Bi_{2.31}Te_{2.69}$	2/2.3	2.16	0.96	0.00	0.89	20
Site-3	0.015	50	$Bi_{2.13}Te_{2.87}$	2/2.7	0.83	1.67	0.85	0.65	22
Site-4	0.040	75	$Bi_{1.99}Te_{3.01}$	2/3	0.20	3.80	0.00	0.00	24
Site-5	0.050	85	$Bi_{2.00}Te_{3.00}$	2/3	0.09	3.91	0.00	0.00	15

WE: 3D AAO220	Applied voltage (V)	Difference applied voltage, ΔV (mV)	Composition	Bi/Te ratio	Texture coefficient ($TC_{(hkl)}$) (hkl)		Growth rate (nm/min)
					(110)	(300)	
Site-1	-0.016	15	-	-	0.62	1.38	33
Site-2	0.003	30	$Bi_{2.06}Te_{2.94}$	2/2.8	0.79	1.21	32
Site-3	0.023	60	$Bi_{1.98}Te_{3.02}$	2/3	1.48	0.52	27
Site-4	0.037	76	$Bi_{2.00}Te_{3.00}$	2/3	1.91	0.09	16
Site-5	0.055	90	$Bi_{1.88}Te_{3.12}$	2/3.3	1.17	0.83	18

Regarding the crystal structure of Bi_2Te_3 in the form of 3D nano-networks, XRD diffractograms only showed two peaks, associated with the (110) and (300) directions. But none of the other crystal orientations that were present in some of the films (sites1 and 3), such as the (015), (205), and (125), could be found. Considering that the deposition conditions at sites 1 and 3 are analogous on both sets of experiments, the only difference arises from the shape with which the material is grown as a film, extending in the in-plane direction to the cm scale, or as nanowires, where the dimensions of the material in the in-plane direction are constricted to the nanoscale. It seems as if in such low dimensional systems the material planes of Bi and Te prefer to align parallel to the nanowires long axis. While in the case of films these planes can be easily disposed of in the plane of the substrate. More in detail, the texture coefficient shows an evolution with the applied voltage. Nanowires are preferably oriented along the (300) direction at -0.016 and 0.003 V,

switching to the (110) above those potentials. In particular, nanowires are almost fully aligned in the (110), according to its T_{Chkl}, at site-4.
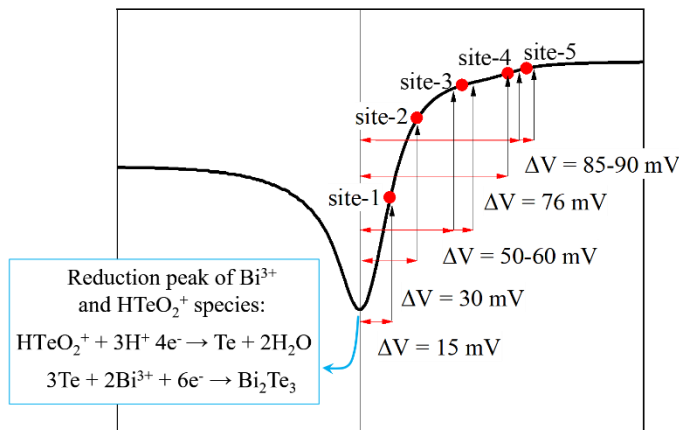
Figure 5.4. Here the different applied potentials at which the samples were deposited are shown as a difference potential, ΔV, with respect to the reduction peak, to determine the position at which they are placed in the CV.

Due to slight changes in the position of the reduction peak, a more accurate way to refer to the deposition potential is as a difference potential ΔV, which stands for the difference between the applied potential (V) and the minimum of the reduction peak in the CV (E_{pc}, in Figure 2.5). Accordingly,

$$\Delta V = V - E_{pc} \qquad (5.1)$$

Using ΔV fixes the ''distance'' at which the deposition takes place from the reduction potential. Then, applying this formula we calculated the distance from the reduction peak (-0.035 V) at which electrodeposition was performed when films were grown under - 0.020, 0.015, 0.04, and 0.05 V. Giving as a result, ΔV of 15, 50, 75, and 85 mV, respectively. In the case of the 3D nano-networks, electrodeposition was carried out at $\Delta V = 15, 30, 60, 76$ and 90 mV, corresponding to an applied voltage, V, of - 0.016 (E_{pc} = -0.031 V), 0.003 (E_{pc} = -0.027 V), 0.023 (E_{pc} = -0.038 V), 0.037 (E_{pc} = -0.039 V) and 0.055 V (E_{pc} = -0.035 V). Figure 5.4 illustrates the position of sites 1-5 around the reduction peak of Bi^{3+} and $HTeO_2^+$ species, as a function of the ΔV potential.

To conclude, we point towards fixing the ΔV at $\Delta V = 76$ mV, which corresponds to the 3DNN220 sample grown at 0.037 V (site-4) showing 2:3 (Bi:Te) stoichiometry and where the Bi and Te layers are fully aligned to the

(110) plane of Bi_2Te_3, with the *c*-axis perpendicular to the length of the longitudinal nanowires in the 3D network.

5.2.2.2. Substrate

In this work, we have employed three different 3D AAO membranes that were fabricated applying t_{MA} pulses of 180, 240, and 540 s. The resulting Bi_2Te_3 3DNNs were characterized by three different periods, *P*, or distance between transverse connections, TCs, of 220, 350, and 680 nm, respectively.

As it has been established from the cyclic voltammetry study presented in section 5.2.1., the type of template that is employed as WE modifies the reduction potential and thus, the optimal deposition voltage for the formation of Bi_2Te_3. This also applies to variations in the transversal channel distance, *P*, of the 3D AAO templates. In Figure 5.3, the displacement of the reduction peak can be observed, moving from around - 0.040V associated to $P = 220$ nm, to a more negative potential of – 0.055 V for a 3D AAO with $P = 350$ nm and if the period of the template is further increased, $P = 680$ nm, the reduction peak is located around -0.070 V. In this situation, we have found that using the same difference potential, previously established at $\Delta V = 76$ mV (from the reduction peak), works for the different 3D AAO templates employed in this thesis. Then, according to *equation 5.1,* we can know the actual voltage that we need to apply in each case, giving a voltage of 40, 20 and below 10 mV for the growth of 3DNN220, 3DNN350, and 3DNN680 samples, respectively.

Moreover, these experiments demonstrate that this ΔV potential (76 mV) could be applied to obtain highly oriented Bi_2Te_3 3DNNs, while having a certain margin of flexibility to introduce changes in the other parameters, such as the WE nature (3D AAO with different $P = 220$, 350 or 680 nm).

5.3. Morphological, compositional, and structural characterization of Bismuth telluride 3DNNs: 3DNN180, 3DNN360, and 3DNN540.

In this section, we will focus on the 3DNN samples (3DNN220, 3DNN350, and 3DNN680) grown at the optimized $\Delta V = 76$ mV, as described in section 5.2.2.2. Here, a more detailed analysis of the morphology and

geometry, chemical composition, and crystal structure of these 3D nanostructures would be provided.

5.3.1. Morphological characterization

Volume skeletonization

Volumen rendering

3D reconstruction
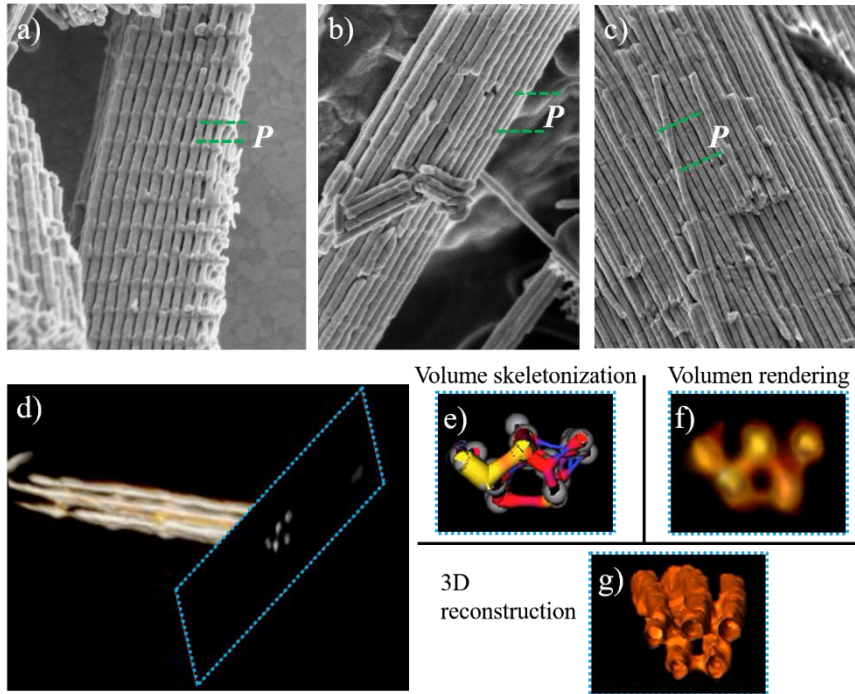
Figure 5.5. SEM micrographs of suspended a) 3DNN220 (P = 220 nm), b) 3DNN350 (P = 350 nm) and c) 3DNN680 (P = 680 nm). d)-g) TEM tomography of sample 3DNN180. d) 2D TEM image of a bunch of interconnected nanowires. The blue dotted rectangle shows the last transversal cut of the nanowires in d), made to that point to build the 3D illustrative images in e), f), and g). e) Represents the volume skeletonization, while f) is the volume rendering of e). And g) corresponds to the fully 3D reconstruction of d).

i)   SEM and TEM

Once the alumina templates were dissolved, SEM images and TEM topographies were taken to further analyse the morphology of the 3DNNs, as shown in Figure 5.5. The removal of the alumina membrane was performed in chromic acid. Then, the nanostructures were filtered, following the procedure described in section 2.1.4.1. The free-standing 3DNNs were kept in an ethanol suspension, which was sonicated for several minutes. Then, a few drops of the nanowires suspension were cast over TEM grids for their observation under SEM. The images reveal that nanowires are still connected

and preserve the order even after sonication, which demonstrates the high mechanical stability of the 3DNNs without the AAO template when compared to conventional 1D nanowires.

Figure 5.5. shows the 3D architecture of the nano-networks (3DNNs), which is defined by the periodic distance between transverse connections (TCs), *P,* and that can be tuned during the fabrication process of the 3D AAO templates (see section 2.1.1.2). Samples 3DNN220, 3DNN350, and 3DNN680, shown in Figure 5.5.a, 5.5b. and 5.5c., are labeled after this parameter. *P* was measured from cross-view SEM images of the 3D nano-networks, obtaining a *P* equal to 220, 350, and 680 nm, respectively. From these images, the precise dimensions of the TCs, as well as the total length of the longitudinal nanowires were also characterized. The diameter of the nanowires was analysed from top-view images of the samples, after mechanical polishing one of their sides (normally, the side covered with Au). All these parameters are recorded in Table 5.3. We must keep in mind that first, the synthesis method and then, how they are measured, introduce an error to the diameter of the nanowires and dimensions of the transversal connections. Therefore, the values given in Table 5.3 are an average value from statistical analysis of many different images, with an error of ±5 nm in the diameter of nanowires and TCs, ±10-30 nm *P*, and in the order of tens of µm length.

Table 5.3. *Dimensions of the Bi$_2$Te$_3$ 3DNNs grown in this chapter.*

Sample name	Nanowire diameter, ϕ (nm)	Distance between neighbour Nws, D_{int} (nm)	Distance between transversal connection, P (nm)	Dimensions of the transverse connections, L_{TC}		Nanowire length, L_{NW} (µm)
				Long length (nm)	Short length (nm)	
3DNN540	52	64	220	35-40	15-20	11.2
3DNN360	53	64	350	35-40	15-20	11.2
3DNN180	54	61	680	35-40	15-20	12.8

Furthermore, a 3D reconstructed image was built from 2D TEM images, as described in detail in section 2.2.4.1., employing TEM tomography. Figure 5.5d. shows a 2D TEM image of a bunch of dissolved interconnected wires. The dotted blue rectangle illustrates one transversal cut across its length at that specific location. Figure 5.5e is the volume of the skeleton of the structure obtained from the reconstruction of the transversal cuts made along the whole length of the nanowires. Figure 5.5f corresponds to the volume rendering of the skeleton in Figure 5.5e. In Figure 5.5g, the 3D reconstruction

of the interconnected nano-networks is taking place, stopping at the position indicated with the blue rectangle. These reconstructions show the 3D connections of the longitudinal nanowires and the different diameters, which match those found in the SEM images.

5.3.2. Compositional analysis

i)   Energy dispersive X-ray spectroscopy (EDX)

EDX analysis was performed to determine the Bi and Te percentage in each sample. To obtain reliable results, measurements were taken in different areas along a cross-sectional cut of the 3DNNs still embedded in the alumina matrix. The conditions employed during the measurements are listed in section 2.2.3.

The Bi:Te ratio as a function of the applied ΔV potential during deposition was investigated, when looking for the optimization of the growth conditions (section 5.2.). In all the experiments, the Bi to Te ratio was found to be 2:3 for $\Delta V = 76$ mV, regardless of any of the other deposition factors such as the transverse channels distance, P, of the 3D AAO template.

ii)   Raman spectroscopy
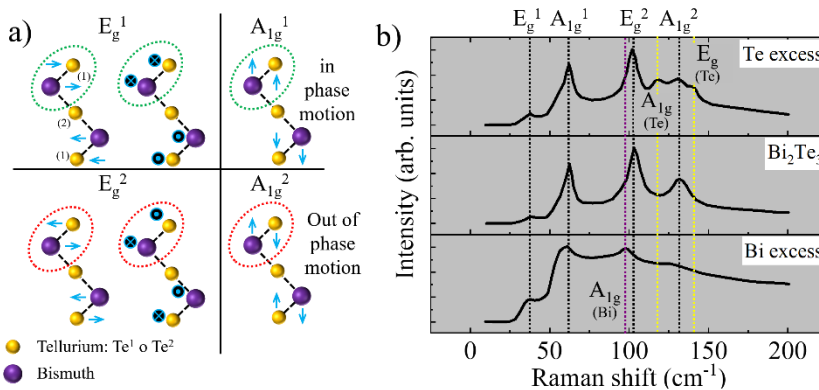
Figure 5.6. *a) Characteristic Raman vibrational modes of Bi_2Te_3. b) Representative Raman spectra of 3DNNs containing Bi excess (bottom), 2:3 Bi to Te ratio (middle), and Te excess (top).*

Raman spectroscopy has proved to be a useful tool to identify the presence of certain chemical species as they vibrate (Raman active vibrational modes) when excited. In particular, it has been previously employed to study the

layered structure of Bi_2Te_3 [430-432]. Furthermore, this technique is particularly useful in detecting the presence of Te nano-clusters in Bi_2Te_3 nanowires and nanoparticles [433, 434].

For simplification, considering the primitive unit cell of the Bi_2Te_3 crystal layered structure (Figure 5.1a) consisting of 5 atoms in the sequence: - (Te^1 – Bi – Te^2 – Bi – Te^1) -, along the c-axis, there are four active Raman modes, E_g^1, A_{1g}^1, E_g^2, and A_{1g}^2, associated to the vibration of the Bi – Te(1 or 2) bonds. Figure 5.6a illustrates how the different bonds vibrate. E_g and A_g modes are differentiated by the motion of atoms in the direction perpendicular and parallel to the c-axis, respectively.

Furthermore, the letter A means that the vibration is singly degenerated, whereas E means that is doubly degenerated. Apart from those distinctions, E_g^1, and A_{1g}^1 modes, in particular, correspond to the in-phase vibration of the Bi-Te^1 bond. Thus, the bond between Bi-Te^2 governs the frequency of E_g^1 and A_{1g}. In the other two, E_g^2 and A_{1g}^2, Bi and Te^1 atoms move in opposite phases. In such a case, the force of the Bi-Te^1 bond will determine the vibration frequency. The frequencies of the Raman active modes for the Bi_2Te_3 binary alloy as well as those corresponding solely to Bi and Te are provided in Table 5.4.

Table 5.4. Comparison of vibrational Raman modes corresponding to Bi_2Te_3, Bi, and Te.

Sample	Raman vibrational modes (cm^{-1})				Ref.
	E_g^1	A_{1g}^1	E_g^2	A_{1g}^2	
Bulk single crystal Bi_2Te_3	36.50	62.50	102	134	[430]
Bi_2Te_3 1D NW		57.80	100.50	127.60	[433]
Bi_2Te_3 3D NNs	37.05	62.61	103.09	130.85	This work
	E	**A$_{1g}$**		**E$_g$**	
Tellurium films	91.30	119.70		139.50	[435]
Tellurium thin films	88	117		137	[433]
	A$_{1g}$		**E$_g$**		
Bismuth films	65		97		[434]

In Figure 5.6b, 3D nano-networks with an excess of Te and Bi are compared to a 3D network with 2:3 (Bi:Te) stoichiometry. In the latter case,

four Raman peaks were observed at 37, 63, 103, and 130cm^{-1}, which are related to the four characteristic vibrational modes of Bi$_2$Te$_3$, $E_g{}^1$, $A_{1g}{}^1$, $E_g{}^{2,}$ and $A_{1g}{}^2$, respectively. When the sample was prepared with Bi excess, the peak located at 102 cm^{-1}, shifts towards 97 cm^{-1}, corresponding to the E_g vibrational mode of Bi. The excess of Te in the 3D nano-network was identified by the presence of two extra peaks found at 119 and 140 cm^{-1} and that were associated with the A_{1g} and E_g vibrational modes of Tellurium. This technique was implemented to double-check the chemical composition of the 3D nanowire networks, complementing EDAX analysis.

5.3.3. Structural characterization

i)   X-Ray diffraction (XRD)

As stated in section 5.2., the evolution of the crystal structure of Bismuth telluride was evaluated while varying the following deposition parameters: the standardized ΔV potential, and the substrate, as described in sections 5.2.2.1 and 5.2.2.2¸ respectively.

Figure 5.7a shows the evolution of the crystal orientation of the 3DNNs grown in a ΔV potential range from 15-90 mV. 3D nano-networks present only two possible orientations the (110) and (300). The XRD diffractogram of the sample grown at $\Delta V = 76$ mV, suggests an almost single-crystal nature, almost fully aligned to the (110). Above and below this ΔV potential there is competition between the two crystal directions. Hence¸ the optimized deposition voltage corresponds to a standardized ΔV potential of 76 mV (with respect to the reduction peak), keeping the T$_{electrolyte}$ = 2 °C and t_{on} =1 s/ t_{off} = 0.1 s.

This is further proved in Figure 5.7b, showing the XRD diffractograms of the final three nano-networks, 3DNN220, 3DNN350, and 3DNN680. In all cases, the nanowires are mostly single crystal, oriented along the (110) direction. The crystallite size obtained from the X-Ray diffractograms in Figure 5.7b ranges between 35 and 40 nm, which is in the order of the size of the TnCs. Nevertheless, as it can be seen in Figure 5.9, t-EBDS measurements show that the 3D nanowire networks maintain the same orientation through hundreds of nanometers along the length of the longitudinal nanowires.
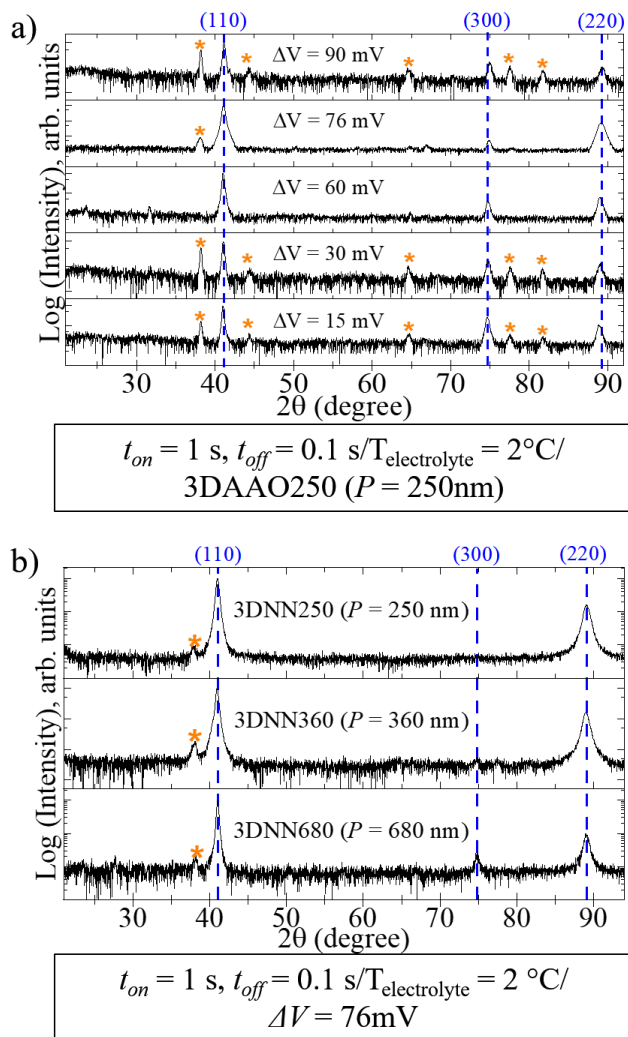
Figure 5.7. *XRD diffractograms taken while varying: a) the difference applied potential, ΔV, and b) the 3DAAO templates used as WE.*

ii)   TEM

TEM measurements in Figure 5.8, show quasi-epitaxial growth along the [110] with the *c*-axis perpendicular to the length of the nanowire, as indicated by the white arrows (Figure 5.8a), corroborating XRD results. Figure 5.8b is an enlarged image of Figure 5.8a where the red dashed lines separate quintuple layers, the yellow arrow follows the growth direction of the Te (in yellow) and Bi (purple balls) atoms, piling up along the nanowire axis. Figure 5.8c

corresponds to ⟨0001⟩ zone-axis high-resolution TEM (HRTEM) image, the value of the inter-planar spacing of the planes, d, was 0.22 nm, which is in good agreement with the d value of the (110) planes of rhombohedral Bi_2Te_3 [414, 417]. Furthermore, the SAED pattern inset of the area in Figure 5.8c, shows a hexagonal symmetry diffraction spot pattern, indicating the high crystal quality of the nanowires, that was indexed to the [110] direction.
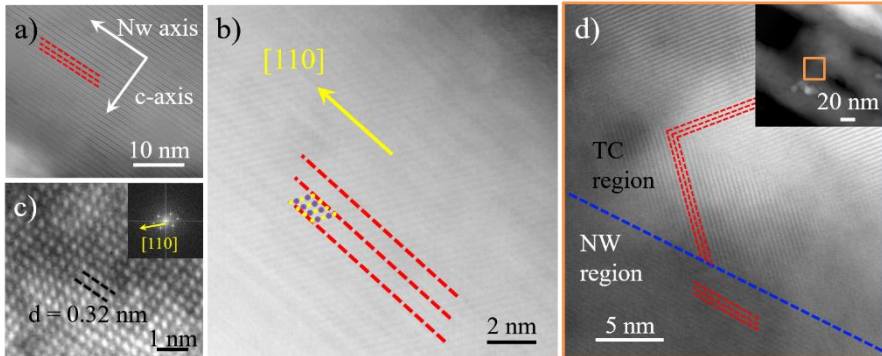
Figure 5.8. HR-TEM analysis of the dissolved sample 3DNN220. a) Image along the length of the nanowire of the 3DNN array. b) is an enlarged image of a), in which the red dotted lines indicate the separation between quintuple layers, and the atomic layers of Bi and Te can be distinguished. c) ⟨0001⟩ zone-axis HRTEM image showing an inter-planar distance of 0.22 nm. The inset image is the corresponding SAED pattern of c), illustrating a hexagonal pattern index to [110] direction, characteristic of single crystals. d) TEM analysis at the intersection between two neighbor wires in the network. The inset shows the intersection region without the zoom.

This technique allows us to study the crystal structure at the transverse connections, Figure 5.8d, where the preferred orientation was still [110] direction. More in detail, the zooming of the area inside the orange rectangle shows the formation a of 60 ° twin boundary, as indicated by the red dashed lines.

iii)   t-EBSD

Transmission electron backscattering diffraction was performed on samples, 3DNN220, 3DNN350, and 3DNN680 to which the XRD diffractograms in Figure 5.7d correspond. This technique has a higher resolution than conventional XRD, which allows us to evaluate if the 3D nanowires are truly single crystalline. Scans can be carried out over larger areas compared to other techniques with similar resolution (i.e. TEM), so statistical analysis can be done along the length of the nanowires covering up to several μm and exploring several nanowires at the same time.
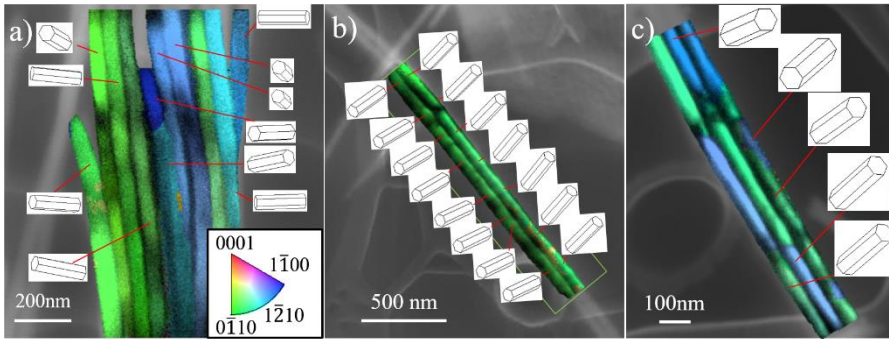
Figure 5.9. t-EBSD analysis along a) an isolated nanowire, b) two interconnected nanowires at every 220 nm (3DNN220) and c) three connected nanowires at every 680 nm (3DNN680). The color mapping indicates the crystal orientation of the nanowires, according to the color scale of the inset triangle.

Figure 5.9a shows a bunch of dissolved nanowires. In the inset, the coloured triangle is defined by the basal plane (0001), two contiguous primary prism planes ($0\bar{1}10$) and ($\bar{1}100$), and the secondary prismatic plane ($1\bar{2}10$), of the hexagonal unit cell of rhombohedral Bi_2Te_3 using Bravais-Miller index system. t-EBSD analysis was performed in the nanowire in the image individually, showing uniform crystal orientation along the analysed length (the crystal orientation was kept over up to 5µm), as indicated by a uniform color. The green and dark blue color correspond to the ($0\bar{1}10$) and ($\bar{1}100$) faces of the hexagonal prims, both equivalent to the (300) plane of rhombohedral Bi_2Te_3 that is measured in XRD, see Figure 5.7d. Whereas, the light blue color ascribes to the ($1\bar{2}10$) secondary face, which can be associated with the (110) plane of the crystal structure, and the strongest diffraction plane found in XRD and TEM. In all cases, the *c*-axis perpendicular is to the wires, as illustrated by the hexagonal prism laying down this axis, while the crystal growth rotates in the plane.

When analysing two interconnected nanowires with an intercanal distance of P = 220 nm (of a 3DNN220 sample) over a section of around 0.5 µm, Figure 5.9b, the crystal orientation is along ($0\bar{1}10$) plane in both the longitudinal wires and in the transverse canals, TCs. Other areas present, however, twin configuration alternating between ($0\bar{1}10$) and ($1\bar{2}10$) planes. This was observed in Figure 5.9c corresponding, in particular, to three interconnected nanowires at every 680 nm that switch color from green to light blue. Hence, we can conclude that some of the nanowires present a twined crystal structure formed by regions that can extend over several hundred nm

with crystal growth along the (300) or (110) planes. Then, at the boundary, we observed the formation of 60° twin boundaries. This type of boundary was reported to be the lowest in energy [436] and was also observed by TEM (Figure 5.8c). Interestingly, its formation seems to be favoured at the intersection between nanowires and TCs, whereas the nanowires segments between two consecutive TCs show uniform color distribution, indicating single crystal quality.

5.3.4. Summary of the morphological and structural characterization

SEM and TEM measurement provide enough experimental proof of the 3D architecture of the nanowire networks, in which longitudinal nanowires are transversely connected to their neighbours at a distance that we can choose.

Moreover, the deposition parameter was effectively optimized to obtain highly oriented nanowires and as desired chemical composition. EDAX measurements corroborate the 2:3 (Bi:Te) stoichiometry of the 3DNNs.

Then, XRD and TEM analysis of the crystal structure of Bi_2Te_3 3DNNs show that the samples are mostly composed of nearly single-crystal nanowires, some of which present twinning between the (110) and (300) planes, but maintaining the orientation over long lengths.

5.4.   Characterization of the thermoelectric properties of Bi_2Te_3 3D nano-networks

The thermoelectric properties of the 3DNNs consisting of Bi_2Te_3 highly oriented along the (110), were investigated in this section. In particular, the Seebeck coefficient, electrical resistivity, and thermal conductivity were measured. The thermoelectric performance of the 3DNNs is compared to bulk Bi_2Te_3, but also other nanostructures such as films and 1D nanowires.

Additionally, we present a preliminary study of the resistance behaviour under an external magnetic field, focusing in the low temperature region (T= 1.8 K). Magnetoresistance measurements can provide information of the contribution of surface states (SS) to the electrical transport.

5.4.1. Electrical resistivity

i) *Out–of–plane electrical resistivity*

a)

b)
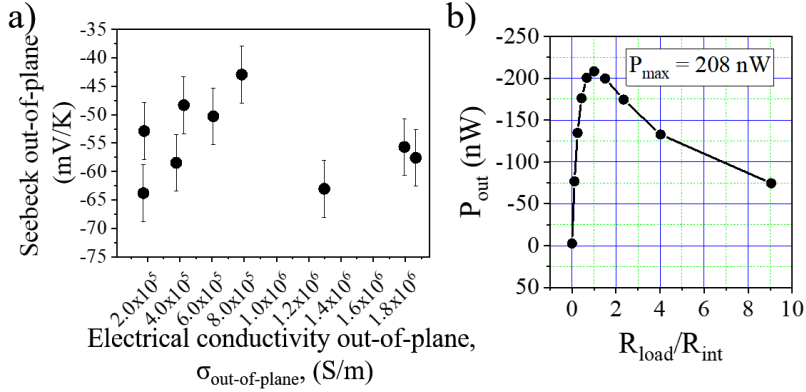
Figure 5.10. Out–of–plane transport properties. a) Seebeck coefficient plotted against the electrical conductivity for several samples with equivalent structure, labeled as 3DNN350, (P = 350 nm). b) Output power of the longitudinal nanowires in the 3D arrange.

During a brief stay at the Jean Lamour Insitute in Metz (France), several 3DNNs (with the same P) were measured in an out-of-plane measurement system consisting of two copper blocks (see Figure 2.10, section 2.3.3.), in which an external current is injected in the direction of the longitudinal nanowires while recording the generated voltage between opposite ends of the nanowires. In this direction, we assume that the TCs do not contribute to the electrical conductivity. The resistance along the nanowires is obtained from the slope of the recorded I-V curves. Then, to calculate the out-of-plane resistivity, measured in $\Omega \cdot m$, we considered the total length of the wires as the thickness of the sample. The electrical conductivity in this direction is of the order of $10^{5\text{-}6}$ S/m, see Figure 5.10a. We have found a high dispersion of the $\sigma_{\perp C}$ data, even for 3DNNs with the same P (each dot represents a particular 3DNN, all of them with $P = 350$ nm). We think that this could be related to the need to optimize the measurement system to the actual dimensions and characteristics of the 3DNN sample pieces, to improve electrical contact, and to stabilize the thermal gradient along the thickness of the 3DNN.

Still, such conductivity values are of the same order of magnitude as the value of Bi_2Te_3 bulk single crystal in the direction perpendicular to the c-axis, $\sigma_{\perp C} \sim 1 \cdot 10^5$ S/m [379]. This agrees well with the crystal structure of the 3DNNs (see section 5.3), characterized by the high crystal quality and quasi-

epitaxial growth of the nanowires along the [110] direction, which is perpendicular to the c-axis of Bi_2Te_3.

Furthermore, in this set up we were able to measure the output power of the longitudinal NWs that form the 3DNNs. This is plotted against the coefficient of the load resistance of the 'circuit', R_{load}, (consisting of the 3DNNs when connected to an output stage) and the intrinsic resistivity of the NWs, R_{int}, which we previously obtained from the *I-V* curves, see Figure 5.10b. When both resistances are equalized, the R_{load}/R_{int} coefficient reaches 1 and the maximum output power of the 'device' is achieved. The average output power of the 3DNNs in the out-of-plane direction was around 200 nW. This is, however, just a preliminary result, considering that the measurement setup system must be optimized.

ii)   *In-plane electrical resistivity*

The resistivity of the 3DNNs was measured in a 4 probe commercial Hall system applying the van der Pauw method, see section 2.3.3. In this in-plane configuration, the current is forced in the direction perpendicular to the NWs and along the TCs. Room temperature measurements of three different 3DNNs with P = 220, 350, and 680 nm, respectively, but of similar total nanowire length around 11-13 µm, gave increasing sheet resistance of 8.6, 18.1, and 20.9 $\Omega \cdot \square$, as recorded in Table 5.5.
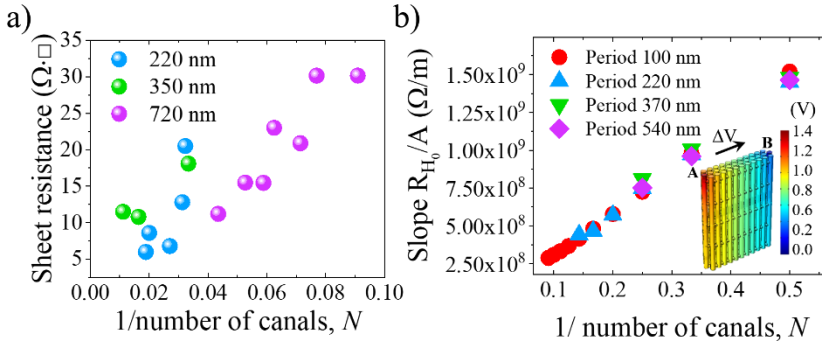
Figure 5.11. *a) Experimental dependence of the sheet resistance with the inverse of N and b) simulated resistance per unit area vs. 1/N.*

To analyse the effective electrical resistivity of these complex nanowire networks we have used COMSOL to model the system considering the specific geometry of the different 3DNNs (as described in *Appendix C.3*). The anisotropic electrical conductivity of the system was taken from the

174

measurements in electrodeposited films [380] and introduced in the electrical conductivity tensor of the material. Then, the steady-state electric potential for a system of N nanowires was simulated, imposing a potential difference in two different nanowire terminals (A and B of the inset image in Figure 5.11b) located at the same side, in analogy with experiments. Two different simulations were run employing a different number of nanowires, and thus increasing the distance between terminals A and B.

The results show that the potential drop in our 3D networks is localized in the interconnecting channels, whereas the resistance along the nanowires can be neglected. Thus, the total resistance of the structure was approximated as

$$R \cong \rho_{TC} \cdot d_{A-B}/(L_{TC} \cdot N) \qquad (5.2)$$

, where ρ_{TC} is the intrinsic resistivity in the direction of the transversal channels, d_{A-B} is the distance between the terminals, N is the number of canals, and L_{TC} is the transversal area of one channel. Note that the total resistance does not depend on the total structure thickness (nanowires length) nor the distance between channels, P. But on the total number of canals, N. This is due to the smaller intrinsic resistivity in the nanowire direction (out-of-plane) along with d_{A-B} being much larger than the thickness of the considered structures Different COMSOL simulations were performed, varying the length of the longitudinal nanowires, L_{NW}, and/or the number of transversal canals, N. This is shown in Figure 5.13b, in which the simulated electrical resistance of several 3DNNs, with P = 100, 220, 370, and 540, is plotted against 1/N. From this graph, we can conclude that the electrical resistance of the 3DNNs does not directly depend on P or the nanowire length (L_{NW}), but the total number of TCs. Since for the same N but different P and L_{NW} the simulated resistance of the different 3DNNs is the same. The higher the number of TCs, the lower is the resistance of the 3D network. The same was observed in the experimental sheet resistance measurements of 3DNNs, with P = 220, 350, and 680, while varying N, as shown in Figure 5.11a.

According to *equation 5.2*, the effective thickness of the 3DNNs, t_{eff}, depends on the total number of TCs present along the longitudinal NWs, N, and the transversal area of one channel, L_{TC}. Hence, t_{eff} can be calculated from the formula,

$$t_{eff} = L_{TC} \cdot N \qquad (5.3)$$

L_{TC} is a fixed parameter at 30 nm, corresponding to the average value of the dimensions of the TCs directly measured from SEM images, (see Table 5.2). Whereas N varies as a function of the total length of nanowires, L_{NW} and the distance P,

$$N = L_{NW}/P \qquad (5.4)$$

Then, the actual values of the resistivity, conductivity, and carrier concentration can be obtained for each of the Bi$_2$Te$_3$ 3D networks, 3DNN220, 3DNN350, and 3DNN680, which are recorded in Table 5.5. The electrical conductivity, σ, and carrier concentration of Bi$_2$Te$_3$ films, also measured in in-plane configuration, are comparable to those of the 3D Bi$_2$Te$_3$ nano-networks (of the order of 10^4 S·m$_{-1}$ and 10^{20} cm^{-3}, respectively). Overall, the electrical conductivity appears to be unaffected by the nanostructuration along the c-axis. Nonetheless, it should be noted that for the same total thickness of a 3D bismuth telluride-based metamaterial, the lower the P, the lower the total electrical resistance.

Table 5.5. *Electrical transport properties measured in the plane.*

Sample name	Total Nws length, L_{NW}, (µm) ± 0.5	Number of TCs, N	Average L_{TC} (nm)	t_{eff} (µm)	Sheet Resistance (Ω·□)	Resistivity, $\rho_{in\text{-}plane}$, (Ω·m) ·10^{-5}	Conductivity, $\sigma_{in\text{-}plane}$ (S·m^{-1}) ·10^4
3DNN220	11.2	48	30	1.70	8.6	1.5± 0.2	6.8 ± 0.6
3DNN350	11.2	26	30	0.90	18.1	1.6± 0.2	6.1 ± 0.6
3DNN680	12.8	14	30	0.50	20.9	1.0± 0.1	9.7 ± 0.9

iii)   *In-plane magnetoresistance*

In-plane magnetoresistance measurements were performed in a 3D Bi$_2$Te$_3$ nanowire network (having P =360 nm) applying the electrical current in the direction parallel to the plane of the alumina membrane, that is, along the transversal channels connecting the nanowires in the network and under a magnetic field up to 140 kOe. Figure 5.12 shows the measured sheet resistance as the applied field is rotated from the direction perpendicular to the sample plane (defined as 0 °) to the in-plane direction parallel to the surface of the AAO membrane, defined as 90°, at a fixed temperature of 1.8 K. The geometrical arrangement and angle values with respect to the nanowire network are indicated in Figure 5.12a.
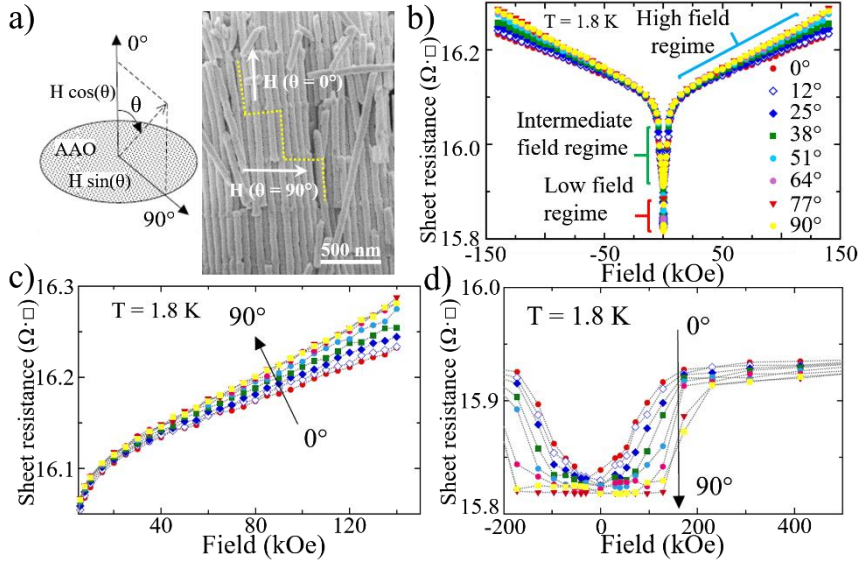
Figure 5.12. a) Magnetoresistance curves with tilting angle from 0° and 90° with the normal to the sample surface b) and c) show an enlargement image of the curves in a) at high and low magnetic fields.

In general, Figure 5.12b, reveals a sharp dip of the resistance at low magnetic fields happening at all angles. This peak is typically associated with the presence of weak anti-localization effects (WAL) due to destructive interference between different trajectories of coherent electron propagation [437, 438]. This WAL effect can present different contributions, coming from bulk states in materials submitted to strong-spin orbit coupling (which produces the spins to rotate in opposite directions) and from the surface states of topological insulators (with opposite spin-momentum locking). As the external magnetic field is increased the WAL effect is destroyed due to the alignment of the spins with the applied field, and the classical regime is reestablished, with the resistance increasing with the increase of the applied field, H.

Figures 5.12c and 5.12d correspond to the magnification of the resistance curves in two different ranges of the magnetic field, at high and low fields, respectively. At first sight, we can identify two different trends of the resistance with the angle rotation. At high fields, Figure 5.12c, the resistance increases with the increasing angle. Whereas, at low fields, Figure 5.12d, it decreases with the angle of the field, from perpendicular (0°) to parallel (90°) to the in-plane current. The WAL effect associated to 2-dimensional (e.g.

surface) transport is sensitive to the component of the magnetic field normal to the direction of the current. In previous reports it has been shown how the WAL peak disappears gradually as the current direction becomes parallel to the magnetic field [439]. Moreover, magnetoresistance curves collapse when plotted against the normal component of the magnetic field. This is clearly the case in the present study for the low field regime (Figs. 5.12d) as the magnetoresistance curve becomes almost perfectly flat at 90° tilt. However, for high fields the magnetoresistance increases with the tilt angle (Fig 5.12c). We have to bear in mind that, due to the arrangement of the nanowire network inside the AAO membrane, current paths in two mutually perpendicular directions are possible (Fig. 5.12a). Therefore, we should stop here and analyze this behavior more in detail. For that, we represent in Figure 5.13a and 5.13b the magnetoresistance as a function of the longitudinal, *H cos(θ)* and transversal, *H sin(θ),* components of the field, for various tilt angles. Here we can see more clearly three different regimes at low, intermediate and high magnetic fields, respectively. At low H (10^1-10^2), the magnetoresistance curves coincide with each other in *H cos(θ)* as long as the tilt of the angle is below 64.29°, ($\theta < 64.29$ °). This indicates a stronger contribution to the WAL effect from current flowing in the plane of the AAO membrane. In this situation, the current flows, predominantly, through the necks joining the individual nanowires in the 3D nanowire network. The system retains such configuration for a magnetic field deviating $\theta < 64.29$ ° from the normal to the plane of the AAO membrane, as illustrated in Figure 5.12a. However, at intermediate and high magnetic fields, in the range of 10^2-10^4 Oe, the magnetoresistance curves collapse with the *H sin(θ)* towards $\theta = 90°$, reaching a plateau. Hence, we interpret this as a conductivity component along the individual nanowires. These results suggest that there are two mutually perpendicular conductive channels in the 3D nanowire networks (see Figure 5.12a). For low H, the current preferably flows along the plane of the AAO, where transport could be associated to topological surface states giving place to the marked WAL signature [440, 441] in Figure 5.12b. At intermediate and high fields, a current component along the individual nanowires can be associated with a less intense WAL effect. In this case a component arising due to the spin-orbit interaction of bulk states [442, 443] could be relevant. In order to gain further insight on the observed phenomena, we have fitted the 0° and 90° curves of the magnetoconductance employing the Hikami-Larkin-Nagaoka (HLN) model [444], Figure 5.13c and 5.13d, respectively.
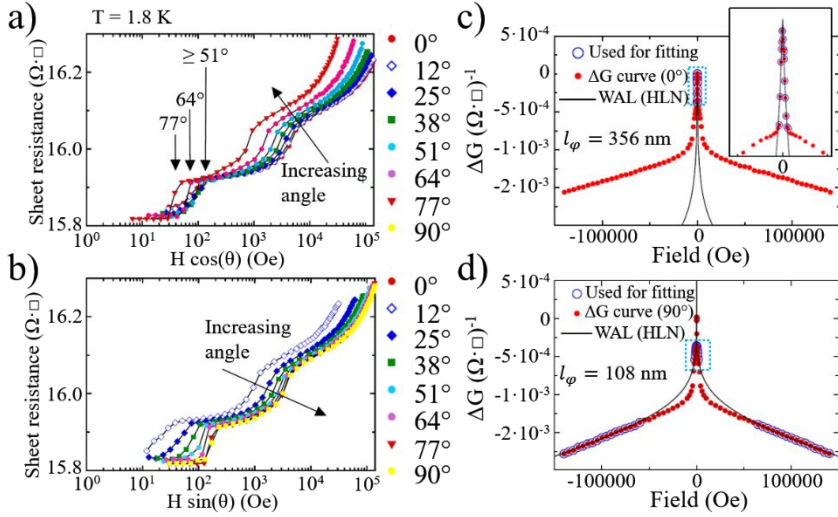
Figure 5.13. *a) Schematic drawing of the experiments where the tilting angle, θ, is defined as the angle from the normal of the AAO membrane. Different paths of the electric current in the 3D nano-network. Representation of the magnetoresistance with the b) H co (θ) and b) H sin (θ). Fitting of the conductance curves at d) θ = 0° and e) θ = 90° employing the HLN model of the WAL effect.*

This model describes the WAL effect on the magnetoresistance in the quantum diffusive regimen and under an external magnetic field, employing two free parameters, α and l_φ. On the one hand, α represents the nature of the spin-orbit interaction in the system and can be related to the number of channels or surfaces that contribute to the WAL effect. Typically α takes 0,-½ and - 1 values. $\alpha = 0$ indicates the suppression of the WAL effect over classical magnetoresistance behavior. $\alpha = -1$ indicates two independent surfaces and $\alpha = -½$ refers to a single channel. The negative sign is interpreted as destructive interference between travelling electrons introducing a negative correction to the magnetoresistance. On the other hand, the coherence length, l_φ, is a magnitude that measures the distance a pair of electrons can travel with opposite spins (contributing to quantum coherent interference) before suffering any decoherence interaction such as electron-electron, electron-phonon scattering, as well as boundary or defect scatterings. The fitting of these two parameters can give an approximate idea of the states (bulk or topological surface states) that dominate the WAL effect.

The HLN model provides a good fitting of the 0° conductance curve in Figure 5.13c in the low field regimen (see inset image), in agreement with

what we observed in Figure 5.13a, giving a value of the coherence length of $l_\varphi = 356$ nm, that we associated with conductivity through the necks joining different nanowires. Remarkably, this would correspond to coherence across approximately five nanowire junctions. However, for the 90° curve we found the best fit at intermediated fields (Figure 5.13d, data points inside the blue box), which further confirms the dependence of the resistance with the sinus component at such fields, displayed in Figure 5.13b. The value obtained for the coherence length ($l_\varphi = 108$ nm) is smaller than the distance between transverse joints along the nanowires, this also points to the participation of bulk states along the nanowires. The difficulty to obtain a good fit in the intermediate and high field regimes points out deviations from the predictions of the HLN model, possibly due to contributions from bulk transport channels. The treatment and understanding of the data measured at higher fields require a different approach, where sources of scattering and the ways in which cyclotron orbits could be realized in such a confined structure would play a role. Such models have not been fully developed yet, and that would not be addressed in this Thesis. However, our experiments lead us to conclude that in such complex system, as the one that we studied here in the form of 3D nanowire network, there could be two different transport channels: in the direction of the longitudinal nanowires or along the transverse connections. Transport through the transverse one is clearly associated with surface states, whereas through along the nanowires could additionally contain the contribution of a strong spin-orbit coupling through bulk states.

5.4.2. Thermal conductivity

i)   *Out-of-plane thermal conductivity*

The thermal conductivity, κ, was measured with the photoacoustic technique along the length of the nanowires (out-of-plane direction, perpendicular to the c-axis of Bi_2Te_3 crystal structure).

Bi_2Te_3 3DNNs of three different transversal channel distances $P = 220$, 350, and 680 nm were measured while still embedded in the alumina matrix. Before the measurement, an 80 nm Ti layer was evaporated on the samples. The samples were measured as multilayered films, and hence, a multilayered model had to be considered. This model consists of three different layers: the titanium film, the region filled by Bi_2Te_3 (that is, alumina and bismuth telluride), and the empty region of the 3DAOO membrane (alumina and air),

where the thermal conductivity of Ti layer and the empty 3DAOO membrane are known variables. Then, following the procedure described in section 2.3.3., we can extract the thermal conductivity value associated with the second layer of our model. For our problem layer, corresponding to the Bi_2Te_3 filled region, the experimental thermal conductivity of the composite material, κ_{comp}, of samples 3DNN220, 3DNN350 and 3DNN680 with $P = 220$, 350 and 680 nm, gives $\kappa_{comp} = 0.509$, 0.578, and 0.790 $W \cdot m^{-1} \cdot K^{-1}$, respectively. At first sight, we observed a significant reduction of the thermal conductivity of the composite, κ_{comp}, as the value of P was decreased down to 220 nm, obtaining a thermal conductivity value as low as 0.5 $W \cdot m^{-1} \cdot K^{-1}$. It is worth noting that this value also includes the heat transport through the alumina matrix with the skeletal conductivity of alumina, κ_{3DAAO}, being 1.25 $W \cdot m^{-1} \cdot K^{-1}$, as reported in [299, 301].

To explain the experimental behaviour of the thermal conductivity in the composite (Bi_2Te_3/alumina matrix) we have considered the nanostructured filling material, Bi_2Te_3 3D nano-network on one hand, and the oxide membrane, on the other.

We have made this distinction because at the nanoscale we can find two types of heat transport: diffusive and ballistic. Diffusive heat conduction is associated with high-frequency phonons (optical phonons) with a small mean free path (compared to the travelling distance to the closets perturbation, i.e. impurities, defects, boundary limits …) and can be described employing Fourier's law.

Ballistic transport is observed when the mean free path of the (acoustic) phonons is longer than the dimension of the medium through which the phonon travels and hence, the thermal conductivity in the material is mostly determined by boundary scattering. The transition between both depends on the specific material and the system characteristic size. In this case, Fourier's model does not suffice to assess deviations from the diffusive regimen towards a ballistic one [445], which requires a more sophisticated model that takes into account not only the intrinsic properties (thermal conductivity, specific heat, …) of the material but also the size or boundary effects.

According to the above, we have employed the hydrodynamic heat transport model, which is explained in detail in *Appendix C.4.1*, to describe the heat conduction of phonons for Bi_2Te_3 semiconductor when nanostructure as 3DNNs [445-447]. This model describes a non–equilibrium system, where

phonons are destroyed at the material surface as the dimension of the material is reduced below the mean free path of phonons suffering normal collisions (momentum-conserving collisions). For illustration, the heat flux at the nanoscale behaves inhomogeneously, as a fluid flowing through a pipe. In this analogy, the wall friction generates an extra viscosity that reduces the fluid's velocity close to the surface of the pipe. Non-local or viscous effects due to momentum destruction at the system boundaries extent to in a region of size $\ell = 55$ nm for Bi_2Te_3, this magnitude is a weighted phonon mean free path (mfp) average, known as non-local length [448], as explained in *Appendix C.4.1*. Capturing all the information of the mfp spectrum in a single parameters easies the comparison between the characteristic size of the sample and the mean free paths of the phonons Whereas, from a Kinetic formalism, for example, this should be done by locally comparing the mfp of the different phonon modes with the system size.

In our work, this length is comparable to the dimensions of nanowires and transverse connections (TCs) in the nanostructured Bi_2Te_3 3DNNs (see Table 5.3), suggesting that in this type of system nonlocal effects would significantly contribute to the heat transport. This model has been able to accurately reproduce the reduction of the lattice thermal conductivity in free-standing Bi_2Te_3 1DNW with the reduction of the nanowire diameter, which follows a non-linear trend. In this work, it could be observed that the influence of nonlocal or viscous effects that contribute to the reduction of the lattice thermal conductivity, was more acute in nanowires with the smallest dimensions [367].

Figure 5.14a. shows the heat flux and temperature steady-state profiles according to the hydrodynamic heat transport model for a free-standing 3D network. In the heat flux profile, we can distinguish two different viscous effects contributing to the reduction of the effective thermal conductivity. Displayed in inset 1, we can observe the reduction of the heat flux as we move from the centre of the nanowire towards the surface, due to phonon-boundary scattering at this interface. And, additionally, in inset 2, which focuses the attention on the intersection between the longitudinal nanowire and the transversal channel connections, TCs, the heat flux streamlines (black lines and arrows) across that region present some curvature, which accentuates as the flux path passes bordering the TCs at opposite sides of the nanowire edges. This curvature can be interpreted as an extra viscous effect that originates due to the presence of TCs.
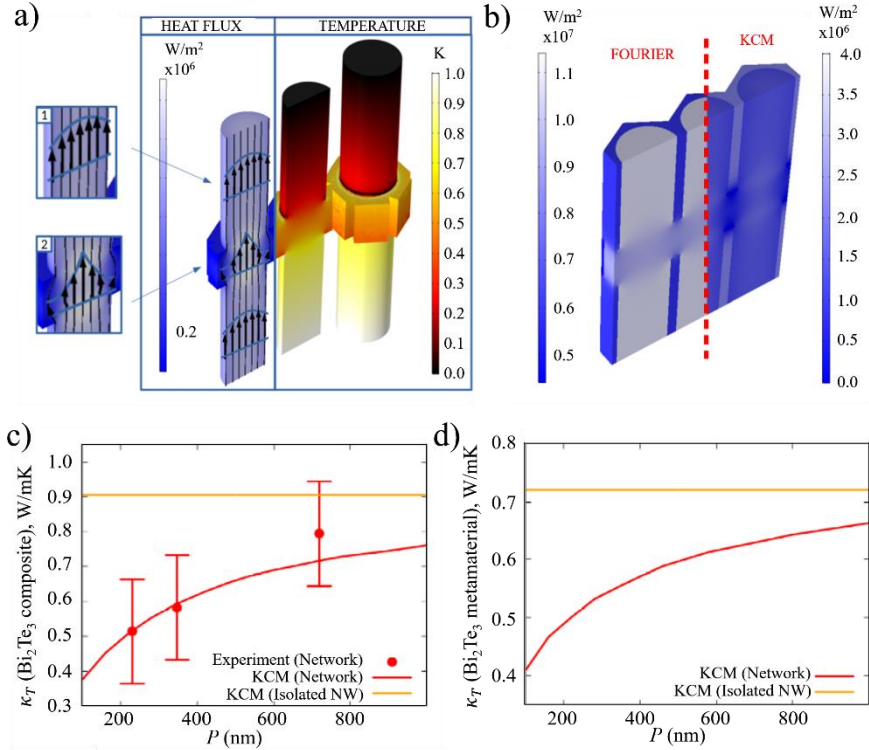
Figure 5.14. Thermal conductivity in the out-of-plane configuration. a) Heat flux and temperature steady-state profiles according to the hydrodynamic heat transport model for a free-standing 3D network. Two different non-local effects reducing the effective thermal conductivity of the structure can be observed: the inhomogeneous heat flux profile in the nanowire (inset 1) and the curvature of the heat flux streamlines in the regions connected by the TnCs (inset 2). b) Heat flow in the 3D-Bi$_2$Te$_3$/alumina composite according to the hydrodynamic heat transport model (KCM) and the (bulk) Fourier approach. Thermal conductivity predicted by the hydrodynamic heat transport model, considering the lattice and electronic contributions c) with and d) without the 3DAAO matrix. The red points in c) correspond to the experimental values of the measured thermal conductivities obtained for ample 3DNN220, 3DNN350, and 3DNN680, while the red line represents the thermal conductivity of the composite obtained from the model for different values of P, and the orange line is the predicted value for a 55 nm diameter Bi$_2$Te$_3$ nanowire array embedded in the alumina matrix. Similarly, in d) the red and orange line corresponds to the κ_T of self-standing Bi$_2$Te$_3$ 3DNNs and Bi$_2$Te$_3$ 1DNWs, respectively.

Quantitatively, both effects combined produce a greater reduction of the thermal conductivity in the 3DNNs compared to the conventionally 1DNW of similar dimension ($d = 55$ nm), from experimental and simulated values of κ recorded in Table 5.6 and Figure 5.14c, respectively. It is worth noting that while for 1D nanowires the reduction of the effective thermal conductivity

could be also attributed to a suppression of phonons with a mean free path larger than the diameter of the wire according to a kinetic interpretation. However, the kinetic theory in terms of phonons suppression cannot predict the extra reduction of the thermal conductivity at the TCs of the 3DNNs. In the regions where the wires are interconnected, the Bi_2Te_3 domain size increases and, thus, the effective thermal conductivity should be increased due to a reduced number of suppressed phonons in those regions. However, the experimental thermal conductivity of the system is reduced in the network as predicted by the hydrodynamic model.

To compare the simulated lattice thermal conductivity values of the Bi_2Te_3 3DNNs while varying the P parameter with the experimental measurements of κ_T (Bi_2Te_3 composite), which were carried out with the 3DNNs embedded in the oxide, two transformations must be performed. The first transformation that is required is the addition of the oxide matrix to the lattice thermal conductivity so that we know the simulated value of κ_T (Bi_2Te_3 composite). In contrast to Bi_2Te_3, the phonon mean free paths in the oxide are much smaller than the geometry characteristic sizes (around only 5 nm [449] vs, tens of nm), and hence, non-local effects are not expected, and Fourier's law can be used to describe these domains, see *Appendix C.4.2*.

Secondly, the contribution of electrons, κ_{el}, must be added to the Bi_2Te_3 lattice conductivity. Since the amorphous oxide membrane is non-conductive, the κ_{el} contributing to the total thermal conductivity in the oxide matrix can be neglected. This is further explained in *Appendix C.4.3*. The sum of the lattice and the electronic contribution to the total thermal conductivity is presented in Figure 5.14c (which includes the oxide matrix) and Figure 5.14d (without the oxide).

As a result Figure 5.14c, shows a remarkable coincidence between the experimental points and the simulated data that is obtained applying the hydrodynamic model. To corroborate this matching, we have also simulated the distribution of the heat flux in the 3DNN composites according to the bulk Fourier description by assuming $\ell = 0$. In such a case, the heat flows preferentially through the nanowires, as displayed in Figure 5.14b. However, when including the hydrodynamic effects that block the heat flow inside the 3D nanonetworks (i.e. $\ell = 55$ nm), the heat flows preferentially through the alumina, since the effective lattice thermal conductivity of the 3D network becomes smaller than that of the amorphous alumina. Hence, it can be

concluded that employing Fourier's law overestimates the effective thermal conductivity inside Bi_2Te_3 3DNN nanostructures.

Also in Figure 5.14c, when compared to the thermal conductivity of 1DNWs of similar diameter, reported in [367], including the alumina template (orange line), the thermal conductivity of the 3DNNs (red line) is reduced due to the presence of the TCs, which, as demonstrated by the hydrodynamic model, introduce an extra vicious effect to the longitudinal nanowires (see inset 2, Figure 5.14a). Furthermore, this reduction is greater if the number of interconnections along the nanowires is increased, which can be easily achieved if the intercanal distance (P) is shortened. This dependence with P is also shown in Figure 5.14c.

Table 5.6. *Measured and calculated values of the thermal conductivity of the 3DNNs (with and without the alumina template).*

	Period P, (nm)	κ_T, 3D Bi_2Te_3 composite (measured) ($W \cdot m^{-1}.K^{-1}$) $\perp c$-axis	κ_T, 3D Bi_2Te_3 composite (calculated) ($W \cdot m^{-1}.K^{-1}$) $\perp c$-axis	κ_T, 3D Bi_2Te_3 metamaterial (calculated) ($W \cdot m^{-1}.K^{-1}$) $\perp c$-axis	κ_T, 3D Bi_2Te_3 metamaterial (calculated) ($W \cdot m^{-1}.K^{-1}$) $\parallel c$-axis
Bi_2Te_3 3DNNs	220	0.509±0.13	0.508	0.501	0.62
	350	0.578±0.13	0.593	0.554	0.58
	680	0.790±0.15	0.717	0.632	0.81

Figure 5.14d, corresponding to the total thermal conductivity of the free-standing 3DNNs without the alumina matrix, κ_T (Bi_2Te_3 metamaterial), follows the same trend with increasing the distance P between TCs, as in Figure 5.14c., but the actual values of κ_T (Bi_2Te_3 metamaterial) when considering only the network is smaller than those of the composite. This is recorded in Table 5.7 for the samples with P = 220, 350, and 680 nm. The orange line in Figure 5.14d represents the predicted value of the thermal conductivity for a 1D Bi_2Te_3 nanowire array (of the same dimensions) with this same model, which gives κ_T(1DNW) = 0.72 W/mK. This value is higher than any of those obtained for the 3DNNs represented by the red curve.

ii)   *In-plane thermal conductivity*

This model also allows us to predict the thermal conductivity in the in-plane direction, that is, parallel to the c-axis and along the transversal nanochannels as described in *Appendix C.4.1.b.*
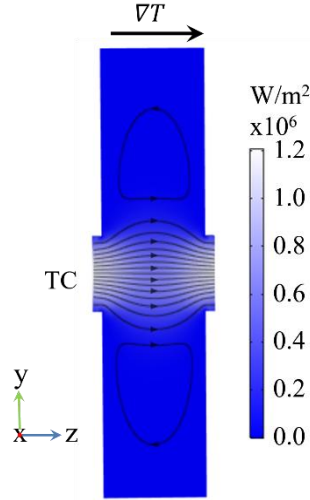
Figure 5.15. *Profile of the heat flux according to the hydrodynamic heat transport model for a free-standing 3D network when the temperature gradient is established between opposite TCs, as indicated by the arrow.*

The calculated values of $\kappa_{\|c}$ for the nano-networks studied in this work were in the range between 0.6-0.8 W·m^{-1}·K^{-1}, see Table 5.7. This value is ~2.5 times lower than the value of $\kappa_{\|c}$ measured in electrodeposited Bi$_2$Te$_3$ films along the same direction [380]. In this direction, the viscous effects at the interconnections are significantly larger than along the longitudinal wire-axis direction due to the smaller size of the TCs and the short distance between nanowires, which cause an enhanced inhomogeneity in the heat flux profile (see Figure 5.15) as observed by the pronounced curvature of the streamlines that represent the heat flux. In this direction, the lattice contribution to the total $\kappa_{\|c}$ is reduced to $\kappa_{latt} \sim 0.1$ W·m^{-1}·K^{-1}, a value that is significantly smaller than the electron contribution $\kappa_{el} \sim 0.6$ W·m^{-1}·K^{-1}. At this point $\kappa_{el} + \kappa_{latt} \simeq \kappa_{el}$, and the Wiedemann-Franz law (*equation C.2.5, in Appendix C*) allows the simplification of $zT = S^2/L$ where L is the Lorentz number. This opens up a new research venue since the zT only depends on their Seebeck coefficient and the Lorentz number.

In addition, we have evaluated the magnitude of the Laplacian term, which measures how far our system is displaced from the equilibrium when the temperature gradient is established in the out of plane direction (along the nanowires) and in-plane (parallel to the transversal nanochannels, TCs), normalized by the heat flux, q.
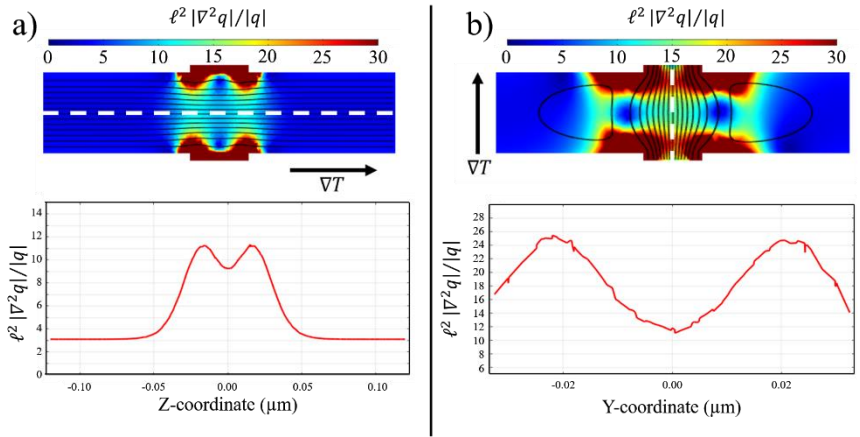
Figure 5.16. *Top, representation of the ratio between the Laplacian term and the heat flux term inside the structure in the situation where the temperature gradient is applied along a) the out-of-plane direction and b) the in-plane direction. Also, the heat flux streamlines have been added in both cases. Bottom, the actual value of the ratio across the white dotted lines in a) and b).*

This is illustrated in Figures 5.16a and 5.16b, respectively. In the graphs, the white dotted lines indicate the direction along which the heat is flowing, and the black lines represent the simulated heat flux. In the case of the thermal gradient applied in-plane (parallel to the transversal nanochannels, TCs), the flux is strongly influenced by the morphology of the structure, presenting even certain closed lines (kind of vortex) in the regions where TCs go through the nanowires. Note that, while in the out-of-plane direction the value of the quotient, $\ell^2|\nabla^2 q|/|q|$, is ~3 (except close to the connection with the TnCs where it grows), in the in-plane direction this quotient is an order of magnitude larger (~20 on average). In our samples, the small sizes of the nanowires and TCs even smaller than the mean free paths of the resistive collisions (non-conserved momentum collisions) impede the system to relax (normal collisions or ballistic transport dominate), but through boundary scattering. Hence, the increase of the Laplacian term is associated with the destruction of phonon momentum at the boundary regions, and which, in the 3DNNs, is especially significant at the transverse connections. This figure helps to visualize with perfect clarity the influence of the TCs, associated with the appearance of important viscous effects that reduce the heat flux in those regions, as previously discussed. The average of $\ell^2|\nabla^2 q|/|q|$ is smaller in the out-of-plane directions, because regardless of the presence of TCs the heat, in this direction, flows for the most part through the wires. In the in-plane

direction, however, heat conduction occurs mainly along the TCs, of smaller size than the diameter of the NW, thus, resulting in an enhancement of the non-equilibrium effects contain by the Laplace term.

5.4.3. Seebeck coefficient

i)   *Out-of-plane Seebeck coefficient*

The out-of-plane electrical Seebeck coefficient in the 3DNNs was determined employing the same setup that we have used in the measurement of the out-of-plane resistance. In this case, the two copper blocks are fixed at different temperatures. And as a consequence, a heat gradient is established between the two sides of the nano-networks, that is, across the length of the nanowires.

The out-of-plane Seebeck values, $S_{out-of-plane}$ (perpendicular to the c-axis), are plotted in Figure 5.10a, against the corresponding out-of-plane electrical conductivity, $\sigma_{out-of-plane}$. In this configuration the measured values of the Seebeck coefficient are in the range from - 40 to - 60 $\mu V \cdot K^{-1}$, in good agreement with the reported values of $S_{out-of-plane}$ for 1DNWs of similar characteristics: nanowires fabricated by electrodeposition with 55 nm diameter, possessing 2:3 stoichiometry and preferred crystal orientation along the [110] direction, ranging between -30 to -57 $\mu V \cdot K^{-1}$ [34, 414, 417, 422]. However, such values of S are considerably smaller than the S coefficient in the direction perpendicular to the c-axis for bulk Bi_2Te_3 of - 240 $\mu V \cdot K^{-1}$. This clashes against the predicted enhancement of the power factor ($S^2\sigma$) when the dimensionality is reduced as in 2D (films) [450] and 1D (nanowires) [265] systems compared to the material bulk (3D) due to the quantization of the energy states. More recently, it was proved that quantum effects only emerged in strongly confined systems, with diameter sizes below 10 nm. Otherwise, the energy states degenerated forming multiple subbands, thus, increasing the density of states at the Fermi level [451]. Still, this does not explain the detrimental effect on the Seebeck coefficient.

Hence, we turn towards the topological insulator nature of Bi_2Te_3 to find a plausible explanation for the reduction of the S. A topological insulator possess two conductive channels: one through the material bulk, consisting of a semiconductor with a small bandgap and a second one across 2D gapless (metallic-like) surface states. While topological surface states play no role in TE transport in bulk materials, as the dimensions of the system are reduced

they may contribute substantially to the transport in nanostructures due to their large surface to volume ratio [452-454]. Electrical transport experiments on Bi_2Te_3 [455, 456] and Bi_2Se_2Te [457] nanowires in the 200–30 nm diameter range revealed that the 2D TI surface channels contribute up to 30–70% of the total electrical conduction. Thus, it is reasonable to assume that the reduction of the S measured along the length of the 55 nm diameter nanowires of the 3DNNs, in the out-of-plane configuration, is related to the contribution of 2D topological surface states that serve as highly conducting channels. While they may enhance the electrical conductivity due to unrestricted electron transport at the material interface, the effect on the Seebeck coefficient is the opposite. First, the increase of the carrier density at this interface reduces the S, in agreement with *equation C.2.5* in *Appendix C.2.1*. Furthermore, the Seebeck coefficient is usually small in materials without a bandgap (metals, see table 5.1), where both types of carriers, electrons, and holes, equally contribute to the Seebeck coefficient, therefore, canceling each other out. Both effects combined can explain the values of the Seebeck coefficient for nanowires reported in the literature, even smaller than those of Bi_2Te_3 films, and can also apply to the $S_{out-of-plane}$ of the 3DNNs, assuming that TCs do not contribute.

ii)   *In-plane Seebeck coefficient*

The Seebeck coefficient was measured in a lab-made system, as described in section 2.3.3. This setup allows determining the Seebeck coefficient along the in-plane direction and it is typically used in the characterization of films, but cannot be employed with 1D nanowires due to the lack of electrical contact between neighbour nanowires of the same array. However, in our 3D nano-networks, the nanowires are connected in the in-plane direction through the transversal channels (TCs) which makes the measurement of this property possible with this kind of setup. The only sample preparation needed before the measurement consisted of removing the Au and Cr layers through chemical etching, as explained in section 2.1.4.3.2 and illustrated in Figure 2.12a.

As mentioned before, the nano-networks were grown fixing the distance between TCs at P =220, 350, and 680 nm, labelled as 3DNN220, 3DNN350, and 3DNN680, respectively. More than one sample of the same kind 3DNN220, 3DNN350, and 3DNN680 were measured in the system, to assure the reproducibility of the results. The Seebeck coefficient obtained was in the range from -103 ± 5 to -127 ± 6 µV·K^{-1}. On average, the Seebeck coefficient

of the 3D nano-networks is around -125 µV·K^{-1}, independently of the distance *P* of the nano-networks, which is consistent with the isotropic character of this transport property.

In nanocrystalline, stoichiometric, and strongly oriented films grown by the same pulsed deposition method, the in-plane Seebeck coefficient measured using the same system was about -58 µV·K^{-1} [380]. In the literature, the Seebeck coefficient of 1D nanowires with 55 nm diameter is in the range of -30 to -57 µV·K^{-1} [34, 414, 417, 422], measured along the nanowire direction (out of plane). 3DNNs show a great enhancement of this transport property over the other two kinds of nanostructures, films, and 1D nanowires, which we should attribute again to the presence of the interconnecting nanochannels (TCs). But also, when compared to the Seebeck values of 3DNNs measured in out-of-plane configuration, recorded in Table 5.7.

To explain this phenomenon, we need to take into consideration the contributions to the Seebeck coefficient: one is directly related to the form of the energy band of the material and the second one is due to the transfer of momentum between phonons and electrons, known as a phonon-drag contribution.

For 2D materials [458], the latter is typically observed at low temperatures and under a temperature gradient ∇T. In these circumstances the average phonon mean free path and the number of normal (momentum-conserving) collisions are increased, which causes the phonon distribution function to be displaced from the local equilibrium, due to the existence of a conserved momentum that cannot be relaxed, adopting the form

$$f = f_{eq} + \vec{\Lambda} \cdot \vec{k} \qquad (5.5)$$

, where $\vec{k}$ is the phonon wavevector and $\vec{\Lambda}$ is a parameter depending on ∇T.

The consequence of that situation on the thermoelectric effect is that, when the electron cloud interacts with the phonons, it absorbs part of this momentum through electron-phonon collisions. As a result, the electron distribution is also displaced from local equilibrium and the electrons get momentum in the direction of the phonon flux, thus causing the increment in the Seebeck coefficient. However, even though phonon drag is usually associated with low-temperature regimens the ultimate condition to observe this effect is that the system must be out of equilibrium. A more general non-equilibrium distribution function has been proposed, that takes into

consideration the presence of inhomogeneities (regardless of the abundance of normal collisions),

$$f = f_{eq} + \vec{\beta} \cdot \vec{q} + G \cdot \nabla \vec{q} \qquad (5.6)$$

, in this equation $\vec{\beta}$ and G depend on the phonon velocity and mean free path [448]. According to this description, the appearance of a spatially varying flux drives the system out of equilibrium. Therefore, in the regions where the heat flux has a larger spatial variation, which in the 3DNNs occurs at the TCs (see Figure 16), the phonon system will be far from equilibrium and phonon drag can emerge. This phonon dragg has a different origin that comes from the nanostructuration of the material, and allows to tailor this new effect by including obstacles to the heat flux to make it follow a trajectory with continuous contractions and expansions as in the 3D network. In contrast to the normal-collisions-related phonon drag, which can only be enhanced by reducing the temperature.Then, using the Boltzmann Transport equation and *equation 5.6*, it can be shown that the emergence of these non-equilibrium effects is associated with the Laplacian term in Hydrodynamic heat transport *equation C.4.2*. Figure 5.16 represents the deviation from equilibrium measured in the out-of plane (Figure 5.16a) and in-plane (Figure 5.16b) directions, taking place at the intersection between longitudinal nanowires and transversal nanochannels. As discussed before, in our samples, the increase of the Laplacian term is not due to an increase of the normal collisions, but it is a consequence of the sample characteristic sizes, which are comparable to the mean free path of the resistive collisions. In such conditions the momentum is only efficiently destroyed in the boundaries, and the phonon momentum cannot be relaxed inside our samples, which might increase the phonon drag contribution. In particular, in the in-plane direction, where transport mostly takes place through TCs (with reduced dimensions with respect to the diameter of the nanowires), the average Laplacian term is the highest (Figure 5.16b). Therefore, we hypothesize that the increase in the Seebeck coefficient in this direction may be due to the emergence of a significant phonon-drag contribution due to an enhanced deviation from the equilibrium of one order of magnitude ($\ell^2 |\nabla^2 q|/|q| \sim 20$) compared to the out of plane direction (average $\ell^2 |\nabla^2 q|/|q| \sim 4\text{-}5$). Still, further work should be done to connect this phenomenological explanation with more fundamental microscopic models providing numerical expressions for the Seebeck coefficient.

Table 5.7. *Thermoelectric properties of Bi₂Te₃ as 3DNNs, 1DNW, film, and single crystal.*

‖ c-axis	Structural Information: Period (P) or diameter (D) in nm	Seebeck, $S_{\text{in-plane}}$ ($\mu V\cdot K^{-1}$)	$\sigma_{\text{in-plane}}$ ($S\cdot m^{-1}$)	$\kappa_{\text{in-plane}}$ ($W\cdot m^{-1}\cdot K^{-1}$)	PF (mW/mK²)	zT (T =298 K)	Ref.
Bi₂Te₃ 3D nanonetwork metamaterial	P=220	-127 ± 6	$(7.1\pm0.6)\cdot10^4$	0.62	1.14	0.55	This work
	P=400	-103 ± 5	$(6.6\pm0.6)\cdot10^4$	0.58	0.70	0.36 (0.43)	
	P= 680	-121 ± 6	$(9.8\pm0.9)\cdot10^4$	0.81	1.43	0.53 (0.60)	
Bi₂Te₃ film	-	-58	$6.7\cdot10^4$	1.2	0.23	0.06	[380]
Bi₂Te₃ single crystal	-	-240	$1.8\cdot10^4$	1.0	1.06	0.31	[379]
⊥ c-axis	Structural Information: Period (P) or diameter (D) in nm	Seebeck, $S_{\text{out-of-plane}}$ ($\mu V\cdot K^{-1}$)	$\sigma_{\text{out-of-plane}}$ ($S\cdot m^{-1}$)	$\kappa_{\text{out-of-plane}}$ ($W\cdot m^{-1}\cdot K^{-1}$)	PF (mW/mK)	zT (T =298 K)	Ref.
Bi₂Te₃ 3D nanonetwork metamaterial	P=220	-	-	0.501	-	-	This work
	P=400	-55 ± 7	$(4.2\pm2.4)\cdot10^5$	0.554	1.27	0.68	
	P= 680	-	-	0.632	-	-	
Bi₂Te₃ nanowires	D = 55	-55	$3.0\cdot10^4$	0.72			[237, 367]
Bi₂Te₃ film	-	-50	$3.2\cdot10^5$	2.4	0.80	0.10	[380]
Bi₂Te₃ single crystal	-	-240	$1.00\cdot10^5$	2.20	5.76	0.78	[379]

Another possibility, that shouldn't be ruled out is the influence of surface states in the 3DNNs. In the in-plane direction, the flux is forced along TC. These surface states can be affected by the reduction in the diameter of the transverse nanochannels (around 35 nm) compared to the diameter of the nanowires (55 nm). For instance, it has been reported an increase of the Seebeck coefficient of $Bi_{0.85}Sb_{0.15}$ NWs by a factor of ~2 when their diameter was reduced to 41 nm from the minimum-Seebeck diameter of 58 nm [454]. This enhancement of the Seebeck coefficient was attributed to the hybridization of the surface states when the diameter size is around two times the wavelength of surface charge carriers. In this region, the bulk-extending tails of surface states from opposing boundaries overlap, and the properties of the surface states are modified. This opens a gap in the surface states [454, 459], reducing their carrier concentration and increasing the Seebeck coefficient.

5.4.4. zT

i) _Out-of-plane and in-plane zT_

Once, the different 3DNNs have been fully characterized regarding their transport properties, σ, κ, and S, we can calculate the figure of merit, zT, of the nanostructures according to _equation C.2.1_. Due to the anisotropic crystal nature of bismuth telluride, which affects the TE performance of the material, we have calculated two different zTs, taking as reference the c-axis of the crystal structure of Bi$_2$Te$_3$: $zT_{\parallel C}$, employing the magnitudes of the σ, κ and S measured in the direction parallel to the c-axis (that is, for highly oriented [110] 3DNNs, the direction perpendicular to the nanowires in the network or in-plane direction). And, $zT_{\perp C}$, when the transport properties in the 3DDNs are measured in the out-of-plane direction, which is along the longitudinal nanowires. The obtained values at RT are $zT_{\parallel C}$, between 0.36 and 0.56 (for the 3D NN with P= 400 nm and P=680 nm, respectively) and $zT_{\perp C}$, of 0.68 (for the 3DNN with P= 400 nm). All these values are summarized in Table 5.7.

Due to the crystal anisotropy of the material we compare, in Table 5.7, the TE properties of our 3DNNs and other Bi$_2$Te$_3$ systems that possess the same crystal orientation and that are produced and measured under similar conditions. Our 3DNNs have shown outstanding performance, with zT values that are comparable or even, that improve those found in a bulk single crystal. We attribute this enhancement of the thermoelectric efficiency to how the material is nanostructured, resulting in an important reduction of the thermal conductivity and an improved Seebeck coefficient compared to other kinds of nanostructures, such as thin films and nanowires, while maintaining similar values of electrical conductivity. The former reaches values as low as 0.5 W·m^{-1}·K^{-1}, as compared to 2.2 W·m^{-1}·K^{-1} for films in the out-of-plane direction perpendicular to the c-axis. This value is still smaller than the reported κ of 1DNW with the same diameter ($\kappa_{\perp C}$ = 0.72). And the latter has experienced more than a two-fold increase, over -100 µV·K^{-1}, reaching even -127 µV·K^{-1}, while both thin-film and nanowires do not exceed - 60 µV·K^{-1}.

5.5. Concluding remarks: Bi$_2$Te$_3$ 3D-NNs

In conclusion, we presented a novel metamaterial based on bismuth telluride, which is a nanostructured material whose properties depend on the

geometrical parameters of the 3D structure. The fabrication technique, based on anodization and electrochemical deposition, is economical and easily scalable. Thanks to the nanostructuration, this thermoelectric metamaterial has a reduced thermal conductivity and an improved Seebeck coefficient compared to thin films and nanowires produced and measured under similar conditions. Both parameters enable an enhancement of the thermoelectric efficiency across the different geometries studied in this work (different distances between transversal connections ranging from 220 to 720 nm) while maintaining similar values of electrical conductivity. The physical phenomena behind the reduction of the thermal conductivity (which reaches values as low as 0.5 W$\cdot$ m^{-1} $\cdot$K^{-1}, compared to 2.2 W$\cdot$m^{-1} $\cdot$K^{-1} for films) and the more than two-fold increase in measured Seebeck coefficient (over -100 μV$\cdot$K^{-1}, reaching even -127 μV$\cdot$K^{-1}, while both thin film and nanowires do not exceed -60 μV$\cdot$K^{-1}) are attributed to the nanostructure of the metamaterial, which can be easily controlled by manipulating the template structure.

Moreover, this metamaterial overcomes the drawbacks that nanowire structures present (difficult handling when the matrix is dissolved, reduced number of measurement methods to characterize their transport properties). The 3D-NNs appear as a quite attractive alternative to electrodeposited thin films, being easily implemented in actual devices and providing one order of magnitude higher zT compared to them.

6. General conclusions.

Throughout this thesis, we have demonstrated the **versatility and utility of 3D porous alumina templates (3D AAOs)** to create novel metamaterials that can generate tailor properties in many different fields. In particular, in this thesis we have demonstrated their interest in generating new or improved properties in **optic, magnetic and thermoelectric materials**. The main conclusions that can be drawn from each of the applications studied in this Thesis could be summarized as follows:

As far as the **optical properties of 3D AAOs** are concerned, which were presented in Chapter 3, it was shown that the 3D alumina templates provide excellent platforms to modulate the interaction and propagation of light inside them via structural engineering of the 3D nanoporous structure. The 3D porous architecture of the membranes can be designed to produce **specific optical response**, which includes environmentally selective reflectance. In the mesoporous network metamaterial, the (artificial) refractive index of the 3D AAOs can be manipulated to **create a broad color palette by structural colour formation**. This last part is extremely useful for the **fabrication of easily readable colorimetric sensors** for environmental monitoring, food safety, homeland security, anticounterfeiting and healthcare applications. But also for the fabrication of **color filters for large-scale applications**, such as display devices, wearable electronics, imaging devices, and solar cells.

The **use of the 3D-AAOs as templates** for nanostructuring different kinds of materials (magnetic and thermoelectric materials, respectively) was explored through chapters 4 and 5. This methodology **allows the synthesis of a new generation of Three-Dimensional (3D) integrated nanostructures** consisting of interconnected nanowires forming a 3D self-sustained network of the desired material. Again, the fabrication method of these nanostructures is easily scalable (electrochemical deposition) and the obtained 3D interconnected nanostructures present properties that differ from the bulk materials, offering the possibility of tailoring them to match different needs.

In the case of **magnetic 3D interconnected nanostructures,** described in Chapter 4, it was shown that **the precise control of both the position and number of transversal nanowires (TCs) influences greatly in the resulting magnetic properties of the structure**. This work demonstrates that large (that is, areas of mm^2 and 5-25 µm thick) Ni nanowires arrays interconnected through TCs can be produced. The properties of these 3D nanostructures give rise to **unexpected magnetization dynamics which radically evolve depending on the TC arrangement.** Therefore, we propose a magnetic framework, where the main magnetic features have been cross-verified by hysteresis loops, first magnetization curves, FORC and micromagnetic simulations. In these scenarios, TCs play a capital role and give rise to a complex landscape of magnetic dynamics within the Ni 3D Nano-Networks (Ni 3DNN). Our results confirm that **TCs behave like pinning sites for the magnetic domain walls and reduce the magnetostatic interactions among NWs**. In particular, TCs contribute to the global homogeneity of the interaction field in the array and this contribution is improved by the shortest separation between TC levels. When the magnetic field is applied in the direction of the nanowires (OOP configuration), TCs limit the effective length for the generation of multiple domain walls, within the nanowire segments. Even more, our model predicts the generation of a particular global ordered magnetization state (corkscrew) during magnetization reversal for the shortest TC distances studied (220 nm). Meanwhile when the field is applied along the TCs (IP configuration), coherent rotation is a common magnetization reversal mechanism for nanowire arrays and 3DNN. However, for nanowire arrays and 3DNN with TC periods of 455 nm, the interaction between static domain walls is inferred as predominant mechanism. On the other hand, for TC with the shortest distance studied (240 nm), both the model and the experimental results excludes the existence of static domain walls, being the interactions of TC and segments also primary drivers.

These results provide a deeper understanding of the magnetic behavior of these novel nanostructures with well-controlled and tuned magnetic properties through the introduction of several levels/periods of TCs. Moreover, **the validated framework of magnetization dynamics and generation/interaction of domain walls, paves the way for controlling the domain walls on new ways of logic computation and sensing or even the future designing a-la-carte of magnetic metamaterials** by the combination of different materials and/or periods within the same 3D nanonetwork .

Finally, the fabrication of **3D Bi$_2$Te$_3$ nanowire networks**, which is the most commonly used **thermoelectric material for room temperature applications**, has also shown how the architecture of the nanostructure influences its properties. In this case, the efficiency of the material for thermoelectric applications, which is determined by intrinsic properties of the material. Nevertheless, **in the 3D Bi$_2$Te$_3$ nanonetwork, the propagation of phonons propagate is affected by the structure**, and thus **the thermal conductivity of the material can be greatly reduced** when compared to bulk values. It has also been shown that the nanostructure affects the Seebeck coefficient of the material, enhancing it when compared to other electrodeposited nanostructures. As a result, both the reduction of thermal conductivity and increase of Seebeck coefficient produce an **enhancement in the thermoelectric efficiency** of the nanostructured material.

Then, as a whole, the **main conclusion of this work** is that **nanostructuration plays an important role in the properties of different materials**, **and the route envisaged in this thesis**, that is, 3D-AAO fabrication and electrochemical replica of the 3D-porous structure**, provides an interesting platform to study these new properties and design materials with desired properties** for different applications. Also, it is important to remark again that their fabrication is done with **easily scalable methods** (aluminium anodization and electrochemical deposition), which makes them attractive candidates for their implementation in real devices.

Appendix A. Predicting structural color formation

A.1. Modeling the multilayered structure of the 3D AAO membranes
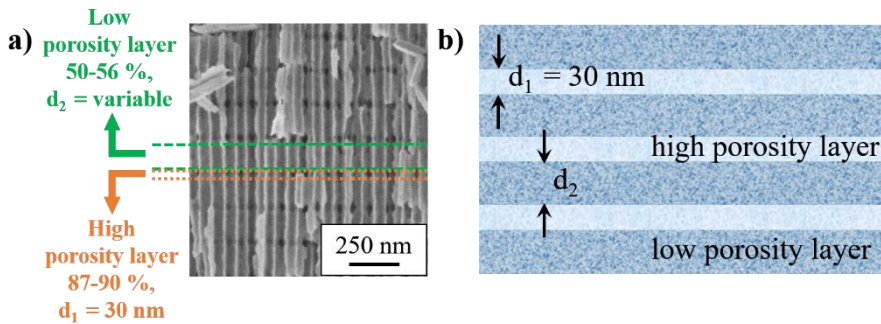
Figure A.1. *a) 3D porous structure of the alumina membranes fabricated in this thesis, which is characterized by a two layer periodic structure, d_1 and d_2, with high and low porosity. b) Schematic of the periodic metamaterial with periodic composition of high-porosity and low-porosity layers characterized by the corresponding effective index value.*

We prepared anodic alumina mesoporous metamaterial samples that exhibit longitudinal pores of around 40−50 nm in diameter extending from the top down, perpendicular to the aluminum surface, and transversal pores of around 30 nm in diameter, which connect longitudinal pores, see Figure A.1a. The horizontal layers with transversal pores can be formed with predefined periodicity in the vertical direction, as explained in detailed in section 2.1.1.2. The inner 3D porous structure of the 3D AAO membranes can be modeled employing a multilayered structure composed of two alternating layers, d_1 and d_2, as shown in Figure A.1b. Each horizontal layer is characterized by an average porosity value. High-porosity layers correspond to the layers with intersecting longitudinal and transverse pores in the SEM image of Figure A.1a, while low-porosity layers are the layers with only longitudinal pores in the fabricated samples.

Bulk alumina is a dielectric material transparent across the visible spectral range [460]. In turn, nanoporous alumina samples can be characterized by effective refractive indices of high- and low porosity layers, which in this work were calculated via the Maxwell−Garnett theory,

$$\varepsilon_{eff} = \varepsilon_m(2p(\varepsilon_a - \varepsilon_m) + \varepsilon_a + 2\varepsilon_m)/(2p(\varepsilon_m - \varepsilon_a) + \varepsilon_a + 2\varepsilon_m) \qquad (A.1)$$

, where ε_m is the permittivity of the material (i.e., alumina), ε_a is the permittivity of the ambient medium (e.g., air or water), and p is the porosity of the material. The porosity values used in the modeling (65/80) were chosen by training the model on measured spectra of multiple fabricated samples to find the unique porosity values that match all the experimentally observed spectral bands of all the samples in the training set.
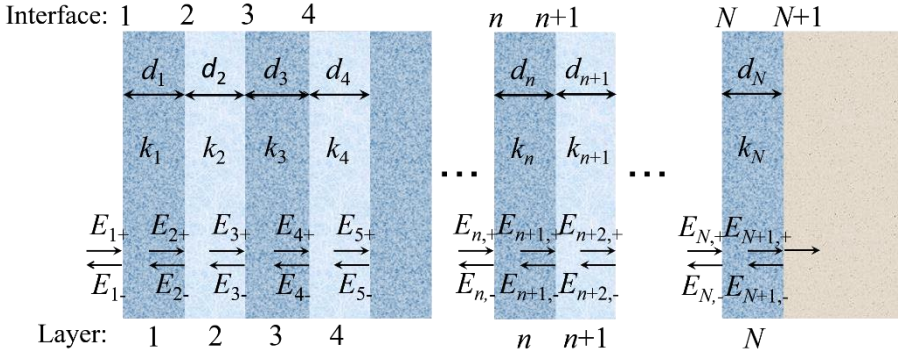
Figure A.2. *Schematic of the modeled multilayer structure with numbering convention of interfaces, layer parameters, as well as the strengths of the incident and reflected electric fields at each interface used in the Transfer Matrix Method calculations.*

Next, predictions of the reflectance spectra of mesoporous metamaterial samples were done by using the semianalytical transfer matrix method (59,60) illustrated in Figure A.2. The reflection coefficient of a multilayered structure $R = |r_1|^2$ can be calculated by using a simple recursive formula,

$$r_n = \frac{E_{n-}}{E_{n+}} = \frac{\rho_n + r_{n+1}e^{-2ik_nd_n}}{1 + \rho_nr_{n+1}e^{-2ik_nd_n}}, n = N, N - 1, ... 1 \qquad (A.2)$$

, where ρ_n is the Fresnel reflection coefficient of the nth material interface, k_n is the normal component of the wavevector in the nth medium, and d_n is the thickness of the nth layer. The recursion is initialized by setting $rN+1 = \rho N+1$. The number of layers in all the calculated structures was equal to 150;

that is, they were composed of 75 periodically repeating pairs of highporosity and low-porosity layers. The spectral positions of the reflection bands (and thus the colorimetric response) do not depend on the number of layers in the structure (see Figure 3.8a), and $N = 150$ was simply chosen to achieve high reflectance within each stopband.
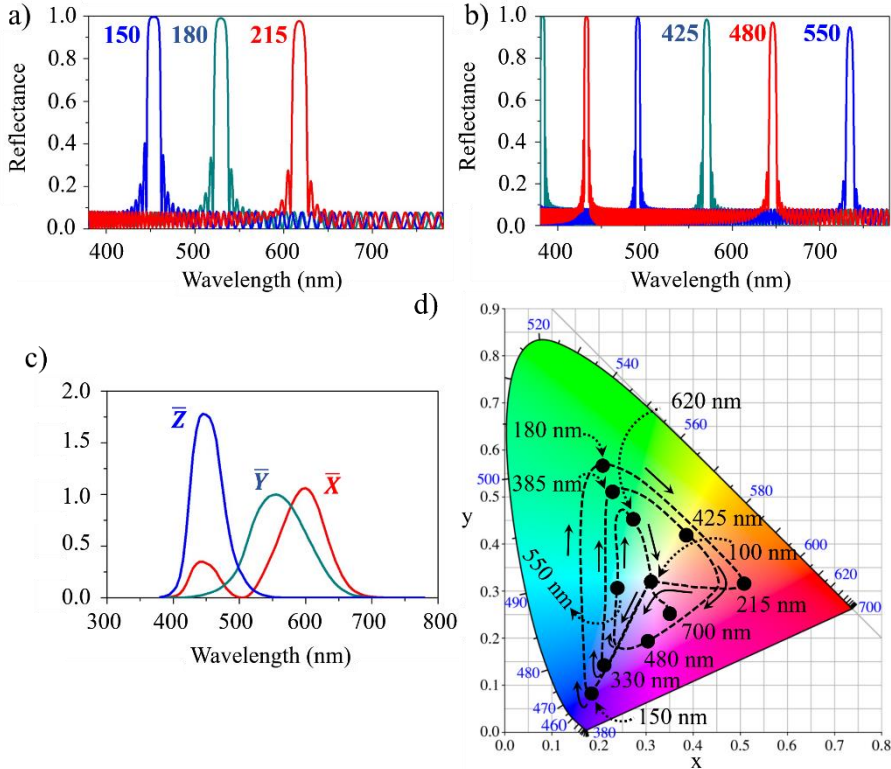
Figure A.3. a) and b) Calculated reflectance spectra of periodic (150 layers thick) structures with varying thickness of the low-porosity layer (with only longitudinal pores), $d_2 =$ 150, 180, 215, 425, 480 and 550, and fixed thickness of the high-porosity layer (with both longitudinal and transverse pores), $d_1 = 30$ nm. c) CIE standard observer color matching functions. d) CIE color space representation (background) with the colors theoretically predicted for structures in Table A.1 shown as dots. The black dashed curve shows the color predictions for structures with continuously increasing low-porosity layer thickness, and the solid arrows illustrate the predicted color evolution direction.

Reflectance spectra of periodic structures predicted via modeling are shown in Figure A.3a and b for several gradually increasing values of sample periodicity, as summarized in table A.1. The high reflectivity peaks in the reflectance spectra in Figure A.3a, b correspond to the formation of the photonic band gaps in the material, where light propagation through the

material is forbidden, and strong reflection occurs instead [461, 462]. It can be seen that with the increased period of the structure (i.e., with increased distance $d_1 + d_2$), the first-order reflection band redshifts (Figure A.3a), and the higher-order bands eventually move into the visible frequency range (Figure A.3b). When compared with the experimental situation the predicted spectra showed good agreement with the measured spectra of the fabricated structures.

Table A.1. *Structural Parameters of the Periodic Mesoporous Structures with Varying Color Predicted by Modeling.*

Period, $d_1 + d_2$ (nm)	130	180	210	245	360	415	455	510	580	650	720
d_2 (nm)	100	150	180	215	330	385	425	480	550	620	700
peak position											
5th order										333	373
4th order									371	415	465
3rd order						353	383	433	492	551	618
2nd order					457	527	571	646	735	824	925
1st order	328	454	529	618	910	1049	1150	1290	1467	1643	1845
Color	white	blue	green	red	blue	green	yellow	purple	cyan	green	pink

Finally, to convert the reflectance spectra into the perceived color prediction for each structure, we used the CIE color space chromaticity diagram, introduced in 1931 by the International Commission on Illumination (CIE, Figure A.3d) [316]. Human eyes have three types of light-sensitive cone cell receptors, which have different sensitivities to different wavelengths in the solar spectrum (Figure A.3c). Combining these sensitivities with the reflectance spectra of different samples, we can predict the perceived color by characterizing it with two coordinates within the CIE color space. In particular, the color coordinates (X, Y) from the reflectance spectra have to be converted to the corresponding tristimulus values (x, y, z) of the CIE XYZ color matching functions. This is achieved by integrating the products of the reflectance coefficient $R(\lambda)$, the corresponding CIE color matching function (Figure A.3c), and the sunlight spectral power distribution,

$$X = \int R(\lambda)I(\lambda)\bar{X}(\lambda)d\lambda \tag{A.3}$$

$$Y = \int R(\lambda)I(\lambda)\bar{Y}(\lambda)d\lambda \tag{A.4}$$

$$Z = \int R(\lambda)I(\lambda)\bar{Z}(\lambda)d\lambda \tag{A.5}$$

and subsequently normalized them as

$$x = X/(X + Y + Z) \tag{A.6}$$

$$y = Y/(X + Y + Z) \tag{A.7}$$

The coordinates on the CIE colorimetric scale corresponding to the calculated reflection spectra of the structures with varying periodicity listed in Table A.1 are shown as black dots in Figure A.3d. They are connected by a black line, which illustrates the evolution of the predicted color with the gradual change of the structure period. Our modeling predicts that by simply varying the period of the structure, we can engineer samples exhibiting structural colors spanning the whole gamut of visible colors achievable with standard RGB technologies. Structures with the smallest periodicities ($d_1 + d_2 \leq 130$ nm) are expected to exhibit no color due to the absence of the forbidden gaps in the visible frequency range (we label them as white, while they are actually nearly completely transparent just like the bulk alumina). With the increase of the structure period, the forbidden band redshifts (see Table 1),

and blue coloring of structures is predicted to emerge, which evolves into green and then red as the period is increased and the reflection band moves through the visible range. As the period of the modeled structures is increased even further, the predicted color converges gradually toward white in the center of the color scale. This is a result of additive color formation due to reflection within multiple forbidden frequency bands, and it is in stark contrast to the pigment color formation mechanism. Pigments produce black color if mixed, owing to additive absorptance of mixed single-color substances [322]. In turn, mixing of reflected light of different wavelengths spanning the whole visible spectrum yields white color (Chapter 3, Figure 3.6).
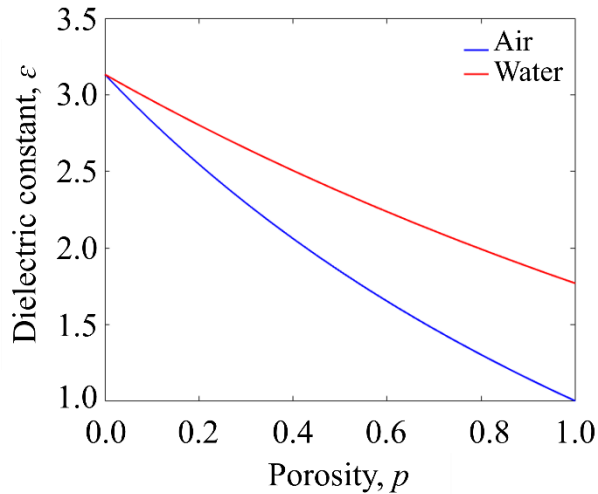
Figure A.4. The effective dielectric constant of porous alumina calculated at a wavelength of 550nm via Maxwell-Garnett method as a function of material porosity. Two cases are considered: pores filled with air (blue line) and pores filled with water (red line).

This model could be also trained in different media. In this work, we have also evaluated the effective reflective index of the 3D porous alumina membranes in water. Figure A.4 shows the effective dielectric constant of porous alumina calculated at a wavelength of 550 nm via Maxwell-Garnett method when ores filled with air (blue line) and pores filled with water (red line) The dielectric constant of bulk Al_2O_3 at this frequency is 3.1329 (n=1.77) [460], and the dielectric constant of water is 1.777 (n=1.333) [463].

Simulations were performed by Yoichiro Tsurimakiat the department of Mechanical Engineering, Massachusetts Institute of Technology, Cambridge, MA 02139, USA.

Appendix B. Micromagnetic simulations

B.1. **Major Cyclic Hysteresis Loops**
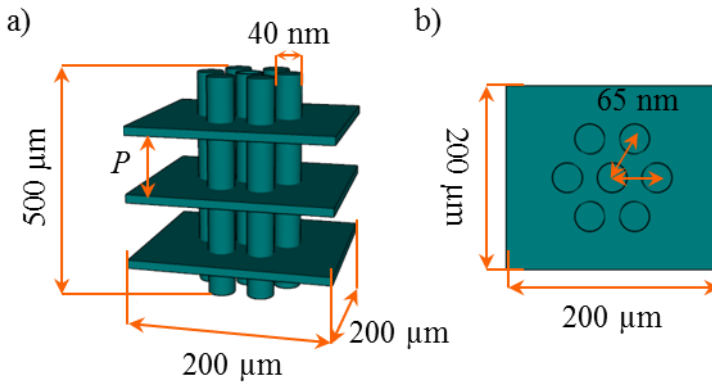
Figure B.1. Representation of the simplified geometry of the 3DNNs used in the simulations. All the parameters are fixed except the distance between planes, P, which has been varied between 10 and 500 nm a) transversal view and b) top view.

Major cyclic hysteresis as a function of the geometry of the structure were simulated using the OOMMF code. The 3DNN structures were simulated considering a simplified geometry, as it is schematically shown in Figures B. 1a and 1b, from cross view and top view, consisting of vertical nanowires and transversal planes of the material, which are used as a simplification of the TCs. The diameter of the nanowires was set at 40 nm for the simulations, the distance between nanowire neighbors was chosen to be 65 nm and the thickness of the planes was fixed at 35 nm. Simulations were run on a fixed number of 7 nanowires in a hexagonal array (one located at the center surrounded by the other six), after confirming that increasing the number of simulated nanowires up to 19 did not produce any qualitative changes in the simulated cycles but increases the time that takes to run the simulations. Also, a fixed number of 3 planes were used for all the simulations (increasing the number of transversal planes up to 5 and 10 only showed to increase the simulation time, but no other changes were observed). Also, according to the

XRD and t-EBS results samples are polycrystalline and thus, it was assumed that the values of the magnetocrystalline (K_I= 0.0 J/m^3) and magnetoelastic anisotropy terms of the magnetic energy average to zero. The saturation value, M_S = 490 ·10^3 A/m, which corresponds to Ni was introduced during the simulations. Then, simulations were performed varying the distance between the transverse planes of material from 10 to 500 nm as shown in Figure 4.7b to 4. 8f in Chapter 4.

In the case of Co , during the simulations, the saturation magnetization was set at 1400 ·10^3 A/m and the additional contribution of anisotropy within the IP direction was also included, for which magnetocrystalline term corresponding to HCP Co has been taken as K_I= 4.3·10^5 J/m^3.

Simulations were done by Dr. Sandra Ruiz Gómez from the Universidad Complutense de Madrid (Spain).

B.2. **Magnetization reversal mechanism**

FORC analysis and interpretation are not straightforward and require further simulations to corroborate any drawn conclusions from the experimental results. Accordingly, micromagnetic simulations were performed using MuMax3.10 software [337]. Based on the morphological analysis of our samples (see Chapter 4) and computational limitations, the 1DNW has been modelled including an array of 12 nanowires with 55 nm diameter, 4 µm of length, and distributed in a hexagonal compact packed (*hcp*) configuration with a center-to-center NW distance of 65 nm. Next, 3DNNs were simulated by adding TCs distributed in levels that have been separated by 250 and 460 nm for 3DNN255 and 3DNN450, respectively. Regarding the magnetic parameters, the standard values for the micromagnetic simulation of Ni NWs were used such as a magneto-crystalline anisotropy constant of K_C= -4.8 x 10^4 erg/cm^3, an exchange stiffness constant of A = 3.4 x 10^{-7} erg/cm, and a magnetization value of M_S = 490 emu/cm^3 [464]. In addition, random 3D Voronoi tessellation was implemented to emulate the size effect of the crystalline grains in the nanostructures. The grain sizes were chosen according to those obtained from the XRD analysis. Both K_C and the exchange coupling between grains were settled to be reduced by 10%. As the Ni exchange length is $l_{ex} \approx$ 4.8 nm, the cell size was chosen to be (3 x 3 x 4) nm^3, and the damping parameter was taken as 0.5 to ensure rapid convergence. Periodic Boundary Conditions (PBC) in the sample plane were included in our simulations.

Simulations were performed by Dr. Ruy Sanz González at Instituto Nacional de Técnica Aeroespacial (INTA), Madrid (Spain).

Appendix C.   Fundamentals   of Thermoelectricity.   Electrical   and thermal transport simulations

C.1.   **Fundamental principles behind thermoelectricity**

C.1.1. Sebeeck, Peltier and Thomson's effects

The first two refer to two opposite phenomena occurring at the junctions between two different conductive or semi-conductive materials, A and B. This connected pair is called a thermocouple. If a temperature gradient is established between the two junctions, due to the different nature of each of the materials (A and B) a potential difference is produced at the two ends where A and B are connected, generating a circulating current in the circuit. This effect is known as the Seebeck effect and mathematically it can be expressed as

$$S_{AB} = S_B - S_A = \frac{\Delta V_B}{\Delta T} - \frac{\Delta V_A}{\Delta T} \tag{C.1.1}$$

, where S_{AB} is the Seebeck coefficient measured in V/K between the two junctions of the thermocouple. S_A and S_B are the absolute Seebeck coefficients of the two materials, A and B, respectively. ΔV_A and ΔV_B are the potential differences that are generated across each material, A and B, as a temperature gradient, ΔT, is applied at the junctions of the two.

The contrary effect was discovered by Peltier, and it is named after him. In this case, as an electric current is injected through the thermocouple one of the junctions increases its temperature while the other sees it reduced. This is due to the transfer of charge carriers from one junction to the other; the one that donates the charge loses heat and the receiver absorbs the heat. The heat flow between the two junctions depends on the direction in which the current is made to flow in the circuit. The Peltier heat generated at the junction per unit is,

$$\dot{Q} = (\Pi_B - \Pi_A)I = \Pi_{AB}I \qquad (C.1.2)$$

in which Π_{AB} is the Peltier coefficient of the thermocouple, while Π_A and Π_B are the individual Peltier coefficients of conductors A and B. I is the electric current.

Separately, the Thomson coefficient considers a single material. It describes the heating or cooling in each material individually when there is an electric current and a simultaneous temperature gradient within the conductor. The heat production rate per unit volume, which will be produced by the conductor as a current density, J, is passed through, can be obtained from the following equation,

$$q = \rho J^2 - \mu J \frac{dT}{dx} \qquad (C.1.3)$$

in this expression, ρ is the resistivity of the material, $\frac{dT}{dx}$ is the temperature gradient across the material and μ is the Thomson coefficient.

The first term of the equation, ρJ^2, represents the none reversible Joule heating of the conductor. And the second one is the actual heat produced by the Thomson effect, which varies sign depending on the direction of J.

If the contribution of Joule heat is neglected, then, the relationships between the three coefficients are as follow

$$\Pi = S \cdot T \qquad (C.1.4)$$

This relation expresses the connection between the Peltier and Seebeck coefficients, Π and S, through the absolute temperature T. In turn, their relationship to the Thomson coefficient, μ, is given by

$$S = \int \frac{\mu}{T} dT \qquad (C.1.5)$$

According to this, the different coefficients are used to describe the same physical principles but paying attention to different phenomena, that is, power generation or heat removal. The dual and reversible character of this phenomenon has been most useful in the fabrication of power generators and cooler devices.

C.2. **Thermoelectric devices efficiency: the figure of merit, zT.**

A thermoelectric device is formed by multiple repeating units, known as modules, electrically and thermally connected. Each module is composed of, if only semiconductors are employed as components, an n-type (with negative charge carriers) and a p-type (positive charge carries) leg. Depending on the applied source (heat or current) this device presents two possible working modes: power generation or refrigeration, represented in Figure C.1, images to the left and right, respectively.
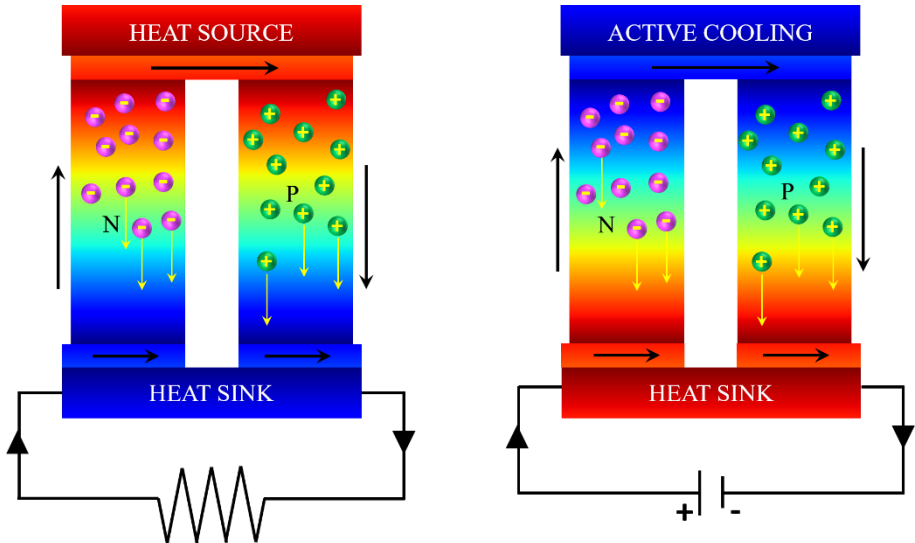
Figure C.1. Thermoelectric generator (left) and thermoelectric cooler (right) modules.

The efficiency of this device depends on the material thermoelectric performance, which is related to its thermoelectric figure of merit *zT*,

$$zT = \frac{S^2 \cdot \sigma}{\kappa} T$$

(C.2.1)

, where *S, σ* and *κ* are the Seebeck coefficient, the electrical and thermal conductivity of the material, respectively. The product of the squared of the Seebeck coefficient times the electrical conductivity, $S^2 \cdot \sigma$, is also known as the power factor, *PF*. The thermal conductivity, κ, includes the transport of heat through phonons (κ_{ph}) and electrons (κ_e), $\kappa = \kappa_{ph} + \kappa_e$. And *T* is the absolute temperature.

Then, the efficiency of the whole decive can be expressed in terms of the figure of merit of each of its components as

$$\eta \ (\%) = 100(\frac{T_H - T_C}{T_H})\frac{\sqrt{1 + zT} - 1}{\sqrt{1 + zT} + (T_H/T_C)}$$

(C.2.2)

, in which η is the efficiency of the material, T_H is the temperature on the hot side and T_C is the temperature at the other end, known as the cold side, which is set at a lower temperature ($T_C < T_H$).

Table .C.1. *Thermoelectric properties of insulators, semiconductors, and metals, taken from reference [465].*

	Insulators	Semiconductors	Metals
S (µV/K)	~ 1000	~ 200	~ 5
σ (Ω·m)$^{-1}$	~ 10^{-12}	~ 10^3	~ 10^6
κ (W/m·K)	~ $2 \cdot 10^{-2}$	~ $2 \cdot 10^{-2}$	~ 10^1
z (K^{-1})	~ $5 \cdot 10^{-17}$	~$2 \cdot 10^{-3}$	~ $3 \cdot 10^{-6}$

Materials can be classified into three different groups according to their transport properties: conductors, semiconductors, and insulators (see Table C.1). From *equation C.2.1*, it is clear that a good thermoelectric material must present a high *PF* ($S^2 \cdot \sigma$) and reduced κ. However, these three parameters are deeply entwined in classical physics, which makes it hard to find a material that fulfills such requirements, simultaneously. And hence, it is not trivial to be able to increase or reduce one magnitude without simultaneously affecting the others.

In general terms, conductor materials present the highest conductivities, for both electrical and thermal transport, and the lowest Seebeck coefficients. On the contrary, insulators have reduced thermal conductivity and the largest S but too small values of σ. Which leaves us with semiconductors as the best-suited materials for thermoelectric applications. Semiconductors with carrier concentrations between 10^{19} - 10^{20} cm^{-3}, show the best compromise between all three parameters, possessing sufficiently high S and σ and still reduced κ. This is illustrated in Figure C.2, in which the evolution of the *zT*, σ, S, and κ

insulator semiconductor metal

$10^{20}10^{21}$

Carrier concentration (cm^{-3})
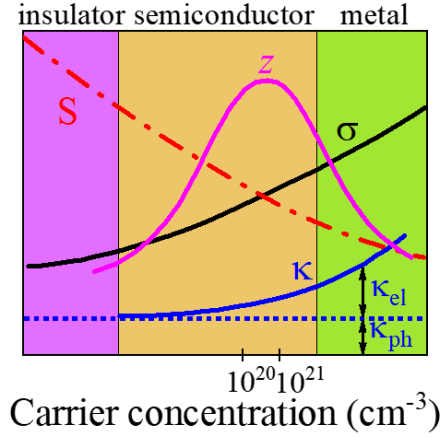
Figure C.2. Illustrates the z (pink line), σ (black), S (red dashed-dotted line), and κ (blue) as a function of the carrier concentration, distinguishing between insulators, semiconductors, and metals. Data were taken from references [373, 465, 466].

as a function of the carrier concentration are plotted together and where a maximum of the *zT* was predicted in the range of $n = 10^{19}$ - 10^{21} cm^{-3}, corresponding to a semiconducting regimen [372, 465, 466].

C.2.1. Relation between the different transport properties that define the Figure of merit, zT.

The Seebeck coefficient is inversely proportional to the carrier concentration, *n*, but it is directly related to the effective mass of the charge carries (electrons or holes), *m**,

$$S \sim \frac{m^*}{n^{2/3}} \tag{C.2.3}$$

While the electrical conductivity follows the opposite trend,

$$\sigma = \mu \cdot n \cdot q = \frac{n \cdot q^2 \cdot \tau}{m^*} \ with \ \mu = \frac{q\tau}{m^*} \tag{C.2.4}$$

, where *q* is the charge of the carriers, *n* carrier concentration or carrier density, and *μ* is the mobility of the carriers, which depends inversely to the effective mass, *m**, and *τ* is the relaxation time of the carriers between two successive collision events.

So if a material has a high *σ*, its *S* is affected oppositely and the *PF* is not raised.

Also, the σ and κ are coupled through the thermal conduction of the electrons (κ_e). According to the Wiedemann-Franz Law

$$\kappa_e = L \cdot \sigma \cdot T \qquad\qquad (C.2.5)$$

, in which κ_e is proportional to the electrical conductivity, σ, and to the temperature, T. L is a proportionality constant, called the Lorenz number.

C.3. Simulations of the electrical conductivity of the Bi₂Te₃ 3DNNs

C.3.1. Electrical resistance along the in plane direction (along transverse connection, TCs)
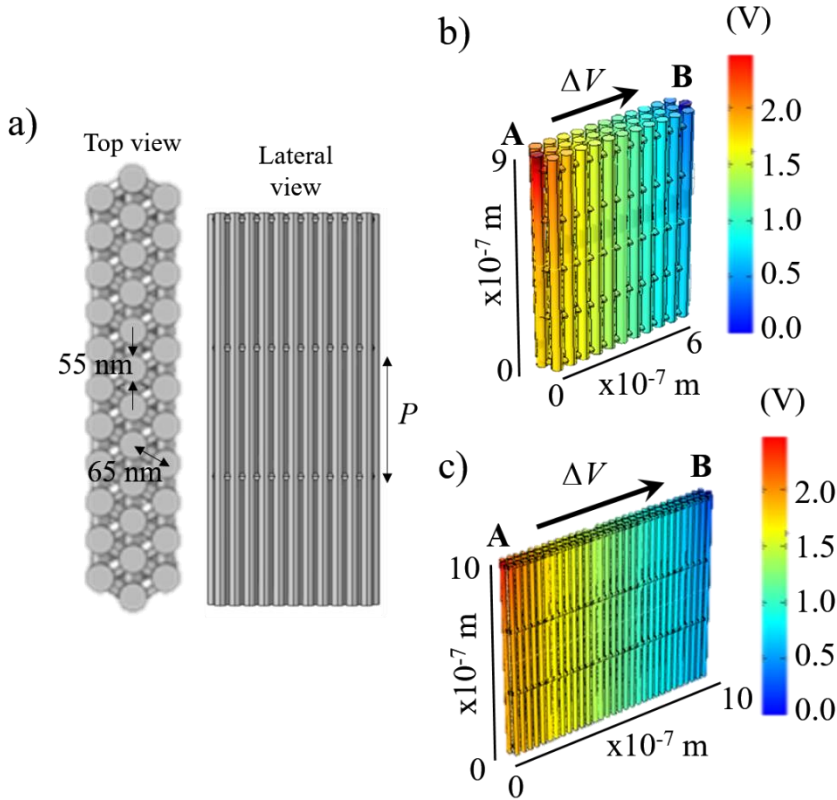
Figure C.3. *a) top view and side view of the 3D nanowire structure used in the COMSOL model. b) and c) results of the steady state solution when the terminals are located at the ends named as A and B.*

Simulations were made to study in more detail the role played by the transversal connections along the nanowires in the measured in-plane resistance of the samples. For which the resistance as a function of the increasing distance between transversal connections was simulated using COMSOL Multiphysics. The intrinsically anisotropic electrical conductivity was taken from the measurements in electrodeposited films [380] and introduced in the electrical conductivity tensor of the material. Then, the steady-state electric potential for a system of N nanowires was simulated, imposing a potential difference in two different nanowire terminals, in analogy with experiments (see Figure C.4b and C.4c for the results obtained in two different structures when modifying the number of nanowires, and thus increasing the distance between the terminals).

Additionally, the model was fed with the actual morphological parameters of the nano-networks, simulating arrays of 16 to under 100 interconnected nanowires with the physical parameters of electrodeposited Bi_2Te_3 samples, this is illustrated in Figure C.3a. Simulations were carried out by Dr. Olga Caballero Calero.

C.4. **Simulations of the thermal conductivity of the Bi_2Te_3 3DNNs**

In this section, we show the complete system of partial differential equations, boundary conditions, and intrinsic material properties required for predicting the heat flux q and the temperature T both in the semiconductor and the oxide domains in steady-state conditions using COMSOL Multiphysics. Only a single periodically repeated geometry cell is simulated. We also show here the inclusion of the electron contribution to the thermal conductivity.

Simulations were performed by Albert Beardo and Dr. F. Xavier Álvarez from Universidad Autónoma de Barcelona (UAB).

C.4.1. Hydrodynamic heat transport model

Heat conduction in the semiconductor domains is described using the conservation of energy (*equation C.4.1*) and the hydrodynamic heat transport equation (*equation C.4.2*) in steady-state [445-447],

$$\nabla \cdot q = 0 \qquad\qquad\qquad (C.4.1.)$$

$$q = -\kappa\nabla T + \ell^2\nabla^2 q \qquad\qquad (C.4.2)$$

, where T is the temperature, q the heat flux, κ the bulk thermal conductivity, introducing κ =2.3 W/mK for bulk Bi_2Te_3 (in the direction perpendicular to the c-axis, see Table 5.1). In *equation C.4.2*, non-local or viscous effects due to the system boundaries are included within the Laplacian term ($\ell^2\nabla^2 q$), here ℓ is the weighted average phonon mean free path, known as non-local length [448], which gives an idea about the system sizes where boundary effects are noticeable.

Additionally, this model incorporates two boundary conditions: one that imposes thermal insulation outside the material,

$$q \cdot n = 0 \qquad\qquad (C.4.3)$$

and a second one that considers the heat flux tangential at the material's boundary,

$$q_t = -C\ell\nabla q_t \cdot \boldsymbol{n} \qquad\qquad (C.4.4)$$

, where $\boldsymbol{n}$ points away from the material and subindex t denotes the tangent-to-the-surface heat flux component. The slip coefficient C depends on the fraction of specular phonon reflections on the boundary, as discussed in [446]. Here we assume diffusive boundary reflections so that C=1. This last condition allows modelling the heat flux reduction in a region of size ℓ near the Bi_2Te_3 nanowire surface due momentum destruction during phonon-boundary scattering.

The 3D geometry of the nano-networks was taken into account by performing the simulations in a single periodically repeated cell that features a nanowire with only one TC level, the length of the straight wire above and below the TCs is defined by P. Hence, the vertical length of the whole unit cell is delimited by P. Accordingly, the effective lattice thermal conductivity of isolated Bi_2Te_3 structures was calculated as

$$\kappa_{latt} = \frac{\int_A q \cdot n dA}{A\Delta T/P} \qquad\qquad (C.4.5)$$

, where $\Delta T/P$ is the temperature gradient imposed along the NW direction (out-of-plane), in which the dimension of the simulated unit cell is defined by the distance P between transverse connections of the 3DNNs, and A is the cross-section area transversal to the temperature gradient.

To calculate the effective thermal conductivity along the NW direction (out-of-plane), simulations were performed applying heat flux periodic boundary conditions and imposing a temperature difference $\Delta T = 1$ K in the NW terminals. And then, we solve *equation C.4.5*.

Predicting the effective thermal conductivity in the in-plane direction, that is, along the TCs direction, using the presented isotropic model, requires using the adequate lattice thermal conductivity tensor, that is $\kappa_{\parallel c} = 0.9$ W/mK, instead of introducing $\kappa_{\perp c} = 2.3$ W/mK.

Furthermore, in this configuration, the temperature difference is imposed in the in plane direction, between two opposed TCs of the same nanowire, which implies modifying the cross-section for integration in *equation C.4.5*.

C.4.2. Fourier transport model

In previous simulations only the filling material, Bi_2Te_3, was considered but to compare the theory with experiments we must incorporate the contribution of the 3D-AAO membrane to the thermal conductivity in the composite material.

In this regard, during the simulations, the oxide domains fill all the space which is not occupied by the Bi_2Te_3 network in each periodically repeated cell. In contrast to Bi_2Te_3, the phonon mean free paths in the oxide are much smaller than the geometry characteristic sizes (around only 5 nm [449] vs, tens of nm), and hence, non-local effects are not expected, and Fourier's law can be used to describe these domains.

$$q_\Gamma + \kappa_{ox} \nabla T_\Gamma = 0 \qquad \qquad (C.4.6)$$

, where $\kappa_{ox} = 1.25$ W·m^{-1}·K^{-1} is the oxide bulk thermal conductivity, q is the local heat flux density, and ∇T is the temperature gradient. Sub-index Γ denotes heat flux and the temperature in the oxide domains.

Simulations were run introducing $\kappa_{ox}=1.25$ W·m^{-1}·K^{-1} [299] in *equation C.4.6* and substituting the thermal insulation boundary condition, *equation C.4.3*, (at the Bi$_2$Te$_3$-air interface) for heat flux continuity between the alumina oxide/Bi$_2$Te$_3$ semiconductor interfaces as

$$q \cdot n = q_\Gamma \cdot n \qquad\qquad (C.4.7)$$

While the boundary condition in *equation C.4.4* does not apply in the oxide region. And inducing a temperature difference of $\Delta T = 1$ K

Finally, from the resulting stationary solutions, we calculate the effective lattice thermal conductivity, κ_{latt}, of the Bi$_2$Te$_3$ structures embedded in the oxide matrix according to *equation C.4.5*, considering both the area covered by Bi$_2$Te$_3$ 3D networks and the oxide.

C.4.3. *Electronic contribution to the total thermal conductivity*

Knowing the electrical conductivity along the Bi$_2$Te$_3$ nanowire, we can use the Wiedemann-Franz law (*equation C.2.5*), where $L=2.44\cdot10^{-8}$ WΩK^{-2} and calculate the electronic contribution to the thermal conductivity, κ_{el}, for this material. Assuming that the out-of-plane electrical conductivity of the 3D network in the direction of the NW is the same as in the isolated NW (the TnCs are not expected to influence electronic transport in the out-of-plane direction), we have employed $\sigma = 3\cdot10^4$ S/m from reference [237], which corresponds to the electrical conductivity in the out-of-plane direction (perpendicular to the *c*-axis) of the Bi$_2$Te$_3$ NWs of the same sizes as ours. We have decided not to employ the experimental values of the out-of-plane electrical conductivity, $\sigma_\perp$, measured in this thesis (see section 5.4.1) due to the high dispersion of the data.

Then, from *equation C.2.5* we obtained $\kappa_{el} = 0.22$ W·m^{-1}·K^{-1}1, the electronic thermal conductivity is weighted by the areal density x_{NW} covered by the NWs with respect to the full structure including the oxide, so that the contribution of the electronic thermal conductivity is $x_{NW} \cdot \kappa_{el}=0.14$ W·m^{-1}·K^{-1}. This value was obtained from the representation of the structure in COMSOL, giving $x_{NW} = 0.64$.

Analogous calculations using the experimentally measured electrical conductivity in the in-plane direction are done to calculate the electronic contribution to the thermal conductivity in the direction of the TnCs (that is, in-plane).

Appendix D. List of publications, contributions to conferences and other scientific activities.

D.1. **Published articles (as first author):**

1) Alejandra Ruiz-Clavijo, Olga Caballero-Calero, Cristina V. Manzano, Xavier Maeder, Albert Beardo, Xavier Cartoixà, F. Xavier Álvarez, and Marisol Martín-González. 3D Bi_2Te_3 Interconnected Nanowire Networks to Increase Thermoelectric Efficiency. ACS Appl. Energy Mater., 4, 13556−13566. 13/01/2021 (DOI: 10.1021/acsaem.1c02129).

2) Alejandra Ruiz Clavijo; Olga Caballero Calero; Marisol Martín González. Revisiting anodic alumina templates: from fabrication to applications. Nanoscale. 13, pp. 2227 - 2265. Royal Society of Chemistry, 07/01/2021. (DOI: 10.1039/d0nr07582e).

3) Alejandra Ruiz Clavijo; Sandra Ruiz Gómez; Olga Caballero Calero; Lucas Pérez; Marisol Martín González.Tailoring magnetic anisotropy at will in 3D interconnected nanowire networks. Physica Status Solidi Rapid Research Letters. 13-10, pp. 1900263. 26/07/2019. (DOI:10.1002/pssr.201900263).

4) Alejandra Ruiz-Clavijo; Yoichiro Tsurimaki; Olga Cabllero Calero; George Ni; Gang Chen; Svetlana V. Boriskina; María Soledad Martín González. Engineering a full gamut of structural colors in all-dielectric mesoporous network metamaterials. ACS Photonics. 5 - 6, pp. 2120 - 2128. 10/05/2018. (DOI: 10.1021/acsphotonics.7b01569).

5) Alejandra Ruiz-Clavijo; Olga Caballero Calero; Marisol Martín González. Three-Dimensional Bi2Te3 Networks of Interconnected Nanowires: Synthesis and Optimization. Nanomaterials (MPDI). 8 - 5, pp. 345. 18/05/2018. (DOI: 0.3390/nano8050345).

D.2.   Participation in other publications:

1) Liliana Vera Londono; Alejandra Ruiz Clavijo; Olga Caballero Calero; Marisol Martín González. Understanding the thermal conductivity variations in nanoporous anodic aluminum oxide. Nanoscale Advances. 2, pp. 4591 - 4603. Royal Society of Chemistry, 17/08/2020. (DOI: 10.1039/D0NA00578A).

2) Begoña Abad; Jon Maiz; Alejandra Ruiz-Clavijo García-Serrano; Olga Caballero Calero; Marisol Martín González. Tailoring Thermal Properties of Materials via Three Dimensional Porous Alumina. Scientific Reports. 09/12/2016. (DOI: 10.1038/srep38595).

3) Pedro Campos Resende; Ruy Sanz; Alejandra Ruiz-Clavijo García-Serrano; Olga Caballero Calero; Marisol Martin Gonzalez. Cylindrical Three-Dimensional Porous Anodic Alumina Networks. Coatings. 6 - 59, pp. 1 - 7. MDPI, 09/11/2016. (DOI: 10.3390/coatings6040059).

D.3.   Works submitted to international conferences:

1) Title of the work: Self-standing three dimensional BiTe nanowire networks.
   Name of the conference: Virtual conference on thermoelectrics
   Type of event: Conference
   Type of participation: Participatory - oral communication
   City of event: Online,
   Date of event: 20/07/2021
   End date: 23/07/2021
   Authors: Alejandra Ruiz Clavijo; Olga Caballero Calero; Marisol Martín González.

2) Title of the work: Tunable magnetic anisotropy in 3D nanowire networks.
   Name of the conference: CMD2020GEFES
   Type of event: Conference
   Type of participation: Participatory - oral communication
   City of event: Madrid - online, Spain
   Date of event: 31/08/2020
   End date: 04/09/2020
   City organizing entity: GEFES,

Authors: Alejandra Ruiz Clavijo; Sandra Ruiz Gómez; Lucas Pérez; Olga Caballero Calero; Marisol Martín González.

3) Title of the work: Thermoelectric properties of bismuth telluride tridimensional nanostructures.
Name of the conference: EMRS Spring Meeting
Type of event: Conference
Type of participation: Participatory - oral communication
City of event: Niza, France
Date of event: 27/05/2019
End date: 31/05/2019
Authors: Alejandra Ruiz Clavijo; Olga Caballero Calero; Marisol Martín González.

4) Title of the work: Characterization of thermoelectric bismuth telluride tridimensional nanostructures.
Name of the conference: EMRS Spring Meeting 2017
Type of event: Conference
Type of participation: Participatory - oral communication
City of event: Strasbourg, France
Date of event: 22/05/2017
End date: 26/05/2017
Authors: Alejandra Ruiz Clavijo; Begoña Abad; Olga Caballero Calero; Marisol Martín González.

D.4. **Stays in public or private research centres:**

1) Entity: Leibniz Institute for Solid State and Materials Research
City of entity: Dresden, Germany
Start-End date: 03/09/2018 - 02/12/2018.   Duration: 3 months
Goals of the stay: Doctorate
Acquire skills developed: During the stay I have been acquainted and trained in instrumental techniques and process such as photolithography, scanning probe thermoelectric measurements at RT and electrical characterization at cryogenic temperatures.
Provable tasks: 1) Development of an electrochemical deposition process for layers and photolithographic microstructures of metallic antimony. 2) Development of an electrochemical powder consolidation process for thermoelectric materials.
Acquired skills developed: During the stay I have been acquainted and trained in instrumental techniques and process such as

photolithography, scanning probe thermoelectric measurements at RT and electrical characterization at cryogenic temperatures.

2) Entity: Institut Jean Lamour
   City of entity: Mezt, France
   Start-End date20/05/2018 - 02/06/2018.   Duration: 13 days
   Funding entity: i-LINK project
   Goals of the stay: Doctorate
   Provable tasks: Measurements of Nano-structured thermoelectric material.

7. Bibliography

1. Jun, Y., P. Nagpal, and D.J. Norris, *Thermally stable organic–inorganic hybrid photoresists for fabrication of photonic band gap structures with direct laser writing.* Advanced materials, 2008. **20**(3): p. 606-610.

2. Wong, S.H., et al., *Highly selective wet etch for high-resolution three-dimensional nanostructures in arsenic sulfide all-inorganic photoresist.* Chemistry of materials, 2007. **19**(17): p. 4213-4221.

3. George, M.C., et al., *Direct fabrication of 3D periodic inorganic microstructures using conformal phase masks.* Angewandte Chemie, 2009. **121**(1): p. 150-154.

4. Rauber, M., et al., *Highly-ordered supportless three-dimensional nanowire networks with tunable complexity and interwire connectivity for device integration.* Nano letters, 2011. **11**(6): p. 2304-2310.

5. Keller, L., et al., *Direct-write of free-form building blocks for artificial magnetic 3D lattices.* Scientific reports, 2018. **8**(1): p. 1-13.

6. Donnelly, C., et al., *Element-specific X-ray phase tomography of 3D structures at the nanoscale.* Physical review letters, 2015. **114**(11): p. 115501.

7. Masuda, H., H. Tanaka, and N. Baba, *Preparation of porous material by replacing microstructure of anodic alumina film with metal.* Chemistry letters, 1990. **19**(4): p. 621-622.

8. Schwirn, K., et al., *Self-Ordered Anodic Aluminum Oxide Formed by H2SO4 Hard Anodization.* ACS Nano, 2008. **2**(2): p. 302-310.

9. Manzano, C.V., J. Martín, and M.S. Martín-González, *Ultra-narrow 12nm pore diameter self-ordered anodic alumina templates.* Microporous and Mesoporous Materials, 2014. **184**: p. 177-183.

10. Lee, W., et al., *Fast fabrication of long-range ordered porous alumina membranes by hard anodization.* Nature Materials, 2006. **5**(9): p. 741-747.

11. Vega, V., et al., *Unveiling the Hard Anodization Regime of Aluminum: Insight into Nanopores Self-Organization and Growth Mechanism.* ACS Applied Materials & Interfaces, 2015. **7**(51): p. 28682-28692.

12. Li, Y., et al., *Fabrication of highly ordered nanoporous alumina films by stable high-field anodization.* Nanotechnology, 2006. **17**(20): p. 5101-5105.

13.   Akiya, S., et al., *Self-ordered porous alumina fabricated via phosphonic acid anodizing.* Electrochimica acta, 2016. **190**: p. 471-479.

14.   Takenaga, A., et al., *Self-ordered aluminum anodizing in phosphonoacetic acid and its structural coloration.* ECS Solid State Letters, 2015. **4**(8): p. P55-P58.

15.   Ono, S., M. Saito, and H. Asoh, *Self-ordering of anodic porous alumina formed in organic acid electrolytes.* Electrochimica Acta, 2005. **51**(5): p. 827-833.

16.   Kikuchi, T., et al., *Fabrication of Self-Ordered Porous Alumina via Etidronic Acid Anodizing and Structural Color Generation from Submicrometer-Scale Dimple Array.* Electrochimica Acta, 2015. **156**: p. 235-243.

17.   Akiya, S., et al., *Nanostructural characterization of large-scale porous alumina fabricated via anodizing in arsenic acid solution.* Applied surface science, 2017. **403**: p. 652-661.

18.   Martín, J., C.V. Manzano, and M. Martín-González, *In-depth study of self-ordered porous alumina in the 140–400 nm pore diameter range.* Microporous and Mesoporous Materials, 2012. **151**: p. 311-316.

19.   Martín, J., et al., *High-aspect-ratio and highly ordered 15-nm porous alumina templates.* ACS applied materials & interfaces, 2013. **5**(1): p. 72-79.

20.   Ferro, L.M., et al., *Use of multivariate analysis on Fabry-Pérot interference spectra of nanoporous anodic alumina (NAA) for optical sensors purposes.* Sensors and Actuators B: Chemical, 2017. **248**: p. 718-723.

21.   Kumeria, T., et al., *Advanced Structural Engineering of Nanoporous Photonic Structures: Tailoring Nanopore Architecture to Enhance Sensing Properties.* ACS Photonics, 2014. **1**(12): p. 1298-1306.

22.   Lee, J., et al., *Graded-lattice AAO photonic crystal heterostructure for high Q refractive index sensing.* RSC Advances, 2015. **5**(88): p. 71770-71777.

23.   Chen, Y., et al., *Rational design of photonic dust from nanoporous anodic alumina films: A versatile photonic nanotool for visual sensing.* Scientific reports, 2015. **5**: p. 12893.

24.   Sriram, G., et al., *Current trends in nanoporous anodized alumina platforms for biosensing applications.* Journal of Nanomaterials, 2016. **2016**.

25.   Tabrizi, M.A., J. Ferré-Borrull, and L.F. Marsal, *Highly sensitive IRS based biosensor for the determination of cytochrome c as a cancer marker by using nanoporous anodic alumina modified with trypsin.* Biosensors and Bioelectronics, 2020. **149**: p. 111828.

26.   Lednicky, T. and A. Bonyár, *Large Scale Fabrication of Ordered Gold Nanoparticle–Epoxy Surface Nanocomposites and Their*

Application as Label-free Plasmonic DNA Biosensors. ACS Applied Materials & Interfaces, 2020.

27. Porta-i-Batalla, M., et al., *3D nanoporous anodic alumina structures for sustained drug release.* Nanomaterials, 2017. **7**(8): p. 227.

28. Simovic, S., D. Losic, and K. Vasilev, *Controlled drug release from porous materials by plasma polymer deposition.* Chemical communications, 2010. **46**(8): p. 1317-1319.

29. Jeon, G., et al., *Electrically actuatable smart nanoporous membrane for pulsatile drug release.* Nano letters, 2011. **11**(3): p. 1284-1288.

30. Kumeria, T., et al. *Modulating molecular transport across peptide-modified nanoporous alumina membranes with light*. in *SPIE BioPhotonics Australasia*. 2016. International Society for Optics and Photonics.

31. Porta-i-Batalla, M., et al., *Sustained, controlled and stimuli-responsive drug release systems based on nanoporous anodic alumina with layer-by-layer polyelectrolyte.* Nanoscale research letters, 2016. **11**(1): p. 372.

32. Mebed, A.M., A.M. Abd-Elnaiem, and N.M. Al-Hosiny, *Electrochemical fabrication of 2D and 3D nickel nanowires using porous anodic alumina templates.* Applied Physics A, 2016. **122**(6): p. 565.

33. Domínguez-Adame, F., et al., *Nanowires: A route to efficient thermoelectric devices.* Physica E: Low-dimensional Systems and Nanostructures, 2019.

34. Manzano, C.V. and M. Martin-Gonzalez, *Electrodeposition of V-VI nanowires and their thermoelectric properties.* Frontiers in chemistry, 2019. **7**: p. 516.

35. Zhang, G., et al., *Design principle of telluride-based nanowire heterostructures for potential thermoelectric applications.* Nano letters, 2012. **12**(7): p. 3627-3633.

36. Wang, H.-P., et al., *Periodic Si nanopillar arrays by anodic aluminum oxide template and catalytic etching for broadband and omnidirectional light harvesting.* Optics express, 2012. **20**(101): p. A94-A103.

37. Shirai, Y., et al., *Improvement in carrier mobility of poly(3,4-ethylenedioxythiophene) nanowires synthesized in porous alumina templates.* Journal of Polymer Science Part B: Polymer Physics, 2011. **49**(24): p. 1762-1768.

38. O'Carroll, D., et al., *Poly(9,9-dioctylfluorene) Nanowires with Pronounced β-Phase Morphology: Synthesis, Characterization, and Optical Properties.* Advanced Materials, 2008. **20**(1): p. 42-48.

39. Manzano, C., et al., *Determining the diffusion mechanism for high aspect ratio ZnO nanowires electrodeposited into anodic aluminum oxide.* Journal of Materials Chemistry C, 2017. **5**(7): p. 1706-1713.

40. Frantz, C.d., et al., *Nonaqueous sol–gel synthesis of anatase nanoparticles and their electrophoretic deposition in porous alumina.* Langmuir, 2017. **33**(43): p. 12404-12418.

41. Bertero, E., et al., *Stainless steel-like FeCrNi nanostructures via electrodeposition into AAO templates using a mixed solvent Cr (III)-based electrolyte.* Materials & Design, 2020: p. 108559.

42. García, J., et al., *Template-assisted Co–Ni alloys and multisegmented nanowires with tuned magnetic anisotropy.* physica status solidi (a), 2014. **211**(5): p. 1041-1047.

43. Salem, M.S., et al., *Composition and diameter modulation of magnetic nanowire arrays fabricated by a novel approach.* Nanotechnology, 2018. **29**(6): p. 065602.

44. Ivanov, Y.P., et al., *Modulated magnetic nanowires for controlling domain wall motion: toward 3D magnetic memories.* ACS nano, 2016. **10**(5): p. 5326-5332.

45. Salem, M.S., et al., *Magnetic properties of cylindrical diameter modulated Ni 80 Fe 20 nanowires: interaction and coercive fields.* Nanoscale, 2013. **5**(9): p. 3941-3947.

46. Zhao, C., et al., *Coaxial carbon–silicon–carbon nanotube arrays in porous anodic aluminum oxide templates as anodes for lithium ion batteries.* Journal of Materials Chemistry, 2012. **22**(24): p. 12193-12197.

47. Proenca, M.P., et al., *6 - Cylindrical magnetic nanotubes: Synthesis, magnetism and applications*, in *Magnetic Nano- and Microwires (Second Edition)*, M. Vázquez, Editor. 2020, Woodhead Publishing. p. 135-184.

48. Žužek Rožman, K., et al., *Electrochemical synthesis and characterization of Fe70Pd30 nanotubes for drug-delivery applications.* Materials Chemistry and Physics, 2012. **133**(1): p. 218-224.

49. Seo, B.I., et al., *ZnO nanotubes by template wetting process.* Physica E: Low-dimensional Systems and Nanostructures, 2007. **37**(1): p. 241-244.

50. Norek, M., et al., *Morphological, structural and optical characterization of SnO2 nanotube arrays fabricated using anodic alumina (AAO) template-assisted atomic layer deposition.* Materials Characterization, 2018. **136**: p. 52-59.

51. Lee, J.S., et al., *Growth of Carbon Nanotubes on Anodic Aluminum Oxide Templates: Fabrication of a Tube-in-Tube and Linearly Joined Tube.* Chemistry of Materials, 2001. **13**(7): p. 2387-2391.

52. Alsawat, M., et al., *Carbon Nanotubes–Nanoporous Anodic Alumina Composite Membranes: Influence of Template on Structural, Chemical, and Transport Properties.* The Journal of Physical Chemistry C, 2017. **121**(25): p. 13634-13644.

53. Back, J.-W., et al., *Fabrication of conducting PEDOT nanotubes using vapor deposition polymerization.* Macromolecular Research, 2011. **19**(1): p. 33-37.

54. Byun, J., et al., *Ultrahigh Density Array of Free-Standing Poly(3-hexylthiophene) Nanotubes on Conducting Substrates via Solution Wetting.* Macromolecules, 2011. **44**(21): p. 8558-8562.

55. Córdova-Castro, R.M., et al., *Nanocone-based plasmonic metamaterials.* Nanotechnology, 2018. **30**(5): p. 055301.

56. Meng, G., et al., *A General Synthetic Approach to Interconnected Nanowire/Nanotube and Nanotube/Nanowire/Nanotube Heterojunctions with Branched Topology.* Angewandte Chemie International Edition, 2009. **48**(39): p. 7166-7170.

57. Sacco, L., et al., *Electrical and morphological behavior of carbon nanotubes synthesized within porous anodic alumina templates.* Journal of Physics: Materials, 2018. **1**(1): p. 015004.

58. Tian, Y., et al., *Y-branched Bi nanowires with metal–semiconductor junction behavior.* Applied Physics Letters, 2004. **85**(6): p. 967-969.

59. Chen, B., et al., *Branched Silicon Nanotubes and Metal Nanowires via AAO-Template-Assistant Approach.* Advanced Functional Materials, 2010. **20**(21): p. 3791-3796.

60. Li, X., et al., *Controlled Synthesis of Germanium Nanowires and Nanotubes with Variable Morphologies and Sizes.* Nano Letters, 2011. **11**(4): p. 1704-1709.

61. Mahima, S., et al., *Synthesis of Platinum Y-Junction Nanostructures Using Hierarchically Designed Alumina Templates and Their Enhanced Electrocatalytic Activity for Fuel-Cell Applications.* Chemistry of Materials, 2008. **20**(3): p. 601-603.

62. Jo, H., et al., *Fabrication of Chemically Tunable, Hierarchically Branched Polymeric Nanostructures by Multi-branched Anodic Aluminum Oxide Templates.* Langmuir, 2016. **32**(25): p. 6437-6444.

63. Zankowski, S.P. and P.M. Vereecken, *Combining High Porosity with High Surface Area in Flexible Interconnected Nanowire Meshes for Hydrogen Generation and Beyond.* ACS Applied Materials & Interfaces, 2018. **10**(51): p. 44634-44644.

64. Kim, N., et al., *Impact of pore size, interconnections, and dynamic conductivity on the electrochemistry of vanadium pentoxide in well defined porous structures.* Physical Chemistry Chemical Physics, 2018. **20**(47): p. 29708-29716.

65. Ruiz-Clavijo, A., et al., *Tailoring Magnetic Anisotropy at Will in 3D Interconnected Nanowire Networks.* physica status solidi (RRL) – Rapid Research Letters, 2019. **13**(10): p. 1900263.

66. Ruiz-Clavijo, A., O. Caballero-Calero, and M. Martín-González, *Three-Dimensional Bi2Te3 Networks of Interconnected Nanowires: Synthesis and Optimization.* Nanomaterials, 2018. **8**(5).

67. Resende, P.M., et al., *Cost-Effective, Flexible, Hydrophobic, and Tunable Structural Color Polymeric Bragg Reflector Metastructures.* Advanced Optical Materials, 2018. **6**(21): p. 1800408.

68. García-Barberá, A., et al., *Three dimensional PEDOT nanowires network.* Synthetic Metals, 2016. **220**: p. 208-212.

69. Navas, D., F. Ilievski, and C.A. Ross, *CoCrPt antidot arrays with perpendicular magnetic anisotropy made on anodic alumina templates.* Journal of Applied Physics, 2009. **105**(11): p. 113921.

70. Vázquez, M., et al., *Ordered magnetic nanohole and antidot arrays prepared through replication from anodic alumina templates.* Journal of Magnetism and Magnetic Materials, 2008. **320**(14): p. 1978-1983.

71. Xiang, Y., et al., *Observation of ferromagnetism in black phosphorus nanosheets with high magnetization by liquid exfoliation.* Solid State Communications, 2018. **281**: p. 1-5.

72. Perez-Taborda, J.A., et al., *Ultra-low thermal conductivities in large-area Si-Ge nanomeshes for thermoelectric applications.* Scientific Reports, 2016. **6**(1): p. 32778.

73. Tang, J., et al., *Holey Silicon as an Efficient Thermoelectric Material.* Nano Letters, 2010. **10**(10): p. 4279-4283.

74. Zeng, Z., et al., *Fabrication of Graphene Nanomesh by Using an Anodic Aluminum Oxide Membrane as a Template.* Advanced Materials, 2012. **24**(30): p. 4138-4142.

75. Thompson, G.E. and G.C. Wood, *5 - Anodic Films on Aluminium*, in *Treatise on Materials Science and Technology*, J.C. Scully, Editor. 1983, Elsevier. p. 205-329.

76. Ruiz-Clavijo, A., O. Caballero-Calero, and M. Martín-González, *Revisiting anodic alumina templates: from fabrication to applications.* Nanoscale, 2021. **13**(4): p. 2227-2265.

77. Chu, S., et al., *Large-scale fabrication of ordered nanoporous alumina films with arbitrary pore intervals by critical-potential anodization.* Journal of The Electrochemical Society, 2006. **153**(9): p. B384-B391.

78. O'sullivan, J. and G. Wood, *The morphology and mechanism of formation of porous anodic films on aluminium.* Proceedings of the Royal Society of London. A. Mathematical and Physical Sciences, 1970. **317**(1531): p. 511-543.

79. Nielsch, K., et al., *Self-ordering Regimes of Porous Alumina: The 10 Porosity Rule.* Nano Letters, 2002. **2**(7): p. 677-680.

80. Ono, S., et al., *Controlling Factor of Self-Ordering of Anodic Porous Alumina.* Journal of The Electrochemical Society, 2004. **151**(8): p. B473.

81. Li, F., L. Zhang, and R.M. Metzger, *On the growth of highly ordered pores in anodized aluminum oxide.* Chemistry of materials, 1998. **10**(9): p. 2470-2480.

82. Hwang, S.-K., et al., *Fabrication of highly ordered pore array in anodic aluminum oxide.* Korean Journal of Chemical Engineering, 2002. **19**(3): p. 467-473.

83. Sulka, G. and K.G. Parkoła, *Temperature influence on well-ordered nanopore structures grown by anodization of aluminium in sulphuric acid.* Electrochimica Acta, 2007. **52**(5): p. 1880-1888.

84. Parkhutik, V. and V. Shershulsky, *Theoretical modelling of porous oxide growth on aluminium.* Journal of Physics D: Applied Physics, 1992. **25**(8): p. 1258.

85. Friedman, A.L., D. Brittain, and L. Menon, *Roles of p H and acid type in the anodic growth of porous alumina.* The Journal of chemical physics, 2007. **127**(15): p. 154717.

86. Pashchanka, M. and J.J. Schneider, *Self-Ordering Regimes of Porous Anodic Alumina Layers Formed in Highly Diluted Sulfuric Acid Electrolytes.* The Journal of Physical Chemistry C, 2016. **120**(27): p. 14590-14596.

87. Sulka, G.D., *Highly ordered anodic porous alumina formation by self-organized anodizing.* Nanostructured materials in electrochemistry, 2008. **1**: p. 1-116.

88. Losic, D. and A. Santos, *Nanoporous Alumina.* Nanoporous Alumina: Fabrication, Structure, Properties and Applications, Springer Series in Materials Science, Volume 219. ISBN 978-3-319-20333-1. Springer International Publishing Switzerland, 2015, 2015.

89. Lee, W. and S.-J. Park, *Porous Anodic Aluminum Oxide: Anodization and Templated Synthesis of Functional Nanostructures.* Chemical Reviews, 2014. **114**(15): p. 7487-7556.

90. Nishinaga, O., et al., *Rapid fabrication of self-ordered porous alumina with 10-/sub-10-nm-scale nanostructures by selenic acid anodizing.* Scientific reports, 2013. **3**: p. 2748.

91. Kikuchi, T., et al., *Self-Ordering Behavior of Anodic Porous Alumina via Selenic Acid Anodizing.* Electrochimica Acta, 2014. **137**: p. 728-735.

92. Akiya, S., et al., *Optimum exploration for the self-ordering of anodic porous alumina formed via selenic acid anodizing.* Journal of The Electrochemical Society, 2015. **162**(10): p. E244-E250.

93. Stępniowski, W.J., et al., *The influence of electrolyte composition on the growth of nanoporous anodic alumina.* Electrochimica Acta, 2016. **211**: p. 453-460.

94. Stojadinovic, S., et al., *Structural and luminescence characterization of porous anodic oxide films on aluminum formed in sulfamic acid solution.* Applied Surface Science, 2008. **255**(5): p. 2845-2850.

95. Kondo, R., et al., *Superhydrophilic and superhydrophobic aluminum alloys fabricated via pyrophosphoric acid anodizing and fluorinated*

SAM modification. Journal of Alloys and Compounds, 2017. **725**: p. 379-387.

96.   Lee, W., K. Nielsch, and U. Gösele, *Self-ordering behavior of nanoporous anodic aluminum oxide (AAO) in malonic acid anodization.* Nanotechnology, 2007. **18**(47): p. 475713.

97.   Bellemare, J., F. Sirois, and D. Ménard, *Fabrication of micrometer-scale self-organized pore arrays in anodic alumina.* Journal of The Electrochemical Society, 2014. **161**(5): p. E75.

98.   Masuda, H., K. Yada, and A. Osaka, *Self-Ordering of Cell Configuration of Anodic Porous Alumina with Large-Size Pores in Phosphoric Acid Solution.* Japanese Journal of Applied Physics, 1998. **37**(Part 2, No. 11A): p. L1340-L1342.

99.   Masuda, H., *Self-Ordering of Cell Arrangement of Anodic Porous Alumina Formed in Sulfuric Acid Solution.* Journal of The Electrochemical Society, 1997. **144**(5): p. L127.

100. Chen, X., et al., *Fabrication of ordered porous anodic alumina with ultra-large interpore distances using ultrahigh voltages.* Materials Research Bulletin, 2014. **57**: p. 116-120.

101. Chu, S.-Z., et al., *Fabrication of Ideally Ordered Nanoporous Alumina Films and Integrated Alumina Nanotubule Arrays by High-Field Anodization.* Advanced Materials, 2005. **17**(17): p. 2115-2119.

102. Jessensky, O., F. Müller, and U. Gösele, *Self-organized formation of hexagonal pore arrays in anodic alumina.* Applied Physics Letters, 1998. **72**(10): p. 1173-1175.

103. Gordeeva, E.O., I.V. Roslyakov, and K.S. Napolskii, *Aluminium anodizing in selenic acid: electrochemical behaviour, porous structure, and ordering regimes.* Electrochimica Acta, 2019. **307**: p. 13-19.

104. Shingubara, S., et al., *Self-Organization of a Porous Alumina Nanohole Array Using a Sulfuric/Oxalic Acid Mixture as Electrolyte.* Electrochemical and Solid-State Letters, 2004. **7**(3): p. E15.

105. Almasi Kashi, M., et al., *Fabrication of Self-Ordered Nanoporous Alumina with 69–115 nm Interpore Distances in Sulfuric/Oxalic Acid Mixtures by Hard Anodization.* Japanese Journal of Applied Physics, 2010. **49**(1): p. 015202.

106. Xu, Y.-f., et al., *A novel method for fabricating self-ordered porous anodic alumina with wide interpore distance using phosphoric/oxalic acid mixed electrolyte.* Materials Letters, 2015. **151**: p. 79-81.

107. Almasi Kashi, M. and A. Ramazani, *Ordered nanoporous alumina membranes formed in oxalic/phosphoric acid using hard anodization.* International Journal of Nanoscience and Nanotechnology, 2010. **6**(2): p. 78-87.

108. Rayat Azimi, H.A., et al., *Fabrication of self-ordered nanoporous alumina with 500–750 nm interpore distances using hard anodization*

in phosphoric/oxalic acid mixtures. Journal of Porous Materials, 2016. **23**(2): p. 357-363.

109. Kanakala, R., et al., *Modeling of porous alumina template formation under constant current conditions.* Journal of the Electrochemical Society, 2005. **152**(1): p. J1-J5.

110. Keller, F., M. Hunter, and D. Robinson, *Structural features of oxide coatings on aluminum.* Journal of the Electrochemical Society, 1953. **100**(9): p. 411.

111. Hunter, M. and P. Fowle, *Factors affecting the formation of anodic oxide coatings.* Journal of the Electrochemical Society, 1954. **101**(10): p. 514.

112. Vrublevsky, I., V. Parkoun, and J. Schreckenbach, *Analysis of porous oxide film growth on aluminum in phosphoric acid using re-anodizing technique.* Applied Surface Science, 2005. **242**(3-4): p. 333-338.

113. Vrublevsky, I., et al., *Study of porous oxide film growth on aluminum in oxalic acid using a re-anodizing technique.* Applied Surface Science, 2004. **227**(1-4): p. 282-292.

114. Vrublevsky, I., et al., *Analysis of chemical dissolution of the barrier layer of porous oxide on aluminum thin films using a re-anodizing technique.* Applied surface science, 2005. **252**(1): p. 227-233.

115. Shimizu, K., et al., *Development of porous anodic films on aluminium.* Philosophical Magazine A, 1992. **66**(4): p. 643-652.

116. Su, Z., G. Hähner, and W. Zhou, *Investigation of the pore formation in anodic aluminium oxide.* Journal of Materials Chemistry, 2008. **18**(47): p. 5787-5795.

117. Siejka, J. and C. Ortega, *An O18 study of field-assisted pore formation in compact anodic oxide films on aluminum.* Journal of The Electrochemical Society, 1977. **124**(6): p. 883-891.

118. Baron-Wiecheć, A., et al., *# 2# 1 Tracer Study of Porous Film Growth on Aluminum in Phosphoric Acid.* Journal of The Electrochemical Society, 2010. **157**(11): p. C399-C407.

119. Takahashi, H. and M. Nagayama, *The determination of the porosity of anodic oxide films on aluminium by the pore-filling method.* Corrosion Science, 1978. **18**(10): p. 911-925.

120. Wu, Z., C. Richter, and L. Menon, *A study of anodization process during pore formation in nanoporous alumina templates.* Journal of the Electrochemical Society, 2007. **154**(1): p. E8-E12.

121. Li, A., et al., *Hexagonal pore arrays with a 50–420 nm interpore distance formed by self-organization in anodic alumina.* Journal of applied physics, 1998. **84**(11): p. 6023-6026.

122. Garcia-Vergara, S., et al., *A flow model of porous anodic film growth on aluminium.* Electrochimica Acta, 2006. **52**(2): p. 681-687.

123. Skeldon, P., et al., *A tracer study of porous anodic alumina.* Electrochemical and Solid-State Letters, 2006. **9**(11): p. B47-B51.

124. Houser, J.E. and K.R. Hebert, *The role of viscous flow of oxide in the growth of self-ordered porous anodic alumina films.* Nature Materials, 2009. **8**(5): p. 415-420.

125. Houser, J.E. and K.R. Hebert, *Stress-driven transport in ordered porous anodic films.* physica status solidi (a), 2008. **205**(10): p. 2396-2399.

126. Hebert, K.R. and J.E. Houser, *A model for coupled electrical migration and stress-driven transport in anodic oxide films.* Journal of The Electrochemical Society, 2009. **156**(8): p. C275-C281.

127. Hoar, T. and J. Yahalom, *The initiation of pores in anodic oxide films formed on aluminum in acid solutions.* Journal of the Electrochemical Society, 1963. **110**(6): p. 614-621.

128. Wood, G. and J. O'sullivan, *The anodizing of aluminium in sulphate solutions.* Electrochimica acta, 1970. **15**(12): p. 1865-1876.

129. Thompson, G., *Porous anodic alumina: fabrication, characterization and applications.* Thin solid films, 1997. **297**(1-2): p. 192-201.

130. Mishra, P. and K.R. Hebert, *Flow instability mechanism for formation of self-ordered porous anodic oxide films.* Electrochimica Acta, 2016. **222**: p. 1186-1190.

131. Hebert, K.R. and P. Mishra, *Model of Stress Generation in Anodic Aluminum Oxide Films: Part I. Origin of Stress at the Film Interfaces.* Journal of The Electrochemical Society, 2018. **165**(14): p. E737-E743.

132. Hebert, K.R. and P. Mishra, *Model of Stress Generation in Anodic Aluminum Oxide Films: Part II. Surface Stress Accumulation Preceding Formation of Self-Organized Pore Arrays.* Journal of The Electrochemical Society, 2018. **165**(14): p. E744-E750.

133. Mishra, P. and K.R. Hebert, *Self-organization of anodic aluminum oxide layers by a flow mechanism.* Electrochimica Acta, 2020: p. 135879.

134. Garcia-Vergara, S., et al., *Formation of porous anodic alumina at high current efficiency.* Nanotechnology, 2007. **18**(41): p. 415605.

135. Garcia-Vergara, S., et al., *Stress generated porosity in anodic alumina formed in sulphuric acid electrolyte.* Corrosion science, 2007. **49**(10): p. 3772-3782.

136. Zhou, F.-y., et al., *Volume expansion factor and growth efficiency of anodic alumina formed in sulphuric acid.* Journal of The Electrochemical Society, 2011. **158**(6): p. C202.

137. Vrublevsky, I., et al., *The study of the volume expansion of aluminum during porous oxide formation at galvanostatic regime.* Applied Surface Science, 2004. **222**(1-4): p. 215-225.

138. Vrublevsky, I., et al., *Effect of the current density on the volume expansion of the deposited thin films of aluminum during porous oxide formation.* Applied Surface Science, 2003. **220**(1-4): p. 51-59.

230

139. Ono, S. and N. Masuko, *The duplex structure of cell walls of porous anodic films formed on aluminum.* Corrosion science, 1992. **33**(3): p. 503-507.

140. Takahashi, H., et al., *Distribution of anions and protons in oxide films formed anodically on aluminum in a phosphate solution.* Journal of The Electrochemical Society, 1984. **131**(8): p. 1856.

141. Mínguez-Bacho, I., et al., *Influence of Sulfur Incorporation into Nanoporous Anodic Alumina on the Volume Expansion and Self-Ordering Degree.* The Journal of Physical Chemistry C, 2015. **119**(49): p. 27392-27400.

142. Zhu, X., et al., *Oxygen bubble mould effect: serrated nanopore formation and porous alumina growth.* Monatshefte für Chemie-Chemical Monthly, 2008. **139**(9): p. 999-1003.

143. Zhu, X., et al., *The study on oxygen bubbles of anodic alumina based on high purity aluminum.* Materials Letters, 2005. **59**(24-25): p. 3160-3163.

144. Li, D., et al., *Self-assembly of periodic serrated nanostructures.* Chemistry of Materials, 2009. **21**(2): p. 253-258.

145. Li, D., et al., *Formation of anodic aluminum oxide with serrated nanochannels.* Nano letters, 2010. **10**(8): p. 2766-2771.

146. Zhu, X.-F., et al., *Electronic currents and the formation of nanopores in porous anodic alumina.* Nanotechnology, 2009. **20**(47): p. 475303.

147. Shuoshuo, C., et al., *Competitive growth of branched channels inside AAO membranes.* Journal of Materials Chemistry, 2010. **20**(9): p. 1794-1798.

148. Ho, A.Y.Y., et al., *Controlled Fabrication of Multitiered Three-Dimensional Nanostructures in Porous Alumina.* Advanced Functional Materials, 2008. **18**(14): p. 2057-2063.

149. Im, W., et al., *Stepped carbon nanotubes synthesized in anodic aluminum oxide templates.* Diamond and related materials, 2004. **13**(4-8): p. 1214-1217.

150. Sousa, C., A. Apolinário, and D. Leitão, *Dendritic nanostructures grown in hierarchical branched pores.* Advances in Nanotechnology, 2014.

151. Krishnan, R. and C.V. Thompson, *Monodomain High-Aspect-Ratio 2D and 3D Ordered Porous Alumina Structures with Independently Controlled Pore Spacing and Diameter.* Advanced materials, 2007. **19**(7): p. 988-992.

152. Guo, D., et al., *Fabrication of a regular tripod Ni–P nanorod array and an AAO template with regular branched nanopores using a current-controlled branching method.* Nanotechnology, 2007. **18**(40): p. 405304.

153.   Zhang, J., C.S. Day, and D.L. Carroll, *Controlled growth of novel hyper-branched nanostructures in nanoporous alumina membrane.* Chemical Communications, 2009(45): p. 6937-6939.

154.   Zakeri, R., et al., *Synthesis and characterization of nonlinear nanopores in alumina films.* Chemistry of materials, 2007. **19**(8): p. 1954-1963.

155.   Jin, S., et al., *Controllable fabrication and microstructure modulation of unique AAO structures based on patterned aluminum surface.* Journal of The Electrochemical Society, 2016. **163**(13): p. H1053-H1059.

156.   Cheng, W., et al., *Tree-like alumina nanopores generated in a non-steady-state anodization.* Journal of Materials Chemistry, 2007. **17**(33): p. 3493-3495.

157.   Hashimoto, H., et al., *α-Alumina membrane having a hierarchical structure of straight macropores and mesopores inside the pore wall.* Journal of the European Ceramic Society, 2018. **38**(4): p. 1836-1840.

158.   Norek, M., W.J. Stępniowski, and D. Siemiaszko, *Effect of ethylene glycol on morphology of anodic alumina prepared in hard anodization.* Journal of Electroanalytical Chemistry, 2016. **762**: p. 20-28.

159.   Hoyer, P., K. Nishio, and H. Masuda, *Preparation of regularly structured porous metal membranes with two different hole diameters at the two sides.* Thin Solid Films, 1996. **286**(1): p. 88-91.

160.   Yi, L., et al., *Novel AAO films and hollow nanostructures fabricated by ultra-high voltage hard anodization.* Chemical Communications, 2010. **46**(2): p. 309-311.

161.   Yi, L., et al., *Investigation of intrinsic mechanisms of aluminium anodization processes by analyzing the current density.* RSC Advances, 2012. **2**(12): p. 5164-5171.

162.   Sulka, G.D., A. Brzózka, and L. Liu, *Fabrication of diameter-modulated and ultrathin porous nanowires in anodic aluminum oxide templates.* Electrochimica Acta, 2011. **56**(14): p. 4972-4979.

163.   Sulka, G.D. and K. Hnida, *Distributed Bragg reflector based on porous anodic alumina fabricated by pulse anodization.* Nanotechnology, 2012. **23**(7): p. 075303.

164.   Liao, J., *Formation of Bottle-Shaped Pores with Petaloid Shoulder within Anodic Alumina.* Surface Engineering and Applied Electrochemistry, 2018. **54**(6): p. 555-561.

165.   Losic, D., M. Lillo, and D. Losic Jr, *Porous alumina with shaped pore geometries and complex pore architectures fabricated by cyclic anodization.* Small, 2009. **5**(12): p. 1392-1397.

166.   Martín, J., et al., *Ordered three-dimensional interconnected nanoarchitectures in anodic porous alumina.* Nature Communications, 2014. **5**(1): p. 5130.

167. Resende, P.M., et al., *Cylindrical three-dimensional porous anodic alumina networks.* Coatings, 2016. **6**(4): p. 59.

168. Lee, W. and J.-C. Kim, *Highly ordered porous alumina with tailor-made pore structures fabricated by pulse anodization.* Nanotechnology, 2010. **21**(48): p. 485304.

169. Bayat, H., et al., *Interplay of Template Constraints and Microphase Separation in Polymeric Nano-Objects Replicated from Novel Modulated and Interconnected Nanoporous Anodic Alumina.* ACS Applied Nano Materials, 2017. **1**(1): p. 200-208.

170. Losic, D. and D. Losic Jr, *Preparation of porous anodic alumina with periodically perforated pores.* Langmuir, 2009. **25**(10): p. 5426-5431.

171. Chen, B., K. Lu, and Z. Tian, *Novel Patterns by Focused Ion Beam Guided Anodization.* Langmuir, 2011. **27**(2): p. 800-808.

172. Smith, J.T., et al., *Highly ordered diamond and hybrid triangle-diamond patterns in porous anodic alumina thin films.* Applied Physics Letters, 2008. **93**(4): p. 043108.

173. Chen, B. and K. Lu, *Moiré pattern nanopore and nanorod arrays by focused ion beam guided anodization and nanoimprint molding.* Langmuir, 2011. **27**(7): p. 4117-4125.

174. Wang, X., et al., *Hierarchical Structural Nanopore Arrays Fabricated by Pre-patterning Aluminum using Nanosphere Lithography.* Small, 2012. **8**(7): p. 972-976.

175. Lu, K., *Newfound capability of focused ion beam patterning guided anodization.* Electrochimica acta, 2012. **63**: p. 256-262.

176. Tian, Z., K. Lu, and B. Chen, *Fundamental mechanisms of focused ion beam guided anodization.* Journal of Applied Physics, 2010. **108**(9): p. 094306.

177. Lu, K. and J. Zhao, *Focused ion beam lithography and anodization combined nanopore patterning.* Journal of nanoscience and nanotechnology, 2010. **10**(10): p. 6760-6768.

178. Shingubara, S., et al., *Formation of aluminum nanodot array by combination of nanoindentation and anodic oxidation of aluminum.* Surface Science, 2003. **532**: p. 317-323.

179. Jaafar, M., et al., *Nanoporous alumina membrane prepared by nanoindentation and anodic oxidation.* Surface science, 2009. **603**(20): p. 3155-3159.

180. Sun, Z. and H.K. Kim, *Growth of ordered, single-domain, alumina nanopore arrays with holographically patterned aluminum films.* Applied Physics Letters, 2002. **81**(18): p. 3458-3460.

181. Kim, B., et al., *Fabrication of Ordered Anodic Aluminum Oxide Using a Solvent-Induced Array of Block-Copolymer Micelles.* Small, 2007. **3**(11): p. 1869-1872.

182.   Yin, A., et al., *Fabrication of highly ordered anodic aluminium oxide templates on silicon substrates.* IET Circuits, Devices & Systems, 2007. **1**(3): p. 205-209.

183.   Stasi, V., et al., *Aluminium pre-patterning for highly ordered nanoporous anodized alumina.* Photonics and Nanostructures-Fundamentals and Applications, 2007. **5**(2-3): p. 136-139.

184.   Kustandi, T.S., et al., *Wafer-Scale Near-Perfect Ordered Porous Alumina on Substrates by Step and Flash Imprint Lithography.* ACS Nano, 2010. **4**(5): p. 2561-2568.

185.   Maria Chong, A., et al., *Soft imprinting: creating highly ordered porous anodic alumina templates on substrates for nanofabrication.* Advanced Functional Materials, 2007. **17**(10): p. 1629-1635.

186.   Masuda, H., et al., *Highly ordered nanochannel-array architecture in anodic alumina.* Applied Physics Letters, 1997. **71**(19): p. 2770-2772.

187.   Masuda, H., et al., *Self-repair of ordered pattern of nanometer dimensions based on self-compensation properties of anodic porous alumina.* Applied physics letters, 2001. **78**(6): p. 826-828.

188.   Lee, W., et al., *Wafer-Scale Ni Imprint Stamps for Porous Alumina Membranes Based on Interference Lithography.* Small, 2006. **2**(8-9): p. 978-982.

189.   Navas, D., et al., *Titanium nitride stamps replicating nanoporous anodic alumina films.* Nanotechnology, 2007. **18**(16): p. 165302.

190.   Matsumoto, F., et al., *Fabrication and electrochemical behavior of nanodisk electrode arrays with controlled interval using ideally ordered porous alumina.* Electrochemical and Solid State Letters, 2004. **7**(11): p. E51.

191.   Choi, J., et al., *Large-area porous alumina photonic crystals via imprint method.* MRS Online Proceedings Library Archive, 2002. **722**.

192.   Fan, Z., et al., *Three-dimensional nanopillar-array photovoltaics on low-cost and flexible substrates.* Nature materials, 2009. **8**(8): p. 648-653.

193.   Wen, L., et al., *Multiple nanostructures based on anodized aluminium oxide templates.* Nature Nanotechnology, 2017. **12**(3): p. 244-250.

194.   Xu, Y., et al., *Highly ordered three-dimensional Ni-TiO2 nanoarrays as sodium ion battery anodes.* Chemistry of Materials, 2015. **27**(12): p. 4274-4280.

195.   Yasui, K., K. Nishio, and H. Masuda, *Fabrication of nanocomposites by filling nanoholes in highly ordered anodic porous alumina by vacuum deposition of metal.* Japanese journal of applied physics, 2005. **44**(9L): p. L1181.

196.   Choi, J., R.B. Wehrspohn, and U. Gösele, *Mechanism of guided self-organization producing quasi-monodomain porous alumina.* Electrochimica Acta, 2005. **50**(13): p. 2591-2595.

197.   Asoh, H., et al., *Detailed observation of cell junction in anodic porous alumina with square cells.* Japanese journal of applied physics, 2004. **43**(9R): p. 6342.

198.   Choi, J., et al., *Fabrication of monodomain alumina pore arrays with an interpore distance smaller than the lattice constant of the imprint stamp.* Journal of Vacuum Science & Technology B: Microelectronics and Nanometer Structures Processing, Measurement, and Phenomena, 2003. **21**(2): p. 763-766.

199.   Shingubara, S., et al., *Reduction of pitch of nanohole array by self-organizing anodic oxidation after nanoimprinting.* Microelectronic engineering, 2010. **87**(5-8): p. 1451-1454.

200.   Masuda, H., et al., *Fabrication of highly ordered anodic porous alumina using self-organized polystyrene particle array.* Chemistry letters, 2004. **33**(5): p. 584-585.

201.   Fournier-Bidoz, S., et al., *Highly ordered nanosphere imprinted nanochannel alumina (NINA).* Advanced materials, 2004. **16**(23-24): p. 2193-2196.

202.   Kapruwan, P., J. Ferré-Borrull, and L.F. Marsal, *Nanoporous Anodic Alumina Platforms for Drug Delivery Applications: Recent Advances and Perspective.* Advanced Materials Interfaces, 2020. **7**(22): p. 2001133.

203.   Rajeev, G., et al., *Advances in Nanoporous Anodic Alumina-Based Biosensors to Detect Biomarkers of Clinical Significance: A Review.* Advanced Healthcare Materials, 2018. **7**(5): p. 1700904.

204.   Aw, M.S., M. Kurian, and D. Losic, *Non-eroding drug-releasing implants with ordered nanoporous and nanotubular structures: concepts for controlling drug release.* Biomaterials Science, 2014. **2**(1): p. 10-34.

205.   Fazli-Abukheyli, R., M.R. Rahimi, and M. Ghaedi, *Electrospinning coating of nanoporous anodic alumina for controlling the drug release: Drug release study and modeling.* Journal of Drug Delivery Science and Technology, 2019. **54**: p. 101247.

206.   Davoodi, E., et al., *Nano-porous anodic alumina: fundamentals and applications in tissue engineering.* Journal of Materials Science: Materials in Medicine, 2020. **31**(7): p. 1-16.

207.   Yanagishita, T., et al., *Carbon Nanotubes with a Triangular Cross-section, Fabricated Using Anodic Porous Alumina as the Template.* Advanced Materials, 2004. **16**(5): p. 429-432.

208.   Yao, Z., et al., *AAO-assisted synthesis of highly ordered, large-scale TiO 2 nanowire arrays via sputtering and atomic layer deposition.* Nanoscale research letters, 2015. **10**(1): p. 166.

209.   Friedman, A.L., *The magnetic and transport properties of template-synthesized carbon-based and related nanomaterials*. 2009, Northeastern University.

210. Gillette, E., et al., *Anodization control for barrier-oxide thinning and 3D interconnected pores and direct electrodeposition of nanowire networks on native aluminium substrates.* Physical Chemistry Chemical Physics, 2015. **17**(5): p. 3873-3879.

211. Meng, G., et al., *Controlled fabrication of hierarchically branched nanopores, nanotubes, and nanowires.* Proceedings of the National Academy of Sciences, 2005. **102**(20): p. 7074-7078.

212. Lee, W., J.-C. Kim, and U. Gösele, *Spontaneous Current Oscillations during Hard Anodization of Aluminum under Potentiostatic Conditions.* Advanced Functional Materials, 2010. **20**(1): p. 21-27.

213. Méndez, M., et al., *Effect of sharp diameter geometrical modulation on the magnetization reversal of Bi-segmented FeNi nanowires.* Nanomaterials, 2018. **8**(8): p. 595.

214. Mistura, G., L. Bruschi, and W. Lee, *Adsorption on highly ordered porous alumina.* Journal of Low Temperature Physics, 2016. **185**(1-2): p. 138-160.

215. Mir, M., M. Shah, and P. Ganai, *Nanoporous anodic alumina (NAA) prepared in different electrolytes with different pore sizes for humidity sensing.* Journal of Solid State Electrochemistry, 2020. **24**: p. 1679-1686.

216. Jeong, C. and H. Ji, *Systematic Control of Anodic Aluminum Oxide Nanostructures for Enhancing the Superhydrophobicity of 5052 Aluminum Alloy.* Materials, 2019. **12**(19): p. 3231.

217. Choudhari, K., et al., *Optical characterizations of nanoporous anodic alumina for thickness measurements using interference oscillations.* Nano-Structures & Nano-Objects, 2019. **19**: p. 100354.

218. Wang, X., et al., *Tuning color by pore depth of metal-coated porous alumina.* Nanotechnology, 2011. **22**(30): p. 305306.

219. Manzano, C.V., et al., *Controlling the color and effective refractive index of metal-anodic aluminum oxide (AAO)–Al nanostructures: morphology of AAO.* The Journal of Physical Chemistry C, 2018. **122**(1): p. 957-963.

220. Xue, J., et al., *Scalable, full-colour and controllable chromotropic plasmonic printing.* Nature communications, 2015. **6**: p. 8906.

221. Chen, Y., et al., *On the generation of interferometric colors in high purity and technical grade aluminum: an alternative green process for metal finishing industry.* Electrochimica Acta, 2015. **174**: p. 672-681.

222. Zhang, S., et al., *The effect of the voltage waveform on the microstructure and optical properties of porous anodic alumina photonic crystals.* Optical Materials, 2019. **98**: p. 109488.

223. Ruiz-Clavijo, A., et al., *Engineering a full gamut of structural colors in all-dielectric mesoporous network metamaterials.* ACS Photonics, 2018. **5**(6): p. 2120-2128.

224. Law, C.S., et al., *Nanoporous anodic alumina photonic crystals for optical chemo-and biosensing: Fundamentals, advances, and perspectives.* Nanomaterials, 2018. **8**(10): p. 788.

225. Santos, A., *Nanoporous anodic alumina photonic crystals: fundamentals, developments and perspectives.* Journal of Materials Chemistry C, 2017. **5**(23): p. 5581-5599.

226. Masuda, H., et al., *Photonic crystal using anodic porous alumina.* Japanese Journal of Applied Physics, 1999. **38**(12A): p. L1403.

227. Zheng, W.J., et al., *Distributed Bragg reflector made of anodic alumina membrane.* Materials Letters, 2009. **63**(8): p. 706-708.

228. Wang, B., et al., *Preparation of photonic crystals made of air pores in anodic alumina.* Nanotechnology, 2007. **18**(36): p. 365601.

229. Rahman, M.M., et al., *Tuning the photonic stop bands of nanoporous anodic alumina-based distributed Bragg reflectors by pore widening.* ACS applied materials & interfaces, 2013. **5**(24): p. 13375-13381.

230. Su, Y., et al., *Controllable preparation of the ordered pore arrays anodic alumina with high-quality photonic band gaps.* Materials Letters, 2011. **65**(17-18): p. 2693-2695.

231. Liu, Y., et al., *Structural coloring of aluminum.* Electrochemistry Communications, 2011. **13**(12): p. 1336-1339.

232. Wang, Y., et al., *Facile synthesis of optical microcavities by a rationally designed anodization approach: tailoring photonic signals by nanopore structure.* ACS applied materials & interfaces, 2015. **7**(18): p. 9879-9888.

233. Santos, A., et al., *Fine tuning of optical signals in nanoporous anodic alumina photonic crystals by apodized sinusoidal pulse anodisation.* Nanoscale, 2016. **8**(43): p. 18360-18375.

234. Santos, A., et al., *Rational engineering of nanoporous anodic alumina optical bandpass filters.* Nanoscale, 2016. **8**(31): p. 14846-14857.

235. Santos, A., et al., *Nanoporous hard data: optical encoding of information within nanoporous anodic alumina photonic crystals.* Nanoscale, 2016. **8**(15): p. 8091-8100.

236. Xu, Q., G. Meng, and F. Han, *Porous AAO template-assisted rational synthesis of large-scale 1D hybrid and hierarchically branched nanoarchitectures.* Progress in Materials Science, 2018. **95**: p. 243-285.

237. Muñoz Rojo, M., et al., *Spatial potential ripples of azimuthal surface modes in topological insulator Bi2Te3 nanowires.* Scientific Reports, 2016. **6**(1): p. 19014.

238. Chong, Y.T., et al., *Multilayered core/shell nanowires displaying two distinct magnetic switching events.* Advanced Materials, 2010. **22**(22): p. 2435-2439.

239. Samardak, A., et al., *Variation of magnetic anisotropy and temperature-dependent FORC probing of compositionally tuned Co-*

Ni alloy nanowires. Journal of Alloys and Compounds, 2018. **732**: p. 683-693.

240.   Manzano, C.V., et al., *Pulsed current-voltage electrodeposition of stoichiometric Bi2Te3 nanowires and their crystallographic characterization by transmission electron backscatter diffraction.* Science and Technology of Advanced Materials, 2019. **20**(1): p. 1022-1030.

241.   González-Souto, L., et al., *The Role of Gold-Alumina Template in the Electrochemical Deposition of CeO2 Nanotubes.* Particle & Particle Systems Characterization, 2019. **36**(10): p. 1900168.

242.   Chen, L., et al., *Iron Oxide Magnetic Nanotubes and Their Drug Loading and Release Capabilities.* Journal of Nanotechnology in Engineering and Medicine, 2009. **1**(1).

243.   Banerjee, P., et al., *Nanotubular metal–insulator–metal capacitor arrays for energy storage.* Nature Nanotechnology, 2009. **4**(5): p. 292-296.

244.   Haspert, L.C., S.B. Lee, and G.W. Rubloff, *Nanoengineering Strategies for Metal–Insulator–Metal Electrostatic Nanocapacitors.* ACS Nano, 2012. **6**(4): p. 3528-3536.

245.   Li, J., et al., *Highly-ordered carbon nanotube arrays for electronics applications.* Applied Physics Letters, 1999. **75**(3): p. 367-369.

246.   Mezni, A., et al., *Size- and shape-controlled synthesis of well-organised carbon nanotubes using nanoporous anodic alumina with different pore diameters.* Journal of Colloid and Interface Science, 2017. **491**: p. 375-389.

247.   Shelimov, K.B., D.N. Davydov, and M. Moskovits, *Template-grown high-density nanocapacitor arrays.* Applied Physics Letters, 2000. **77**(11): p. 1722-1724.

248.   Nguyen, T.N.A., et al., *Effect of flattened surface morphology of anodized aluminum oxide templates on the magnetic properties of nanoporous Co/Pt and Co/Pd thin multilayered films.* Applied Surface Science, 2018. **427**: p. 649-655.

249.   Maximenko, A., et al., *Perforated alumina templates as a tool for engineering of CoPd film magnetic properties.* Journal of Magnetism and Magnetic Materials, 2019. **477**: p. 182-189.

250.   Jung, I., et al., *Fabrication of a graphene nanomesh using a platinum nano-network as a pattern mask.* Nanoscale, 2014. **6**(12): p. 6482-6486.

251.   Papadopoulos, C., et al., *Electronic Transport in Y-Junction Carbon Nanotubes.* Physical Review Letters, 2000. **85**(16): p. 3476-3479.

252.   Pitzschel, K., et al., *Magnetic reversal of cylindrical nickel nanowires with modulated diameters.* Journal of Applied Physics, 2011. **109**(3): p. 033907.

253. Ivanov, Y.P., M. Vázquez, and O. Chubykalo-Fesenko, *Magnetic reversal modes in cylindrical nanowires.* Journal of Physics D: Applied Physics, 2013. **46**(48): p. 485001.

254. Da Col, S., et al., *Observation of Bloch-point domain walls in cylindrical magnetic nanowires.* Physical Review B, 2014. **89**(18): p. 180405.

255. Wieser, R., U. Nowak, and K.-D. Usadel, *Domain wall mobility in nanowires: Transverse versus vortex walls.* Physical Review B, 2004. **69**(6): p. 064401.

256. Yan, M., et al., *Beating the Walker limit with massless domain walls in cylindrical nanowires.* Physical review letters, 2010. **104**(5): p. 057201.

257. Fernandez-Roldan, J.A., et al., *Magnetization pinning in modulated nanowires: From topological protection to the "corkscrew" mechanism.* Nanoscale, 2018. **10**(13): p. 5923-5927.

258. Samanifar, S., et al., *Magnetic alloy nanowire arrays with different lengths: Insights into the crossover angle of magnetization reversal process.* Journal of Magnetism and Magnetic Materials, 2017. **430**: p. 6-15.

259. Salaheldeen, M., et al., *Anomalous in-plane coercivity behaviour in hexagonal arrangements of ferromagnetic antidot thin films.* Journal of Magnetism and Magnetic Materials, 2019. **491**: p. 165572.

260. Bran, C., et al., *Magnetic hardening and domain structure in Co/Pt antidots with perpendicular anisotropy.* Journal of Physics D: Applied Physics, 2017. **50**(6): p. 065003.

261. Gao, H., et al., *Field emission of large-area and graphitized carbon nanotube array on anodic aluminum oxide template.* Journal of Applied Physics, 2003. **93**(9): p. 5602-5605.

262. Davydov, D.N., et al., *Resistance and tunneling spectra of aligned multiwalled carbon nanotube arrays.* Journal of Applied Physics, 2000. **88**(12): p. 7205-7208.

263. Kshirsagar, C., et al., *Accurate Intrinsic Gate Capacitance Model for Carbon Nanotube-Array Based FETs Considering Screening Effect.* IEEE Electron Device Letters, 2008. **29**(12): p. 1408-1411.

264. Jang, W.Y., et al., *Electrical characterization of individual carbon nanotubes grown in nanoporous anodic alumina templates.* Applied Physics Letters, 2004. **84**(7): p. 1177-1179.

265. Hicks, L. and M.S. Dresselhaus, *Thermoelectric figure of merit of a one-dimensional conductor.* Physical review B, 1993. **47**(24): p. 16631.

266. Dresselhaus, M., et al., *Low-dimensional thermoelectric materials.* Physics of the Solid State, 1999. **41**(5): p. 679-682.

267.   Li, Y., et al., *Preparation of Aluminum Nanomesh Thin Films from an Anodic Aluminum Oxide Template as Transparent Conductive Electrodes.* Scientific Reports, 2016. **6**(1): p. 20114.

268.   Masuda, H. and M. Satoh, *Fabrication of gold nanodot array using anodic porous alumina as an evaporation mask.* Japanese Journal of Applied Physics, 1996. **35**(1B): p. L126.

269.   Wang, Y., et al., *Rational design of ultra-short anodic alumina nanotubes by short-time pulse anodization.* Electrochimica Acta, 2015. **154**: p. 379-386.

270.   Paunovic, M. and M. Schlesinger, *Fundamentals of electrochemical deposition*. Vol. 45. 2006: john wiley & sons.

271.   Pierce, P.E., Z. Kovac, and C. Higginbotham, *The kinetics and mechanism of film growth during the electrodeposition process.* Industrial & Engineering Chemistry Product Research and Development, 1978. **17**(4): p. 317-322.

272.   Bicelli, L.P., et al., *A review of nanostructural aspects of metal electrodeposition.* Int. J. Electrochem. Sci, 2008. **3**(4): p. 356-408.

273.   Beck, F., *Fundamental aspects of electrodeposition of paint.* Progress in Organic coatings, 1976. **4**(1): p. 1-60.

274.   Jayakrishnan, D.S., *Electrodeposition: the versatile technique for nanomaterials*, in *Corrosion protection and control using nanomaterials*. 2012, Elsevier. p. 86-125.

275.   Srinivasan, S., *Electrode/electrolyte interfaces: Structure and kinetics of charge transfer*, in *Fuel Cells*. 2006, Springer. p. 27-92.

276.   Matsumoto, M., *Electrocapillarity and double layer structure*, in *Electrical Phenomena at Interfaces*. 2018, Routledge. p. 87-99.

277.   Grahame, D.C., *The electrical double layer and the theory of electrocapillarity.* Chemical reviews, 1947. **41**(3): p. 441-501.

278.   Watt, I.M., *The principles and practice of electron microscopy*. 1997: Cambridge University Press.

279.   Dunlap, M. and J. Adaskaveg, *Introduction to the scanning electron microscope: Theory, practice, & procedures.* Presented by the facility for advanced instrumentation. UC Davis, 1997.

280.   Goldstein, J.I., et al., *X-Rays*, in *Scanning Electron Microscopy and X-Ray Microanalysis*. 2018, Springer New York: New York, NY. p. 39-63.

281.   Nolze, G. and A. Winkelmann, *Crystallometric and projective properties of Kikuchi diffraction patterns.* Journal of Applied Crystallography, 2017. **50**(1): p. 102-119.

282.   Sneddon, G.C., P.W. Trimby, and J.M. Cairney, *Transmission Kikuchi diffraction in a scanning electron microscope: A review.* Materials Science and Engineering: R: Reports, 2016. **110**: p. 1-12.

283. Trimby, P.W., *Orientation mapping of nanostructured materials using transmission Kikuchi diffraction in the scanning electron microscope.* Ultramicroscopy, 2012. **120**: p. 16-24.

284. Brodusch, N., H. Demers, and R. Gauvin, *Nanometres-resolution Kikuchi patterns from materials science specimens with transmission electron forward scatter diffraction in the scanning electron microscope.* Journal of Microscopy, 2013. **250**(1): p. 1-14.

285. Pérez-Arantegui, J., *Microscopy | Electron Microscopy☆*, in *Encyclopedia of Analytical Science (Third Edition)*, P. Worsfold, et al., Editors. 2019, Academic Press: Oxford. p. 19-29.

286. Norton, M.G. and C. Suryanarayana, *X-Ray diffraction: a practical approach.* 1998: Plenum Press.

287. Sadiku, M.N., *Elements of electromagnetics*. Vol. 428. 2001: Oxford university press New York.

288. Mayergoyz, I., *Mathematical models of hysteresis.* IEEE Transactions on magnetics, 1986. **22**(5): p. 603-608.

289. Pike, C.R., A.P. Roberts, and K.L. Verosub, *Characterizing interactions in fine magnetic particle systems using first order reversal curves.* Journal of Applied Physics, 1999. **85**(9): p. 6660-6667.

290. Nolas, G.S., J. Sharp, and J. Goldsmid, *Thermoelectrics: basic principles and new materials developments*. Vol. 45. 2001: Springer Science & Business Media.

291. Rowe, D.M., *Thermoelectrics handbook: macro to nano*. 2018: CRC press.

292. Ramsden, E., *Hall-effect sensors: theory and application*. 2011: Elsevier.

293. http://hyperphysics.phy-astr.gsu.edu/hbase/magnetic/Hall.html. 28/10/21].

294. Pauw, L., *A method of measuring specific resistivity and Hall effect of discs of arbitrary shape.* Philips Research Reports, 1958. **13**(1): p. 1-9.

295. Alqahtani, F., et al. *Four point probe geometry modified correction factor for determining resistivity*. in *Micro/Nano Materials, Devices, and Systems*. 2013. International Society for Optics and Photonics.

296. Chwang, R., B. Smith, and C. Crowell, *Contact size effects on the van der Pauw method for resistivity and Hall coefficient measurement.* Solid-State Electronics, 1974. **17**(12): p. 1217-1227.

297. Instruments, K., *Performing van der Pauw Sheet Resistance Measurements Using the Keithley S530 Parametric Tester*. 2012, no.

298. Heaney, M.B., *Electrical conductivity and resistivity.* Electrical measurement, signal processing, and displays, 2003. **7**(1).

299. Abad Mayor, B., *Medidas de transporte térmico de materiales termoeléctricos mediante la técnica fotoacústica: del material en volumen a la nanoescala.* 2017.

300. Arisaka, T., M. Otsuka, and Y. Hasegawa, *Measurement of thermal conductivity and specific heat by impedance spectroscopy of Bi2Te3 thermoelectric element.* Review of Scientific Instruments, 2019. **90**(4): p. 046104.

301. Abad, B., et al., *Tailoring thermal conductivity via three-dimensional porous alumina.* Scientific Reports, 2016. **6**(1): p. 38595.

302. Abad, B.a., J. Maiz, and M. Martin-Gonzalez, *Rules to determine thermal conductivity and density of anodic aluminum oxide (AAO) membranes.* The Journal of Physical Chemistry C, 2016. **120**(10): p. 5361-5370.

303. Manzano, C., et al., *The influence of thickness, interpore distance and compositional structure on the optical properties of self-ordered anodic aluminum oxide films.* Journal of Materials Chemistry C, 2016. **4**(32): p. 7658-7666.

304. Zhi-Yuan, L., et al., *Optical transmission spectra of anodic aluminum oxide membranes with a dual layer-by-layer structure.* Chinese Physics Letters, 2009. **26**(5): p. 054213.

305. Abbasimofrad, S., et al., *Tuning the optical properties of nanoporous anodic alumina photonic crystals by control of allowed voltage range via mixed acid concentration.* Journal of Physics and Chemistry of Solids, 2018. **118**: p. 221-231.

306. Yan, P., et al., *Fabrication of one-dimensional alumina photonic crystals with a narrow band gap and their application to high-sensitivity sensors.* Journal of Materials Chemistry C, 2013. **1**(8): p. 1659-1664.

307. Shang, G., et al., *Influence of dielectrics with light absorption on the photonic bandgap of porous alumina photonic crystals.* Nano Research, 2016. **9**(3): p. 703-712.

308. Shang, G.L., et al., *Preparation of narrow photonic bandgaps located in the near infrared region and their applications in ethanol gas sensing.* Journal of Materials Chemistry C, 2013. **1**(34): p. 5285-5291.

309. Chen, Y., et al., *Biomimetic nanoporous anodic alumina distributed Bragg reflectors in the form of films and microsized particles for sensing applications.* ACS applied materials & interfaces, 2015. **7**(35): p. 19816-19824.

310. Law, C.S., et al., *Structural tailoring of nanoporous anodic alumina optical microcavities for enhanced resonant recirculation of light.* Nanoscale, 2018. **10**(29): p. 14139-14152.

311. Kumeria, T., et al., *Structural and Optical Nanoengineering of Nanoporous Anodic Alumina Rugate Filters for Real-Time and Label-*

Free Biosensing Applications. Analytical Chemistry, 2014. **86**(3): p. 1837-1844.

312. Kumeria, T., et al., *Nanoporous Anodic Alumina Rugate Filters for Sensing of Ionic Mercury: Toward Environmental Point-of-Analysis Systems.* ACS Applied Materials & Interfaces, 2014. **6**(15): p. 12971-12978.

313. Nemati, M., et al., *Assessment of binding affinity between drugs and human serum albumin using nanoporous anodic alumina photonic crystals.* Analytical chemistry, 2016. **88**(11): p. 5971-5980.

314. Santos, A., et al., *Realisation and advanced engineering of true optical rugate filters based on nanoporous anodic alumina by sinusoidal pulse anodisation.* Nanoscale, 2016. **8**(3): p. 1360-1373.

315. Choi, K., et al., *Super-Antireflective Structure Films with Precisely Controlled Refractive Index Profile.* Advanced Optical Materials, 2017. **5**(3): p. 1600616.

316. Smith, T. and J. Guild, *The CIE colorimetric standards and their use.* Transactions of the optical society, 1931. **33**(3): p. 73.

317. Helmholtz, H.v., *LXXXI. On the theory of compound colours.* The London, Edinburgh, and Dublin Philosophical Magazine and Journal of Science, 1852. **4**(28): p. 519-534.

318. Maxwell, J.C. and Q. Zaidi, *On the theory of compound colours, and the relations of the colours of the spectrum.* Color Research & Application, 1993. **18**(4): p. 270-287.

319. Sherman, P.D., *Colour vision in the nineteenth century: the Young-Helmholtz-Maxwell theory*. 1981: CRC Press.

320. Le Blon, J.C., *Coloritto or the Harmony of Colouring in Painting*. 2020: Routledge.

321. MacAdam, D.L., *Subtractive color mixture and color reproduction.* JOSA, 1938. **28**(12): p. 466-480.

322. Munsell, A.H., *A pigment color system and notation.* The American Journal of Psychology, 1912. **23**(2): p. 236-244.

323. Nam, H., et al., *Inkjet printing based mono-layered photonic crystal patterning for anti-counterfeiting structural colors.* Scientific reports, 2016. **6**(1): p. 1-9.

324. Heo, Y., et al., *Lithographically Encrypted Inverse Opals for Anti-Counterfeiting Applications.* Small, 2016. **12**(28): p. 3819-3826.

325. Tao, H., et al., *Silk-based conformal, adhesive, edible food sensors.* Advanced Materials, 2012. **24**(8): p. 1067-1072.

326. Gundlach, B.S., et al., *Enhancing human color vision by breaking binocular redundancy.* arXiv preprint arXiv:1703.04392, 2017.

327. Thiaville, A. and Y. Nakatani, *Domain-wall dynamics in nanowiresand nanostrips.* Spin dynamics in confined magnetic structures III, 2006: p. 161-205.

328. Schabes, M.E., *Micromagnetic theory of non-uniform magnetization processes in magnetic recording particles.* Journal of magnetism and magnetic materials, 1991. **95**(3): p. 249-288.

329. Metlov, K.L. and Y. Lee, *Map of metastable states for thin circular magnetic nanocylinders.* Applied Physics Letters, 2008. **92**(11): p. 112506.

330. Fernández-Pacheco, A., et al., *Three-dimensional nanomagnetism.* Nature communications, 2017. **8**(1): p. 1-14.

331. Burks, E.C., et al., *3D Nanomagnetism in low density interconnected nanowire networks.* Nano Letters, 2020. **21**(1): p. 716-722.

332. Meng, F., et al., *Non-planar geometrical effects on the magnetoelectrical signal in a three-dimensional nanomagnetic circuit.* ACS nano, 2021. **15**(4): p. 6765-6773.

333. Jamet, S., et al., *Head-to-head domain walls in one-dimensional nanostructures: An extended phase diagram ranging from strips to cylindrical wires*, in *Magnetic Nano-and Microwires*. 2015, Elsevier. p. 783-811.

334. Vázquez, M., et al., *Magnetic properties of densely packed arrays of Ni nanowires as a function of their diameter and lattice parameter.* Journal of applied physics, 2004. **95**(11): p. 6642-6644.

335. Béron, F., et al., *Extracting individual properties from global behaviour: first-order reversal curve method applied to magnetic nanowire arrays.* Electrodeposited Nanowires and their Applications Vienna: IN-TECH, 2010: p. 167-88.

336. Piraux, L., et al., *Anisotropic transport and magnetic properties of arrays of sub-micron wires.* Journal of Magnetism and Magnetic Materials, 1997. **165**(1-3): p. 352-355.

337. Vansteenkiste, A., et al., *The design and verification of MuMax3.* AIP advances, 2014. **4**(10): p. 107133.

338. Peixoto, T. and D. Cornejo, *Characterizing magnetic interactions in Ni nanowires by FORC analysis.* Journal of Magnetism and Magnetic Materials, 2008. **320**(14): p. e279-e282.

339. Ciureanu, M., et al., *First order reversal curves (FORC) diagrams of Co nanowire arrays.* Journal of nanoscience and nanotechnology, 2008. **8**(11): p. 5725-5732.

340. Lavin, R., et al., *Magnetic characterization of nanowire arrays using first order reversal curves.* IEEE transactions on magnetics, 2008. **44**(11): p. 2808-2811.

341. Kou, X., et al., *Memory effect in magnetic nanowire arrays.* Advanced materials, 2011. **23**(11): p. 1393-1397.

342. Palmero, E.M., et al., *Magnetic interactions in compositionally modulated nanowire arrays.* Nanotechnology, 2016. **27**(43): p. 435705.

343. Sergelius, P., et al., *Statistical magnetometry on isolated NiCo nanowires and nanowire arrays: a comparative study.* Journal of Physics D: Applied Physics, 2016. **49**(14): p. 145005.

344. Proenca, M.P., et al., *Identifying weakly-interacting single domain states in Ni nanowire arrays by FORC.* Journal of Alloys and Compounds, 2017. **699**: p. 421-429.

345. Dobrotă, C.-I. and A. Stancu, *What does a first-order reversal curve diagram really mean? A study case: Array of ferromagnetic nanowires.* Journal of applied physics, 2013. **113**(4): p. 043928.

346. Dobrotă, C.-I. and A. Stancu, *Tracking the individual magnetic wires' switchings in ferromagnetic nanowire arrays using the first-order reversal curves (FORC) diagram method.* Physica B: Condensed Matter, 2015. **457**: p. 280-286.

347. Pierrot, A., F. Béron, and T. Blon, *FORC signatures and switching-field distributions of dipolar coupled nanowire-based hysterons.* Journal of Applied Physics, 2020. **128**(9): p. 093903.

348. Proenca, M., et al., *Angular first-order reversal curves: an advanced method to extract magnetization reversal mechanisms and quantify magnetostatic interactions.* Journal of Physics: Condensed Matter, 2014. **26**(11): p. 116004.

349. Béron, F., M. Knobel, and K.R. Pirota, *Magnetostatic behaviour of antidot arrays under the local influence of nanopillars.* Journal of Physics D: Applied Physics, 2012. **45**(50): p. 505002.

350. Gräfe, J., et al., *Combined first-order reversal curve and X-ray microscopy investigation of magnetization reversal mechanisms in hexagonal antidot lattices.* Physical Review B, 2016. **93**(1): p. 014406.

351. Sun, L., et al., *Magnetization reversal in kagome artificial spin ice studied by first-order reversal curves.* Physical Review B, 2017. **96**(14): p. 144409.

352. Béron, F., et al., *Magnetic behavior of Ni/Cu multilayer nanowire arrays studied by first-order reversal curve diagrams.* IEEE Transactions on Magnetics, 2008. **44**(11): p. 2745-2748.

353. Rotaru, A., et al., *Interactions and reversal-field memory in complex magnetic nanowire arrays.* Physical Review B, 2011. **84**(13): p. 134431.

354. Palmero, E.M., et al., *Stepwise magnetization reversal of geometrically tuned in diameter Ni and FeCo bi-segmented nanowire arrays.* Nano Research, 2019. **12**(7): p. 1547-1553.

355. Maurice, J.-L., et al., *Microstructure of magnetic metallic superlattices grown by electrodeposition in membrane nanopores.* Journal of magnetism and magnetic materials, 1998. **184**(1): p. 1-18.

356. Scarani, V., B. Doudin, and J.-P. Ansermet, *The microstructure of electrodeposited cobalt-based nanowires and its effect on their*

magnetic and transport properties. Journal of magnetism and magnetic materials, 1999. **205**(2-3): p. 241-248.

357.   Paulus, P., et al., *Low-temperature study of the magnetization reversal and magnetic anisotropy of Fe, Ni, and Co nanowires.* Journal of Magnetism and Magnetic Materials, 2001. **224**(2): p. 180-196.

358.   Ferré, R., et al., *Magnetization processes in nickel and cobalt electrodeposited nanowires.* Physical Review B, 1997. **56**(21): p. 14066.

359.   Bran, C., et al., *Magnetization ratchet in cylindrical nanowires.* ACS nano, 2018. **12**(6): p. 5932-5939.

360.   Bran, C., et al., *Co/Au multisegmented nanowires: A 3D array of magnetostatically coupled nanopillars.* Nanotechnology, 2017. **28**(9): p. 095709.

361.   Ruiz-Gómez, S., et al., *Observation of a topologically protected state in a magnetic domain wall stabilized by a ferromagnetic chemical barrier.* Scientific reports, 2018. **8**(1): p. 1-6.

362.   Tritt, T.M. and M. Subramanian, *Thermoelectric materials, phenomena, and applications: a bird's eye view.* MRS bulletin, 2006. **31**(3): p. 188-198.

363.   Kim, S.I., et al., *Dense dislocation arrays embedded in grain boundaries for high-performance bulk thermoelectrics.* Science, 2015. **348**(6230): p. 109-114.

364.   Prasad, R. and S.D. Bhame, *Review on texturization effects in thermoelectric oxides.* Materials for Renewable and Sustainable Energy, 2020. **9**(1): p. 1-22.

365.   Peranio, N. and O. Eibl, *Gliding dislocations in Bi2Te3 materials.* physica status solidi (a), 2009. **206**(1): p. 42-49.

366.   Huber, T., et al., *Thermoelectric prospects of nanomaterials with spin-orbit surface bands.* Journal of Applied Physics, 2012. **111**(4): p. 043709.

367.   Rojo, M.M., et al., *Thermal conductivity of Bi 2 Te 3 nanowires: how size affects phonon scattering.* Nanoscale, 2017. **9**(20): p. 6741-6747.

368.   Gadea, G., A. Morata, and A. Tarancon, *Semiconductor nanowires for thermoelectric generation*, in *Semiconductors and Semimetals*. 2018, Elsevier. p. 321-407.

369.   Persson, A.I., et al., *Thermal conductance of InAs nanowire composites.* Nano letters, 2009. **9**(12): p. 4484-4488.

370.   Hochbaum, A.I., et al., *Enhanced thermoelectric performance of rough silicon nanowires.* Nature, 2008. **451**(7175): p. 163-167.

371.   Chen, C., et al., *Robustness of topological order and formation of quantum well states in topological insulators exposed to ambient environment.* Proceedings of the National Academy of Sciences, 2012. **109**(10): p. 3694-3698.

372. Snyder, G.J. and E.S. Toberer, *Complex thermoelectric materials.* Materials for sustainable energy: a collection of peer-reviewed research and review articles from Nature Publishing Group, 2011: p. 101-110.

373. Venkatasubramanian, R., et al., *Thin-film thermoelectric devices with high room-temperature figures of merit.* Nature, 2001. **413**(6856): p. 597-602.

374. Goldsmid, H., A. Sheard, and D. Wright, *The performance of bismuth telluride thermojunctions.* British Journal of Applied Physics, 1958. **9**(9): p. 365.

375. Mishra, S., S. Satpathy, and O. Jepsen, *Electronic structure and thermoelectric properties of bismuth telluride and bismuth selenide.* Journal of Physics: Condensed Matter, 1997. **9**(2): p. 461.

376. Greenaway, D.L. and G. Harbeke, *Band structure of bismuth telluride, bismuth selenide and their respective alloys.* Journal of Physics and Chemistry of Solids, 1965. **26**(10): p. 1585-1604.

377. Delves, R., et al., *Anisotropy of the electrical conductivity in bismuth telluride.* Proceedings of the Physical Society (1958-1967), 1961. **78**(5): p. 838.

378. Goldsmid, H., *Recent studies of bismuth telluride and its alloys.* Journal of Applied Physics, 1961. **32**(10): p. 2198-2202.

379. Jacquot, A., et al., *Thermoelectric properties as a function of electronic band structure and microstructure of textured materials.* Journal of electronic materials, 2010. **39**(9): p. 1861-1868.

380. Manzano, C.V., et al., *Anisotropic effects on the thermoelectric properties of highly oriented electrodeposited Bi 2 Te 3 films.* Scientific reports, 2016. **6**(1): p. 1-8.

381. Fleurial, J., et al., *Thermal properties of high quality single crystals of bismuth telluride—Part I: Experimental characterization.* Journal of Physics and Chemistry of Solids, 1988. **49**(10): p. 1237-1247.

382. Bos, J.-W.G., et al., *Structures and thermoelectric properties of the infinitely adaptive series (Bi 2) m (Bi 2 Te 3) n.* Physical Review B, 2007. **75**(19): p. 195203.

383. Dirmyer, M.R., et al., *Thermal and electrical conductivity of size-tuned bismuth telluride nanoparticles.* small, 2009. **5**(8): p. 933-937.

384. Zhao, L., et al., *Enhanced thermoelectric and mechanical properties in textured n-type Bi2Te3 prepared by spark plasma sintering.* Solid State Sciences, 2008. **10**(5): p. 651-658.

385. Yu, F., et al., *Enhanced thermoelectric figure of merit in nanocrystalline Bi 2 Te 3 bulk.* Journal of Applied Physics, 2009. **105**(9): p. 094303.

386. Mehta, R.J., et al., *A new class of doped nanobulk high-figure-of-merit thermoelectrics by scalable bottom-up assembly.* Nature materials, 2012. **11**(3): p. 233-240.

387. Saleemi, M., et al., *Synthesis, processing, and thermoelectric properties of bulk nanostructured bismuth telluride (Bi 2 Te 3).* Journal of Materials Chemistry, 2012. **22**(2): p. 725-730.

388. Scheele, M., et al., *Synthesis and thermoelectric characterization of Bi2Te3 nanoparticles.* Advanced Functional Materials, 2009. **19**(21): p. 3476-3483.

389. Kim, D.-H., et al., *Fabrication and thermoelectric properties of crystal-aligned nano-structured Bi2Te3.* Journal of alloys and compounds, 2011. **509**(17): p. 5211-5215.

390. Kim, D.-H. and T. Mitani, *Thermoelectric properties of fine-grained Bi2Te3 alloys.* Journal of alloys and compounds, 2005. **399**(1-2): p. 14-19.

391. Stavila, V., et al., *Wet-chemical synthesis and consolidation of stoichiometric bismuth telluride nanoparticles for improving the thermoelectric figure-of-merit.* ACS applied materials & interfaces, 2013. **5**(14): p. 6678-6686.

392. Li, C., et al., *Dual-functional aniline-assisted wet-chemical synthesis of bismuth telluride nanoplatelets and their thermoelectric performance.* Nanotechnology, 2017. **28**(23): p. 235604.

393. Mi, J.-L., et al., *Biomolecule-assisted hydrothermal synthesis and self-assembly of Bi2Te3 nanostring-cluster hierarchical structure.* ACS nano, 2010. **4**(5): p. 2523-2530.

394. Fu, J., et al., *Bi 2 Te 3 nanoplates and nanoflowers: Synthesized by hydrothermal process and their enhanced thermoelectric properties.* CrystEngComm, 2012. **14**(6): p. 2159-2165.

395. Zhao, X., et al., *Bismuth telluride nanotubes and the effects on the thermoelectric properties of nanotube-containing nanocomposites.* Applied Physics Letters, 2005. **86**(6): p. 062111.

396. Purkayastha, A., et al., *Low-temperature, template-free synthesis of single-crystal bismuth telluride nanorods.* Advanced Materials, 2006. **18**(4): p. 496-500.

397. Kulsi, C., et al., *Thermoelectric properties of nanostructured bismuth telluride (Bi 2 Te 3) with annealing time and its composite with reduced graphene oxide (RGO).* Journal of Materials Science: Materials in Electronics, 2019. **30**(2): p. 1850-1860.

398. Ju, H., M. Kim, and J. Kim, *A facile fabrication of n-type Bi2Te3 nanowire/graphene layer-by-layer hybrid structures and their improved thermoelectric performance.* Chemical Engineering Journal, 2015. **275**: p. 102-112.

399. Ju, H. and J. Kim, *Preparation and structure dependent thermoelectric properties of nanostructured bulk bismuth telluride with graphene.* Journal of Alloys and Compounds, 2016. **664**: p. 639-647.

400. Li, S., et al., *Graphene quantum dots embedded in Bi2Te3 nanosheets to enhance thermoelectric performance.* ACS applied materials & interfaces, 2017. **9**(4): p. 3677-3685.

401. Peranio, N., O. Eibl, and J. Nurnus, *Structural and thermoelectric properties of epitaxially grown Bi 2 Te 3 thin films and superlattices.* Journal of Applied Physics, 2006. **100**(11): p. 114306.

402. Huang, B., et al., *Low-temperature characterization and micropatterning of coevaporated Bi 2 Te 3 and Sb 2 Te 3 films.* Journal of Applied Physics, 2008. **104**(11): p. 113710.

403. Kim, D.-H. and G.-H. Lee, *Effect of rapid thermal annealing on thermoelectric properties of bismuth telluride films grown by co-sputtering.* Materials Science and Engineering: B, 2006. **131**(1-3): p. 106-110.

404. Na, J., et al., *Preparation of bismuth telluride films with high thermoelectric power factor.* ACS applied materials & interfaces, 2016. **8**(47): p. 32392-32400.

405. Lei, C., M. Burton, and I. Nandhakumar, *Facile production of thermoelectric bismuth telluride thick films in the presence of polyvinyl alcohol.* Physical Chemistry Chemical Physics, 2016. **18**(21): p. 14164-14167.

406. Zou, H., D. Rowe, and S. Williams, *Peltier effect in a co-evaporated Sb2Te3 (P)-Bi2Te3 (N) thin film thermocouple.* Thin Solid Films, 2002. **408**(1-2): p. 270-274.

407. Giani, A., et al., *Growth of Bi2Te3 and Sb2Te3 thin films by MOCVD.* Materials Science and Engineering: B, 1999. **64**(1): p. 19-24.

408. Yonezawa, S., T. Tabuchi, and M. Takashiri, *Atomic composition changes in bismuth telluride thin films by thermal annealing and estimation of their thermoelectric properties using experimental analyses and first-principles calculations.* Journal of Alloys and Compounds, 2020. **841**: p. 155697.

409. Jin, Q., et al., *Enhanced thermoelectric properties of bismuth telluride films with in-plane and out-of-plane well-ordered microstructures.* Scripta Materialia, 2016. **119**: p. 33-37.

410. Yamauchi, K. and M. Takashiri, *Highly oriented crystal growth of nanocrystalline bismuth telluride thin films with anisotropic thermoelectric properties using two-step treatment.* Journal of Alloys and Compounds, 2017. **698**: p. 977-983.

411. Zou, H., D.M. Rowe, and G. Min, *Growth of p-and n-type bismuth telluride thin films by co-evaporation.* Journal of crystal growth, 2001. **222**(1-2): p. 82-87.

412. Bottner, H., et al., *New thermoelectric components using microsystem technologies.* Journal of microelectromechanical systems, 2004. **13**(3): p. 414-420.

413. Huang, H., W.-l. Luan, and S.-t. Tu, *Influence of annealing on thermoelectric properties of bismuth telluride films grown via radio frequency magnetron sputtering.* Thin Solid Films, 2009. **517**(13): p. 3731-3734.

414. Chen, C.-L., et al., *Fabrication and characterization of electrodeposited bismuth telluride films and nanowires.* The Journal of Physical Chemistry C, 2010. **114**(8): p. 3385-3389.

415. Deng, Y., et al., *Growth and transport properties of oriented bismuth telluride films.* Journal of Alloys and Compounds, 2011. **509**(18): p. 5683-5687.

416. Morikawa, S., Y. Satake, and M. Takashiri, *Characteristics of nanostructured bismuth telluride thin films fabricated by oblique deposition.* Vacuum, 2018. **148**: p. 296-302.

417. Lee, J., et al., *Tuning the crystallinity of thermoelectric Bi2Te3 nanowire arrays grown by pulsed electrodeposition.* Nanotechnology, 2008. **19**(36): p. 365701.

418. Zhou, J., et al., *Thermoelectric properties of individual electrodeposited bismuth telluride nanowires.* Applied Physics Letters, 2005. **87**(13): p. 133109.

419. Mavrokefalos, A., et al., *Thermoelectric and structural characterizations of individual electrodeposited bismuth telluride nanowires.* Journal of Applied Physics, 2009. **105**(10): p. 104318.

420. Hamdou, B., et al., *Thermoelectric Characterization of Bismuth Telluride Nanowires, Synthesized Via Catalytic Growth and Post-Annealing.* Advanced Materials, 2013. **25**(2): p. 239-244.

421. Kojda, D., et al., *The effect of a distinct diameter variation on the thermoelectric properties of individual Bi0. 39Te0. 61 nanowires.* Semiconductor Science and Technology, 2014. **29**(12): p. 124006.

422. Shin, H.S., et al., *Twin-driven thermoelectric figure-of-merit enhancement of Bi 2 Te 3 nanowires.* Nanoscale, 2014. **6**(11): p. 6158-6165.

423. Lee, J., et al., *Power factor measurements of bismuth telluride nanowires grown by pulsed electrodeposition.* physica status solidi (RRL)–Rapid Research Letters, 2010. **4**(1-2): p. 43-45.

424. Manzano, C.V., et al., *Thermoelectric properties of Bi 2 Te 3 films by constant and pulsed electrodeposition.* Journal of Solid State Electrochemistry, 2013. **17**(7): p. 2071-2078.

425. Peranio, N., et al., *Stoichiometry controlled, single-crystalline Bi2Te3 nanowires for transport in the basal plane.* Advanced Functional Materials, 2012. **22**(1): p. 151-156.

426. Jin, C., et al., *Electrochemical fabrication of large-area, ordered Bi2Te3 nanowire arrays.* The Journal of Physical Chemistry B, 2004. **108**(6): p. 1844-1847.

427. Li, L., et al., *Pulsed electrodeposition of single-crystalline Bi2Te3 nanowire arrays.* Nanotechnology, 2006. **17**(6): p. 1706.

428. Trahey, L., C.R. Becker, and A.M. Stacy, *Electrodeposited bismuth telluride nanowire arrays with uniform growth fronts.* Nano Letters, 2007. **7**(8): p. 2535-2539.

429. Martın-González, M.S., et al., *Insights into the electrodeposition of Bi2Te3.* Journal of The Electrochemical Society, 2002. **149**(11): p. C546.

430. Russo, V., et al., *Raman spectroscopy of Bi-Te thin films.* Journal of Raman Spectroscopy: An International Journal for Original Work in all Aspects of Raman Spectroscopy, Including Higher Order Processes, and also Brillouin and Rayleigh Scattering, 2008. **39**(2): p. 205-210.

431. Richter, W. and C. Becker, *A Raman and far-infrared investigation of phonons in the rhombohedral V2–VI3 compounds Bi2Te3, Bi2Se3, Sb2Te3 and Bi2 (Te1− xSex) 3 (0< x< 1),(Bi1− ySby) 2Te3 (0< y< 1).* physica status solidi (b), 1977. **84**(2): p. 619-628.

432. Zhao, Y., et al., *Interlayer vibrational modes in few-quintuple-layer Bi 2 Te 3 and Bi 2 Se 3 two-dimensional crystals: Raman spectroscopy and first-principles studies.* Physical Review B, 2014. **90**(24): p. 245428.

433. Rodríguez-Fernández, C., et al., *The fingerprint of Te-rich and stoichiometric Bi2Te3nanowires by Raman spectroscopy.* Nanotechnology, 2016. **27**(7): p. 075706.

434. Mott, D., et al., *Bismuth, antimony and tellurium alloy nanoparticles with controllable shape and composition for efficient thermoelectric devices.* physica status solidi (a), 2011. **208**(1): p. 52-58.

435. Torrie, B., *Raman spectrum of tellurium.* Solid State Communications, 1970. **8**(22): p. 1899-1901.

436. Medlin, D., et al., *Structure of the (0001) basal twin boundary in Bi 2 Te 3.* Journal of Applied Physics, 2010. **108**(4): p. 043517.

437. Gracia-Abad, R., et al., *Omnipresence of Weak Antilocalization (WAL) in Bi2Se3 Thin Films: A Review on Its Origin.* Nanomaterials, 2021. **11**(5): p. 1077.

438. Khalaf, E. and P. Ostrovsky, *Boundary scattering effects on magnetotransport of narrow metallic wires and films.* Physical Review B, 2016. **94**(16): p. 165431.

439. Shrestha, K., et al., *Weak antilocalization effect due to topological surface states in Bi2Se2. 1Te0. 9.* Journal of Applied Physics, 2017. **122**(14): p. 145901.

440. Krieg, J., et al., *Magnetotransport measurements on Bi2Te3 nanowires electrodeposited in etched ion-track membranes.* Journal of Physics and Chemistry of Solids, 2019. **128**: p. 360-366.

441. Kim, H.-S., et al., *Quantum electrical transport properties of topological insulator Bi2Te3 nanowires.* Current Applied Physics, 2016. **16**(1): p. 51-56.

442. Sangiao, S., et al., *Quantitative analysis of the weak anti-localization effect in ultrathin bismuth films.* EPL (Europhysics Letters), 2011. **95**(3): p. 37002.

443. He, H.-T., et al., *Impurity effect on weak antilocalization in the topological insulator Bi 2 Te 3.* Physical review letters, 2011. **106**(16): p. 166805.

444. Hikami, S., A.I. Larkin, and Y. Nagaoka, *Spin-orbit interaction and magnetoresistance in the two dimensional random system.* Progress of Theoretical Physics, 1980. **63**(2): p. 707-710.

445. Torres, P., et al., *Emergence of hydrodynamic heat transport in semiconductors at the nanoscale.* Physical review materials, 2018. **2**(7): p. 076001.

446. Beardo, A., et al., *Hydrodynamic heat transport in compact and holey silicon thin films.* Physical Review Applied, 2019. **11**(3): p. 034003.

447. Alajlouni, S., et al., *Geometrical quasi-ballistic effects on thermal transport in nanostructured devices.* Nano Research, 2021. **14**(4): p. 945-952.

448. Sendra, L., et al., *Derivation of a hydrodynamic heat equation from the phonon Boltzmann equation for general semiconductors.* Physical Review B, 2021. **103**(14): p. L140301.

449. Kaviany, M. and A. Kanury, *Principles of heat transfer.* Appl. Mech. Rev., 2002. **55**(5): p. B100-B102.

450. Hicks, L.D. and M.S. Dresselhaus, *Effect of quantum-well structures on the thermoelectric figure of merit.* Physical Review B, 1993. **47**(19): p. 12727.

451. Cornett, J.E. and O. Rabin, *Thermoelectric figure of merit calculations for semiconducting nanowires.* Applied Physics Letters, 2011. **98**(18): p. 182104.

452. Rittweger, F., et al., *Signature of the topological surface state in the thermoelectric properties of Bi 2 Te 3.* Physical Review B, 2014. **89**(3): p. 035439.

453. Gooth, J., et al., *Thermoelectric performance of classical topological insulator nanowires.* Semiconductor Science and Technology, 2014. **30**(1): p. 015015.

454. Cassinelli, M., et al., *Influence of surface states and size effects on the Seebeck coefficient and electrical resistance of Bi 1− x Sb x nanowire arrays.* Nanoscale, 2017. **9**(9): p. 3169-3179.

455. Hamdou, B., et al., *Surface state dominated transport in topological insulator Bi2Te3 nanowires.* Applied Physics Letters, 2013. **103**(19): p. 193107.

456. Tian, M., et al., *Dual evidence of surface Dirac states in thin cylindrical topological insulator Bi 2 Te 3 nanowires.* Scientific reports, 2013. **3**(1): p. 1-7.

457. Bao, L., et al., *Weak anti-localization and quantum oscillations of surface states in topological insulator Bi 2 Se 2 Te.* Scientific reports, 2012. **2**(1): p. 1-7.

458. Miele, A., et al., *Phonon-drag thermopower and weak localization.* Physical Review B, 1998. **58**(19): p. 13181.

459. Hinsche, N.F., et al., *Impact of the topological surface state on the thermoelectric transport in Sb2Te3 thin films.* Acs Nano, 2015. **9**(4): p. 4406-4411.

460. Palik, E.D., *Handbook of optical constants of solids*. Vol. 3. 1998: Academic press.

461. Yablonovitch, E., *Inhibited spontaneous emission in solid-state physics and electronics.* Physical review letters, 1987. **58**(20): p. 2059.

462. John, S., *Strong localization of photons in certain disordered dielectric superlattices.* Physical review letters, 1987. **58**(23): p. 2486.

463. Hale, G.M. and M.R. Querry, *Optical constants of water in the 200-nm to 200-μm wavelength region.* Applied optics, 1973. **12**(3): p. 555-563.

464. Fernández-Roldán, J.A., Y.P. Ivanov, and O. Chubykalo-Fesenko, *Micromagnetic modeling of magnetic domain walls and domains in cylindrical nanowires*, in *Magnetic Nano-and Microwires*. 2020, Elsevier. p. 403-426.

465. Wood, C., *Materials for thermoelectric energy conversion.* Reports on progress in physics, 1988. **51**(4): p. 459.

466. Haras, M. and T. Skotnicki, *Thermoelectricity for IoT–A review.* Nano Energy, 2018. **54**: p. 461-476.